How do faults grow in magmatic rifts? LiDAR and InSAR observations of the Dabbahu rift segment, Afar, Ethiopia.

Barbara Hofmann

Submitted in accordance with the requirements for the degree of
Doctor of Philosophy

The University of Leeds
School of Earth and Environment
November 2013

Declaration

The candidate confirms that the work submitted is her own and that appropriate credit has been given where reference has been made to the work of others.

First and foremost I would like to thank my supervisors Tim Wright and Douglas Paton from the University of Leeds, Julie Rowland from the University of Auckland and Charlotte Vye-Brown from the British Geological Survey for their tremendous support, encouragement and patience. I am truly grateful.

Many thanks go to Sheona, Helene and Suzanne who were there for my greatest moments as well as the not so good ones. Thanks to all the great people who made me feel so welcome when I first arrived especially Dulce, Matt, Ian, Karen and Tom and to the ones who saw me through till the end especially Jo, Luke, Hannah, Julia, Emma, Luke, Haggis and Sandra. And of course thank you Richard for fixing all the big and small IT problems.

Matt Parker, your unwavering believe in me and and enthusiasm for everything science always reminded me why I was doing this. I wish you were still here to see this.

Ben, thank you for just being there and making me laugh.

And finally I would like to thank my family. Without their continuous support and encouragement I would have never started on this route of science and I'm very glad I did.

Dyke intrusions and normal faulting play an important role during continental break-up but little is known about how the normal faults develop. Direct evidence of dyke-induced faulting is limited by the lengthy repeat times between individual rifting episodes, the small amount of subaerial rift zones and until recently the technical ability to record small surface changes across large areas. The most recent (2005-2010) rifting episode at the Dabbahu rift segment, Afar, Ethiopia provided a unique opportunity to study dyke-induced fault growth. The combination of new high-resolution topographic LiDAR data and interferometric synthetic aperture radar (InSAR) data provides information of cumulative as well as incremental fault throw.

In this thesis I use high-resolution LiDAR data of the Dabbahu rift segment to reveal a dense network of short fault segments (>3400) at various stages of fault linkage set in flood basalt plains. I develop and present a semi-automatic algorithm that extracts throw along surface fault traces from the high-resolution LiDAR DEM. The largest amount of throw (∼80 m) is found on faults towards the east of the rift segment. At the central Ado'Ale volcanic edifice predominant bookshelf faulting is evident which might be an indication of a lateral shift of the dykes towards the east. I use the throw data to derive a strain field for the rift. Faults record ∼140 m of extension, implying extensive resurfacing.

I derived displacement data from two LiDAR surveys and InSAR data, for two separate dyke intrusions. Both data sets show that faults are re-activated in a broad, 3-4 km wide, asymmetric zone parallel to the dyke induced subsidence with the majority of the new throw being accumulated on 1-2 large west-dipping fault structures in the east. The incremental displacement-length, $d - L$, data presented here is the first quantitative study of accumulation of new fault throw across an entire rift segment. Incremental throw across linkage zones suggest two types of behaviour once fault linkage is complete. 1) Individual fault segments maintain the ability to slip independently. This was previously only observed during analogue modelling. 2) The connected faults act as one throughgoing fault with slip unaffected by the linkage zone. The combination of these two processes might be responsible for the commonly observed small-scale corrugation in $d - L$ data. In contrast to published fault growth models, I present evidence that the remnant fault tip of a linkage zone does not necessarily become inactive once linkage is complete, and that linkage zones do not 'catch up' through accelerated throw once linkage is complete.

Contents

List of Figures

List of Tables

Chapter 1

Introduction

The 2005-2010 rifting episode at the Dabbahu rift segment, Afar, Ethiopia, was the first rifting episode that was extensively monitored with remote sensing. In this thesis I use satellite and high-resolution topographic data to investigate how faults grow in a magmatic system that is otherwise almost inaccessible.

In this chapter I will summarise the current understanding of normal fault growth. I will then introduce the Dabbahu rifting segment, Ethiopia, in the context of the Afar Depression and give an overview of the 2005-2010 rifting episode. I will conclude this chapter with the aims of this thesis and an outline.

1.1 Normal faults - initiation and propagation

Normal faults are found worldwide at divergent plate boundaries as well as volcanic edifices (Rubin and Pollard, 1988). They play a major role in the formation of basins, mining and hydro-carbon exploration and understanding their initiation and propagation is of great importance to mitigating earthquake hazards. Displacement-length profiles of isolated normal faults within uniform lithology typically show maximum displacement at the centre, tapering to zero at the fault tips (e.g. Rippon, 1984, Barnett et al., 1987, Dawers et al., 1993), indicating that slip accumulates at the interior of the fault thereby increasing the stress at the fault tips and causing lateral fault growth (Scholz, 1991). These observations gave rise to the expectation of a scaling law relating maximum displacement and fault length.

Finding such a scaling relationship has proven to be difficult as most of the data sets only span 1-2 orders of magnitude and exhibit a large amount of scatter (Fig. 1.1). The scatter has been attributed to a number of different reasons: differences in measurement type (Gillespie et al., 1992), rock properties and tectonic setting (Cowie and Scholz, 1992a), mechanical stratigraphy (Schultz and Fossen, 2002), kinematics (Bürgmann et al., 1994, Gross et al., 1997), fault linkage (Peacock and Sanderson, 1991, Bürgmann et al., 1994, Cartwright et al., 1995, Wojtal, 1996, Willemse et al., 1996, Willemse, 1997), propagation history (Peacock and Sanderson, 1996), reactivation (Kim et al., 2001) and intrinsic scale variation (Watterson, 1986, Wojtal, 1994, 1996, Gross et al., 1997). Fig. 1.1 shows a maximum displacement vs. fault length plot (d_{max}/L ratio) of previously published work on normal faults (figure taken from Kim and Sanderson, 2005).

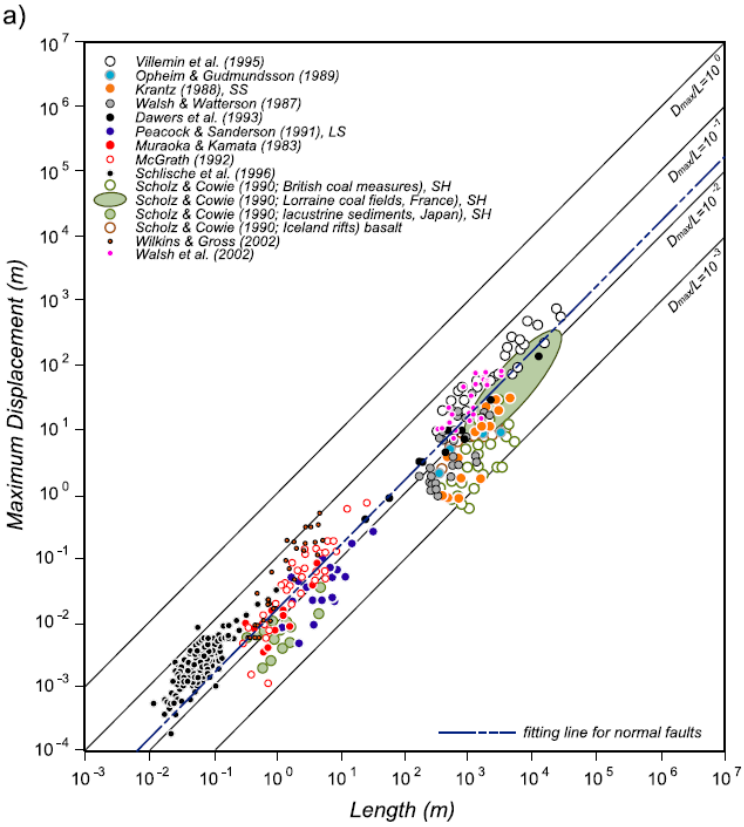

Figure 1.1: Displacement-length scaling relationship of normal faults derived from different data sets. Reprinted from Kim and Sanderson (2005) with permission from Elsevier.

Nevertheless, two widely accepted models for fault propagation have been developed distinguishing between isolated fault growth and segmented fault growth (Fig. 1.2). The former is in agreement with early observations proposing a smooth single slip surface that increases in length and/or displacement as it evolves (e.g. Watterson, 1986,

Walsh and Watterson, 1987, 1988, Marrett and Allmendinger, 1991, Cowie and Scholz, 1992b,a). They propose a relationship of the form $d_{max} = cL^n$ with c dependent on rock properties. For isolated faults a linear relationship ($n = 1$) between d_{max} and L is most commonly observed (Fig. 1.3 a, e.g. Dawers et al., 1993, Cowie and Scholz, 1992a). Other models propose $n > 1$ leading to a faster accumulation of displacement (Fig. 1.3 b, e.g. Walsh and Watterson, 1987) and the extreme case proposed by Walsh et al. (2002) in which the fault length remains constant after its initial formation (Fig. 1.3 c). Fig. 1.3 d illustrates a step-like growth model for linked faults (e.g. Cartwright et al., 1995).
Larger normal faults are usually formed through linkage of smaller fault segments (e.g. Childs et al., 1995, Dawers and Anders, 1995) and understanding how this interaction influences fault growth and segment geometry has been the focus of several studies since the 1990s (e.g. Morley et al., 1990, Peacock and Sanderson, 1991, Trudgill and Cartwright, 1994, Dawers and Anders, 1995, Cartwright et al., 1995, Willemse et al., 1996, Crider and Pollard, 1998, Gupta and Scholz, 2000, Peacock, 2002).

Peacock and Sanderson (1991) first observed that fault linkage modifies the expected $d-L$ pattern of isolated fault segments. Combining field observations (e.g. Cartwright et al., 1995) and results from numerical modelling (e.g. Willemse et al., 1996, Willemse, 1997), Gupta and Scholz (2000) presented a detailed model for fault growth through fault linkage (Fig. 1.4). Initially the two isolated fault segments grow independently forming a classic bow-shaped $d-L$ pattern (Fig. 1.4 a). As the fault segments approach each other models of Coulomb stress changes and boundary element models suggest that lateral propagation towards each other is encouraged until they enter each others "stress shadow", which impedes lateral propagation (Fig. 1.5, Hodgkinson et al., 1996, Ackermann and Schlische, 1997, Gupta et al., 1998, Willemse et al., 1996). The $d-L$ profile becomes increasingly asymmetric, steepening towards the interacting fault tip (Fig. 1.4 b, c, d). Once linkage is complete the combined fault is expected to behave similar to an isolated fault growing in lateral and vertical direction, and the displacement deficit across the former ramp is expected to reduce.

On the surface, fault linkage is expressed through the tilting of beds and the formation of a relay ramp between two overlapping fault segments (Fig. 1.6). As the process continues, the faults start curving towards each other and minor short en-echelon faults and fissures are formed across the ramp. At this stage the faults are referred to as 'soft

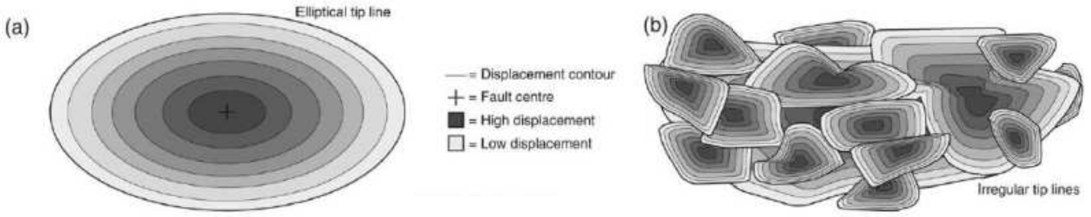

Figure 1.2: Schematic of idealised vs. real fault slip distribution. a) Idealised normal fault: Tip-line is elliptical with maximum displacement at the centre gradually tapering to zero at the tip. b) Segmented normal fault: Interaction between segments disturbs the elliptical shape of single slip events which accumulate to the overall displacement. Reprinted from Peacock (2002) with permission from Elsevier.

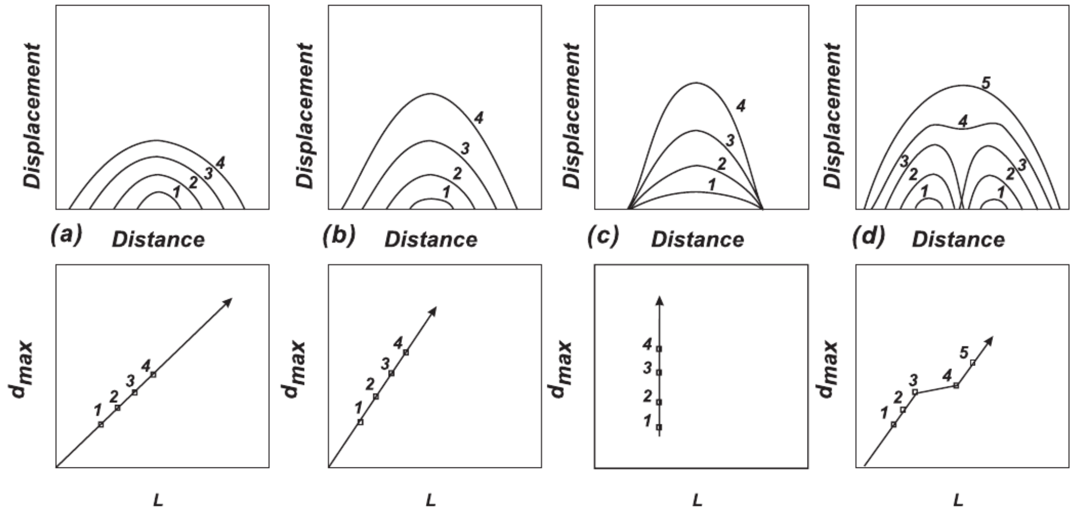

Figure 1.3: Different fault growth models: a) Constant d_{max}/L ratio with n=1; b) d_{max}/L ratio with n>1; c) Constant length model (Walsh et al., 2002); d) Fault linkage model (e.g. Peacock and Sanderson, 1991, Cartwright et al., 1995, Kim et al., 2000, Gupta and Scholz, 2000). Reprinted from Kim and Sanderson (2005) with permission from Elsevier.

linked' but may already be joined at depth (Fig. 1.6 a, e.g. Trudgill and Cartwright, 1994, Davies et al., 1997, Peacock and Parfitt, 2002). In the next stage the ramp is breached by a throughgoing fault connecting the two segments along a single irregular fault. The faults are now 'hard linked' (Fig. 1.6 b). Breaching has been observed across both the upper ramp and/or lower ramp (e.g. Trudgill and Cartwright, 1994, Crider and Pollard, 1998, Çiftçi and Bozkurt, 2007). If breached across the upper ramp the tip of the rear segment connects with the front segment (Fig. 1.6 c), while if breached across the lower ramp the fault tip of the the front segment curves towards the rear segment (Fig. 1.6 d). In both cases the remaining fault tip is believed to become inactive. In the case of upper-ramp breaching the ramp gets destroyed as the connected

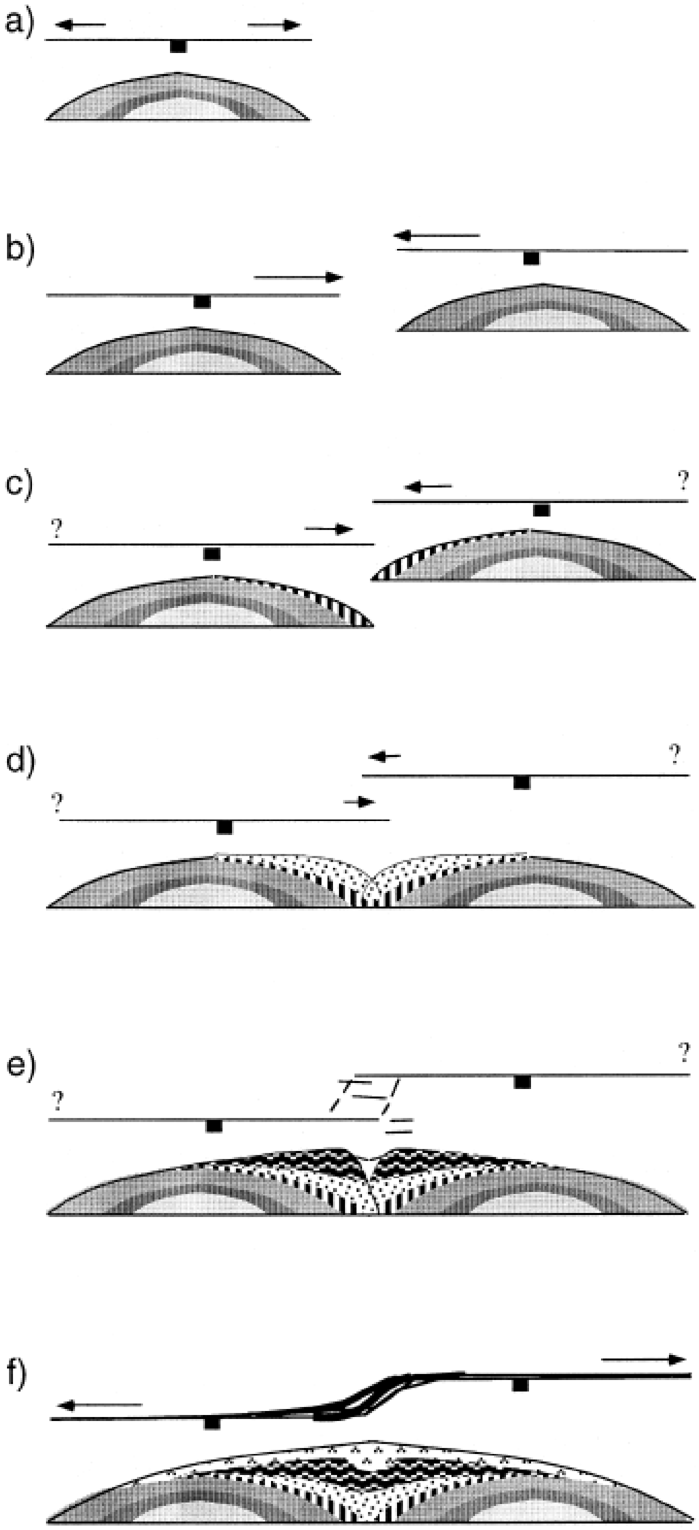

Figure 1.4: Conceptual model of fault growth by linkage. Arrows indicate direction of fault propagation, shading in $d - L$ shape illustrate individual slip events: a) isolated fault; b) fault segments propagate towards each other encouraged by each others stress field; c and d) lateral propagation is suppressed by the stress field, asymmetric accumulation of displacement; e) critical stress drop is reached linkage occurs, f) Linkage is complete, lateral propagation recommences, displacement deficit has been reduced. Reprinted from Gupta and Scholz (2000) with permission from Elsevier.

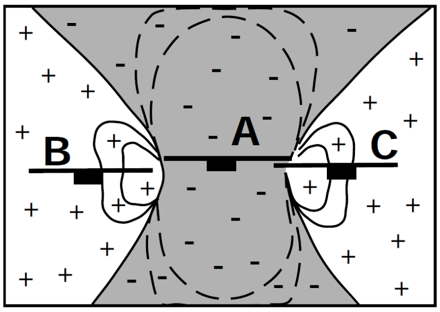

Figure 1.5: Coulomb stress changes (after Hodgkinson et al., 1996) induced by normal fault slip on the central structure A. All three fault structures (A, B and C) dip at 60°. Grey area: region of stress enhancement suppressing fault slip; white area: region of stress relaxation encouraging fault slip. Republished with permission of GEOLOGICAL SOCIETY OF AMERICA, from Gupta et al. (1998); permission conveyed through Copyright Clearance Center, Inc.

fault accumulates displacement. Boundary element modelling suggests that the type of breaching is dependant on the direction of the fault step in relation to the direction of oblique slip (Crider, 2001). Particularly across extensive rift systems, a great diversity in relay structure and associated graben formation has been observed. This diversity has been associated with the initial spacing and overlap between faults (Allken et al., 2013) and may be affected by the relative age of the structures in respect of the entire array and mechanical anisotropy of the deformed medium (Trudgill and Cartwright, 1994).

Linkage zones, fault segments and segment boundaries play a great role in earthquake dynamics and hazard mitigation (e.g. Wesnousky, 1986, Crone and Haller, 1991, Wesnousky, 2008). Ruptures have been observed to both jump across soft linked relay zones as well as stop at segment boundaries (Crone and Haller, 1991, Wesnousky, 2008) and it is still unclear if segment boundaries are temporary or permanent features.

1.2 Afar depression

Located mainly in Ethiopia and set within a thick layer of Paleogene flood basalts, the Afar Depression is part of the triple junction separating the Nubian, Arabian and Somalian plates (Fig. 1.7) and is one of the few places where the final stages of continental breakup can be witnessed (e.g. Hayward and Ebinger, 1996).

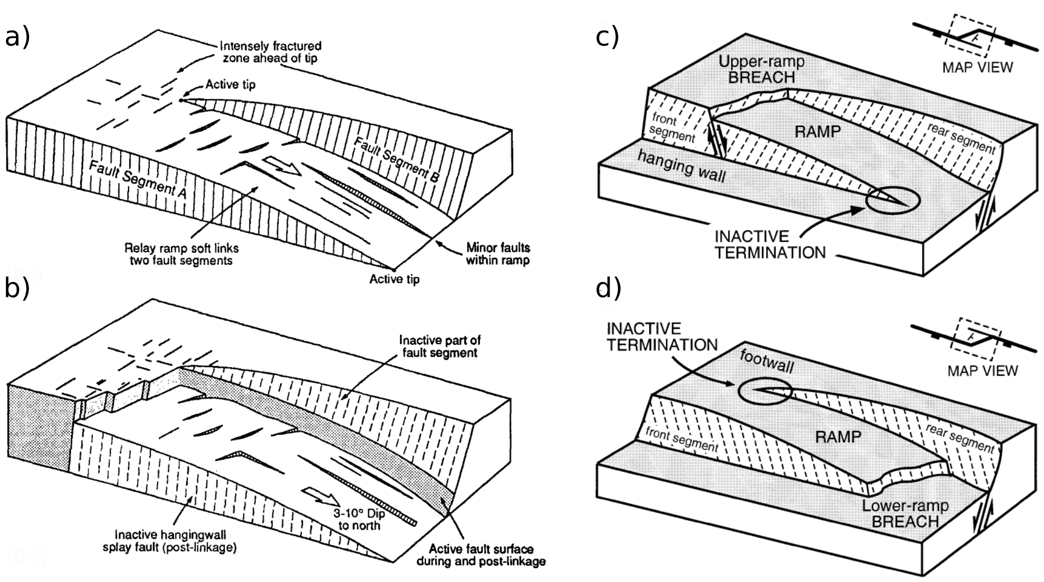

Figure 1.6: Relay ramps. a) Intact relay ramp, faults are 'soft linked'; b) Breached relay ramp, faults are 'hard linked'; c) Upper-ramp breach, faults are connected from the tip of the rear segment; d) Lower-ramp breach, faults are connected from the front segment. In both cases the remaining fault tip is assumed to become inactive. Republished with permission of GEOLOGICAL SOCIETY OF AMERICA from (a) and b) from Trudgill and Cartwright, 1994) permission conveyed through Copyright Clearance Center, Inc. c) and d) reprinted from Crider (2001) with permission from Elsevier.

The Afar depression, also called the Danakil depression, forms a triangle and is enclosed by the large border faults of the Ethiopian plateau in the West and the Somalian plateau to the southeast. In the northeast the isolated Danakil horst block separates the low-lying depression, with areas up to 120 m below sea level, from the Red Sea (Fig. 1.7).

Rifting is associated with the Afar plume (e.g. Hofmann et al., 1997, Bastow et al., 2008) and commenced towards the end of, or shortly after the emplacement of the flood basalts 31-29 Ma ago (e.g. Wolfenden et al., 2005). Since then, the Gulf of Aden and the Red Sea north of 14° N, have progressed to oceanic spreading (e.g. Manighetti et al., 1998). South of 14° N the Red Sea is subaerial. GPS measurements indicate a north-south transgression of extension between 16° N - 13° N. In the north, extension occurs completely at the Red Sea rift; in the south, extension occurs within the Danakil Depression (McClusky et al., 2010). Hayward and Ebinger (1996) and Wolfenden et al. (2005) show that as rifts mature the large border faults are abandoned and new intrarift graben are formed. Lahitte et al. (2003) have suggested that this is accompanied by a change of volcanism from mainly rhyolite to basalt flows. Strain is then further focused forming magmatic rift segments with localised dyke intrusions before it finally transforms into oceanic spreading.

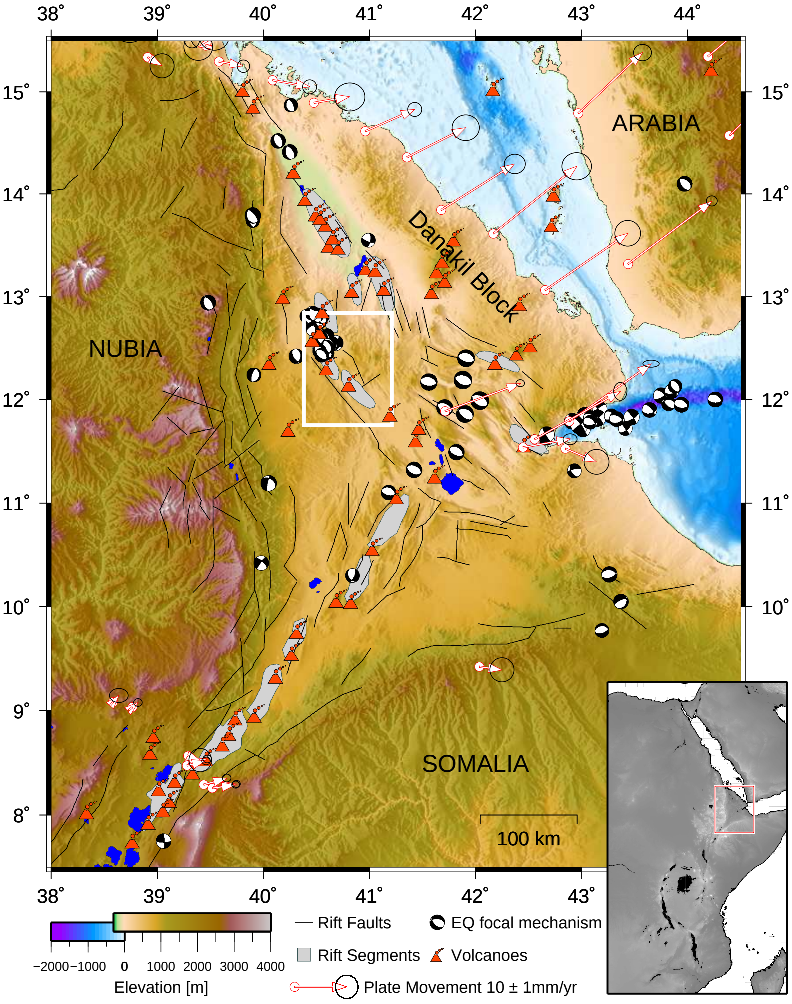

Figure 1.7: Overview of the the Afar depression. White rectangle marks the location of the Dabbahu rift segment. Black lines indicate rift faults, grey polygons outline rift segments both after Hayward and Ebinger (1996), arrows show annual plate movement with respect to Nubia after McClusky et al. (2010), volcanoes from Siebert and Simkin (2002), lower hemisphere projection fault plane solutions, 1976-2013, from Dziewoński et al. (1981), Ekström et al. (2012). DEM after Amante and Eakins (2008).

Dates within the Afar region are sparse, but since the last 3 Ma (Lahitte et al., 2003) rifting activity has been localised on magmatic segments. The Afar depression is dominated by NNW-trending faulted magmatic segments at 55-85 km intervals and shield volcanoes such as Erta Ale, Tat Ale and Alyata (Beyene and Abdelsalam, 2005, Barberi et al., 1972, Hayward and Ebinger, 1996). Typically, individual segments are elongated (60 x 10 km) zones with fissure lava flows, aligned basaltic scoria cones, volcanic edifices, shallow seismicity, positive gravity anomalies, collapsed graben and tilted fault blocks (e.g. Barberi and Varet, 1977, Hayward and Ebinger, 1996). Similar observations have been made at oceanic ridge segments (e.g. Pollard and Aydin, 1984).

1.3 2005-2010 Dabbahu rifting episode

The most recent rifting episode commenced in September 2005 at the Dabbahu segment (Fig. 1.7 white box and Fig. 1.8), which forms, together with the currently inactive Harraro segment, the Manda-Harraro rift zone (Rowland et al., 2007). The Dabbahu segment is approximately ∼60 km long and ∼15 km wide and is characterised by its two active rhyolitic volcanoes Dabbahu and Gab'ho in the North and the dissected Ado'Ale volcanic complex (AVC) at its centre.

The onset of the 2005-2010 rifting episode was marked by a $M_w \approx 4.3$ earthquake on 4 September 2005 (Ayele et al., 2009) and was followed by a month-long period of intermittent seismic activity along the length of the segment, (Fig. 1.8) (e.g. Wright et al., 2006, Rowland et al., 2007, Ebinger et al., 2008, Ayele et al., 2009).

In the 4 weeks until the 4 October 2005, 420 earthquakes were recorded. From 20-23 September seismicity was located mainly at the northern part beneath the volcanoes Dabbahu and Gab'ho. On the 24th seismicity shifted to the Ado'Ale complex and migrated northwards at an estimated rate of 15-30 cm/s (Ayele et al., 2009).

Eyewitnesses observed a small explosive silicic eruption on September 26 at Da'Ure northeast of Dabbahu volcano (Fig. 1.8; Yirgu et al., 2006, Ayele et al., 2007). The eruption caused the opening of a 500 m long, 100 m wide and 60 m deep vent oriented north-south (Wright et al., 2006). During a subsequent field campaign, recent fault slip of up to 3 m, along fault scarps of approximately 2 km length, were visible as light bands on fault scarps north of AVC, as well as recently opened fissures (Fig. 1.9; Rowland et al., 2007).

Surface deformation data derived from satellite radar and optical image matching (Wright et al., 2006, Ayele et al., 2007, Grandin et al., 2009, Barisin et al., 2009)

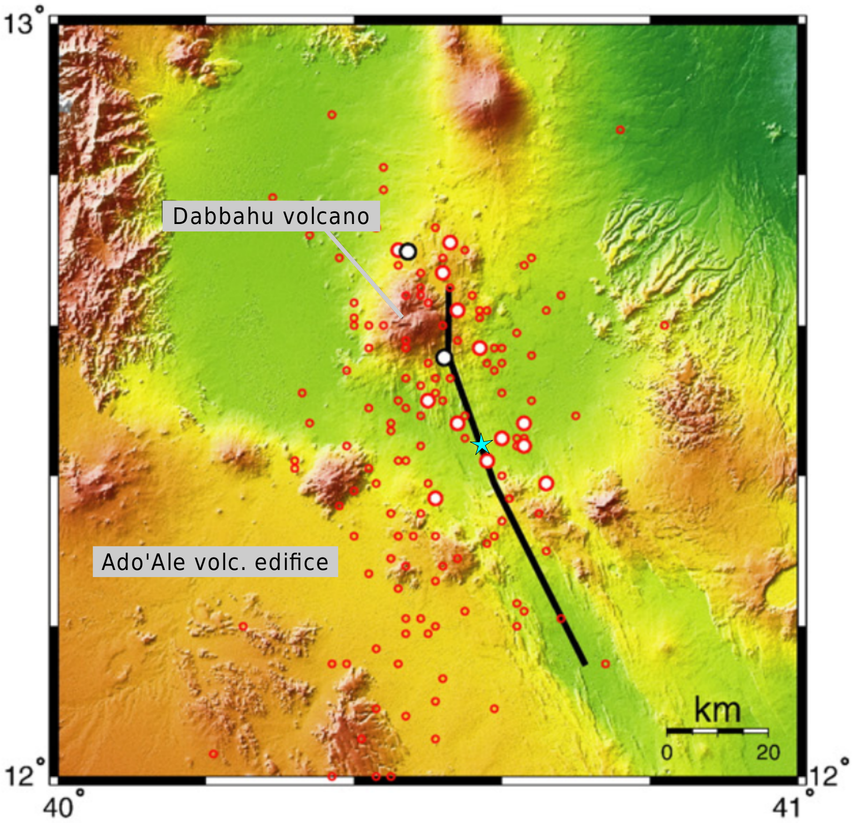

Figure 1.8: Dabbahu rift segment dominated by the Dabbahu and Gab'ho volcanoes in the North and the Ado'Ale volcanic edifice at the centre. Location of the September 2005 dyke intrusion (black) and associated seismicity (red). Blue star location of figure 1.9. Modified after Ayele et al. (2007) with permission of Elsevier.

showed meter scale surface deformation along the entire 65 km of the rift segment. A 25 km-wide zone was uplifted by up to 1.5 m at the flanks of the rift while the centre (2-3 km-wide zone) of the rift subsided by as much as 2 m, with maximum horizontal opening of 6 m. Dabbahu and Gab'ho volcano subsided by 2-3 m. The surface displacements and observed seismicity are characteristic for laterally propagating magmatic dyke intrusions (Rubin and Pollard, 1988). Simple elastic modelling suggests the dyke intrusion to be situated between 2-9 km depth with an estimated 2-3 km^3 intruded volume (Wright et al., 2006, Grandin et al., 2009).

3D surface displacements generated from SPOT4 imagery and InSAR showed asymmetrical flank uplift, with an eastward shift of the intrusion axis compared to the segment axis. Apparent slip on bounding faults was distinctly offset along the rift's length

Figure 1.9: Approximately 3 m of fresh fault slip caused by the September 2005 intrusion. Location 12.42 N 40.57 W marked by blue star in figure 1.8. Photo personal communication J Rowland.

which is best fit by a 80° W dipping dyke and fault slip on one side of the intrusion (Barisin et al., 2009). Estimates of moment release show a significant difference of an order of magnitude between the geodetic moment release ($\sim 8.0 \times 10^{19}$ Nm) and the seismic moment release ($\sim 6.7 \times 10^{18}$ Nm) (Wright et al., 2006, Grandin et al., 2009, Ayele et al., 2009).

Since this initial dyke intrusion 13 smaller events have occurred (Wright et al., 2012). Elastic modelling and seismicity studies suggest that the later dykes were fed from a magma source close to the Ado'Ale complex and emplaced to the east of the geomorphic axis (e.g. Hamling et al., 2009, Ebinger et al., 2008, Keir et al., 2009). Fig. 1.10 displays the distribution of the individual dyking events over time and space. During three of the later intrusions small short-lived basaltic eruptions (hours-days) occurred south of Ado'Ale (Ferguson et al., 2010).

1.4 Thesis aims and outline

Although initiation and propagation of normal faults has been the focus of many studies since the 1980s, observations of fault growth are limited to analogue models (Mansfield and Cartwright, 2001) and individual earthquake ruptures (e.g. Wesnousky, 2008).

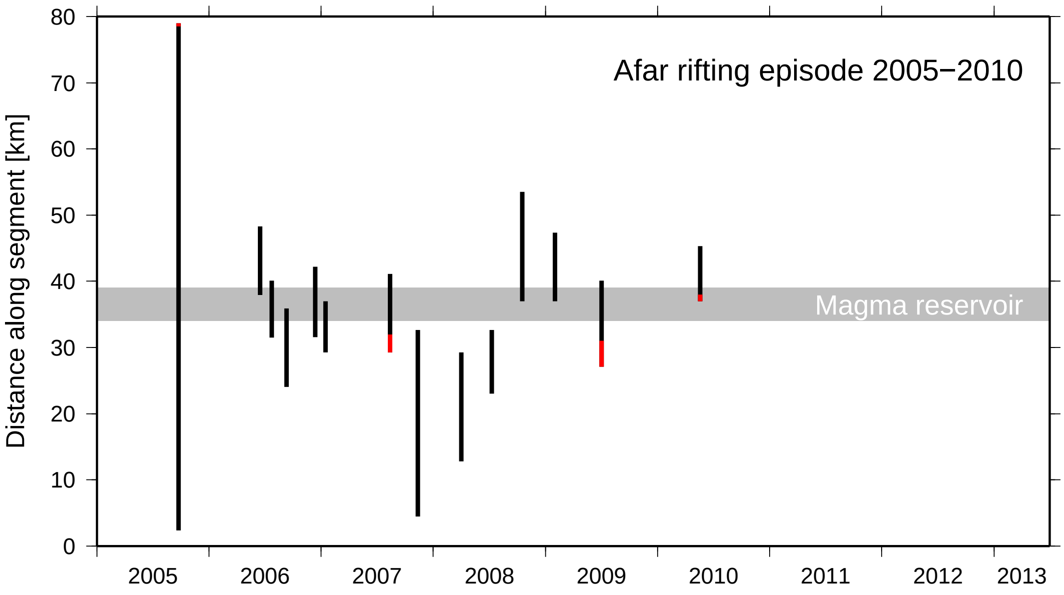

Figure 1.10: Extent and timing of the 14 dyke intrusions along the Dabbahu rift. Black dyke length, red fissure eruption length Grey approximated location of Magma reservoir below AVC (modified after Hamling et al., 2009)

Fault growth models infer the incremental steps of fault growth from the cumulative data. The extensive remote monitoring of the surface deformation during the 2005-2010 rifting episode at the Dabbahu segment provides a unique opportunity to study dyke-induced fault growth and compare existing fault growth models with incremental fault growth patterns.

Specifically this thesis aims to

- investigate the use of high-resolution LiDAR and InSAR data to quantify cumulative and incremental fault displacement.
- use the data to test models of fault growth.

This thesis is composed of 6 chapters including this introduction:

- Chapter 2: I introduce the high-resolution LiDAR and InSAR data sets which form the base of my thesis including some details on data acquisition and processing (§ 2).
- Chapter 3: I describe my semi-automatic algorithm which routinely extracts throw vs. fault length from the 2009 high-resolution LiDAR data set and also

measures slip, that occurred during the October 2008 intrusion, from the InSAR data and slip, that occurred during the May 2010 dyking event, from differential LiDAR data (§ 3).

- Chapter 4: I apply my algorithm to the fault segments. I examine the overall behaviour of the fault segments, examine fault linkage zones, show examples of the derived $d - L$ profiles and estimate the strain recorded in the faults within the Dabbahu rift segment (§ 4).
- Chapter 5: I use InSAR and differential LiDAR data to identify the location and shape of slip induced by lateral dyke intrusions from October 2008 and May 2010 and use the results to test models of fault growth (§ 5).
- Chapter 6: I summarise my results and conclude (§ 6).

Chapter 2

Data sets

My work is based primarily on two high-resolution airborne LiDAR surveys and I also use InSAR (Interferometric synthetic aperture radar) to measure fault displacement during two dyke intrusion events at the Dabbahu rift segment, Afar. In this chapter, I will first describe the LiDAR principles and acquisitions, and then introduce the two data sets and the data processing. In the second part I will explain the principles of InSAR, describe the characteristics of the ALOS satellite data used, and outline the main data processing steps applied.

2.1 LiDAR

With the development of the laser, and the precise knowledge of its wavelength and beam divergence, laser ranging became a highly accurate method to measure distances. It was first developed in the 1960s by NASA and lunar laser ranging (LLR) started with the placement of retroreflectors on the moon during the Apollo 11 mission in 1969 (Bender et al., 1973). Until the 1990s laser ranging was limited to point measurements, but with technological advances it became possible to survey areas and airborne LiDAR (LIght Detection And Ranging) has since been applied to questions in a range of diverse applications including urban development, forestry, agriculture, archaeology and geoscience (e.g. Maune, 2001, Lim et al., 2003, Passalacqua et al., 2010, Fernandez, 2011).

The two airborne LiDAR surveys which I use in this thesis cover the central section of the Dabbahu segment and were acquired by the United Kingdom Natural Environment Research Council's Airborne Research and Survey Facility (NERC ARSF).

2.1.1 Airborne LiDAR

Fig. 2.1 shows the principle of airborne LiDAR. The main component is the laser unit, which is attached to the bottom of the aircraft, here a Dornier 228:D-CALM, and consists of the transmitter, receiver and a moving mirror which distributes the laser pulses across the width of the recorded swath. When the laser pulse hits a reflector it is returned to the receiver where its travel time and scan angle is recorded and converted into range to the reflector. The pulse will not only be returned by the ground but also by any clouds and sand in the air and vegetation above the ground surface. The Leica ALS50-II LiDAR system, which was used for both surveys, stores the first three returns and the last return, which corresponds to the return from the ground, for each laser pulse. Airborne LiDAR systems commonly use diode-pumped lasers which can produce short, large intensity Gaussian shaped pulses at high repetition rates. The laser of the ALS50-II has a wavelength of 1064 nm with a nominal output beam divergence of 0.22 mrad at the $1/e^2$ point (Geosystems AG, 2007) which translates into a ground footprint of ~70 cm diameter for the average survey flight altitude of 3400 m above mean ground level (amgl) for the 2009 LiDAR survey and ~50 cm diameter for the average survey flight altitude of 2600 m amgl for the 2012 survey. It is further equipped with an oscillating mirror, which compared to rotating mirrors, ensures that every pulse is directed towards the ground. This effectively doubles the nominal scan frequency of the instrument because two scan lines are recorded during each oscillation cycle (Ussyshkin and Boba, 2008). The sinusoidal scan pattern of the system leads to a higher density of returns along the swath edges in the scan direction but relatively poor coverage in the flight direction (Fig. 2.2a). At the swath centre the distribution of returns in flight direction and scan direction are more equal, ~2 m in both directions for the 2009 survey (Fig. 2.2b). Return spacing along scan direction depends on pulse repetition frequency (PRF), scan frequency and flight altitude, whereas spacing in flight direction primarily depends on the aircraft's speed and its altitude. The swath width on the ground is governed by the flight altitude and scan angle. Therefore the density of illuminated points on the ground and with it the maximum resolution of the resulting digital elevation model (DEM) is dependant on a combination of flight altitude amgl, PRF, scan frequency, scan angle and mirror movement and degree of overlap between individual swaths. ALS50-II LiDAR specifications can be found in table 2.1. In order to georeference each return the aircraft is further equipped with a GPS antenna and a high-accuracy inertial measurement unit (IMU).

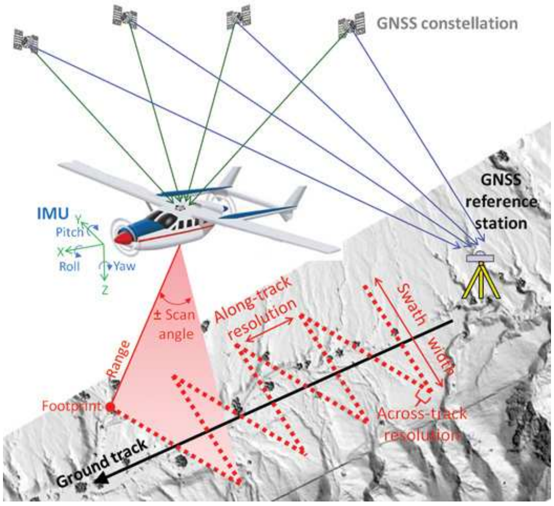

Figure 2.1: Principle of airborne LiDAR taken from (Fernandez, 2011). The laser unit is attached to the bottom of the aircraft. An oscillating mirror distributes the laser pulse across the swath width perpendicular to the flight direction. Swath width is dependent on the scan angle and flight altitude. Forward motion of the aircraft creates a zig-zag scan pattern. The aircraft is also equipped with a IMU and GPS system which in combination with ground based GPS stations enables accurate positioning of the aircraft and returns.

max Pulse repetition frequency (PRF)	150000 Hz
max field of view (FOV)	75°
max flight altitude	6000 m agl
saved returns	1st, 2nd, 3rd, last return

Table 2.1: Leica ALS50-II LiDAR specifications

2.1.2 Surveys

October 2009 survey:

The survey was acquired during 25-27 October 2009. Fig. 2.3 shows the outline of the survey (blue) covering the central section of the Dabbahu segment. It encompasses the volcanoes Dabbahu and Gabho in the North and stretches South past the regional capital Semera (DASM). Additional to the roughly 10-15 km wide and 60 km long main polygon multiple cross-lines were acquired to tie in with other surveys carried out by members of the Afar consortium such as magnetotelluric and gravity measurements. The figure further shows the locations of the Afar consortium's continuous GPS (cGPS)

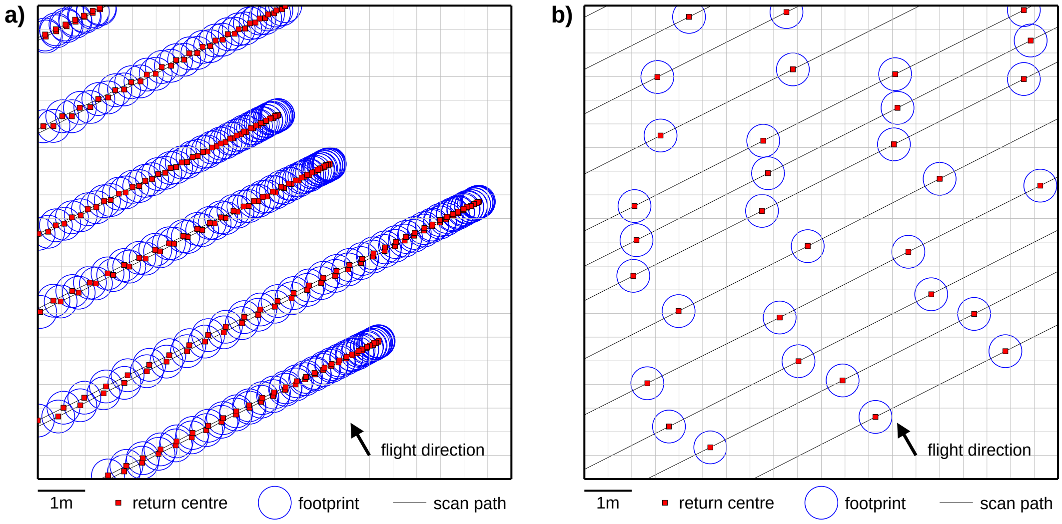

Figure 2.2: Example return distributions along swath edge (a) and in the swath centre (b) from the 2009 LiDAR survey. Each swath is ~3000 m wide. Blue circles outline the footprint of each return, ~70 cm in diameter, and red squares indicate the centre of the return. Thin black lines show the scan path. Black arrow indicates the flight direction.

stations (yellow triangles) which were used as base stations for the LiDAR survey. The entire survey covers an area of 2100 km^2 with the central section covering 1400 km^2. The survey consists of 55 flight tracks of ~3000 m width. In total over 900×10^6 returns were recorded. Weather conditions during all three survey days were very clear with only slight haze reducing data quality to 7-9 out of 10 on the ARSF's qualitative scale. On average the survey was acquired at 3400 m amgl. Details for each survey day can be found in tables 2.2 and 2.3.

Date	Area	avg. alt. amgl.	Gnd speed	PRF	Scan freq.	FOV
25.10.09	Mid	3400 m	303 km/h	76200 Hz	58 Hz	24
26.10.09	North	3400 m	305 km/h	79200 Hz	41 Hz	24
27.10.09	South	3400 m	333 km/h	78200 Hz	41 Hz	24

Table 2.2: Column 1-4: Survey acquisition details: date, survey area, average flight altitude amgl., ground speed; column 5-7: Instrument settings: pulse repetition frequency, scan frequency, field of view

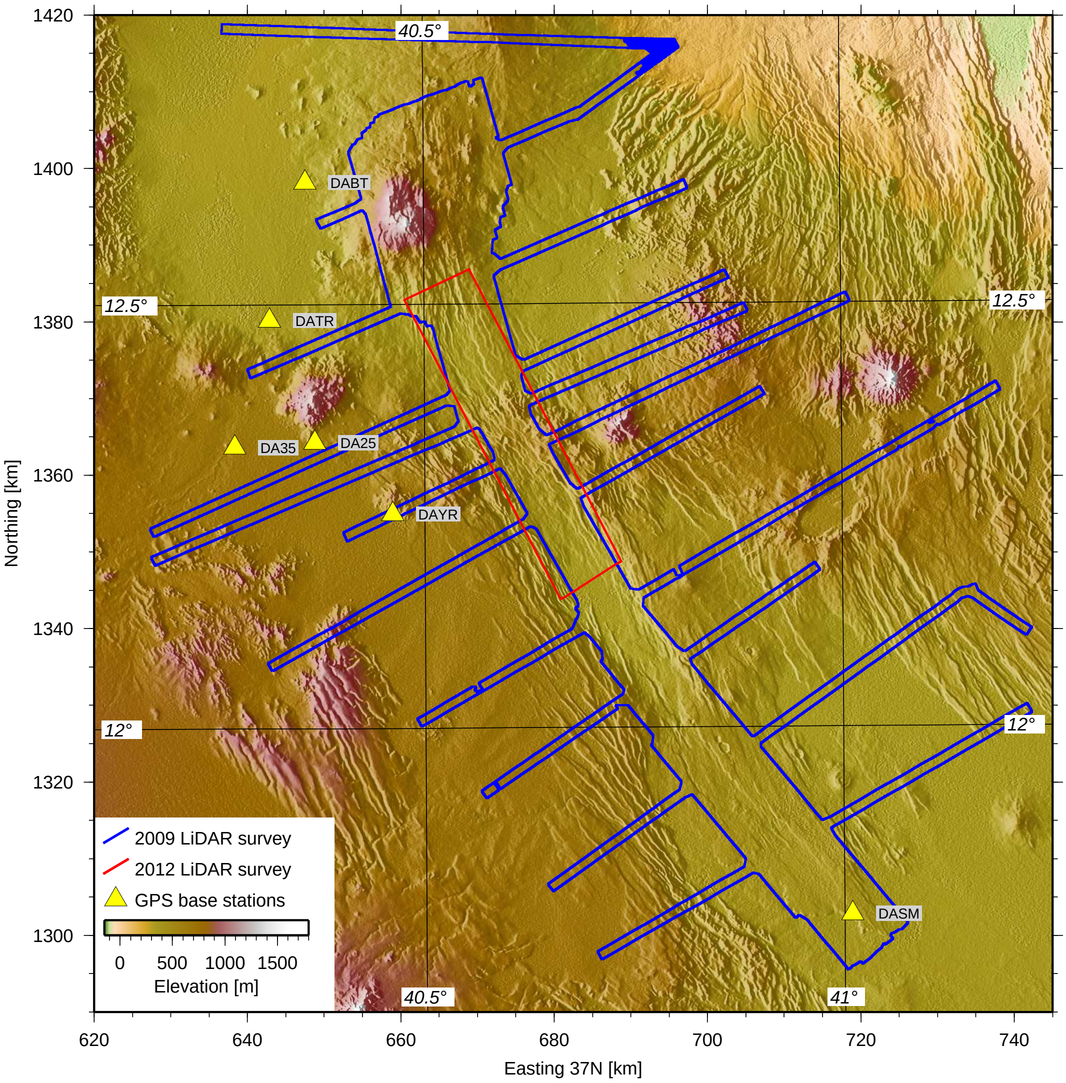

Figure 2.3: LiDAR surveys. Outline of the 2009 LiDAR survey in blue and the 2012 LiDAR survey in red. Yellow triangles show location of GPS stations used as base stations for georeferencing.

Date	Cloud	Shadow	Illumination	Data qual.	GPS base station
25.10.09	0 %	0 %	90 %	9/10	DA25, DAYR, ARSF
26.10.09	5 %	5 %	90 %	8/10	DABT, DATR, DA35
27.10.09	5 %	5 %	70 %	7/10	DAYR, DASM, DA25

Table 2.3: Column 1-5: Survey quality details: date, cloud coverage, area shadowed, illumination, data quality out of 10; column 6: cGPS station used as base stations

November 2012 survey:

The second survey covered only the very central section of the Dabbahu segment across the AVC marked by the red polygon in figure 2.3. It consists of 26 flight tracks of ∼1790 m width covering an area of 405 km^2. The data set was acquired during two days in November 2012 with excellent weather conditions (9-10 out of 10). In comparison to the 2009 survey this survey was flown at a lower altitude (∼2600 m amgl). The survey was acquired in multiple pulse in air (MPiA) mode which sends a second laser pulse before the reflections of the first pulse is received, allowing an increase in the effective PRF (106800 Hz) (Roth and Thompson, 2008). The total number of returns for this survey is over 1.2×10^9. Details of the survey can be found in tables 2.4 and 2.5.

Date	avg. alt. amgl.	Gnd speed	PRF	Scan freq.	FOV
13.-14.11.2012	2600m	250 km/h	106800 Hz	55.3 Hz	19

Table 2.4: Column 1-3: Survey acquisition details: date, average flight altitude amgl., ground speed; column 4-6: Instrument settings: pulse repetition frequency, scan frequency, field of view

Date	Cloud	Shadow	Illumination	Data qual.	GPS base station
13-14.11.2012	0 %	0 %	90 %	9/10	DA25, DAYR, DA45

Table 2.5: Column 1-5: Survey quality details: date, cloud coverage, area shadowed, illumination, data quality out of 10; column 6: cGPS station used as base stations

2.1.3 Georeferencing returns

This part of the processing was carried out by the NERC ARSF.

Within the earth centred WGS-84 Cartesian reference system (C(X,Y,Z)) the position ($\mathbf{r}_{ce}^{C}$) of the measured point (e) is determined by

$$\mathbf{r}_{ce}^{C} = \mathbf{r}_{cg}^{C} + \mathbf{r}_{gl}^{C} + \mathbf{r}_{le}^{C} \tag{2.1}$$

where $\mathbf{r}_{cg}^{C}$ points from the centre of the reference frame to the onboard GPS antenna, $\mathbf{r}_{gl}^{C}$ points from the GPS antenna to the firing point of the laser, and $\mathbf{r}_{le}^{C}$ is the vector from the laser to point (e) on the ground (e.g. Vaughn et al., 1996). Vectors are indicated by bold lower case letters, matrices by bold capital letter. Superscript letters indicate the reference frame.

$\mathbf{r}_{cg}$ is directly determined through kinematic positioning, which was first introduced by (Krabill and Martin, 1987). It requires the onboard GPS station to be synchronised with a ground based GPS station before and after the flight.

$\mathbf{r}_{gl}$ is measured within the local reference frame of the LiDAR system (B) which is generally defined along the aircraft's main axes (X^B: along its centre line, Y^B: along its right wing, Z^A: positive downwards). In order to rotate B into C it first needs to be rotated into the earth right handed gravitational reference frame O (Z positive toward the earth and perpendicular to the WGS-84 ellipsoid, X north and parallel to the ellipsoid). The necessary rotation angles are measured by the IMU which measures yaw (β rotation around Z^B), pitch (α rotation around Y^A) and roll (ψ, rotation around X^B). They are defined positive if rotation is counterclockwise. The rotation relationship between O and C is defined by latitude (ϕ) and longitude(λ) recorded by the GPS antenna.

$\mathbf{r}_{le}$ is measured within the reference frame of the laser unit with its Z^L axis pointing in the lasers firing direction. Its rotation counterclockwise relative to A is defined by its mounting parameters $\Delta\beta, \Delta\alpha, \Delta\psi$ and the mirror rotation angle (γ).

This results in the LiDAR equation

$$\mathbf{r}^C_{ce} = \mathbf{r}^C_{cg} + \mathbf{R}^{-1}(\lambda, \phi - 90, 0)\mathbf{R}^{-1}(\beta, \alpha, \psi)(\mathbf{R}^{-1}(\Delta\beta, \Delta\alpha, \Delta\psi)\mathbf{R}^{-1}(\gamma)\mathbf{r}^L_{le} + \mathbf{r}^B_{gl}) \tag{2.2}$$

with the 3-dimensional rotation matrix $\mathbf{R}(a, b, c)$ rotating about x-, y- and z-axis by the angles a, b, c respectively.

2.1.4 Error estimation

Besides obvious errors introduced by false reflectors such as clouds or sand in the air, measurement errors of the instrument need to be considered. Huising and Gomes Pereira (1998), Baltsavias (1999), Latypov (2002), Glennie (2007) have provided detailed descriptions of errors and their effects on the data set. Errors are subdivided into random and systematic errors. The former is based on the precision of the system measurements while systematic errors are due to mounting parameters and biases in the system measurements.

The standard procedure to estimate errors for topographic data sets is to take easily recognisable landmarks, such as hilltops or house corners, for which elevation and posi-

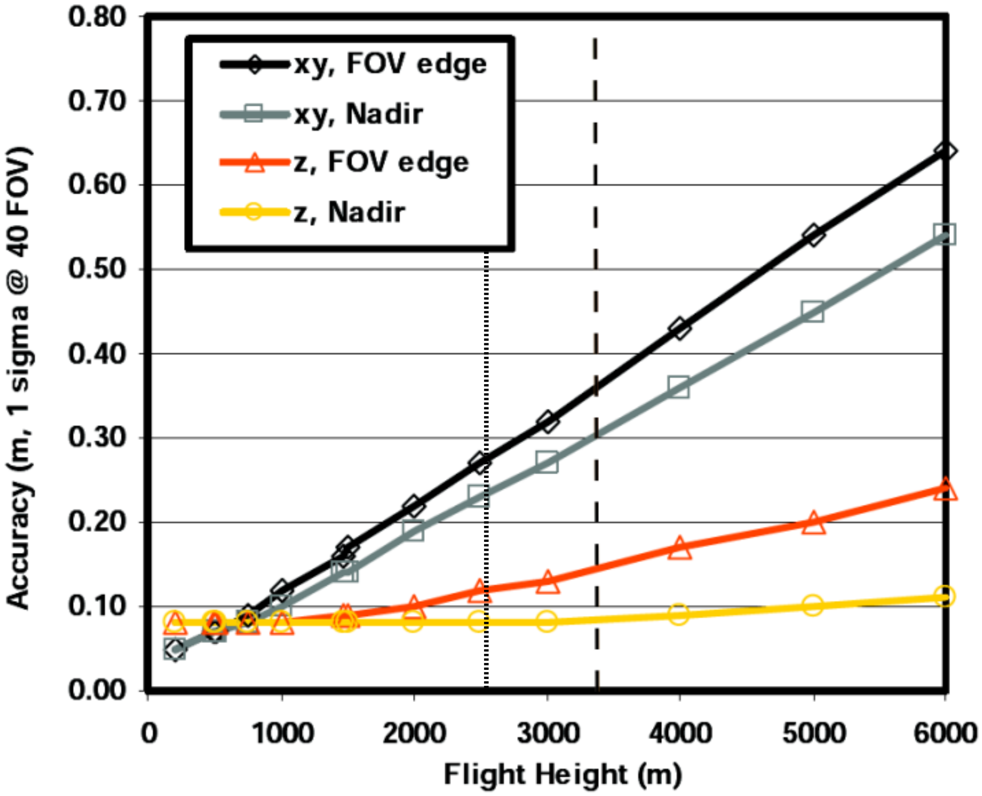

Figure 2.4: Accuracy of the Leica ALS50-II vs. flight height (from Geosystems AG, 2007). Accuracy estimated for a FOV of 40°. Horizontal accuracy at the FOV edge in black and at the nadir in grey. Vertical accuracy at the FOV edge in red and at the nadir in yellow. Dashed line at 3400 m for the 2009 survey. Dotted line at 2600 m flight height of the 2012 survey.

tion are well known and compare them with their values in the data set (Maune, 2001). NERC ARSF perform calibration flights and compare the LiDAR elevation data with ground control points every time the LiDAR system is removed from the aircraft. Since February 2009 NERC ARSF report an issue with the boresight roll angle of the Leica ALS-II sensor. According to Leica® Geosystems this issue has presented itself in other Leica® Geosystems LiDAR sensors and is currently under investigation. Boresight roll bias causes a linear vertical tilt across the swath width (e.g. Habib et al., 2010). A calibration flight at the end of September 2009, shows mean vertical error of 3.1±2.2 cm for operation at 1350 m flight altitude and 4.1±5.4 cm for operation at 2600 m altitude. Roll boresight errors of of ~2-5 cm were reported but considered insignificant by NERC ARSF (ARSF, 2009). The calibration flight in July 2012 exhibited vertical errors of 3.9±10.3 cm for 800 m flight altitude and 5±5 cm for a survey height of 2400 m which

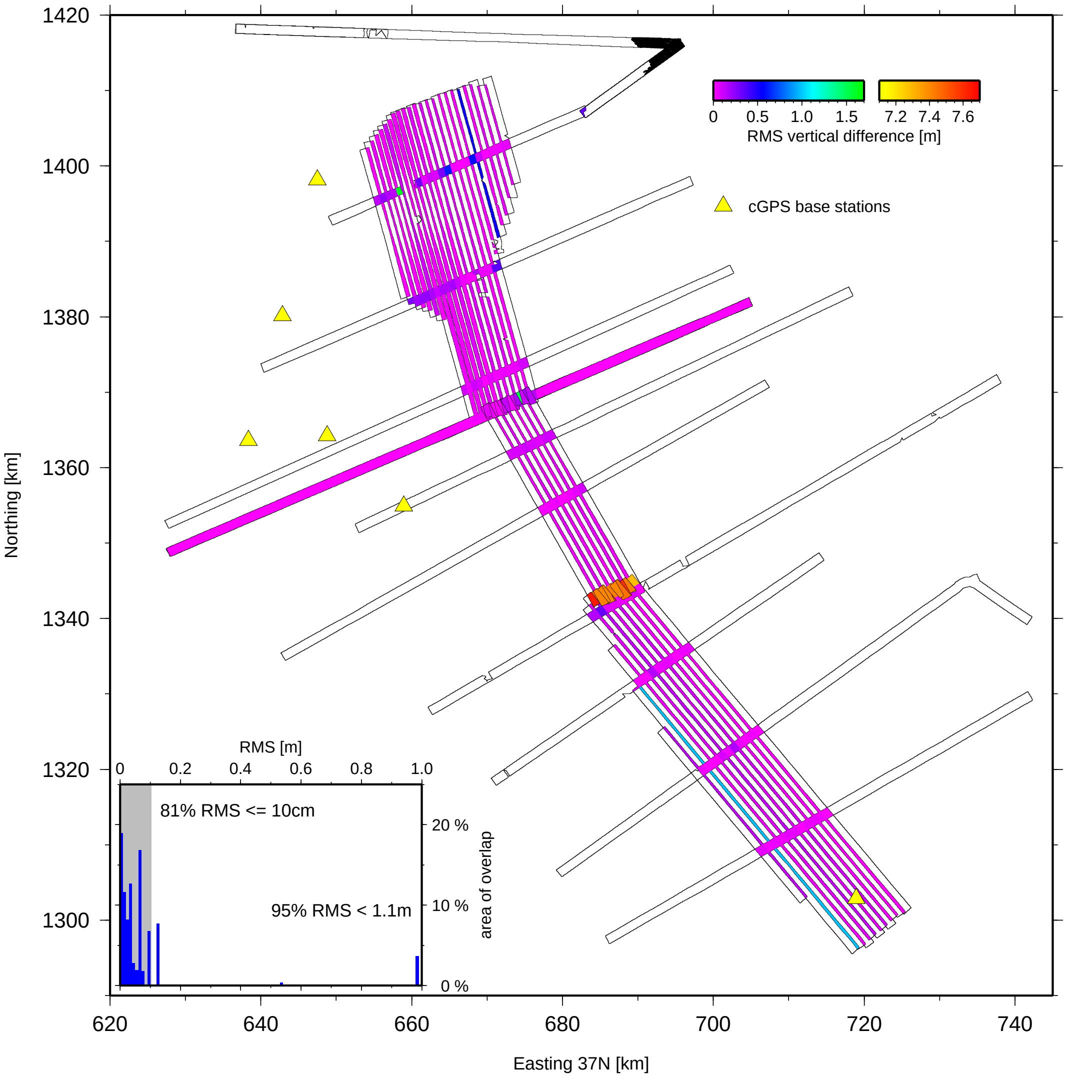

Figure 2.5: RMS relative vertical error estimated from areas of overlap between individual flight lines. The colour of each overlap corresponds to its mean RMS vertical variation. Yellow triangles show the location of cGPS stations used as base stations. The lack of stations in the South is the most likely reason for the difference of ∼7 m between data from the first and third day of the survey. The histogram shows RMS relative vertical variation versus the percentage of total overlap. More than 81% of the area has relative variation of less than 10 cm and for more than 95% the error is below 1.1 m.

is close to the flight altitude of 2600 m of the 2012 survey. The systematic roll boresight error was 9-13 cm at the edge of the flight lines (ARSF, 2012). NERC ARSF manually correct for this using the overlapping areas of individual flight swaths as guide and iterate the processing to remove relative trends between the point clouds. If there is no overlap no correction is currently applied by NERC ARSF. Leica® Geosystems specify vertical and horizontal errors with respect to the flight altitude (Fig. 2.4) which are at the FOV edge approximately 15 cm vertical and 37 cm horizontal for the 2009 survey and 12 cm vertical and 28 cm horizontal for the 2012 survey.

It is also common to install ground control points which can be recognised in the data sets prior to the survey. For the Dabbahu rift no well measured landmarks exist nor was it possible to access the centre of the rift to install control points. Initially no second LiDAR survey was scheduled and for the purpose of studying fault displacement the accuracy of the 2009 LiDAR survey is sufficient. However, to get an estimate on the relative vertical error of the 2009 survey I calculated the RMS differences pixel by pixel for the area of overlap between individual flight lines, assuming that the horizontal position is correct. Fig. 2.5 shows the results of this analysis. More than 81% of the total area of overlap exhibit RMS values of $\leq$ 10 cm and 95% have RMS values $\leq$ 1.1 m. Larger errors of 7.4 m are obvious towards the South where flight lines of day one and three overlap. This offset is most likely a consequence of problems with two of the cGPS stations in the South of the survey during the time of acquisition. The offset is hardly visible in the finished DEM and has a negligible if any effect on my fault displacement work presented in § 4. Errors introduced through the boresight roll bias and possible other factors between individual flight tracks become significant during the differencing of the two LiDAR data sets in § 5.3.1. Various methods for strip adjustment to remove this bias exist. Favalli et al. (2009) for example developed an automatic algorithm to remove systematic errors from LiDAR data without the presence of ground control points but within the time frame of my thesis I was not able carry out these corrections. The magnitude of the error between the two LiDAR data sets will be discussed in detail in § 5.3.1.

2.1.5 Post-processing

The survey data was delivered by the NERC ARSF as a georeferenced point cloud (vertical datum:WGS84, projection:UTM 37N, horizontal datum ETRF89). The ASCII files contain time, Easting, Northing, elevation, intensity, classification, return number, number of returns for given pulse and scan angle rank. The classification values are according to the American Society of Photogrammetry and Remote Sensing (ASPRS) standard for LiDAR point classes. Noisy points are classified as 7, by default points are classified as 1.

To created the DEMs of the bare earth I kept only the last return of each pulse and removed any returns flagged as noisy during the processing by the NERC ARSF.

Due to the size of the data set I split the survey area up into 1.4 x 1.4 km^2 tiles overlapping each other by 200 m in each direction. I calculated the surface for each tile using a natural neighbour interpolation (TriScatterInterp, MATLAB, 2012). Natural neighbour interpolation has proven to be the preferred interpolation method when recreating topographic surfaces with scattered data points and sharp gradient changes (Gold, 1989). Fig. 2.6 illustrates the natural neighbour interpolation. A set of data points can be described by its Delauney triangulation, which connects each data point with all of its neighbours. Another description of an irregular spaced data set is achieved by the Voronoi tessellation. Here a cell is created around each data point enclosing the area which is closer to its data point than any other point in the data set. The Voronoi cell bisects the connection of two neighbouring points (Fig. 2.6 a). To create a regular spaced surface grid, nodes are inserted into the data set (cross). the new point creates its own Voronoi cell which consists of area formerly belonging to the Voronoi cells of its neighbours (yellow polygon). In the natural neighbour interpolation each neighbour influences the value of the new grid node according to the size of the area of its former cell taken over by the new point (Fig 2.6 b). The resulting surface is 'smooth' or C^1 continuous everywhere except at the data points, which is an advantage over nearest neighbour interpolations, which are discontinuous along the triangulation edges.

In a final step I merged the created surface tiles using the mosaicing function of the ERDAS ER Mapper 2011® software (ERDAS, 2011).

Fig. 2.7 shows the number of last returns per 10 x 10 m^2 squares for the 2009 survey. On average 54 returns are counted per cell which corresponds to an average resolution of approx. 2 m^2. However, the number of returns increase significantly for areas where

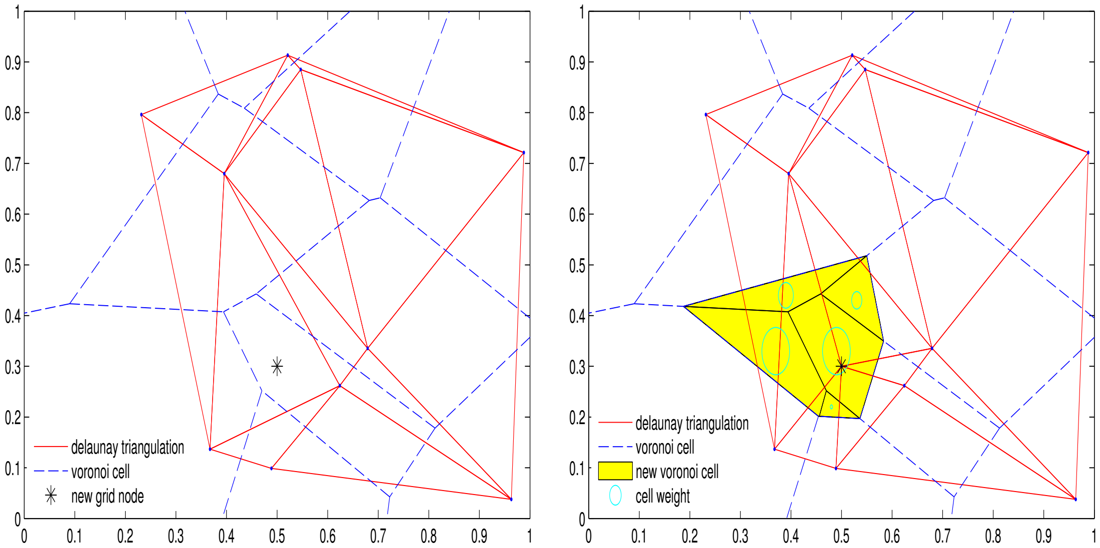

Figure 2.6: Illustration of the natural neighbour interpolation. Delauney triangulation (red) and Voronoi tessellation (blue) of a data set before insertion of a new grid node (a) and after (b). The introduction of the new point creates a new Voronoi cell that occupies area formerly belonging to the cells of its neighbours. The influence of the neighbouring points on the value of the new point is proportional to the portion of the new grid nodes cell which previously belonged to the neighbouring point's Voronoi cell.

flight tracks overlap. The statistical analysis shows that 31% of the 10 x 10 m^2 cells are hit by more than 100 returns, which signifies a resolution better than 1 m^2 and only 1% have more than 400 returns, which indicates a resolution better than 0.5 x 0.5 m^2. I calculated the surface across a fault scarp at 4 different resolutions to decide on the ideal resolution of the DEM for my fault study (Fig. 2.8). In order to accurately determine the displacement of a fault, it is necessary to clearly identify the footwall cutoff (§ 3, Fig. 3.1). At 5 x 5 m^2 pixel size (Fig. 2.8, top left) the cutoff can not be clearly distinguished from a more gentle sloping monoclinal feature. This highlights one of the problems when analysing remotely acquired surface data. Depending on data resolution and griding surface structures can easily be missed or be mistaken for other features. The cutoff becomes visible at 1 x 1 m^2 pixel size (top right) but its exact position remains blurred. Stepping down to 0.5 x 0.5 m^2 pixel size (bottom left) the cutoff is sharp and clearly visible. At 0.1 x 0.1 m^2 pixel size (bottom right) the cutoff is very sharp and small features along the fault surface become visible. However the data set resolution does not allow for interpretation at that scale. I therefore chose to calculate the full DEM with 0.5 x 0.5 m^2 resolution. It provides the clearest image of the fault cutoffs and maintains the high resolution of the data set. The final size of

the DEM amounts to 210 GB, when stored as a 4-byte floating point grid.
Fig.2.9 shows the number of last returns per 10 x 10 m^2 square for the 2012 survey. On average the number of returns per cell is 160, which is three times the amount of the 2009 survey. 24% of the cells are hit by more than 400 returns, which relates to a true 0.5 x 0.5 m^2 resolution. I calculated the DEM (23 GB) for this survey also to 0.5 x 0.5 m^2 resolution. Throughout my thesis I refer to these 0.5 x 0.5 m^2 pixels size DEMs as the high-resolution LiDAR DEMs and unless stated otherwise all analysis is carried out on them.

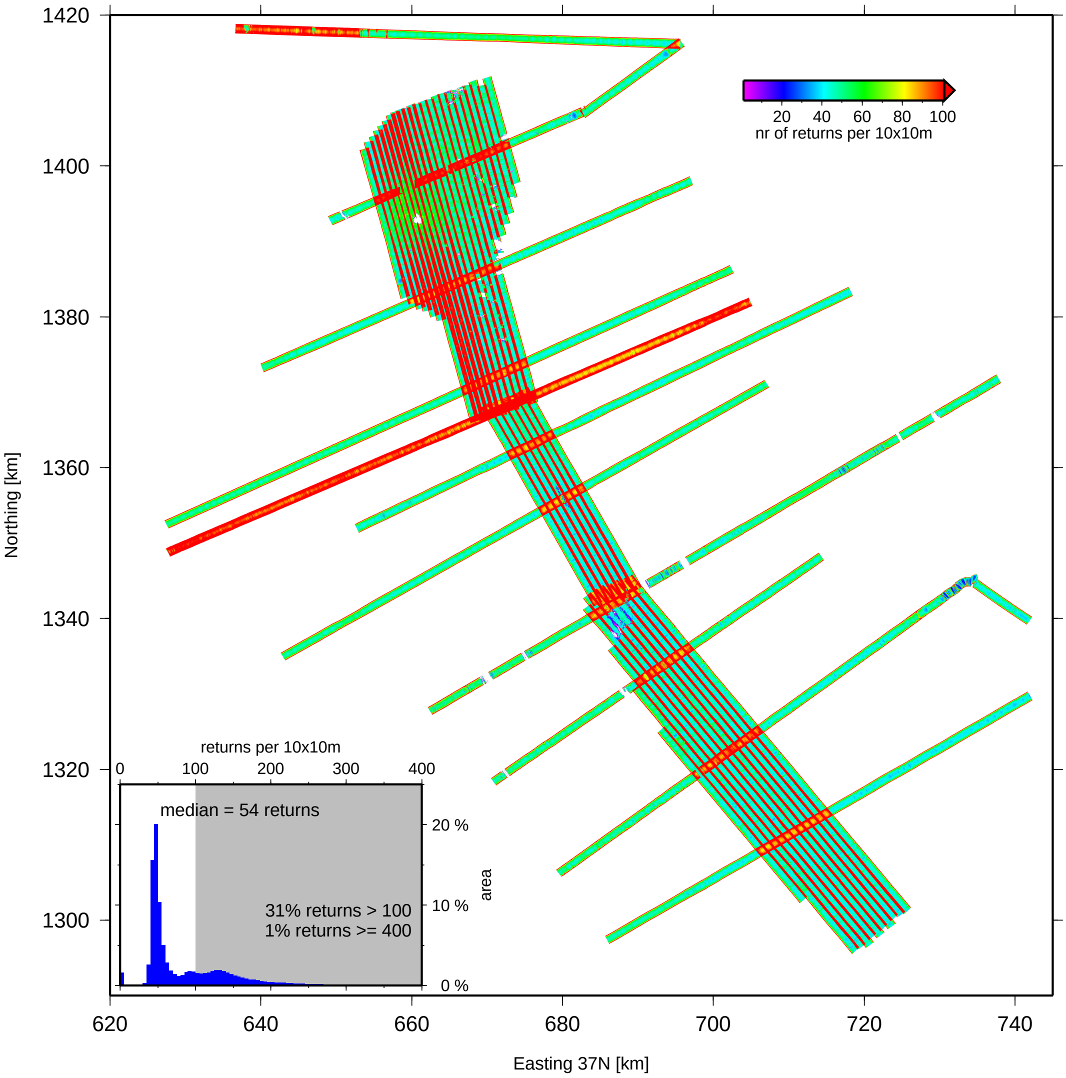

Figure 2.7: LiDAR last returns per 100 m^2 for the 2009 survey. Areas passed by only one flight line are on average hit by 54 last returns per 10 x 10 m^2. In areas of overlap the number of last returns rises significantly to over 100 per 10 x 10 m^2. 31% of the 10 x 10 m^2 cells of the survey area are hit by more than 100 return and only 1% is hit by ≥ 400 returns.

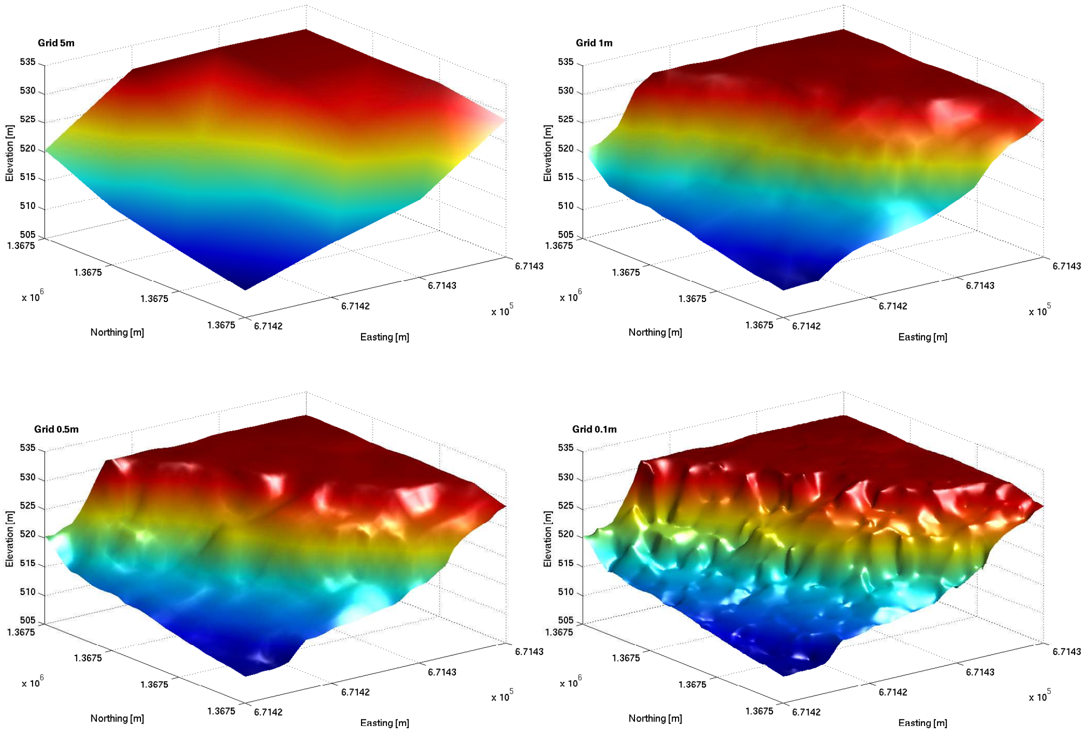

Figure 2.8: Comparison of different LiDAR resolution DEMs covering a fault scarp. Area 15 x 15 m^2. Top left 5 x 5 m^2 pixel, top right 1 x 1 m^2 pixel, bottom left 0.5 x 0.5 m^2 pixel, bottom right 0.1 x 0.1 m^2 pixel.

Figures 2.10 and 2.11 illustrate the topographic detail provided by the high-resolution LiDAR DEM (c and d) in comparison to the global 90 x 90 m^2 SRTM DEM (Shuttle Radar Topography Mission) (a) and the 6 x 6 m^2 DEM (b) I created from SPOT5 satellite data (courtesy of Sophie Houtot). I chose two areas with different topographic expressions. Figure 2.10 shows a close up of the northern flank of the Dabbahu volcano. Figure 2.10d shows a close-up of the 2009 LiDAR DEM marked by the rectangle on image c. The high-resolution LiDAR DEM allows for the identification of lava flow patterns of former extrusions. The second example (Fig. 2.11) is taken from the rift centre north of the Ado'Ale volcanic complex which exhibits multiple sub-parallel fault scarps and fissures. It is also the most complex part of the segment, as the segment changes direction from NW-SE to NNW-SSE, causing rhombohedral blocks and complicated fault intersections. The close-up image (Fig. 2.11d) of area marked by the rectangle in image c shows a fault and graben structure. Small scale variations at the footwall as well as details on the graben floor are visible.

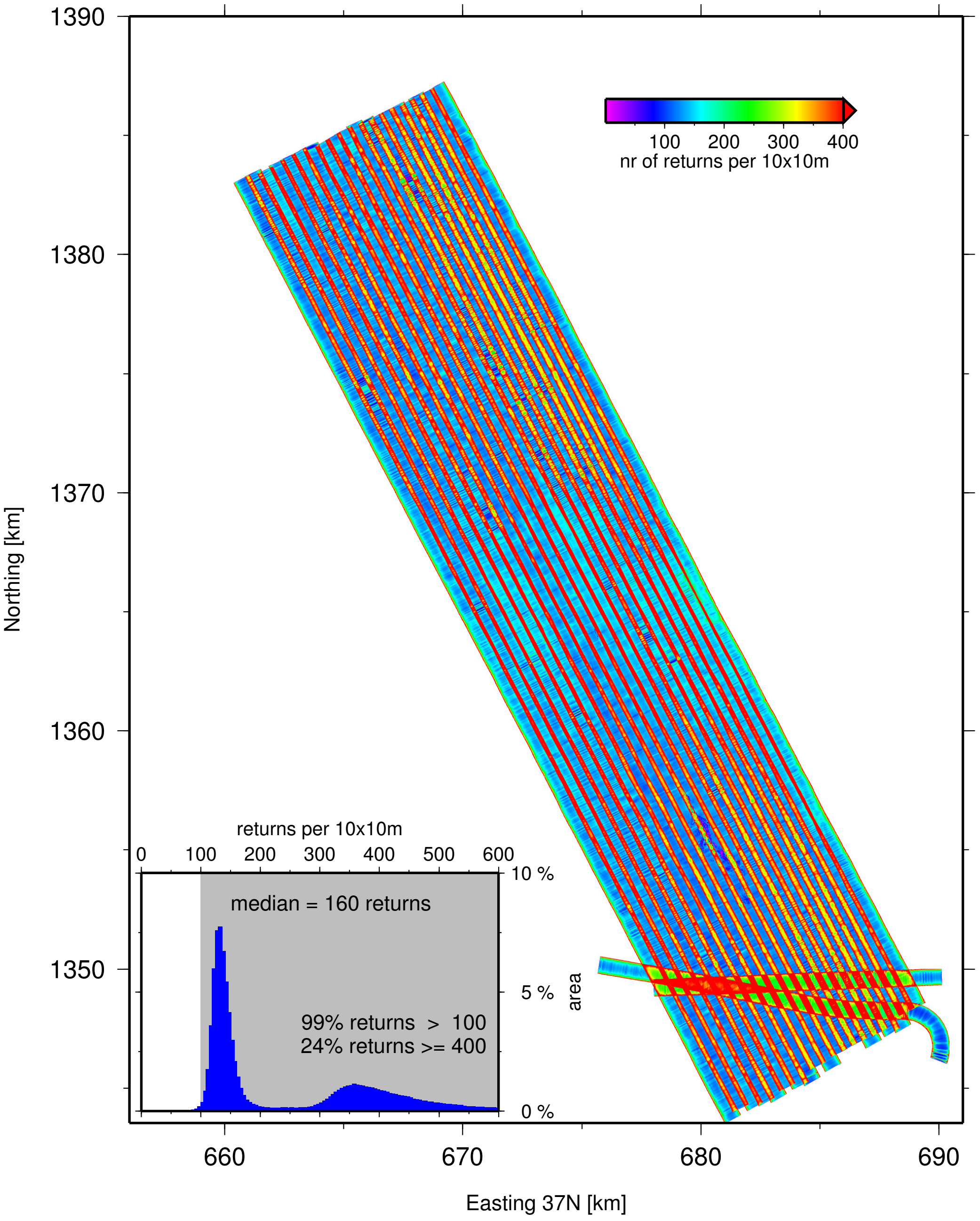

Figure 2.9: LiDAR last returns per 100 m^2 for the 2012 survey. Areas passed by only one flight line are on average hit by 160 last returns per 10 x 10 m^2. In areas of overlap the number of last returns rises significantly to over 300 per 10 x 10 m^2. 99% of the 10 x 10 m^2 cells of the survey area are hit by more than 100 returns and 24% is hit by $\geq$ 400 returns.

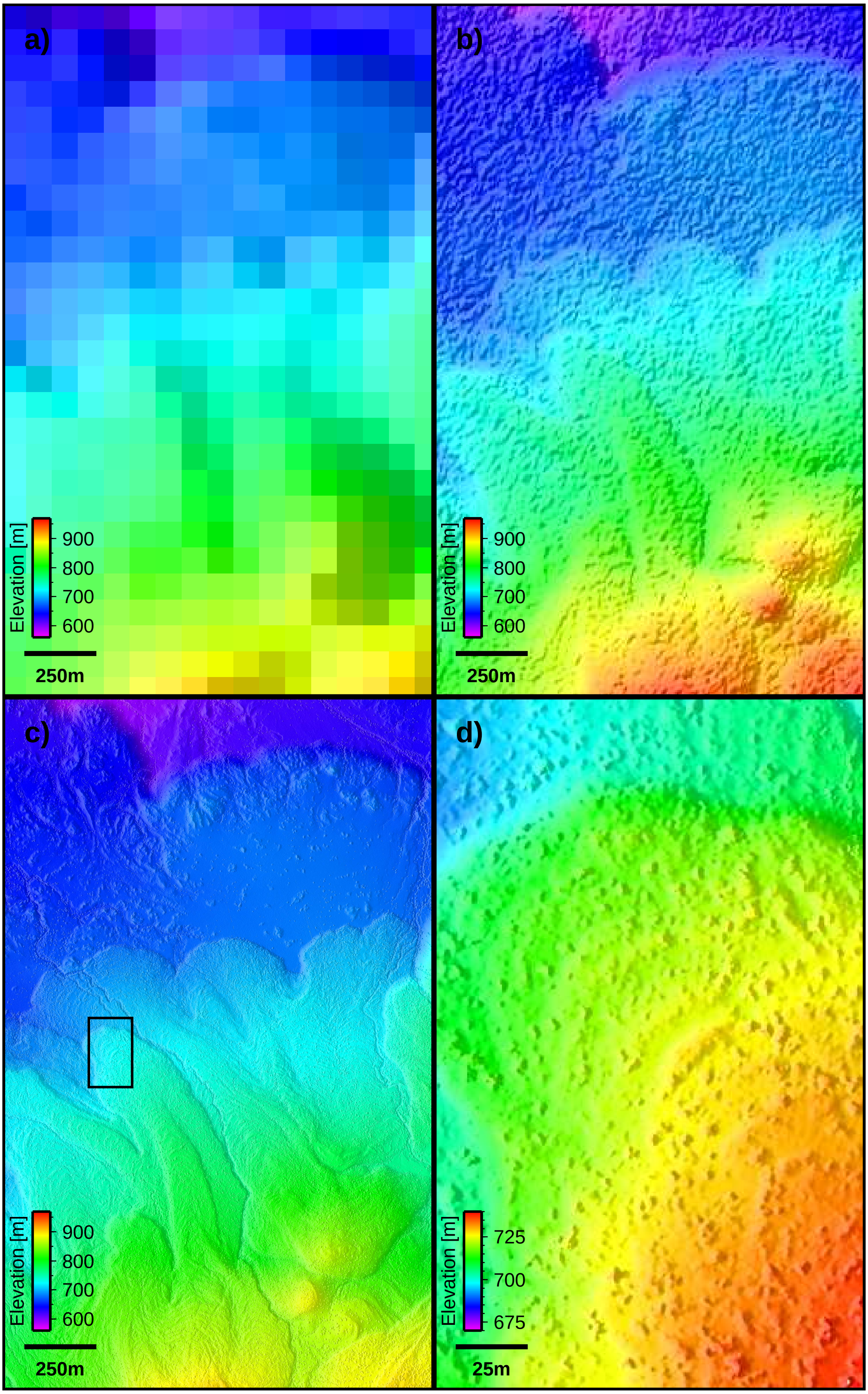

Figure 2.10: Comparison of different DEM resolutions showing lava flows at the North of the Dabbahu volcano (Top right corner 12.67 N/40.45 W). a) 90 x 90 m^2 SRTM DEM, b) 6 x 6 m^2 SPOT5 DEM, c) 0.5 x 0.5 m^2 2009 LiDAR DEM, d) close-up 0.5 x 0.5 m^2 2009 LiDAR DEM showing area marked by black box in c). Images are shaded with sun in SW.

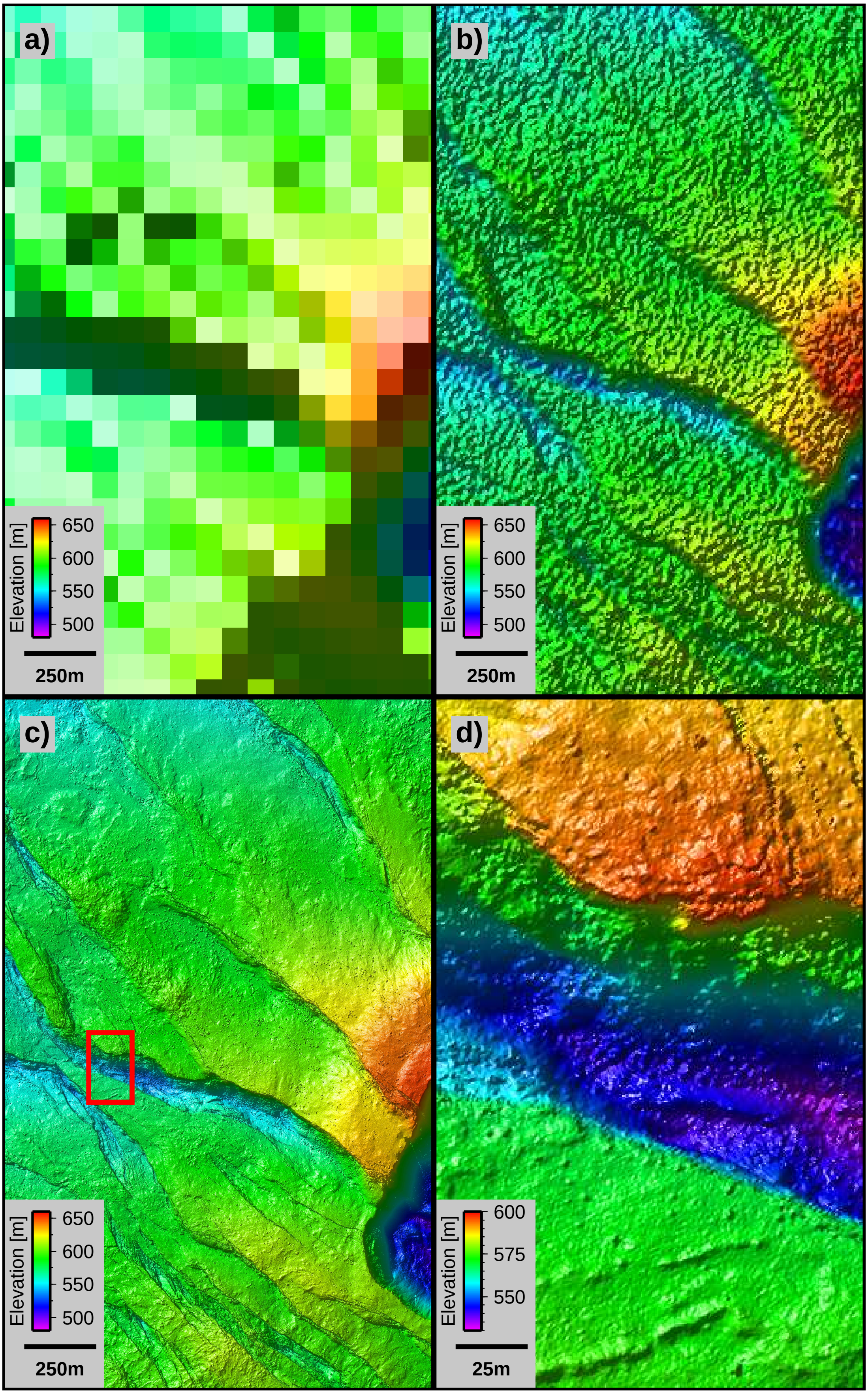

Figure 2.11: Comparison of different DEM resolutions. Example of the fault structures at the Ado'Ale volcanic complex (Top right corner 12.35 N/40.58 W). a) 90 x 90 m^2 SRTM DEM, b) 6 x 6 m^2 SPOT5 DEM, c) 0.5 x 0.5 m^2 2009 LiDAR DEM, d) close-up 0.5 x 0.5 m^2 2009 LiDAR DEM showing area marked by red box in c). Images are shaded with sun in SW

2.2 InSAR

Synthetic aperture radar interferometry (InSAR) is a powerful tool to study crustal deformation (Massonnet and Feigl, 1998, Bürgmann et al., 2000). Radar instruments acquiring SAR images are side looking and are carried by aircraft or spacecraft (Curlander and McDonough, 1991). The amplitude of a SAR image can be related to the scattering properties of the earth (e.g. Hooper et al., 2012) but the phase of a single SAR image is essentially meaningless. However, the difference between the phase of two images observing the same ground, assuming the backscattering characteristics have not changed, can be interpreted as the change in range (distance) from the satellite to the surface. Mathematically the phase difference is derived by the multiplication of one SAR image with the complex conjugate of the second thereby creating the familiar interferogram (Hanssen, 2001, Rosen et al., 2000). The phase of the newly formed interferogram is the phase change between the two SAR images.

SAR satellites are distinguished by their radar wavelength (X-band 3 cm; C-band 5.6 cm and L-band 23 cm). The longer the wavelength the more coherent is the interferogram and the easier it is to unwrap. For each of the 14 dyke intrusions of the recent rifting episode at the Dabbahu segment, ENVISAT (C-band) data have been acquired and for four intrusions ALOS data are available (Fig. 2.12). Unfortunately the short wavelength ENVISAT data decorrelates over the centre of the rift axis where the majority of the faults are located. I therefore use the longer wavelength (23 cm) L-band ALOS data for my study which maintains better coherence above the intrusions as shown in figure 2.13. ALOS (Advanced Land Observing satellite) is a Japanese satellite and was launched in January 2006. It provided data from May 2006 until April 2011. ALOS was in a 98.16° sun-synchronous orbit at ∼700 km altitude, with a 46-day repeat. At the Dabbahu segment its incident angle, γ, is 34.2°.

Data processing

I used the standard ROI_PAC packages (Rosen et al., 2004) to process the satellite data. It creates the interferogram from the image pairs, corrects the phase for factors not related to true surface deformation and finally unwraps the phase turning it into the continuous phase.

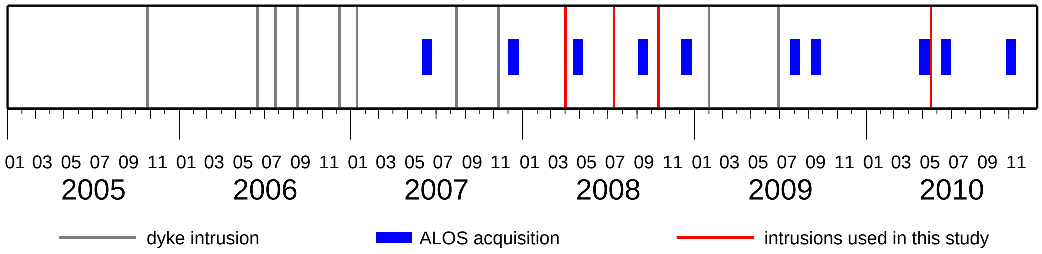

Figure 2.12: ALOS acquisitions in relation to the individual dyke intrusions. Grey: Events not captured, red: events captured, blue time of ALOS acquisition.

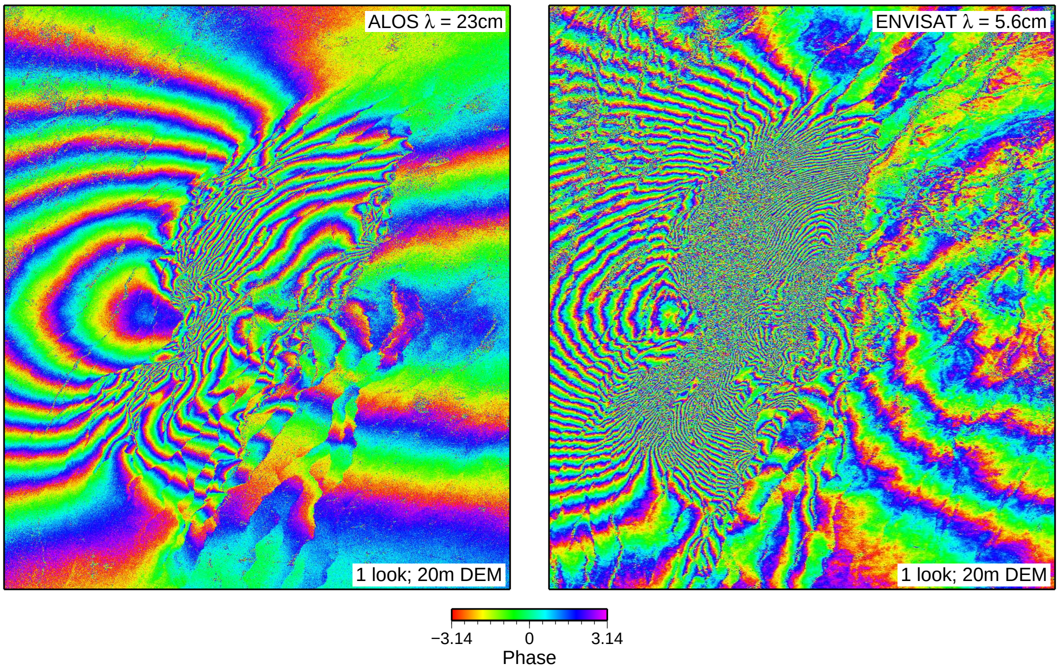

Figure 2.13: Comparison between ALOS (left) and ENVISAT (right) data for the October 2008 intrusion. Images cover the same area and have similar satellite viewing geometry (ascending orbits). Both interferograms are processed at 1 Rlook. The ENVISAT interferogram has a high $d\phi/dx$ ratio across the rift center.

The phase equation $\Delta\Phi$ is

$$\Delta\Phi = \Delta\Phi_{geom} + \Delta\Phi_{topo} + \Delta\Phi_{atm} + \Delta\Phi_{noise} + \Delta\Phi_{def} \tag{2.3}$$

and the individual contributions are (e.g. Massonnet and Feigl, 1998):

- Geometric contribution, $\Delta\Phi_{geom}$, which is caused by the offset in position of the satellites between the first and the second acquisition. It typically the largest contribution to the phase, creating hundreds of fringes across the image. Using the a-priori information of satellite orbits the geometric contribution is routinely removed during the processing.

- Topographic contribution, $\Delta\Phi_{topo}$, which is related to the error of the DEM and affects the resolution of the interferogram. I will address the topographic contribution in more detail in the following section.

- Atmospheric contribution $\Delta\Phi_{atm}$, which is the result of changed atmosphere conditions between the acquisitions. Temperature, pressure and water vapour content control the refractive index of the atmosphere and thereby the phase delay of the radar wave. The introduced signal correlates to the underlying topography and this relationship can be used for simple corrections. Current research focuses on atmospheric changes and the development of improved techniques to correct for it (e.g. Elliott et al., 2008, Li et al., 2009).

- Noise contribution $\Delta\Phi_{noise}$, which is due to noise and small errors of the orbit and look angle (Hooper et al., 2007).

- Ground deformation $\Delta\Phi_{def}$, which is the sought-after signal.

The resolution at which an interferogram can ideally be processed depends partly on the resolution and accuracy of the available DEM and the perpendicular baseline, $B_\perp$. The altitude of ambiguity, h_a, (Eq. 2.4) is the altitude difference which causes a phase change of 2π after all other contributions to the phase change have been removed (interferogram flattening).

$$h_a = \frac{\lambda R sin(\gamma)}{2B_\perp} \tag{2.4}$$

h_a is inversely proportional to $B_\perp$ and dependant on the incidence angle γ. This means the larger the perpendicular baseline is the more accurate the DEM has to be to prevent

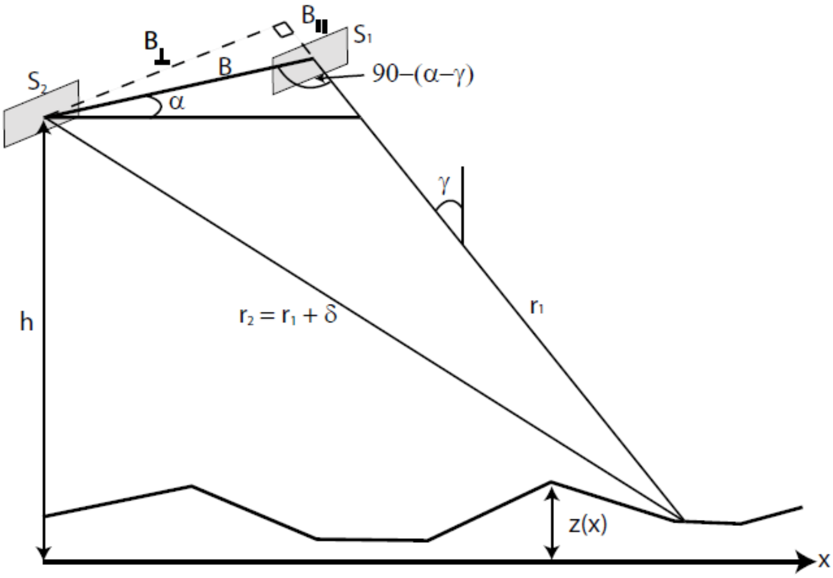

Figure 2.14: Imaging geometry for radar interferometry. S1 and S2 are the satellite positions during different image acquisitions. They are separated by the baseline B with its components $B_{\perp}$ and $B_{||}$ perpendicular and parallel respectively to the look direction. γ is the incidence angle of the first acquisition. Reprinted with permission from Hamling (2010); originally modified from Bürgmann et al. (2000)

the introduction of large topographic errors.

Some of the ALOS pairs have perpendicular baselines of ~2000 m. To minimise the topographic error in my analysis, I created a DEM matching the 20 x 20 m^2 ALOS resolution from the 2009 LiDAR DEM. I then merged the new 20 x 20 m^2 LiDAR DEM with an oversampled SRTM DEM Farr et al. (2007). This was necessary because ROI_PAC requires the DEM to extend as far as the SAR image. The DEM manipulations were carried out using ERDAS ERMapper. Figure 2.15 shows the same interferogram processed with the 20 x 20 m^2 merged LiDAR DEM on the left and processed with an 20 x 20 m^2 DEM created by oversampling the SRTM DEM on the right. The perpendicular baseline is ~2000 m. In the area covered by the LiDAR DEM the resolution is visibly improved.

In the imaging geometry of side-looking radar systems the dimension across-track is referred to as range and the dimension parallel to the flight direction is the azimuth. The referencing of pixels between two radar images uses a concept referred to as a "look". Raw interferograms with 1 range look (Rlook) and 1 azimuth look (Alook) are usually very noisy due to for example temporal decorrelation and baseline offset. It is common practise to average over neighbouring pixels, called complex multilooking, to improve the signal to noise ratio (e.g. Rodriguez and Martin, 1992, Goldstein and Werner, 1998, Lee et al., 1998). ROI_PAC uses a fixed mask approach to average the pixels creating pixels of roughly the same size in ground range and azimuth. For ALOS data this means that data processed at 1 Rlook are made of 1 look in range and 5 looks in azimuth, corresponding to roughly one 20 x 20 m^2 pixel.

The standard filtering procedure applied by the ROI_PAC package is a power spectrum filter (Goldstein and Werner, 1998), but it leads to smoothing of the sharp edges in the interferogram. To preserve the sharp edges caused by fault slip I applied a 3 x 3 pixel median filter instead. The final step of the processing is the phase unwrapping, which transforms the cyclic phase into an unambiguous continuous phase, Ψ. This is achieved by finding the integer number of cycles, n, to be added to each pixel of the wrapped phase, Φ, (Equ. 2.5) (e.g. Ferretti et al., 2007)

$$\Psi = \Phi + 2\pi n \tag{2.5}$$

Phase unwrapping algorithms assume that the unwrapped phase is ‘smooth’ and that changes occur ‘slowly’. While this is true for many parts of the interferogram phase, discontinuities caused by, for example, slip on faults leads to unwrapping errors which have to be manually fixed. I used the software ERDAS ERMapper to carry out the corrections. I identified and mapped the inconsistencies in the unwrapped interferogram and then added or subtracted the appropriate number of cycles to the phase. A final unwrapped interferogram is shown in figure 2.16.

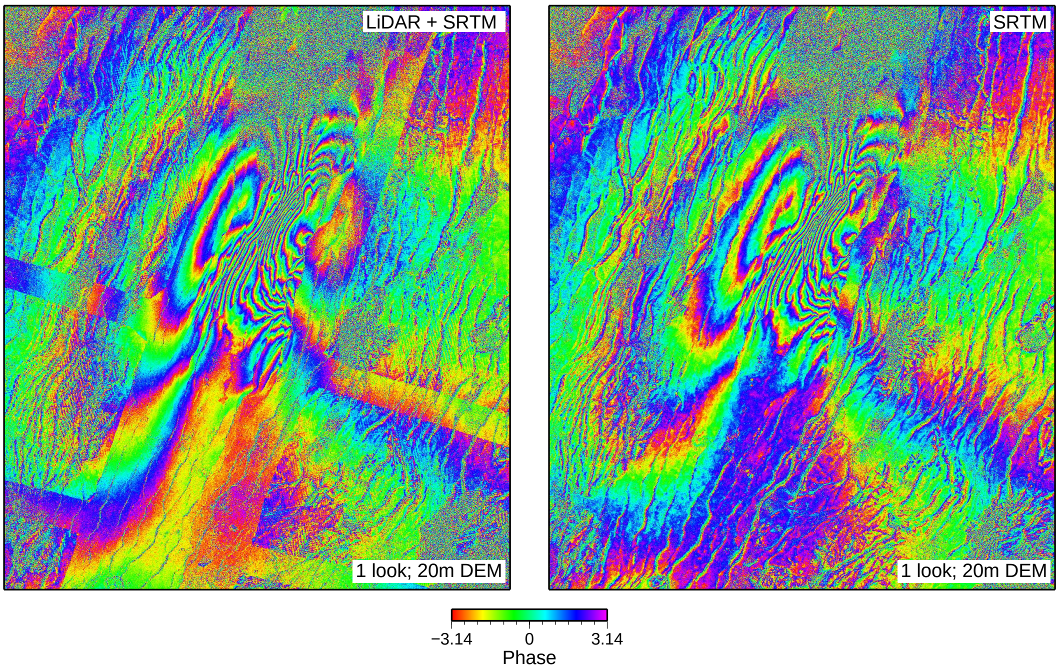

Figure 2.15: Demonstration of the influence of the high resolution LiDAR DEM on the InSAR results. Left: Interferogram processed with 20 x 20 m^2 DEM derived from the LiDAR and SRTM DEM Farr et al. (2007). Right: Interferogram processed with 20 x 20 m^2 DEM created from oversampled SRTM DEM. For the interferogram with a relatively large perpendicular baseline (~2000 m) the improvements through the LiDAR DEM are clearly visible.

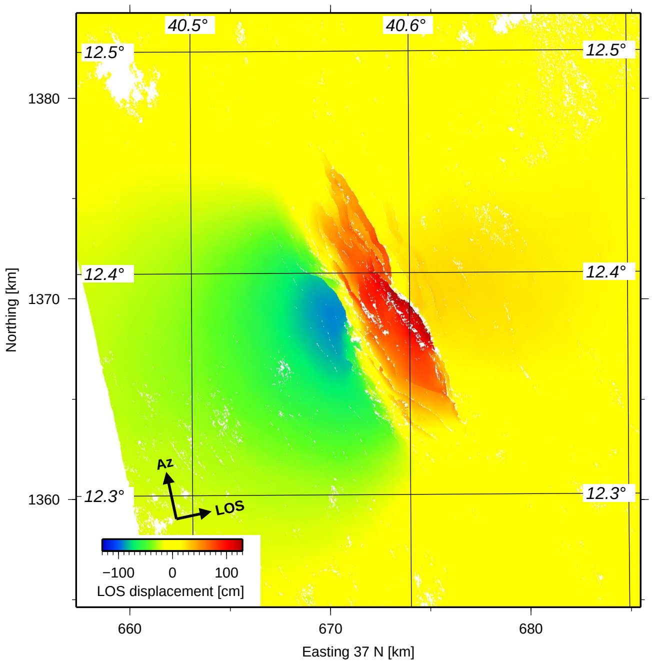

Figure 2.16: Unwrapped interferogram of the October 2008 dyke intrusion. Red: increased line of sight distance caused by subsidence at the rift centre. Blue: decreased LOS distance due to uplift at the flank.

Chapter 3

Fault throw algorithm

3.1 Introduction and motivation

The fundamental constraint on models of fault growth are the shape of displacement-length ($d - L$) profiles. Until recently displacement-length data were mostly derived from field measurements and seismic surveys (e.g. Walsh and Watterson, 1988, Cowie and Scholz, 1992a,b, Gillespie et al., 1992, Bürgmann et al., 1994, Cartwright et al., 1995, Mansfield and Cartwright, 1996). Due to recent technological advances, high-resolution remote sensing data have become more widely available and studies of faults are increasingly based on digital elevation models (DEMs) (e.g. Manighetti et al., 2001, Acocella et al., 2003, Polit et al., 2009, Begg and Mouslopoulou, 2010).
In this chapter I develop an algorithm for automatic measurement of fault throw, which is commonly used as a proxy for displacement of normal faults. Regardless of data set, for accurate measurements of displacement or throw it is necessary to identify the position of the foot- and hangingwall cutoffs. The cutoffs are defined as the intersections between the hangingwall and the footwall with the fault plane (Fig. 3.1 a). In reality, the cutoffs are more difficult to identify due to undulations on the fault blocks, irregular and eroded fault scarps, and fault drag and debris on the hangingwall (Fig. 3.1 b). Movement on the fault causes the beds on the adjacent fault blocks to bend and form monoclinal features parallel to the fault scarp which are defined as fault drag (e.g. Kearey, 2009).

Several techniques have been applied to extract fault displacement or throw from DEMs. Manighetti et al. (2001) manually picked elevation profiles along the top and

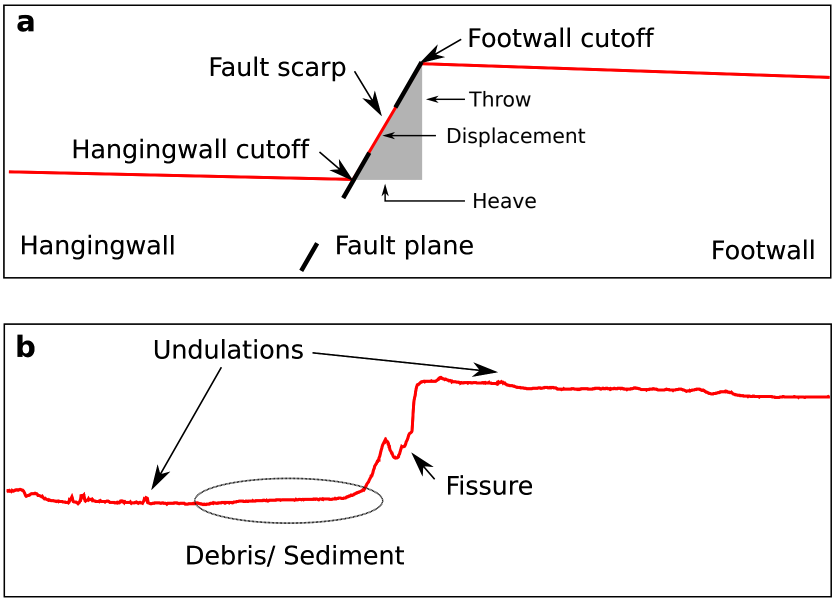

Figure 3.1: a) Cross section profile sketch of a normal fault. b) Cross section profile of real normal fault with undulations on footwall and hanging wall, fissures on the fault scarp and tilted beds, debris and sediments obscuring the hangingwall cutoff.

the base of fault scarps and calculated throw. Begg and Mouslopoulou (2010) manually extracted elevation profiles along the hanging- and footwall block with additional cross profiles to calculate the vertical offset between the blocks and Polit et al. (2009) manually determined throw from profiles crossing the fault scarps. Each of these techniques are labour intensive and differences in measurement procedures have been identified as one factor for scatter in the published data sets of fault $d_{max} - L$ (Gillespie et al., 1992). The aim of this chapter therefore is to develop an algorithm to extract throw along fault traces that can be applied consistently and rapidly to various fault data sets.

Multiple algorithms and software packages exist that attempt to automatically identify and trace faults in surface data set using different approaches. Shaw and Lin (1993) for example identify faults by measuring the topographic curvature within a small circular moving window. The two principal curvatures are used to quantify the topography. Variation of the window size allows for the identification and separation of faults into those with smaller and larger displacement but it does not provide quantitative measurements of fault throw.

Finally, the quantity of information available in the high-resolution topographic data sets is increasing rapidly. The 2009 LiDAR data covers 2000 km^2 and contains over 1000 fault segments. Most software packages used for visualisation of remotely acquired data (e.g. Petrel® and ARCGIS®) are not designed to handle such large data sets. They often require subdivision of the data set prior to uploading and a computer with sufficiently large working memory and powerful graphics card. Even with appropriate software (e.g. Geovisionary®) it takes several months to manually pick the cutoffs of the over 3500 fault segments, which were traced by C. Vye-Brown (Vye-Brown et al., 2012) within my research area (§ 4.2).

I therefore decided to develop a MATLAB® algorithm to measure fault throw along surface fault traces by automatically identifying the hanging and footwall cutoffs along the fault trace. It reduces the amount of subjectivity of the picking process by applying consistent criteria to every structure throughout the data set. Furthermore the algorithm reduces processing time, is independent of specialist software, and can run on a standard desktop computer.

In this chapter I first describe the fault structures observed at the Dabbahu segment before explaining the individual steps of the algorithm and the rationale behind them in detail. The final part focuses on my choices for the parameter values and discusses the possible sources of errors. The resultant algorithm is generally applicable to normal fault zones.

3.2 Geomorphological features of normal faults at the Dabbahu rift segment

Normal faults and open fissures are common structures within volcanic rift zones (Rubin and Pollard, 1988). At the Dabbahu segment at the Afar rift they are extremely well exposed due to very limited vegetation and low erosion rates (e.g. Rowland et al., 2007), which are also ideal conditions for airborne LiDAR. Small-scale features typical for faults in basaltic sequences and usually only visible in the field are therefore clearly visible in the high-resolution LiDAR DEM § 2.1. The most common features of normal faults in volcanic terrains were described by (Holland et al., 2006), based on work in

Hawaii and analogue models. They are illustrated in figure 3.2 and are:

1. Subvertical fault scarps, which are formed because of the preferential failure along the weak cooling joints in Basalt lava flows;
2. Open fissures at the base of the fault scarp, caused as the hangingwall pulls away from the footwall. They can be several meter wide and deep;
3. Tilted blocks of the original monoclinal flexure, which can be formed as the hangingwall gets stuck on an asperity or form due to a change of fault dip at depth;
4. Syn-rifting lava flows, which occur as fissure eruptions along the fault or flow across the top of the fault scarp;
5. Open fissures, which are often formed along the footwall due to localised tensile stresses induced during the faulting process.

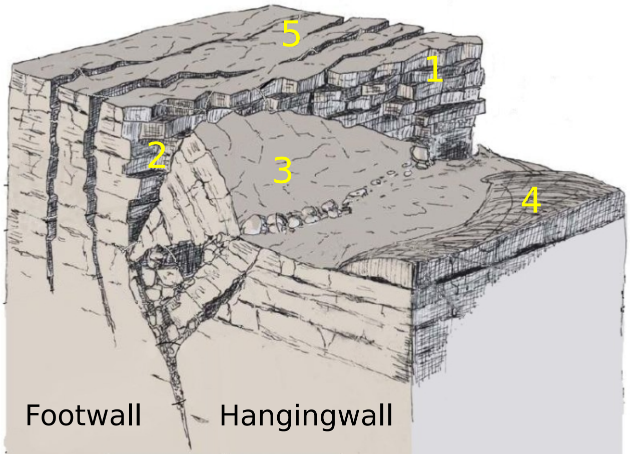

Figure 3.2: Extensional features in Basalt. 1. subvertical fault scarp, 2. open fissure at hangingwall, 3. limb of the original monoclinal flexure, 4. lava flow, 5. open fissure. Figure modified from Holland et al. (2006) with permisson from Elsevier.

Figures 3.3 and 3.4 are photographs and 3D views of the DEM produced with Petrel® showing examples of these secondary features at the Dabbahu segment. While the detail provided by the LiDAR DEM is spectacular, the complexity of the fault structures at the Dabbahu rift segment makes their analysis more difficult.

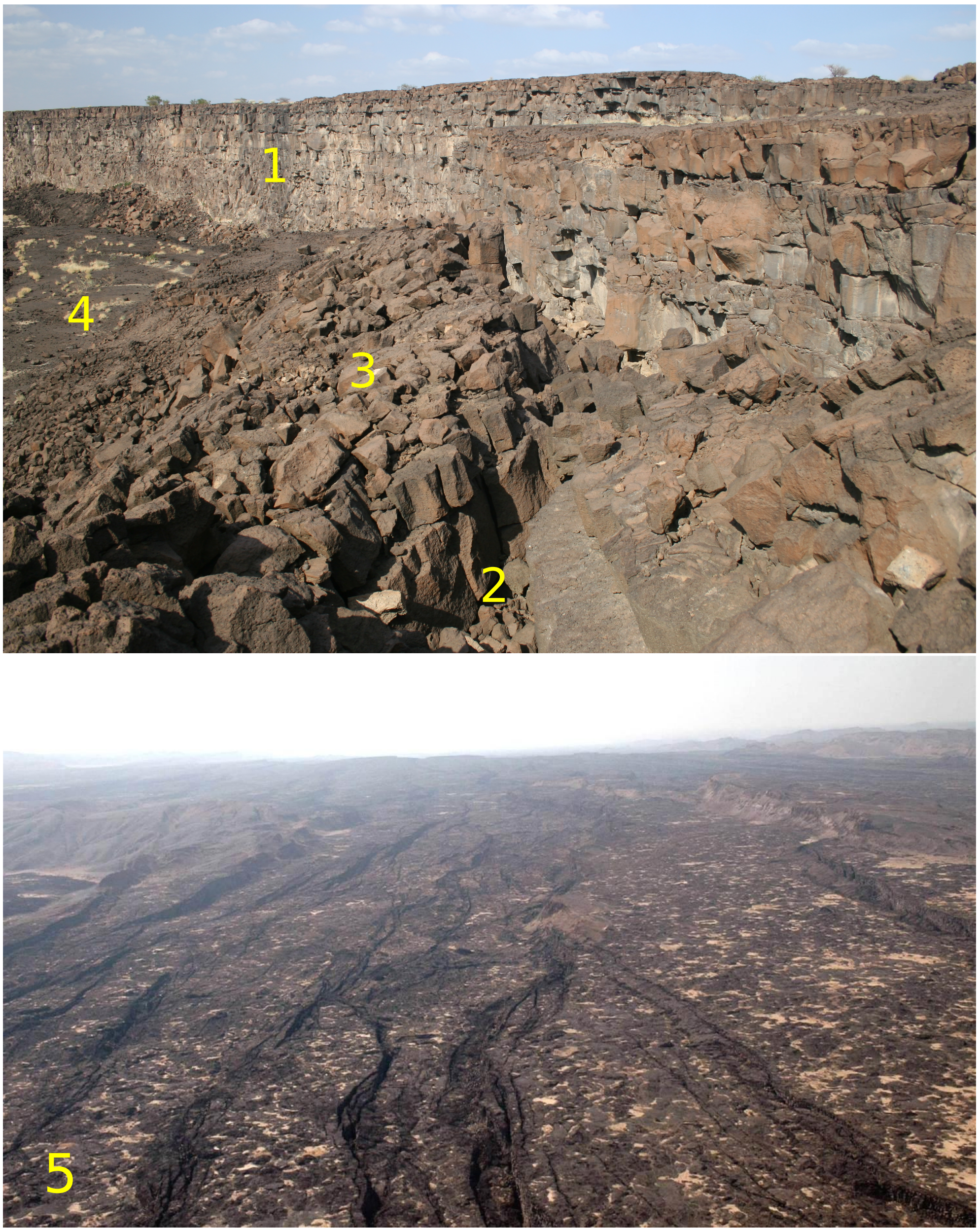

Figure 3.3: Top: Fault scarp (1) with debris within the hanging wall in the distance and a limb of the original monoclinal flexure (3) in the front with a small partly filled fissure (2). Visible throw on fault 50 m . In the left hand corner a recent lava flow is visible (12.43°N/40.57°W, Photo courtesy J. Rowland); bottom: View along the rift with faults and open fissures, looking South from the Ado'Ale volcanic complex (scale: ~10 km across) (Photo courtesy L. Baker)

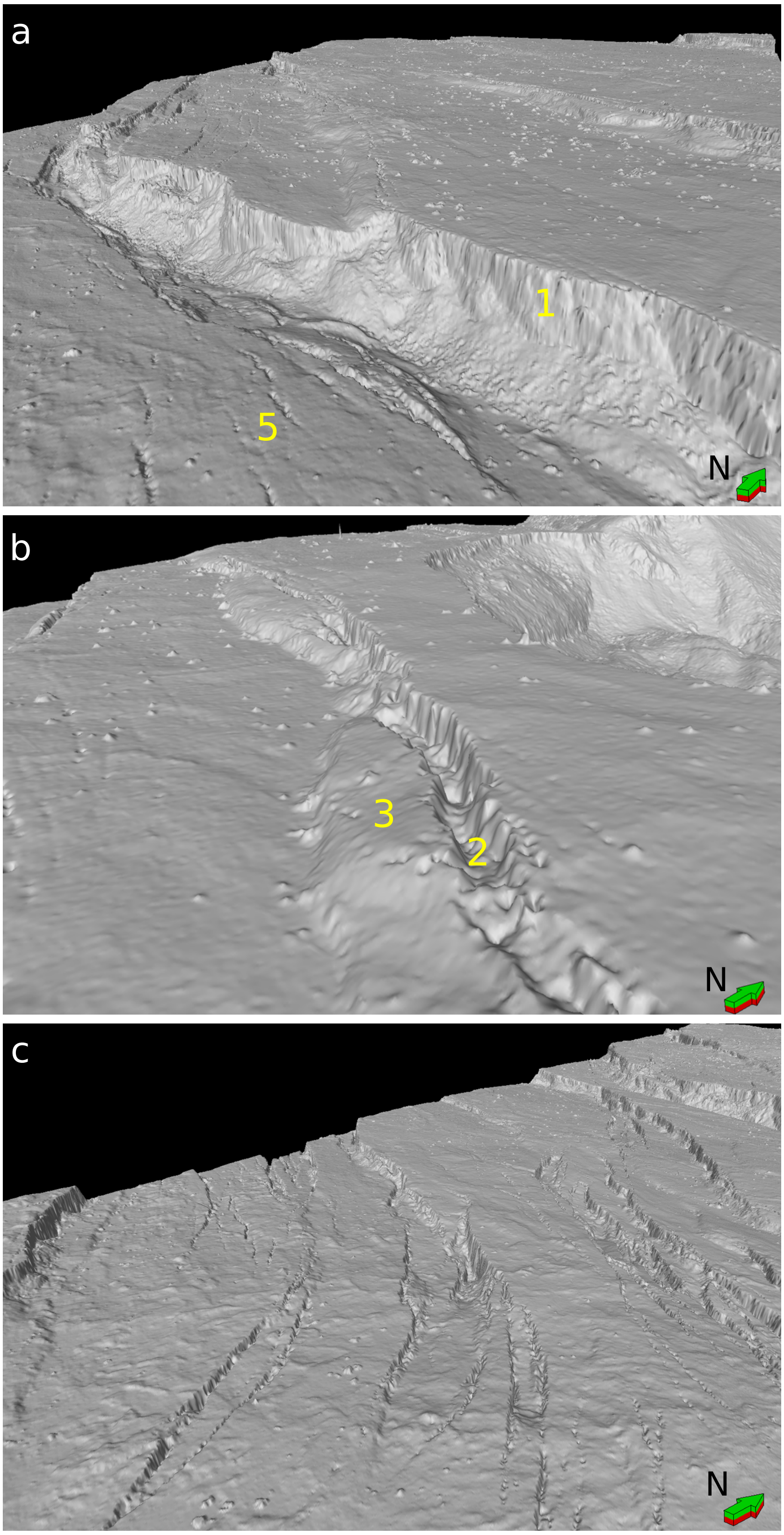

Figure 3.4: 3D views of the LiDAR DEM of different fault features created with Petrel®. Their locations are shown in Fig. 3.5. a) Fault scarp (1) with significant debris within hanging wall. Throw ∼50 m. The EW striking fault cross-cuts a NW-SE trending monoclinal feature (throw ∼7 m) on the foot wall. In the foreground small open fissures (5); b) Fault scarp with tilted monocline (3) and fissure (2) within hanging wall. Throw ∼10-15 m; c) System of closely spaced faults and fissure forming narrow graben structures and horse-tail splays. Image ∼500 m across. Locations of examples marked in figure 3.5.

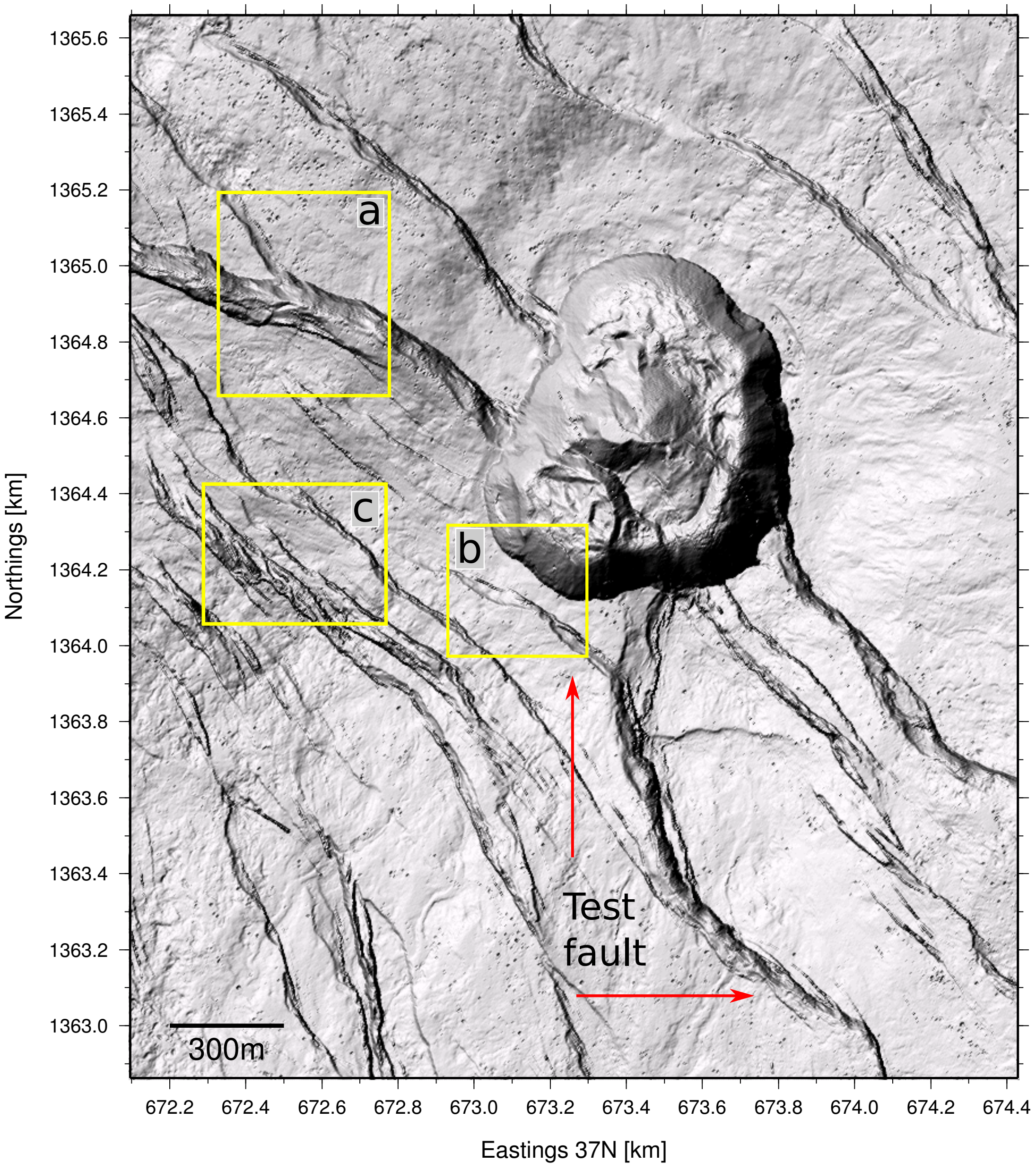

Figure 3.5: Section of the LiDAR DEM. Yellow boxes correspond to the locations of the examples shown in figure 3.4. Red arrows mark the fault used for testing in the following sections. Coordinates in UTM Zone 37N.

3.3 Description of the algorithm

3.3.1 Aim and strategy

My aim was to develop an algorithm to extract throw as a proxy for fault displacement from the 0.5 x 0.5 m^2 high-resolution LiDAR DEM. I chose to work on the high resolution LiDAR DEM (0.5 x 0.5 m^2) without additional filtering or downsampling to maintain the high information content of the data set. To achieve this I determine foot and hangingwall cutoff along the surface fault trace from equally spaced profiles perpendicular to the direction of strike. The footwall cutoff is usually clearly visible and relatively easy to determine within the mainly flood basalts. It is a sharp change from the almost flat footwall block to the high gradient at the top of the fault scarp. The hangingwall cutoff is often obscured by monoclinal flexures, debris and fissures. I therefore designed the algorithm to detect the point at which all fault related deformation and drag comes to an end.

Deriving precise fault displacement measurements depends on being able to accurately identify and measure fault length and displacement or throw. Kim and Sanderson (2005), Kim et al. (2004), Gupta et al. (1998) argue that damage zones and monoclines at fault tips are part of the fault length and that fault drag, which is expressed by deflected, monoclinal layers parallel to the fault (e.g. Kearey, 2009), often masks the real displacement. Furthermore, if working with surface data the visible fault trace does not necessarily correspond to the maximum fault length at depth, nor does the visible fault throw. During the development of the algorithm I focused on including the fault drag at the hangingwall and attempted to account for monoclines extending beyond the visible fault.

3.3.2 Step-by-step description

The input data for my algorithm are mapped surface fault traces and the 2009 high-resolution LiDAR DEM. While I developed the algorithm with fault traces which were manually picked on the LiDAR DEM fault traces derived by any method can be used as input data. For each of the fault traces the algorithm determines the fault's overall strike by fitting a linear regression curve to the mapped trace. The dip direction is determined by comparing the elevation on either side of the fault trace on 10 equally spaced profiles. The cutoffs are then extracted individually for each profile along the trace. The number of profiles depends on the chosen spacing. Its influence is demonstrated in § 3.4.2.

After determining the strike and dip direction of the fault, the algorithm extracts topographic profiles from the LiDAR DEM. The profiles are 600 m long, centred on the manually picked fault trace, and approximately perpendicular to strike. Regardless of the dip direction of the fault the profiles are extracted from west to east. The basic steps of the algorithm are illustrated in Fig. 3.6 which shows a subsection of a profile across a fault scarp. The intersection of the manually picked fault trace with the profile (MP [1]) is marked with a green triangle. The fault breaks almost vertically to the west of MP but downward sloping is already visible in the east, commencing at a small fissure. Beyond the fissure the footwall, is almost level. The subvertical part of the fault scarp is joined by a relatively flat monoclinal feature extending westwards for ∼50 m. The feature has a throw of ∼10 m.

The first step is to establish that the profile in fact intersects a fault scarp. This is especially important if the input trace is picked at lower resolution, where it is difficult to pick the fault extent precisely. I adopted the strict definition that a fault needs to have a clear surface break, which shows up as a potentially very small step in the topography, and a maximum in its first derivative, f', the gradient (Fig. 3.6 b). I impose a minimum threshold of 1 on the gradient which correlates to a minimum dip of 45°. I chose this low threshold to ensure that the lower angle faults set within the rhyolites could be included in the analysis. The low angle is further necessary to reliably identify small offsets at the fault tips.

In many cases monoclines with significant throw (> 1 m) extend beyond the fault trace. In an attempt to include this information into my analysis I introduced a second lower threshold of 0.5 if the first one is not met. It translates to a 30° dip or a throw of 25 cm over 50 cm which is close to the accuracy of the LiDAR measurements. Monoclines do not have a footwall cutoff, therefore the values derived across them are less reliable.

The faults at the Dabbahu segments are closely spaced and profiles often intersect more than one fault scarp. To prevent the selection of a neighbouring structure, the

---

[1] Symbols used in this section are defined in table 3.1

Abbreviation	
MP	manual pick
PC	possible cutoffs on profile
A and B	neighbouring PCs on profile $A = (A_x,A_y)$; $B = (B_x,B_y)$
$tmpA$	$tmpA = (tmpA_x,tmpA_y)$ temporary holding cell
sm	horizontal search margin
fpw	horizontal footwall plain width
hpw	horizontal hangingwall plain width
v_{min}	minimum significant vertical offset
v_{max}	Maximum tolerated vertical offset
fw	maximum tolerated horizontal fissure opening
sd	search direction sd=1: westward, sd=2: eastward

Table 3.1: Table of abbreviations and parameters of the algorithm. Capital letter (1-4) refer to points with x and y position on the profile. Lower italic letters (5-10) refer to adjustable parameter of either horizontal width or vertical offset. Lower case letter (11) direction variable.

surface break has to be within a pre-defined distance of MP, indicated by the grey box in Fig. 3.6 b. I use ±30 m for this search margin.

During manual picking I rely on the ability to assess the entire profile, recognise secondary features and discard insignificant changes in order to pick the best cutoffs. Here I rely on the gradient to indicate changes along the profile and multiple parameters to evaluate their significance. In an ideal schematic case (Fig. 3.1 a) the gradient is zero except across the fault scarp and the cutoffs are the points just before and just after this signal. In real data all of the secondary fault features (§ 3.2) lead to signals in the gradient and it is therefore more robust to look for the planes that terminate at the fault scarp and extract their endpoints. These planes are the intact portions of the footwall and hangingwall. A fault is therefore identified as the entire structure separating the intact portions of the footwall and hangingwall. To be classified as intact, I require the plane width (pw) to be at least 30 m.

To identify the footwall and hangingwall cutoff I first identify potential cutoffs (PC), and then determine which of them are the real cutoffs. I determine the PCs by first setting all insignificant signals in the gradient, which are mainly caused by long wavelength undulations on the surface, to zero, using a threshold of 0.5. I then extract the

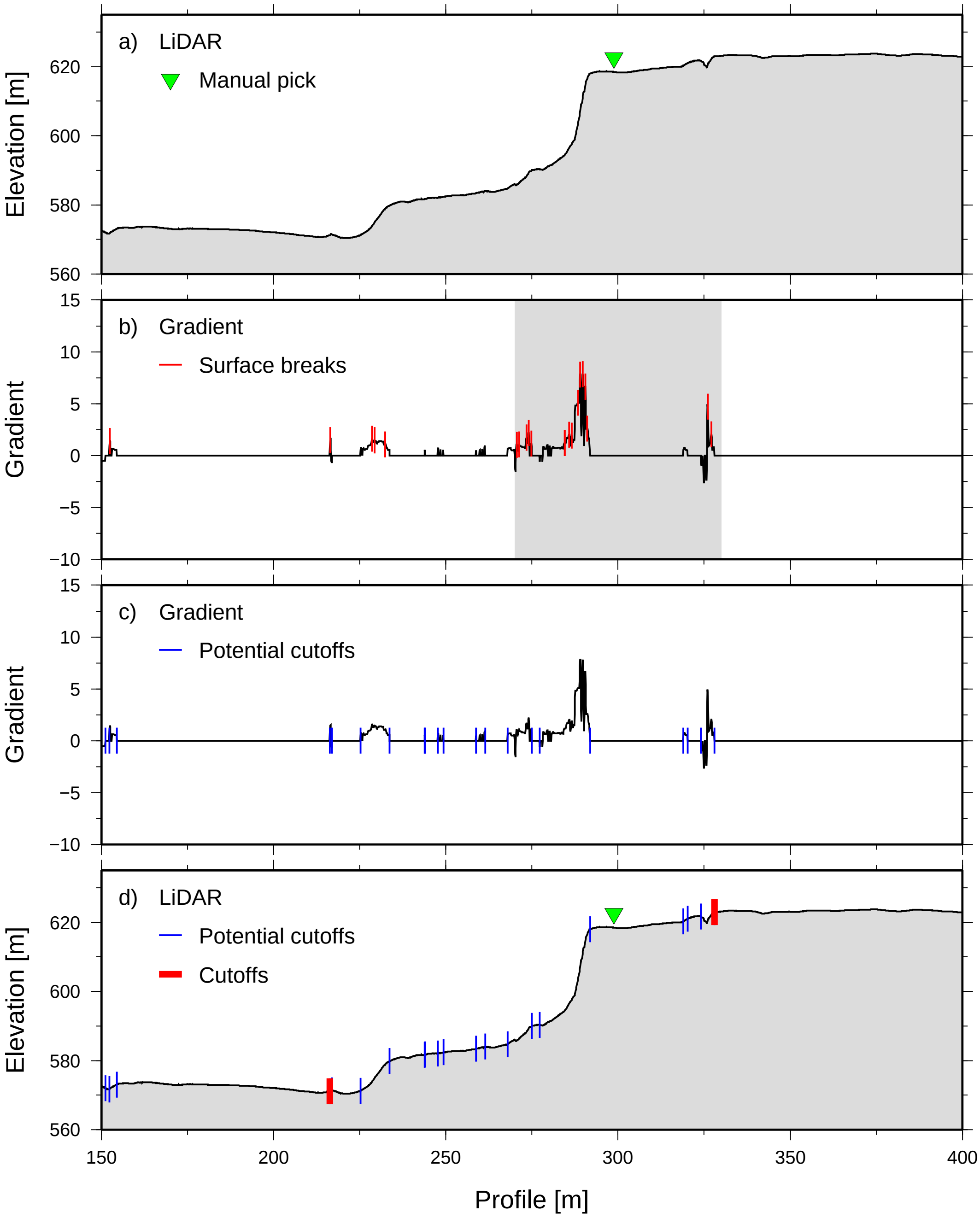

Figure 3.6: Illustration of the individual processing steps of the algorithm on a example profile. a) Section of topographic profile extracted from the LiDAR DEM. Green triangle marks the position of the manual fault pick. b) Gradient of the profile. Marked in red gradient maxima indicating surface breaks. Grey box indicates the margin in which a surface break has to be present for the algorithm to proceed. c) Simplified gradient with values below 0.5 set to 0. Potential cutoffs marked in blue. d) Topographic profile with potential cutoffs and final hanging- and footwall cutoff in red.

PCs which are all points (i) for which the following relationship is true. $f'(i) = 0$ and $f'(i-1) \neq 0$ or $f'(i+1) \neq 0$ (Fig. 3.6c, blue marker), where $f'(i)$ is the gradient at the ith stored height value in the profile.

Once the PCs are established, footwall and hangingwall cutoffs are determined (Fig. 3.6d, red marker). I first extract the footwall cutoff using the steps summarised in the flowchart in figure 3.7. The algorithm starts at MP and selects the first two PCs west ($sd = 1$) of it (A and B). At the first checkpoint, I check if the horizontal distance between A and B is equal or greater then the required plane width (pw) of 30 m. If this is not the case I assess the elevation difference between A and B. From this several scenarios can be distinguished.

1. If the elevation drop is at least 0.5 m (v_{min}), B is either on the fault scarp or in an open fissure.
    (a) By definition a fissure only opens horizontally but has no vertical offset. I defined that B is positioned in a fissure if there is a point (P) within 40 m (fissure width, fw) of A that is at least at the same height as A. In that case I set $A = B$ and initiate the next run by selecting the next PC in the search direction.
    (b) If no such point, P, can be found, B is positioned on the fault scarp and the search in this direction is terminated.
        i. If $sd = 1$, A is used as the starting point for the eastward search ($sd = 2$). This second round is necessary to assure the correct identification of the footwall cutoff for faults dipping towards the west and the east as well as allow for the case that the MP was picked on the fault scarp.
        ii. If $sd = 2$, A is the footwall cutoff.
2. If the elevation rise is larger than 0.5 m A and B are situated on the fault scarp. The cutoff has not yet been found. B becomes $A (A = B)$ and the next pass through the loop is initiated. B is the next PC in the search direction of A.
3. If the elevation changes by less than 0.5 m up or down the situation is undetermined and I use the temporary variable $tmpA$ to resolve it.

   (a) If $tmpA$ is empty, A is stored in $tmpA$ for potential later analysis ($tmpA = A$). I then set $A = B$ and start the next pass.

   (b) If $tmpA$ already exists, I test if the distance between $tmpA$ and B is $\leq pw$.

      i. If $\mid B_x - tmpA_x \mid \geq pw$ and $sd = 1$, $tmpA$ becomes the starting point ($A = tmpA$) for the search in easterly direction ($sd = 2$). The variable $tmpA$ is cleared.

         - If the algorithm is already searching eastwards ($sd = 2$) $tmpA$, is the footwall cutoff.

      ii. If $\mid B_x - tmpA_x \mid < pw$ it sets $A = B$ and starts the next pass. $tmpA$ is kept.

If the distance between A and B is equal or larger than pw, the algorithm has found the plane on top of the footwall. In the case $tmpA$ was previously assigned A and $sd = 1$ I terminate the search in westward direction and initiate the eastward search ($sd = 2$). If $sd = 2$ A is the footwall cutoff.

Once the footwall cutoff is detected I use a similar strategy to search for the hangingwall cutoff (Fig. 3.8). A, B and $tmpA$ are cleared. I start at the footwall cutoff (A) and select the first PC in the down dip direction (B). For the unlikely case that the hangingwall cutoff is not found before the algorithm reaches the last PC on the profile I include a failsafe: If A is the last PC on the profile the algorithm checks if $tmpA$ exists and select either A or $tmpA$ as hangingwall cutoff.
Usually, B exists and the algorithm analyses the vertical offset between the two points.

1. If B drops by at least 0.5 m, B is usually positioned on the fault scarp in which case $A = B$ and the next pass through the loop is initiated. $tmpA$ is cleared

2. If B rises by more than 5 m (v_{max}) the algorithm checks if the rise is due to an open fissure at the hangingwall. Generally these features are horizontally close to the footwall cutoff, hence the algorithm checks if the rise is within the predefined distance from the footwall. I again use 40 m for the fissure width defined for the footwall cutoff.

   (a) If the fissure criteria are met $A = B$ and the next pass commences.

   (b) If it is not a fissure the hangingwall cutoff is A. The most common case for this scenario is a relatively narrow graben where the cutoff has to be determined in the absence of a distinct plane.

3. If none of the first two cases are applicable the algorithm calculates the horizontal distance between A and B.
   (a) If $\mid B_x - \mathrm{A}_x \mid \geq pw$, A is the hangingwall cutoff.
   (b) If $\mid B_x - A_x \mid < pw$, it is unclear.
      i. If $tmpA$ is empty it set $tmp = A$ and $A = B$ and starts the next pass.
      ii. If $tmpA$ exists the algorithm looks at the vertical offset between A and $tmpA$.
         - If it drops by at least 0.5 m the next pass through the loop is initiated with $A = B$. $tmpA$ is cleared.
         - If it rises by more than 5 m it again checks for the presence of a fissure. If the algorithm identifies a fissure it initiates the next pass with $A = B$. $tmpA$ is kept. If it is not a fissure the hangingwall cutoff is the lowest PC of the three (A, B and $tmpA$).
         - If none of the first two cases are applicable the algorithm calculates the horizontal distance between A and B.
           If $\mid B_x - A_x \mid \geq pw$, the hangingwall is the lowest PC of the three (A, B and $tmpA$). If $\mid B_x - A_x \mid < pw$, another pass through the loop is started with $A = B$. $tmpA$ is kept.

After the cutoffs have been determined I calculate the throw, which is the elevation difference between the footwall cutoff and the hangingwall cutoff. The results of my algorithm are stored in an ascii file containing throw, and x, y, z-position of both cutoffs. The algorithm also generates 3-D line plots for each fault showing the profiles, the manual picked fault trace and the cutoffs for a visual quality control. I show a 3-D line plot in § 3.4.1 figure 3.16.

3.3.3 Curve fitting

The fault structures at the Dabbahu rift segment and their secondary features are very complex and detection errors are inevitable. In order to better assess the shape

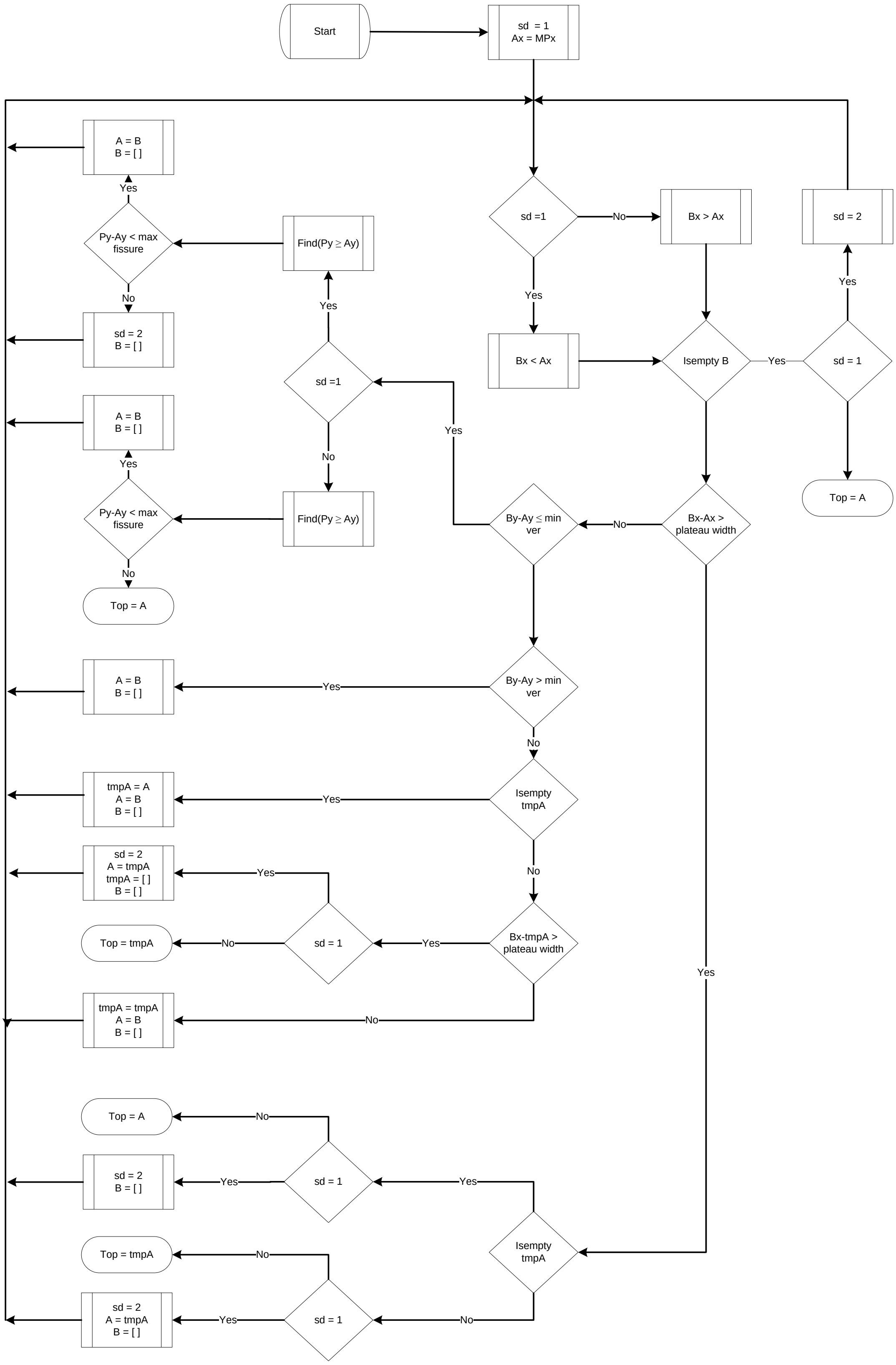

Figure 3.7: Flowchart of the steps taken by the algorithm to determine the footwall cutoff. The algorithm starts at the manual pick of the fault trace. It assesses horizontal and vertical offset of neighbouring PCs until the footwall cutoff is found.

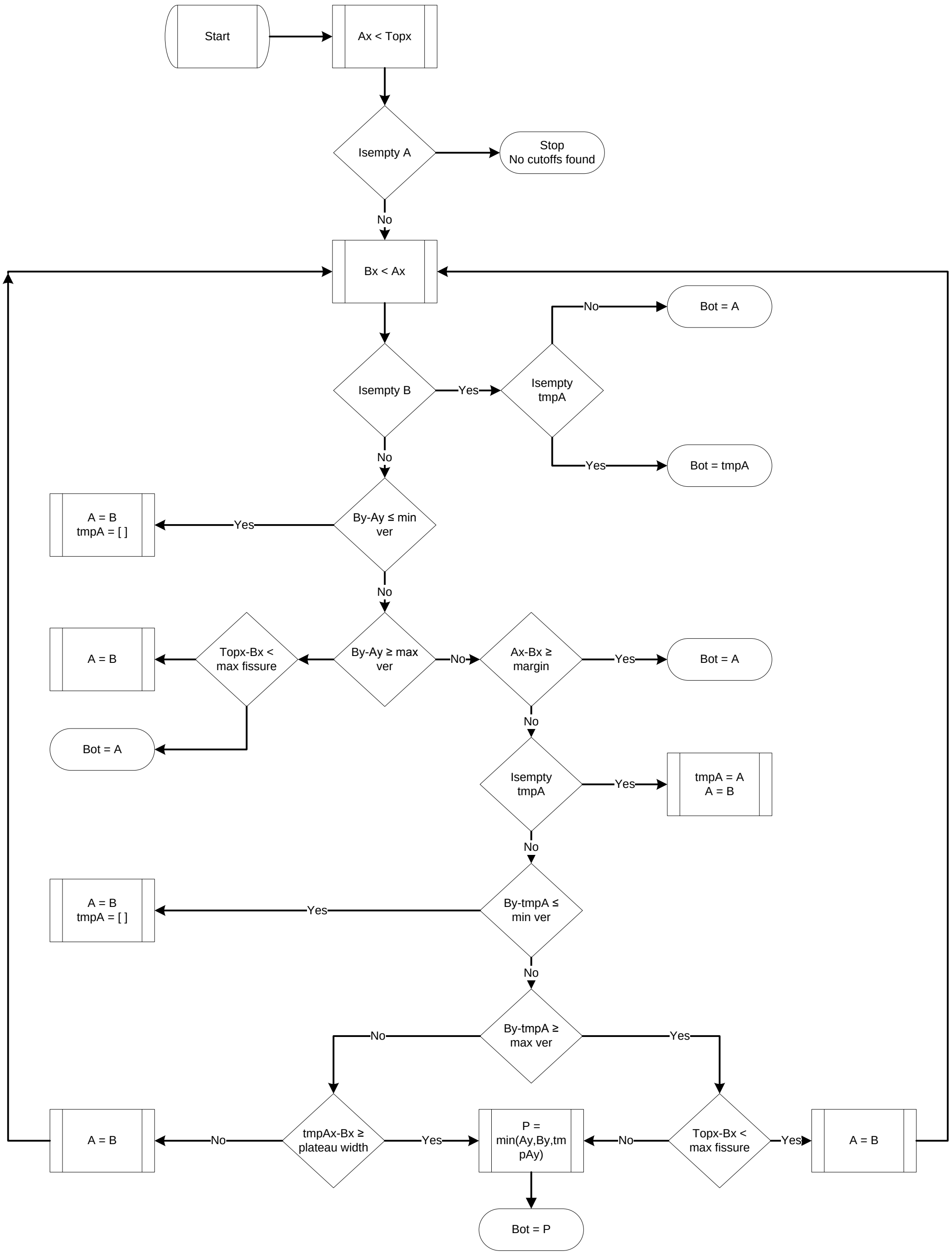

Figure 3.8: Flowchart of the steps taken by the algorithm to determine the hangingwall cutoff.

of the $d - L$ curves I apply a robust local regression (*rloess*) to the $d - L$ curves which is insensitive to outliers. The *rloess* method was first introduced by Cleveland (1979). It is developed on the assumption that any small data subsets can be fitted with 2nd order polynomials ($f(x) = ax^2 + bx + c$) but, in contrast to other regression methods makes no assumption on the overall shape of the data set. The size of the data subset can be adjusted according to the data set. For each point x, where x is the distance along the fault, the method determines the best fitting regression curve for the data subset centring on point x. *Rloess* finds the best regression parameter through an iterative process. After each successful iteration it applies a tri-cube weighting function T (equ. 3.1, fig 3.9 red), which enhances the influence of points vertically closer to the model.

$$\begin{aligned} T(x) = (1 - |t(x)_0 - t(x)_m|^3)^3 \quad &\text{for} \quad |t(x)_0 - t(x)_m| < 1 \\ T(x) = 0 \quad &\text{for} \quad |t(x)_0 - t(x)_m| \geq 1 \end{aligned} \tag{3.1}$$

were $t(x)_0$ is the measured throw at point x and $t(x)_m$ is the modelled throw at point x.

This is the standard local regression method after which the rms (root mean square) for each point is calculated. To remove outliers the robust version applies a bi-square weighting function B (eq. 3.2, fig 3.9 blue) to the rms of the best fitting curve.

$$\begin{aligned} B(x) = (1 - |t(x)_0 - t(x)_m|^2)^2 \quad &\text{for} \quad |t(x)_0 - t(x)_m| < 1 \\ B(x) = 0 \quad &\text{for} \quad |t(x)_0 - t(x)_m| \geq 1 \end{aligned} \tag{3.2}$$

Bi-square weighting sets large rms values to 0 which will then not be included in the final iteration.

My standard settings are 10 points per data subset which correlates to 200 m with 20 m profile spacing. The *rloess* method works best on large data sets I therefore decided to decrease the profile spacing to 5 m if fewer than 50 points are available.

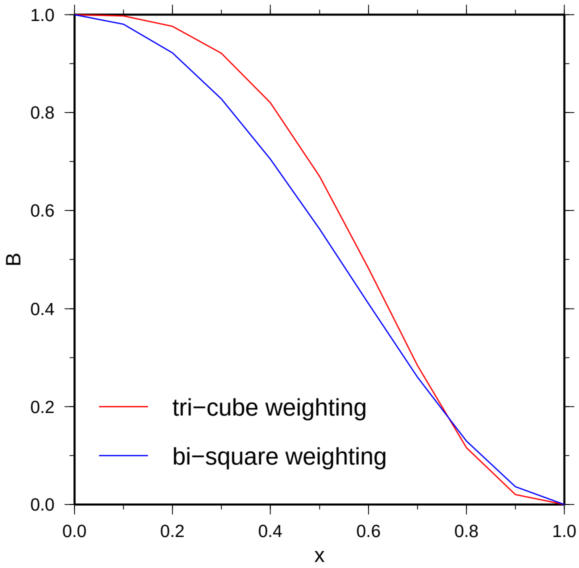

Figure 3.9: Tri-cube (red), bi-square (blue) weighting function.

3.4 Optimising the parameters for the Dabbahu rift segment

3.4.1 Parameters affecting the quality of the cutoffs

The quality of the cutoffs and thereby the accuracy of the throw, is dependent on the values chosen for the six parameters (sm, fpw, hpw, v_{min}, v_{max}, fw, Table 3.2). Each of the parameters influences the results to different degrees. To illustrate this, I handpicked the hangingwall and footwall cutoffs for 80 profiles along a fault structure, chosen because it exhibits a large range of different features, and compare them to the cutoffs retrieved by the algorithm for a range of different parameter values. The chosen fault structure is marked in Fig. 3.10. The main structure is set within closely-spaced neighbouring faults. The smaller, NNW-oriented structure turns into a monocline towards the north of the image (1). Just south of the small crater it links with a larger NNE trending fault (2). At its southern end of the image a small graben structure is visible at the hangingwall (3). Along both fault scarps fissures of varying depth, terraces and monoclines are present (4).

Below I describe each of the 6 parameters. I test how each of the parameters affects the quality of the cutoffs and which values lead to the best results.

- Search margin (sm) and footwall plain width (fpw):

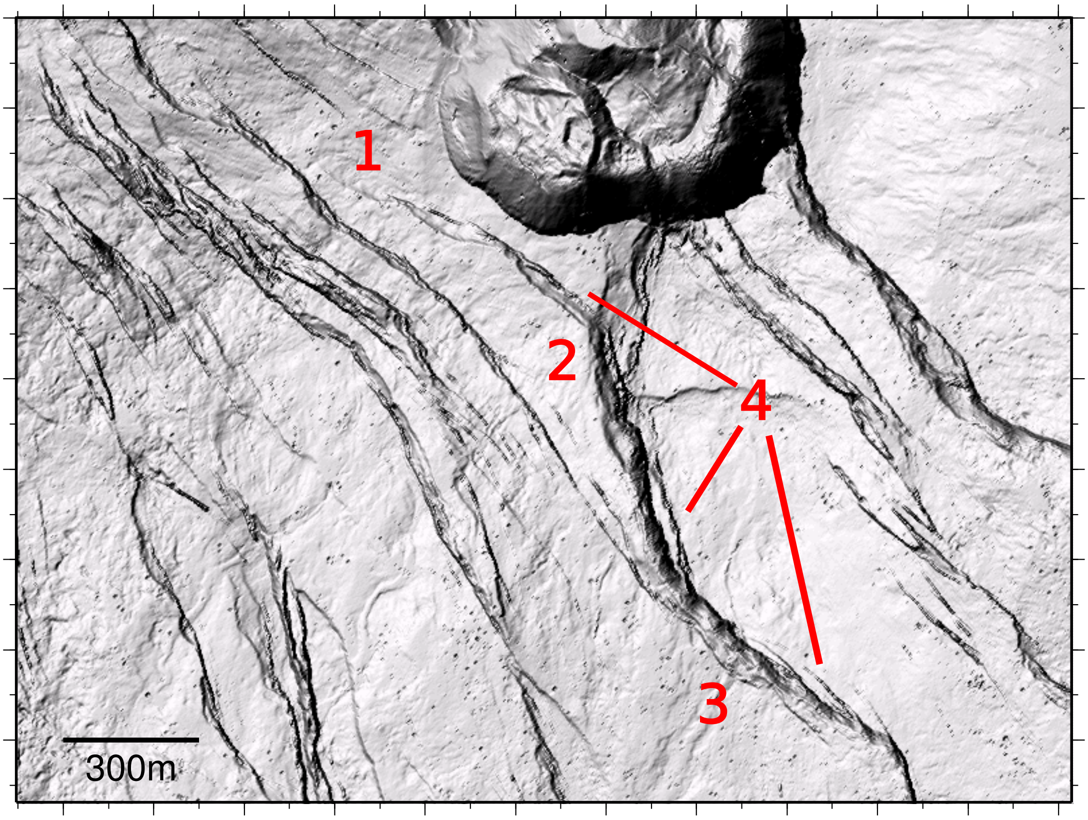

Figure 3.10: Example test fault featuring a variety of common fault features. 1. Fault tapering into a monocline, 2. Linkage zone, 3. Graben at hangingwall, 4. Small fissures, monoclinal flexure, terraces.

The main parameters influencing the footwall cutoff are search margin, plain width and the position of the manual pick. The majority of the fault traces are picked on the top of the footwall but they are sometimes placed on the fault scarp. To illustrate that the algorithm is designed to deal with both scenarios I used the original fault trace picked above the fault scarp and shifted it westwards so that the trace was positioned on the fault scarp. I then carried out the following tests using the trace picked above the scarp and the trace placed on the scarp as input. To test the influence of sm and fpw I applied my algorithm to the test fault varying the search margin at 10 m intervals between 10 to 100 m and the footwall plain width between 10 to 50 m also at 10 m intervals. Figure 3.11 shows the misfit between the measured and handpicked hangingwall cutoff for each of the 80 profiles and each of the 50 parameter combinations as individual points (4000 measurements) for both input traces (Left: above scarp, right: on scarp).

Regardless of parameter combination the footwall cutoff is well extracted with 77%, if the trace is position above the scarp, and 72%, if the trace is placed on the scarp, of the measurements being within ±1 m vertically from the handpicked footwall cutoff. The horizontal misfit is larger with 60% of the measurements being within ±5 m from the handpicked cutoffs. The figure also shows that if the trace is picked on the fault scarp larger outliers in both vertical and horizontal direction are likely to occur if the parameter values are not well chosen.

I then calculated the mean misfit between the measured footwall cutoff and the handpicked footwall cutoff from the 80 profiles for each parameter combination. The mean vertical (top) and horizontal (bottom) misfit are presented in figure 3.12 by colour-coded dots (left: trace above scarp, right: trace on scarp). It reiterates that if the fault trace is picked on the footwall the vertical cutoff is within 1 m of the handpicked cutoff. The average offset increases slightly if picked on the scarp and the effect of the parameter is more apparent. The horizontal offset increases with increasing parameter values. I chose 30 m for both parameters. A 20 m search margin would slightly improve the horizontal offset but has no effect on the vertical component. The slightly larger search margin allows me to deal with larger picking errors during the manual picking process, which I believe to be more important.

- Hangingwall plain width (*hpw*) and maximum tolerated vertical offset (v_{max}): The hangingwall cutoff is mainly controlled by the plain width *hpw* and the maximum tolerated vertical offset v_{max}. Again I derived the hangingwall offset for a range of *hpw* and v_{max} values and compared them to the manually picked offsets of the 80 profiles. *hpw* ranges from 5 to 50 m at 5 m intervals and v_{max} ranges from 1 to 10 m at 1 m intervals. In figure 3.13 top I show the misfit between the measured and handpicked hangingwall cutoff for each of the 80 profiles and each of the parameter combinations as individual points. The majority (57%) of the derived hangingwall cutoffs are within ±1 m vertical of the handpicked cutoff. The horizontal misfit is distributed over a larger range, up to -167 m. 42% of the derived cutoffs are within ±5 m of the handpicked one. The figure 3.13 shows that a poor choice of parameters is more likely to cause the hangingwall cutoff to be extracted too close to the fault scarp, which leads to an underestimation of the derived throw. The mean misfit determined from the 80 profiles for each

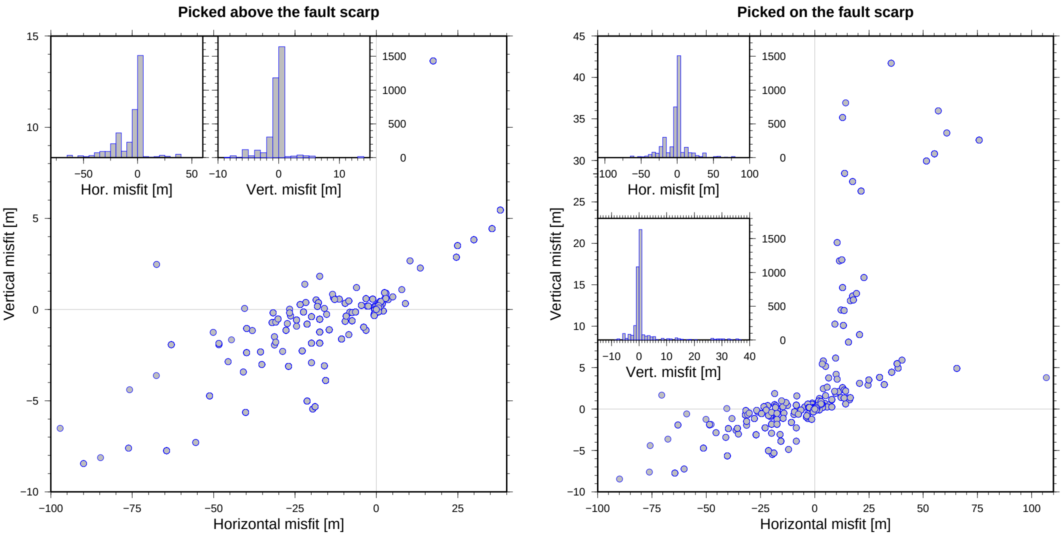

Figure 3.11: Distribution of vertical and horizontal differences between footwall cutoffs extracted by the algorithm for different parameter settings and the manually picked footwall cutoffs. 4000 measurements for 50 parameter combinations and 80 profiles. Left: Fault trace picked above fault scarp, right: Fault trace picked on fault scarp. Parameter settings: *sm* ranges from 10 to 100 m and *pw* ranges from 10 to 50 m both at 10 m intervals.

parameter combination is presented in Fig. 3.13 bottom. It shows that the vertical and horizontal misfit is mainly dependent on *hpw* and reduces with increasing values up to *hpw*=30 m. No significant reduction of the misfit is achieved by increasing *hpw* further. The influence of v_{max} is small but the misfit in both directions increases slightly for values above 5 m. For the faults at the Dabbahu rift segment I have chosen *hpw* = 30 m and $v_{max} = 5$ m.

- Minimum significant vertical offset (v_{min}):
  v_{min} influences both the hanging and footwall cutoffs and helps to determine the end of a plain. Keeping the other parameters fixed at their best values (table 3.2) I varied v_{min} between 0.2 and 1 m at 0.1 m intervals. Figure 3.14 shows the mean vertical (left) and horizontal (right) misfit for both foot- and hangingwall cutoff derived from the 80 profiles. The mean misfit for the footwall cutoff is larger for values below 0.4 m but shows very little variation for values between 0.4 m and 1 m for both the vertical and horizontal component. The hangingwall cutoff exhibits a minimum misfit at 0.4 and 0.5 m for both components. I chose 0.5 m, which means that if the vertical offset between two PCs is less than 0.5 m

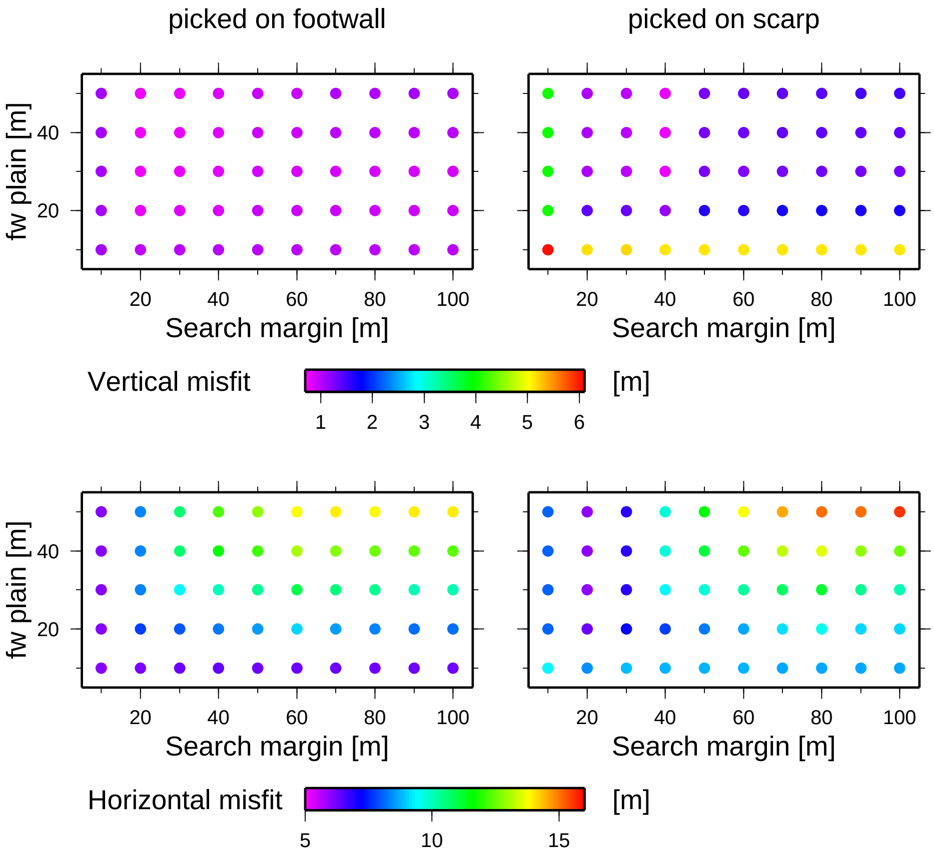

Figure 3.12: Influence of search margin and plain width on footwall cutoff quality. Each point shows the average offset of the calculated footwall cutoffs, per parameter setting, from the manually picked footwall cutoffs. Top row: vertical offset, bottom row: horizontal offset. Left: Trace picked on footwall, right: trace picked on fault scarp.

the section between them is considered flat. PCs are separated by at least one pixel, which translates to a maximum slope dip of 26° between the two points. PCs are usually separated by more than one pixel, relating to smaller slope angle.

- Fissure width fw:

  Both footwall and hangingwall cutoff are affected to a small degree by the fissure width fw. The sole function of fw is to allow the detection of fissures at the hanging and footwall cutoff and prevent the algorithm from prematurely terminating its search. To demonstrate this I applied the algorithm to the test fault and only

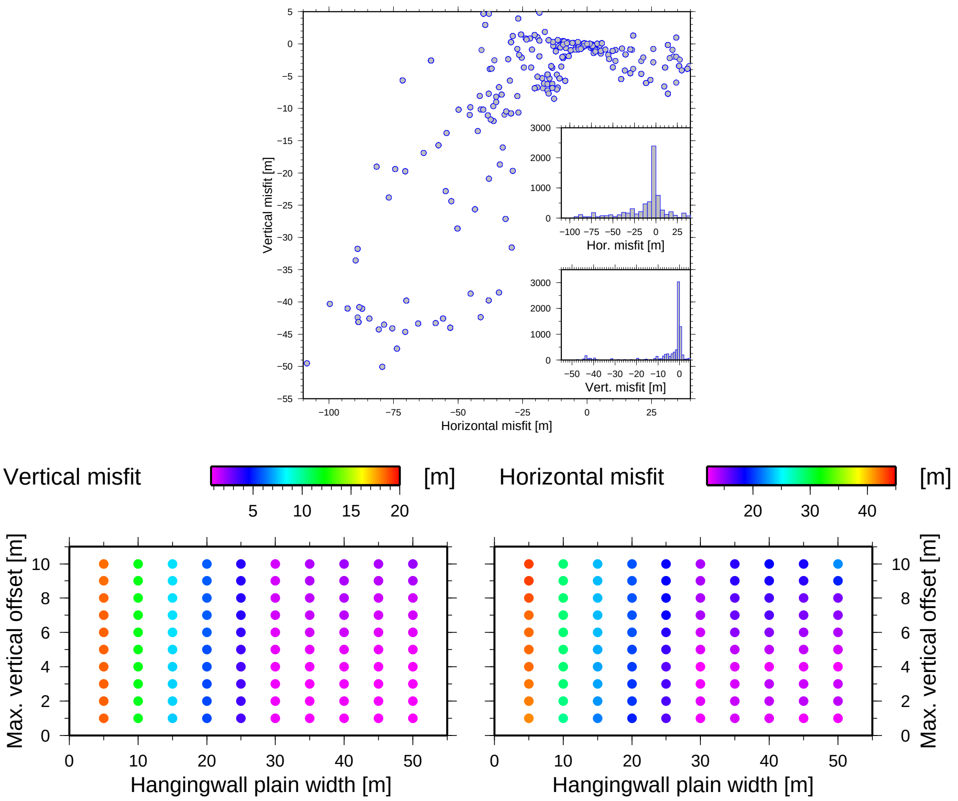

Figure 3.13: Influence of parameter settings on hangingwall cutoff. Top: Distribution of vertical and horizontal misfit between algorithm derived and handpicked hangingwall cutoff for 80 profiles and 100 parameter combinations of *hpw* and v_{max}. *hpw* ranges from 5 to 50 m at 5 m intervals and v_{max} ranges from 1 to 10 m at 1 m intervals. Bottom: Mean misfit collected for each parameter combination. Left vertical offset, right: horizontal offset

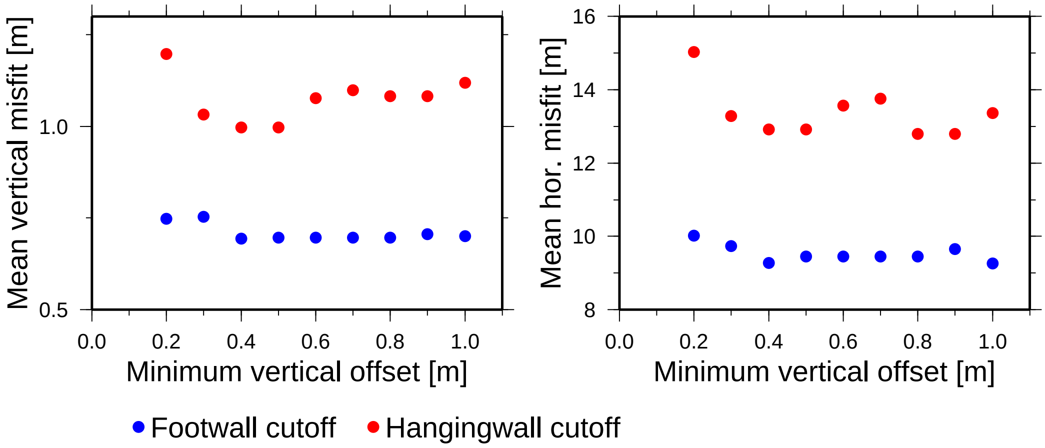

Figure 3.14: Influence of the minimum vertical offset (v_{min}) on the quality of the foot- and hangingwall cutoff. The minimum vertical offset (v_{min}) is plotted vs. the mean misfit between the algorithm derived and the handpicked cutoffs for 80 profiles. Left: mean vertical misfit, right: mean horizontal misfit. Blue: footwall cutoff, red: hangingwall cutoff.

varied fw from 0 to 100 m at 5 m intervals. The other parameters are set to their optimised values listed in table 3.2. Figure 3.15 shows the mean vertical (left) and horizontal (right) misfit vs. fissure width for both the footwall cutoff (blue) and the hangingwall cutoff (red). It illustrates that the footwall cutoff is hardly affected by fw. The influence on the hangingwall cutoff is more pronounced. If fw is smaller than 20 m or larger than 60 m the mean vertical and horizontal misfit increase significantly by ∼1 m and 3 m respectively. The minimum mean misfit is achieved with a fw between 20 m and 60 m. I chose 40 m. Real fissures are not usually that wide but fissure-like features at the hangingwall can extend over 10s of meters.

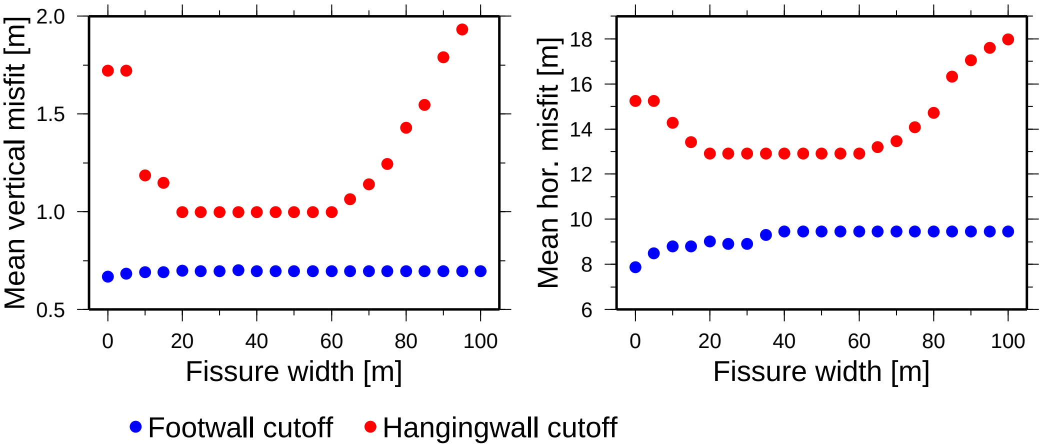

Figure 3.15: Influence of the fissure width on the quality of the foot- and hangingwall cutoff. The fissure width is plotted vs the mean misfit between the algorithm derived and the hand-picked cutoffs for 80 profiles. Left: mean vertical misfit, right: mean horizontal misfit. Blue: footwall cutoff, red: hangingwall cutoff.

Parameter	Abbreviation	Value
Search margin	sm	30 m
Footwall plain width	fpw	30 m
Hangingwall plain width	hpw	30 m
Minimum significant vertical offset	v_{min}	-0.5 m
Maximum tolerated vertical offset	v_{max}	5 m
Maximum tolerated fissure opening	fw	40 m

Table 3.2: Chosen algorithm parameters optimised for the normal faults at the Dabbahu rift segment.

Figure 3.16 shows the results derived with the chosen parameter (Table 3.2). Line plots like this one are routinely produced by my algorithm to allow a visual quality control if desired. The lines show the individual profiles. On the bottom the manual picks for hanging and footwall cutoff are marked in yellow and pink respectively. The middle and top plot are distinguished by the location of the manually picked fault trace. In the middle image the trace (green) was positioned on the fault scarp and in the top image the trace (green) is picked on the footwall. Extracted hanging and footwall cutoffs are marked in blue and red respectively. The cutoffs derived from the two differently positioned fault traces are very similar with only small changes in the location of the footwall cutoff. They are also very similar to the manually picked cutoffs. The line plot also shows that the algorithm coped well with the small fissures along the footwall cutoff and the monoclines and small graben structure along the hangingwall cutoff. Figure 3.17 shows the difference between the handpicked fault and the results derived from my algorithm in terms of the $d-L$ plot. All three curves are very similar. The most significant variation occurs at the peak where the $d-L$ shape derived from the trace positioned on the fault scarp drops below the other two curves. The mean variation in throw between the handpicked values and those derived from the fault trace positioned above the fault scarp is -0.25 with std of 5.18 m and -0.88 with std of 5.42 m for those derived for the fault trace placed on the fault scarp. The mean variation of throw between the two algorithm derived measurements is 0.78 with std of 2.91 m.

3.4.2 Factors affecting the $d-L$ shape

In this section I show how the $d-L$ shape of a fault at the Dabbahu rift segment is influenced by the quality of the input fault trace and the spacing of the profiles and discuss the necessary constraints to ensure a stable performance of my algorithm. I also discuss the error estimation.

- Mapped fault trace:

  The first test is to determine the necessary fault mapping resolution. The mapping resolution is the resolution at which the fault trace is mapped and has to be distinguished from the high-resolution 0.5 x 0.5 m^2 LiDAR DEM from which the algorithm always determines the throw of the fault. Fig. 3.18 shows the effects of the fault mapping resolution on the resulting $d-L$ pattern. The structure,

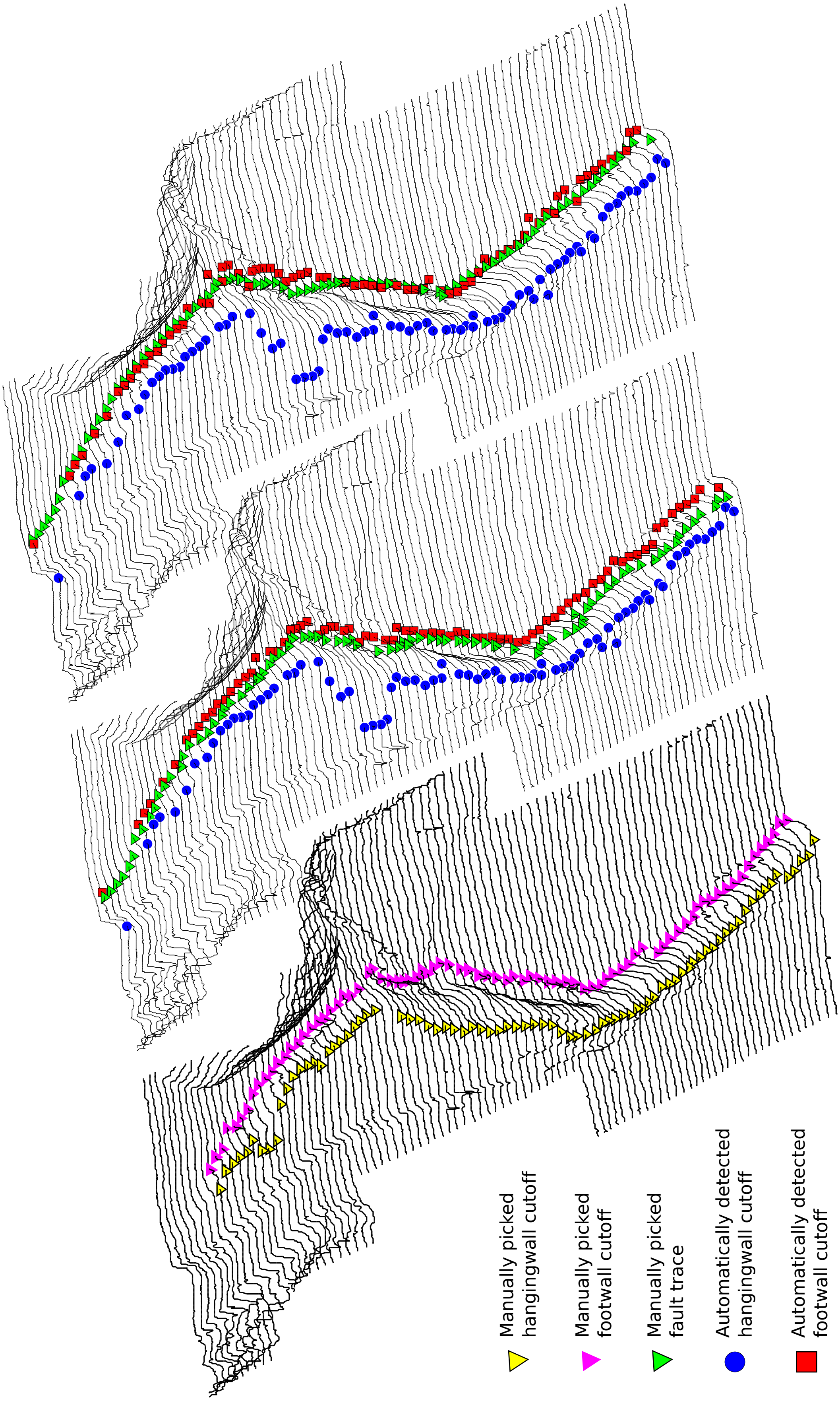

Figure 3.16: Standard 3-D line plot produced by the algorithm. Topographic profiles in black. Bottom: Manually picked cutoffs, hangingwall yellow, footwall pink. Middle: Cutoffs derived by the algorithm from fault traces manually mapped on the fault scarp (green), hangingwall cutoff blue, footwall cutoff red. Top: Cutoffs derived from fault trace manually mapped on footwall.

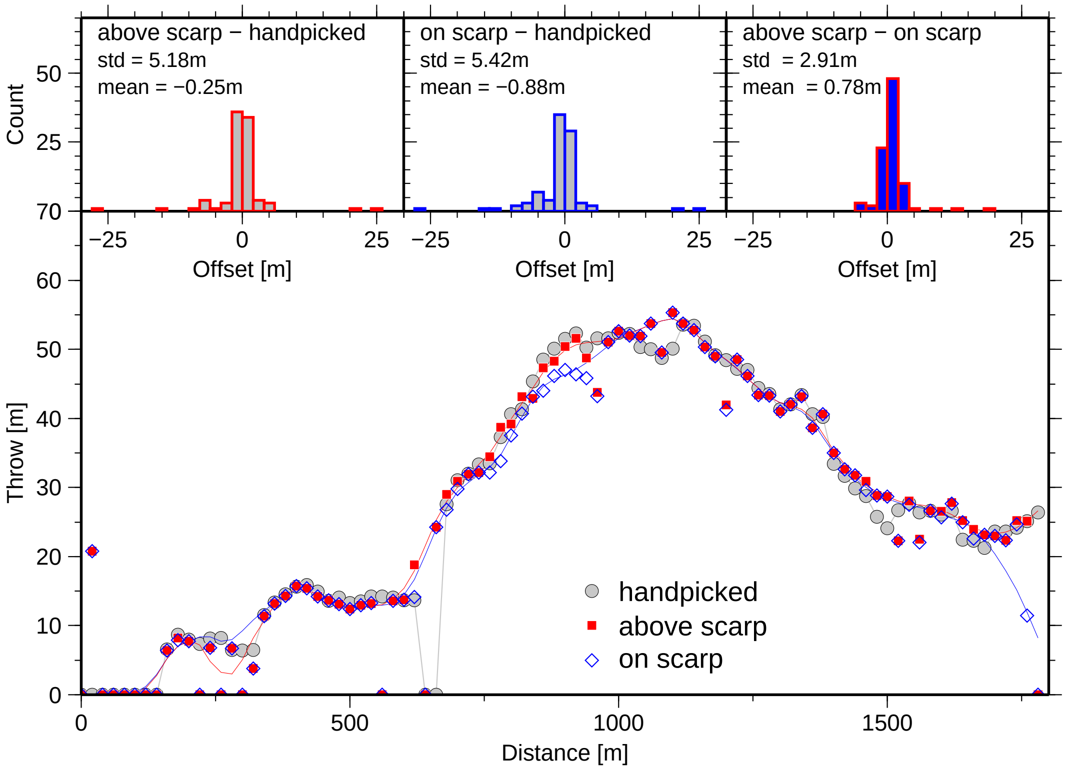

Figure 3.17: Comparison between handpicked and algorithm derived $d - L$ profiles. Bottom panel $d - L$ profile derived from handpicked values (grey circles) and algorithm derived. Red squares show values derived for a fault trace picked above the fault scarp. Blue diamonds mark values derived for a fault trace placed on the fault scarp. Red and blue line show the corresponding *rloess* fitted curves. Top row presents histogram of throw offset between handpicked and above the scarp values (left), between handpicked and on the scarp values (middle) and the difference between the two algorithm derived measurements (right).

which is marked on the map in the top far left panel of figure 3.18, was manually traced by D. Paton on DEMs with 20 x 20 m^2, 5 x 5 m^2 and 0.5 x 0.5 m^2 pixel size. I asked D. Paton to perform the fault picking to avoid my personal bias on the results. I generated the lower resolution DEMs from the 0.5 x 0.5 m^2 LiDAR DEM using simple boxcar averaging in ERDAS ERMapper. My algorithm's standard line plots in the top row show cross profiles at 20 m interval extracted from the 0.5 x 0.5 m^2 DEM with the manual picks marked in yellow and foot- and hangingwall cutoffs in red and blue respectively.

At 20 x 20 m^2 grid resolution (Fig. 3.18 top row, panel 2) the offset between manual and actual picks are too large in many places, which results in the displacement-length profile being incomplete (bottom far left). This is due to the settings of the algorithm, which are optimised for the closely spaced faulting in the Dabbahu segment. The setting demands the footwall cutoff to be within ± 30 m of the manual pick to prevent accidental shifting onto a neighbouring structure. In the case of the 20 x 20 m^2 resolution DEM a picking error of one pixel is therefore sufficient for the fault structure not to be detected. At 5 x 5 m^2 grid resolution foot- and hangingwall are continuously picked and a comparison between its $d-L$ profile and the profile derived from the 0.5 x 0.5 m^2 pixel size grid shows only small differences. The vertical difference between the two curves is 0.9±0.8 m. The largest differences of ∼4.5 m are located close to the maximum of the curve. This shows that it is sufficient to map fault traces on a lower resolution DEM of 5 x 5 m^2 pixel size, which improves the manageability of the large data set during manual fault mapping.

- Horizontal spacing between manual picks along the fault trace: The 2nd test focuses on the horizontal spacing between the manual picks along the fault trace. The algorithm extrapolates linearly between two points forming a continuous polyline along the entire fault trace. The intersection between this polyline and a cross profile determines the initial point (MP) from which the search for the footwall cutoff begins. If the spacing between the picks is too large the polyline will deviate too far from the real fault trace, preventing the algorithm from detecting the fault. To find the maximum spacing I used the manual picks which had been picked at pixel level on the 5 x 5 m^2 DEM and reduced the number of picks to one pick per 10 m, 50 m, 100 m, 500 m and 1000 m. After running my algorithm with each of these point sets as input, I calculated the difference between their displacement-length profile and the reference profile with 5 m pick spacing. Fig. 3.19 shows the results of this analysis. It is apparent that there is little difference between the curves up to 100 m pick spacing. At larger spacings (500 m and 1000 m) the polyline deviates too far from the actual fault trace and the fault scarp can no longer be detected with the parameters chosen for the Dabbahu rift segment. The bottom plot shows this more clearly with the misfit in relation to the reference 5 m spacing curve increasing from on average 0.6 m to ∼10 m and 3000 m for spacings of 500 m and 1000 m respectively. It should therefore be sufficient to pick the fault trace roughly every 100 m.

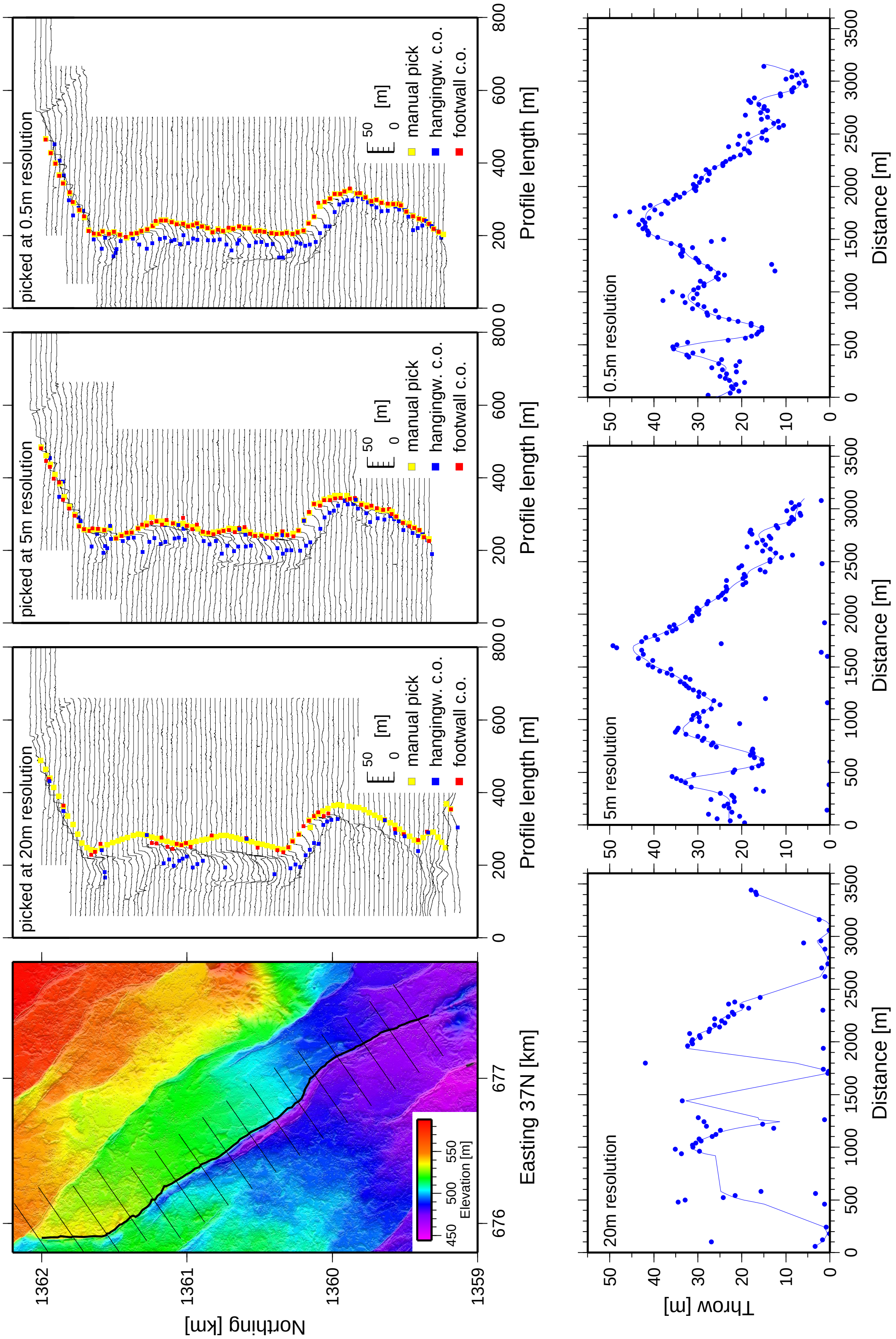

Figure 3.18: Comparison between $d - L$ shapes derived from fault traces picked at different DEM resolutions. Test fault structure marked on DEM (top left panel). On the line plots in the top row the manual fault trace is marked in yellow, hangingwall cutoffs in blue and footwall cutoffs in red. The fault was traced at 20 m, 5 m and 0.5 m resolution (left to right). Bottom row shows the corresponding $d - L$ curves. Circles mark the derived throw, line shows the *rloess* fitted curve of the measurements.

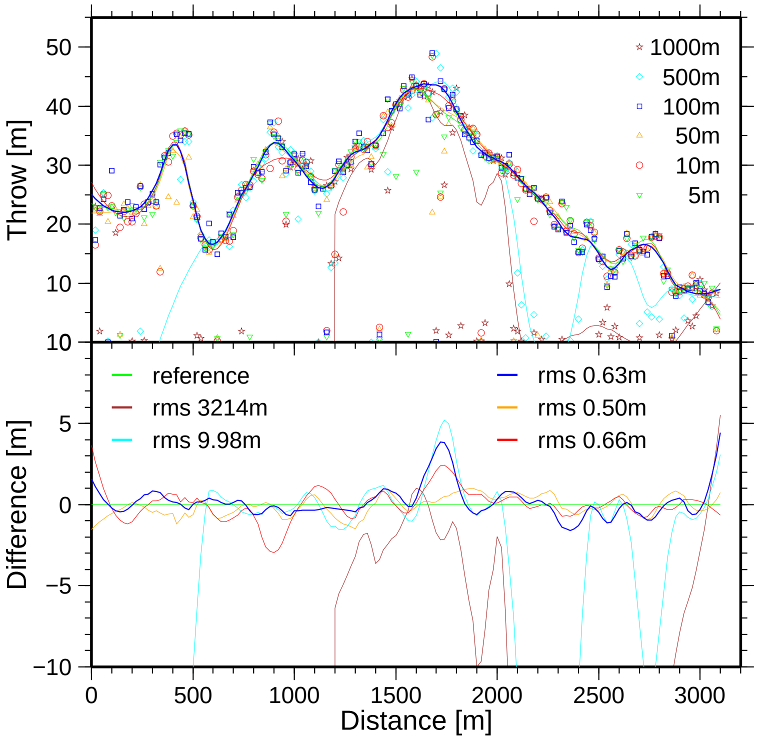

Figure 3.19: Influence of horizontal spacing between manual picks along the fault trace on the $d-L$ shape. Top panel: Throw vs. fault length colour and symbol coded for the different pick spacings including fitted *rloess* curves. Bottom panel: Difference between reference $d-L$ profile (5 m) and $d-L$ shapes for larger pick spacing (10, 50, 100, 500, 1000 m).

- Profile spacing:

  Fig. 3.20 illustrates the influence of the spacing between profiles used to pick cutoffs on the shape of the $d-L$ curve. The *rloess* curve (red) is calculated for 200 m windows. At the extreme case of sampling every 1 m small undulations in the surface of foot and hanging wall are picked up, which are no major concern for my study. Sampling at 5 m interval reduces this 'noise' level but most actual small scale features are still captured. 20 m spacing appears to be the limit at which smaller scale segmentation is reliably picked up. At 50 m spacing segmentation is blurred but the main shape is still visible. At a 100 m spacing the shape starts transforming into the shape classically expected for individual faults and at 500 m spacing only a very basic, almost elliptical shape is visible. Not only does the shape lose its detail with increasing measurement spacing but also the maximum value decreases as measurements are taken away from the maximum value. The density of measurement taken along a fault scarp therefore has a large influence on the shape and on the ratio between maximum throw and fault length (d_{max}/L). As a default I run the algorithm with 20 m profile spacing with a smoothing window for the *rloess* curve fitting of 10 points (200 m).

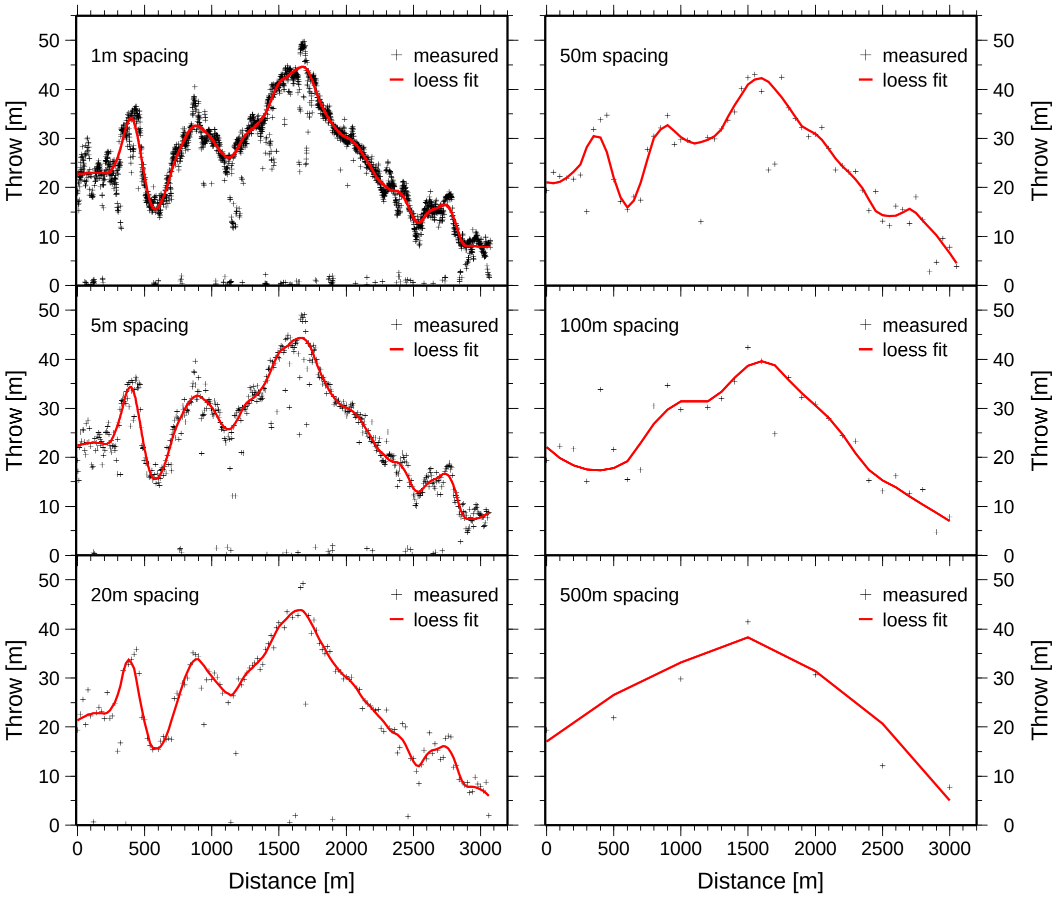

Figure 3.20: Comparison of the influence of the profile spacing on $d - L$ shape. Each panel shows the $d - L$ pattern of the same fault measured with different profile spacing. Left column top to bottom: 1 m, 5 m and 20 m profile spacing. Right column top to bottom: 50 m, 100 m and 500 m profile spacing. Black crosses: measurements, red line: *rloess* fitted curve calculated with 200 m window size.

- Error estimation:

  I also attempted to estimate the error of the derived $d - L$ profile. I assess to what extent the $d - L$ shape is affected by the position of the profiles. I extracted 20 $d - L$ shapes with 20 m profile spacing, for the same fault by moving the first profile one metre further along the trace. The result is shown in figure. 3.21. Individual $d - L$ curves and corresponding measurements are plotted in the same colour (Fig. 3.21 top). Visually all 20 shapes are very similar. To estimate the error I calculated the mean fit curve from all *rloess* fitted curves (Fig. 3.21 bottom panel black line) and calculated the standard deviation (std) between the curves for each point of the profile (red). The histogram inset shows the distribution of the std with a mean std of 0.8±0.3 m which is the same as uncertainties observed during field measurements (Dawers and Anders, 1995).

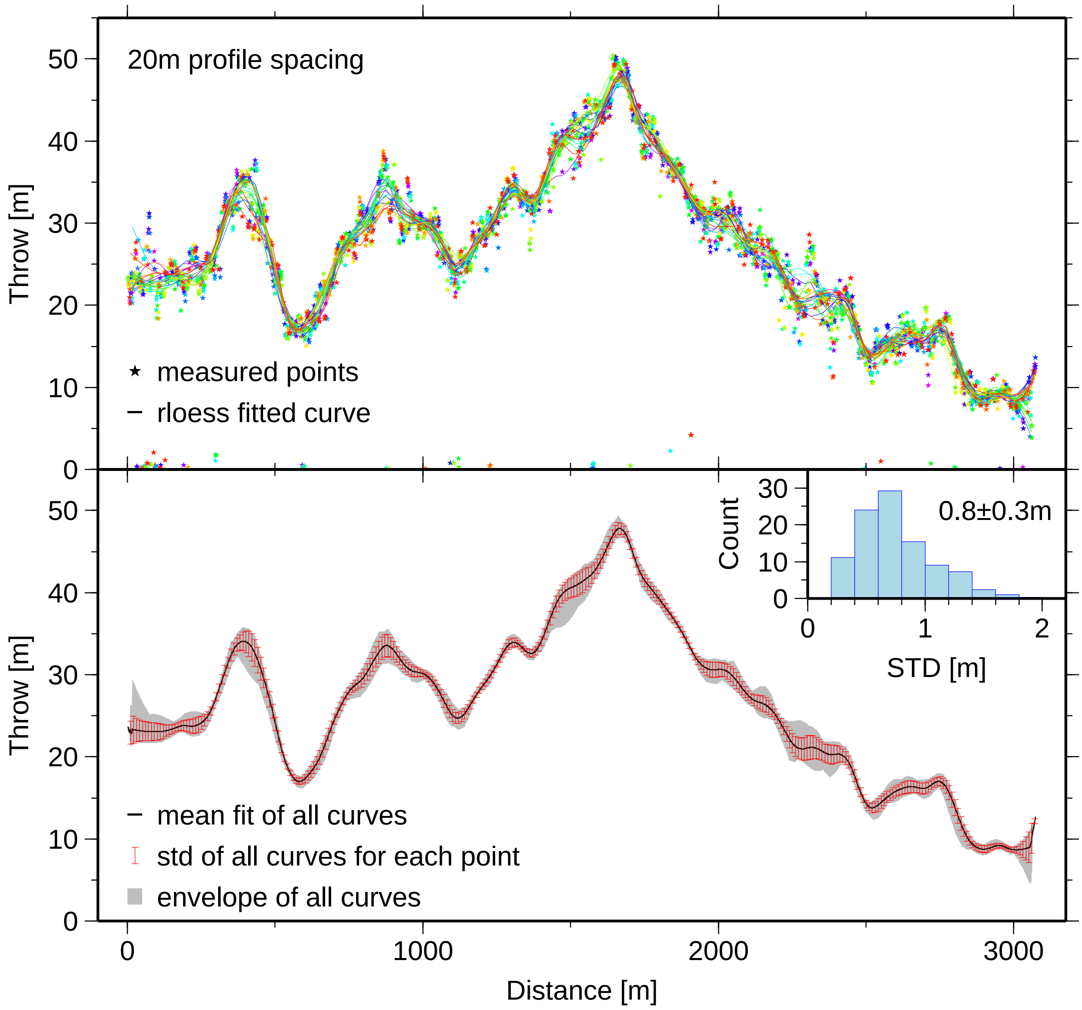

Figure 3.21: Illustration of the influence of profile position on the $d-L$ shape. 20 $d-L$ shapes derived for one fault with 20 m profile spacing. The position of the first profile is shifted by 1 m along strike of the fault trace for each $d-L$ shape. Top: Each $d-l$ shape is colour-coded and represented by its measurements (stars) and its *rloess* curve. Bottom: Envelope of all *rloess* curves in grey. Mean $d-L$ shape in black, standard deviation of all curves for each point in red. Inset: Histogram of the standard deviation.

3.4.3 Algorithm vs. differential GPS

During the field campaign for the second LiDAR acquisition I was able to survey one fault using differential GPS (dGPS). The centre of the rift is inaccessible without helicopter or camel support, but one of the few accessible fault structures is located just outside of the regional capital Semera (Fig. 3.22). It strikes at 143° and is ~ 2.5 km long with a maximum throw of ~ 26 m. At its north-westerly end it is cut by the main road connecting Ethiopia with the ports of Djibouti. A selection of photographs are shown in Fig. 3.23.

As expected, the footwall cutoff along the majority of the fault can easily be identified and I took measurements as close to the scarp as safely possible (Fig. 3.23 B) . In some parts a secondary small fissure runs parallel to the footwall cutoff. The hangingwall is obscured along the majority of the structure by monoclines and debris (Fig. 3.23 C and E). Two large monoclines are particularly complex with multiple fissures and terraces (Fig. 3.24). In addition a considerable amount of sand,silt and sediments have accumulated on the hangingwall further obscuring the cutoff.

I decided to measure the hangingwall cutoff as close as possible to the visible end of the fault scarp features (monoclines, debris etc) where the hangingwall visually turned into a plane (Fig. 3.23 F). Measurements are taken roughly every 20 m along half of the fault structure. Figure 3.25 shows a comparison between the measurements obtained using the dGPS (blue circles) and the cutoffs derived by my algorithm (red squares) from the 0.5 x 0.5 m^2 LiDAR DEM. dGPS measurements are vertically corrected for a static offset of 6 m. For the comparison I projected the dGPS measurements and derived cutoffs, spaced every 5 m, onto a profile parallel to strike (Fig. 3.25, grey line) and used only the closest point along strike for each dGPS point for the calculation.

Comparing the footwall cutoffs shows very close correlation between the two types of measurement with an average discrepancy of -1 ± 2 m vertically and 2 ± 6 m horizontally. The vertical misfit compares well to uncertainties of ± 1 m reported for throw measurements from field studies (e.g. Dawers and Anders, 1995). The horizontal misfit is primarily due to the dGPS measurements being taken slightly to the west of the real cutoff for safety reasons. Results for the hangingwall show a similar match for the vertical measurement with differences of 1.5 ± 2 m. dGPS measurements appear systematically picked above the algorithm values and a significantly larger discrepancy for the horizontal component (94 ± 62 m) is observed. This difference is caused by the slope of the hangingwall. In the field the hangingwall appeared to be flat, but the cross profiles show a gentle downward slope likely related to the influx of sediments which causes the wide offset.

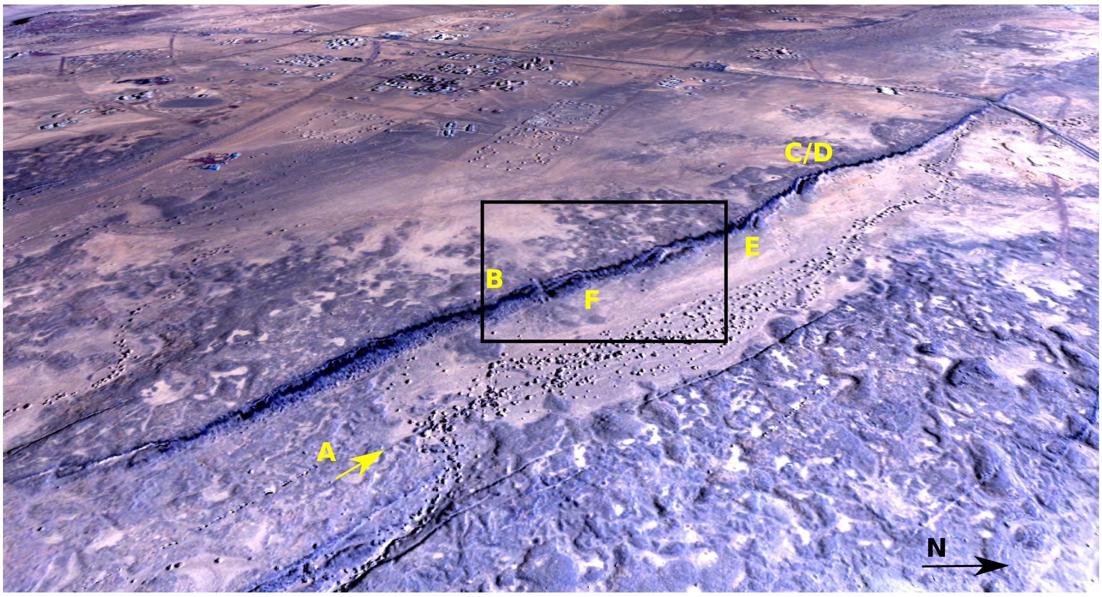

Figure 3.22: Birdseye view of the Semera fault created with Geovisonary from the LiDAR DEM and aerial photographs. Semera is visible towards the West in the background. The fault is $\sim$ 2.5 km long and gets intersected by the main road in the NW (top right). The hangingwall is widely covered with sediments which can be identified by their light colour. Letters on the image correlate to the photographs shown in Fig. 3.23. The yellow arrow indicates the viewing direction of photo A. A close-up of the area within the black box is shown in Fig. 3.24.

Figure 3.23 ***(facing page)*****:** Photographs of the Semera fault. Location of photographs are indicated on Fig. 3.22. A: View along the fault looking NW; B: Measuring the footwall cutoff next to a small fissure on the footwall; C: View of the large monocline structure in NE direction; D: Look into the large monocline structure; E: Side on view of monocline structure. Yellow ovals mark the position of our guard for reference; F: Measurement of hangingwall cutoff at bottom of a monocline.

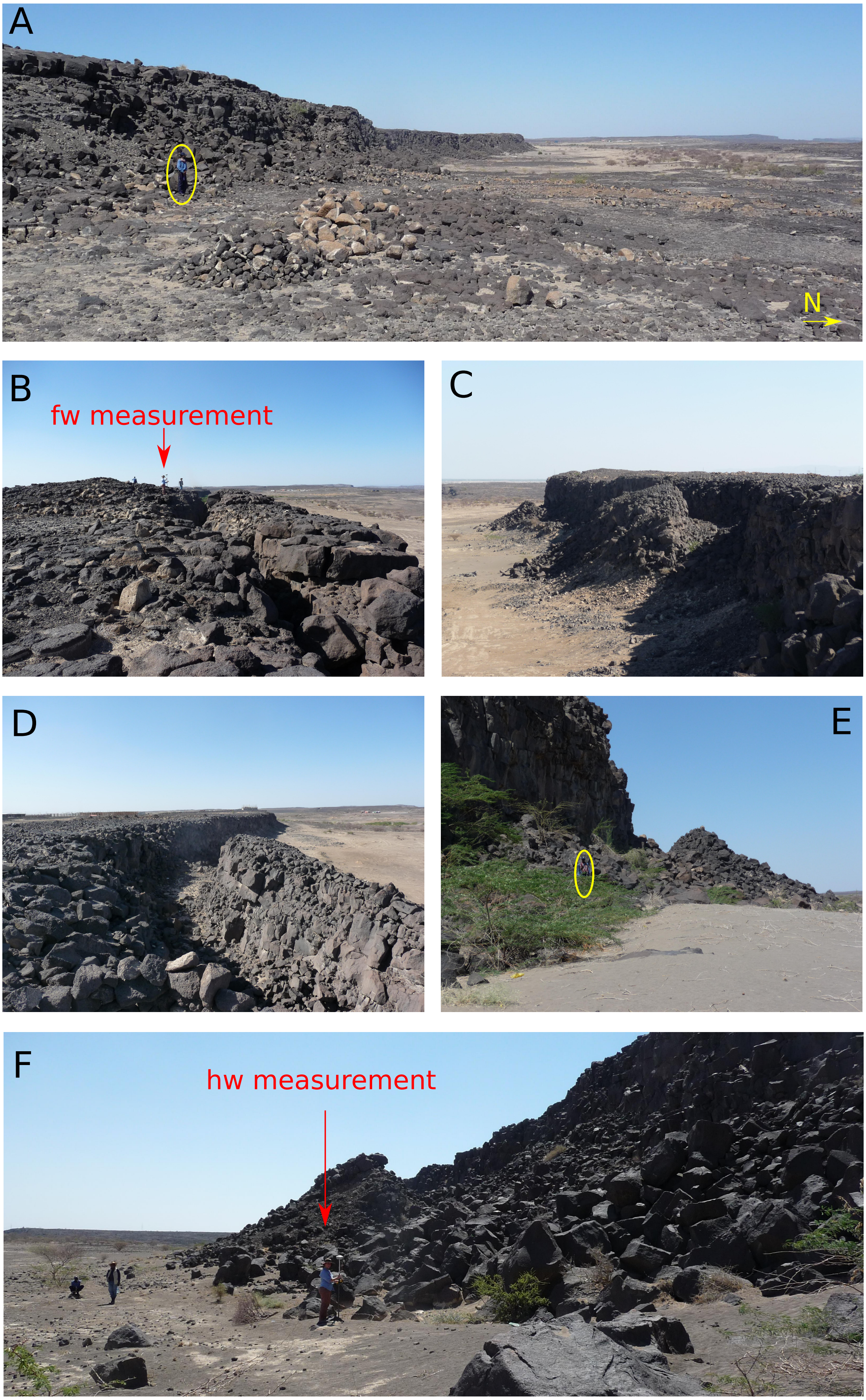
A
N
B
fw measurement
C
D
E
F
hw measurement

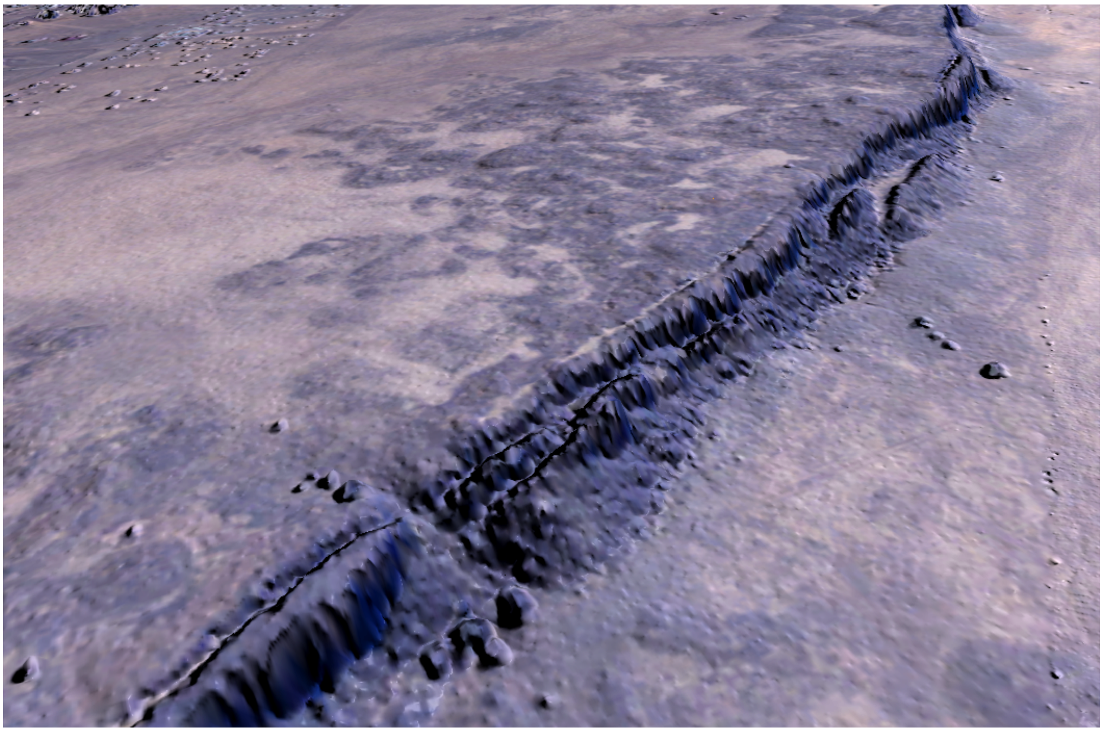

Figure 3.24: Close-up image of large complex monoclinal flexure at the Semera fault (black box in fig 3.22. The Image shows the LiDAR DEM draped with the aerial photos acquired during the survey. The figure is produced with Geovisionary®. The monoclinal structures are up to ~ 35 m wide. It appears as if complex structures are formed as the monoclinal feature detaches from the fault scarp creating fissures of different width which are partly filled with sediments and large debris.

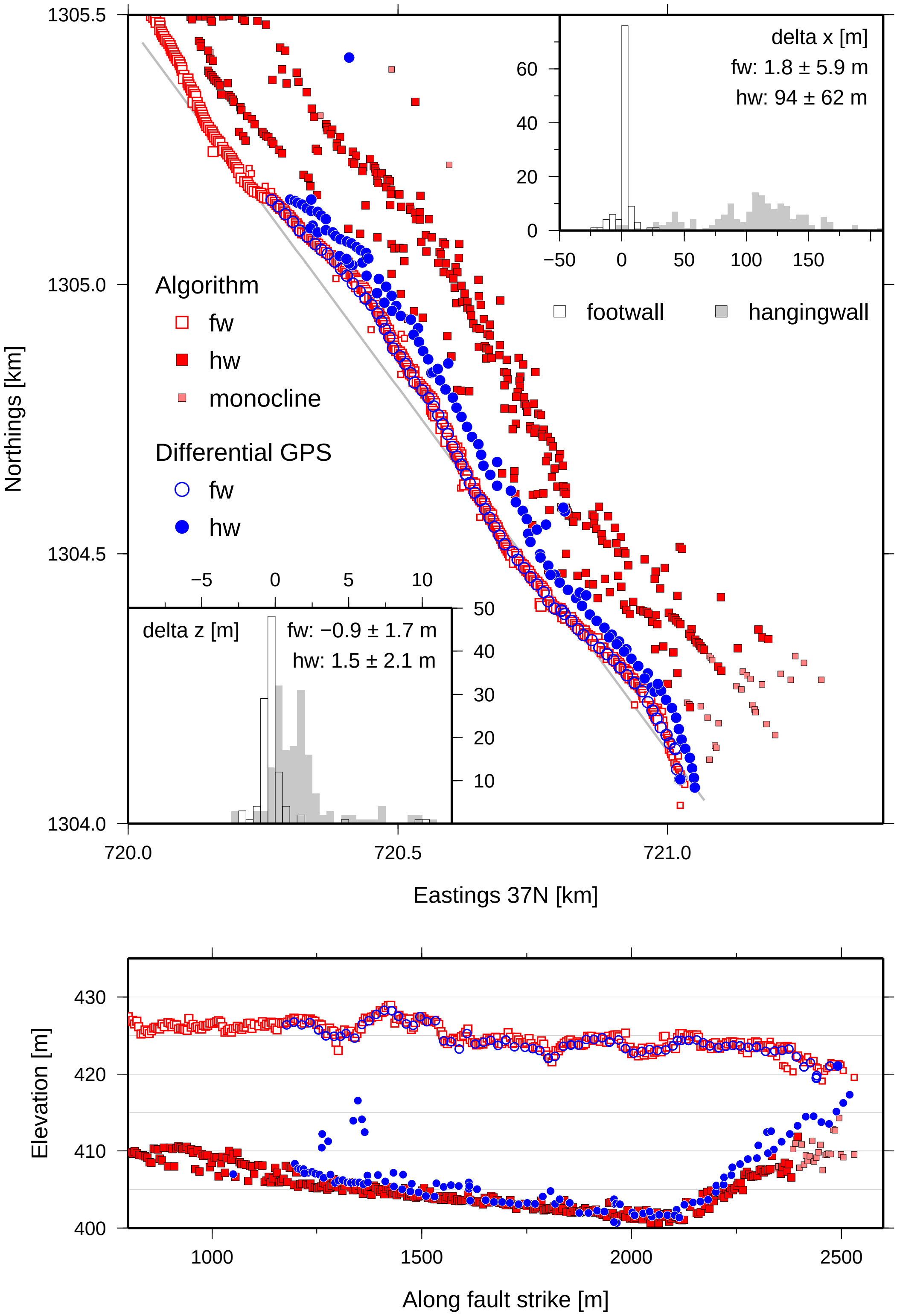

Figure 3.25: Comparison between dGPS measurements (blue circles) and values extracted by the algorithm (red squares). Footwall cutoffs (fw) marked by open symbols, hangingwall cutoffs (hw) marked by filled symbols. Measurements along the monocline fault tip are marked by smaller symbols. Top panel: Map view of the cutoff positions; corners: histogram of discrepancy between dGPS measurements and values derived by the algorithm for footwall (white) and hangingwall cutoff (grey); top right corner horizontal difference; bottom left corner: vertical difference. Bottom panel: Side view along fault strike of cutoff positions. Measurements of the footwall cutoff show a small vertical and horizontal discrepancies of -1 ± 2 m and 2 ± 6 m respectively. Larger offset are visible for the hangingwall cutoff with 1.5 ± 2 m vertical and 94 ± 62 m horizontal.

3.5 Limitations

Here I discuss some general limitations of my algorithm.

- Fault linkage zones:
  Fault linkage zones pose a challenge to my algorithm in particular if the linkage process is advanced. If the fault tips are horizontally separated by less than 30 m my algorithm will not necessarily be able to separate the structures. It is therefore still essential that the linkage zone is visually inspected in the DEM to assess the stage of linking.

- Small throw vs. large throw:
  When assessing the quality of the derived picks the size of the fault structure has to be considered. The larger and longer the segment is the more reliable are the derived cutoffs. This is due to a number of factors. The more developed the fault is, the clearer are the real cutoffs and therefore the likelihood for my algorithm to detect the correct cutoffs is improved. Also the longer the fault is the more measurements exist which improves the quality of the *rloess* fit. Furthermore while the absolute error should not change between small and large faults, small errors have a much greater effect on smaller faults.

- Further errors:
  Further factors contributing to errors in my analysis are: errors in the LiDAR DEM, faulty cutoffs derived by the algorithm and errors introduced through the *rloess* curve fitting. Apart from these technical errors, my decision to extract the hangingwall cutoff at the end of the deformation zone may also introduce errors. The width of the deformed area at the hangingwall can vary from a few meters up to 200 m in a few cases. Bookshelf faulting is common at the Dabbahu segment (§ 4). and I observed block rotations of approximately 1-10° (Fig. 3.26), which may cause an underestimation of throw by a few meters as the hangingwall cutoff is picked on the upward slope of the tilted block. Theoretically it is possible to fit a plane along the hangingwall block and extrapolate it to the fault scarp, to derive

the more true hangingwall cutoff. I did attempt this and found it introduced more problems than it solved for the Dabbahu rift segment. As mentioned previously the normal faults at the Dabbahu segment exhibit a high degree of interaction and are very densely spaced. For the results to be more accurate it would therefore be necessary to first determine the precise area through which a plane could be fitted, which would requires that all the fault structures and their secondary features in the area are identified.

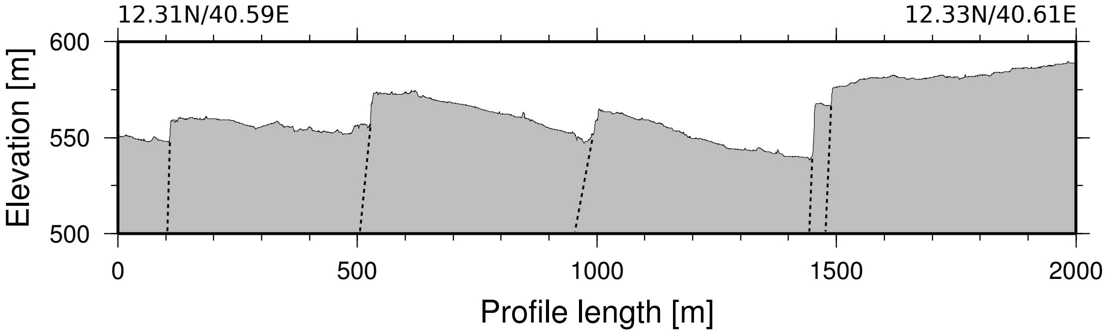

Figure 3.26: Topographic profile, at the centre of the Ado'Ale volcanic complex, showing bookshelf faulting with rotated fault blocks.

3.6 Summary

In this chapter I have presented my algorithm to extract throw along fault traces from high-resolution LiDAR data. The derived throw values are of similar quality to those mapped in the field or manually picked on the LiDAR DEM. My algorithm follows strict criteria to identify the fault cutoffs and throw and therefore reduces the subjectivity during the fault analysis. It is further independent of specialist software and can be applied to any size data set. In addition to the surface data it only requires a set of fault traces.

For the faults at the Dabbahu rift segment the traces can be roughly mapped every 100 m on a lower resolution 5 x 5 m^2 DEM or derived by other methods as long as they are within the constraints discussed in § 3.4.2. My algorithm can be adjusted by 6 parameters (Table 3.3 1-6) which affect the quality of the individual throw measurements (§ 3.4.1), and 2 further parameters (Table 3.3 7-8) that influence the resolution of the $d - L$ shape (§ 3.4.2). The values shown here provide the best results for the steep normal faults at the Dabbahu rift segment.

Search margin	sm	30 m
Footwall plain width	fpw	30 m
Hangingwall plain width	hpw	30 m
Minimum significant vertical offset	v_{min}	-0.5 m
Maximum tolerated vertical offset	v_{max}	5 m
Maximum tolerated fissure opening	fw	40 m
Profile spacing		20 m and 5 m
rloess window size		10 points

Table 3.3: Best algorithm parameters for the Dabbahu rift segment.

My algorithm forms the basis of the quantitative analysis of my thesis. I apply the algorithm to the entire fault population of the Dabbahu rift segment in § 4. The algorithm is easily adjustable to other data sets and I am therefore able to apply it to the deformation data derived from InSAR and the two LiDAR data sets in § 5 and extract measurements of fresh throw related to dyke intrusions.

Chapter 4

Normal faulting at the Dabbahu rift segment

In this chapter I investigate the current state of faulting at the Dabbahu rift segment. I first describe the geomorphology of the Dabbahu rift segment and introduce the fault map which forms the input data set for my algorithm (§ 3), after which I focus on the results of my displacement analysis. In particular I look at the differences in dip direction and throw along the rift segment and examine the linkage zones. In the third part I use the results of my analysis to map the strain across the segment.

4.1 Geomorphology of the Dabbahu rift segment

The Dabbahu segment (Fig. 4.1) forms, together with the currently inactive Harraro segment, the Manda-Harraro rift zone (Rowland et al., 2007). It is approximately 60 km long and 15 km wide, heavily dissected by normal faults and fissures and contains two active centres of silicic volcanism, Dabbahu and Gab'ho in the north, and the dissected Ado'Ale volcanic complex (AVC) at its centre. My work focuses on the normal faulting that occurs predominantly within the basalts of the rift segment. North of the AVC the segment is orientated in NNW-SSE direction and the narrow axial graben is well defined. Within and to the south of the AVC the rift axis changes to a more NW-SE direction. According to, for example, van Wyk de Vries and Merle (1996) and Lahitte et al. (2003) the considerable topographic load of the edifice could be an important factor in the development of the rift and its faults. Throughout the rest of my thesis I will refer to the region south of Dabbahu and north of the AVC as the northern section and the region within and south of the AVC as the southern section. These are marked by the grey boxes in figure 4.1.

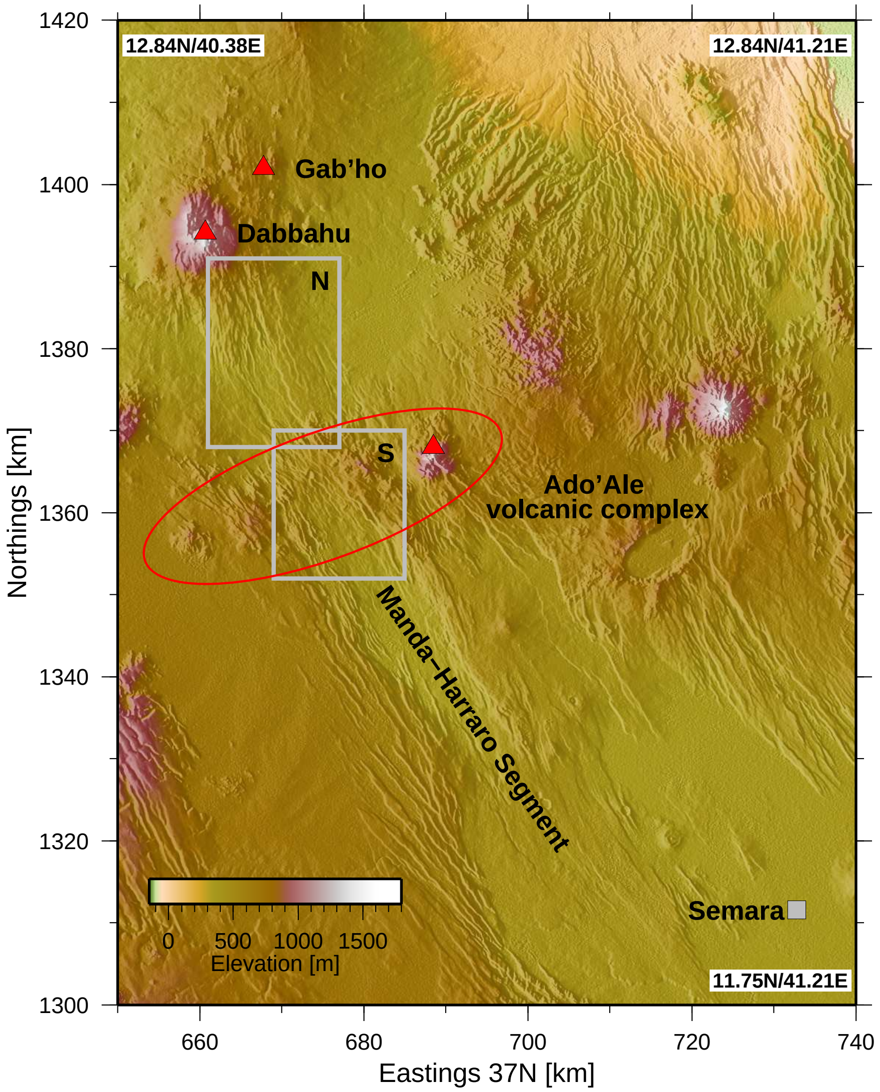

Figure 4.1: The Dabbahu rift segment, as part of the Manda-Harraro rift zone, with its two active volcanoes Dabbahu and Gab'ho in the North and the dissected Ado'Ale volcanic complex in the centre. Grey boxes mark the focus areas of this thesis. Map: 1 arc sec SRTM DEM Farr et al. (2007).

A geological map of the Dabbahu segment was created by Vye-Brown et al. (2012) and was derived from field work and remote sensing data, including the high-resolution 2009 LiDAR DEM and the SPOT 5 DEM (§ 2.1). In figures 4.2 and 4.3 I present the corresponding parts of the geological map for the northern and southern sections, respectively. The basalt flows are coloured according to their relative age. ^{40}Ar/^{39}Ar dating suggest resurfacing of the northern central section within the last 2-30 ka, progressively older flows are located at increasing distances from the rift axis (200 ka) (Ferguson et al., 2013). In the southern part, the individual basalt flows appear to be wider and cover the full width between the two sides of the edifice.

The most recent, very small scale lava flows erupted between 2007-2010 as part of the rifting episode (§ 1.3). The small short-lived basaltic eruptions (hours-days) occurred south of Ado'Ale (Fig. 4.3; Ferguson et al., 2010). The eruptions in August 2007 and June 2009 took place at the same location with the later one extending the fissure system of the previous eruption (Fig. 4.3). Using flow thickness measurements Ferguson et al. (2010) estimated the total erupted volume to be $17.4\text{-}26.8\times 10^6$ m^3, covering an area of roughly 4.5 km^2. The erupted volume was sufficient to resurface the area, burying all surface fault traces. During the latest dyke intrusion in May 2010 another small eruption took place within the AVC (Fig. 4.3) lasting ~6 h (personal communication Talfan Barnie). From the two LiDAR surveys (§ 2.1) I estimated the extruded volume to be 230,000±4,000 m^3, which is roughly 100 times smaller than the volume erupted in 2007 and 2009. I will present the details of this calculation in § 5.3.3.

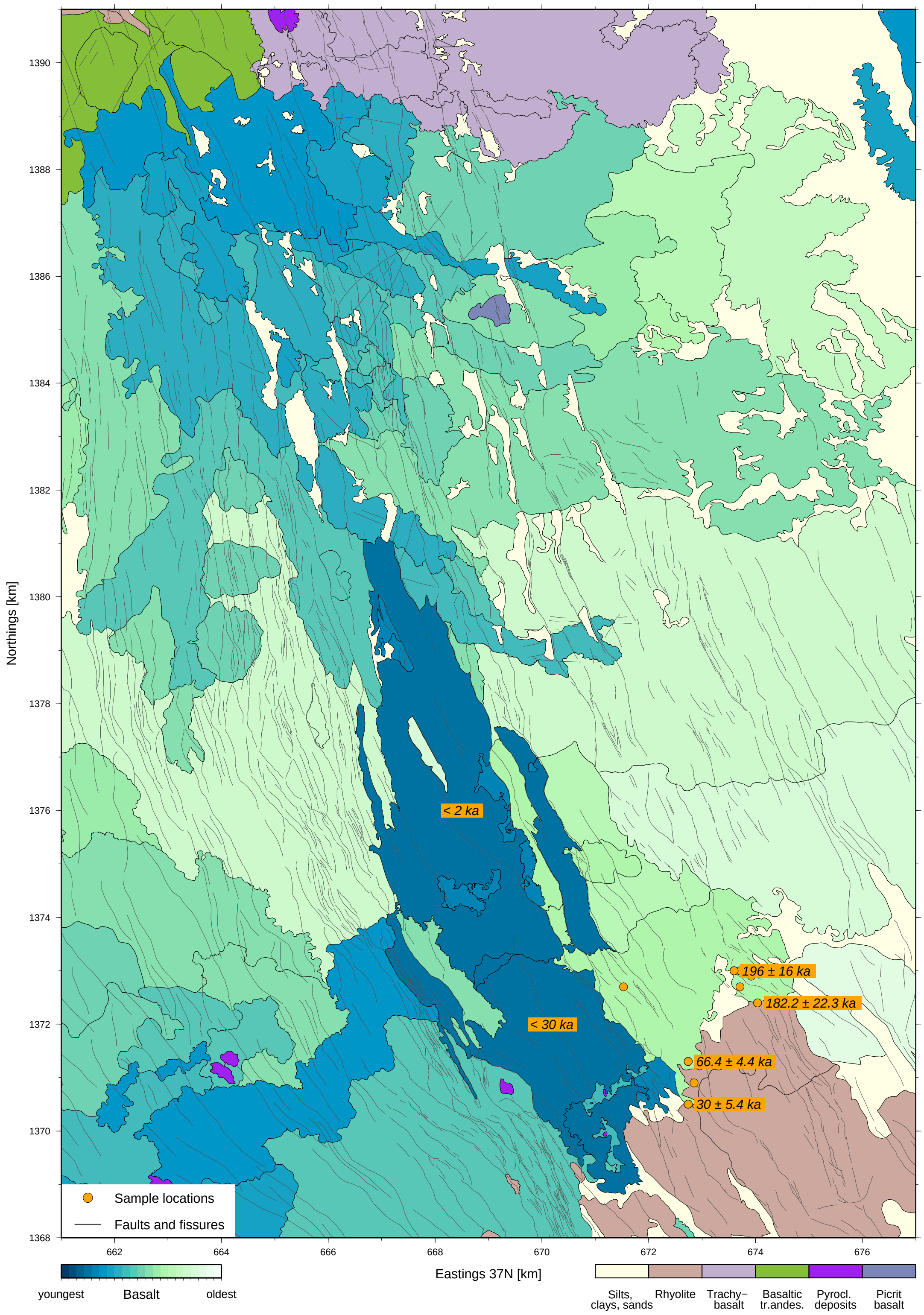

Figure 4.2: Geological map of the northern part of the Dabbahu rift segment after Vye-Brown et al. (2012) BGS©NERC including ^{40}Ar/^{39}Ar dates from Ferguson et al. (2013). Basalt flows are separated by relative age. Location of the figure marked by box N in figure 4.1.

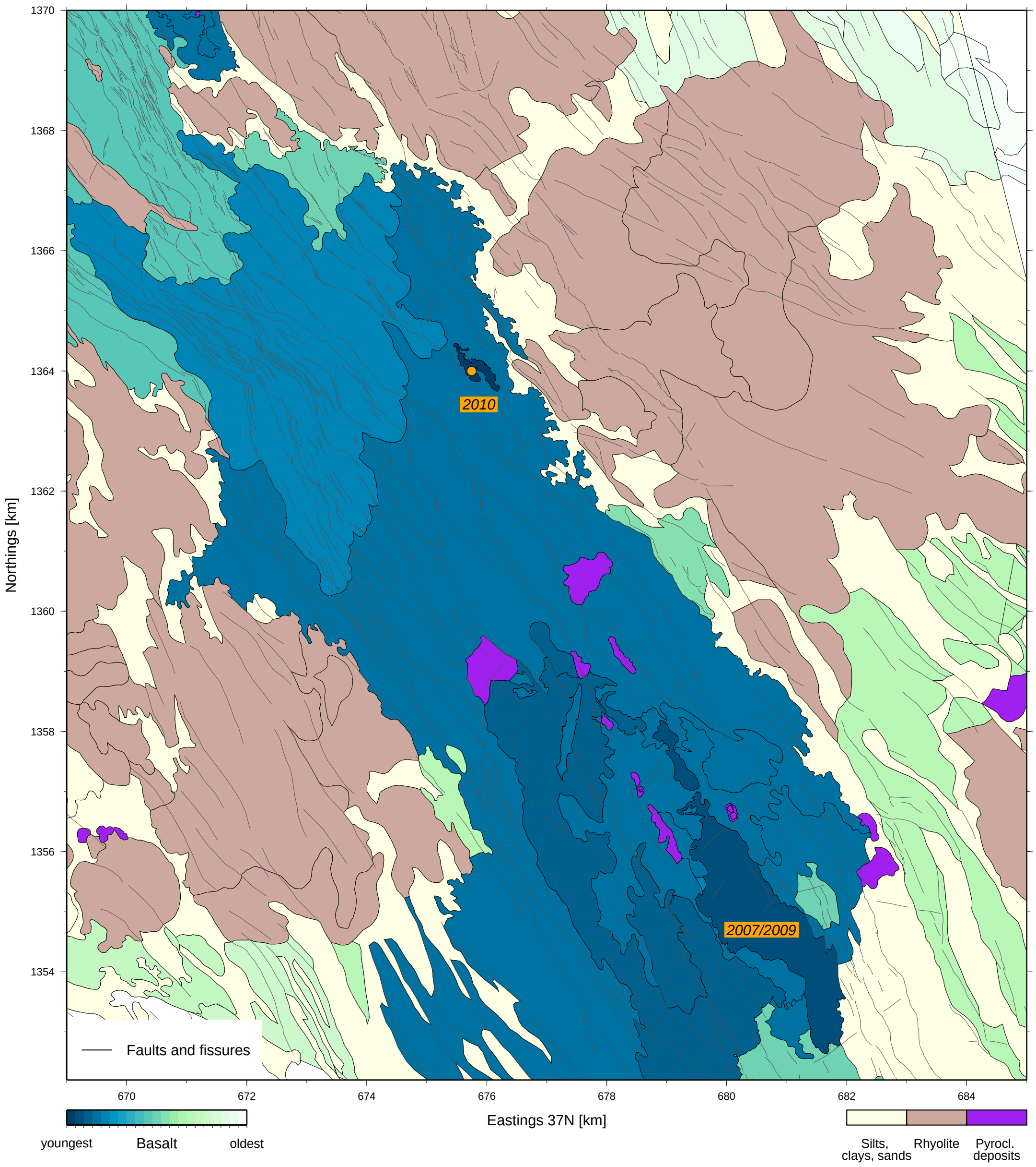

Figure 4.3: Geological map of the southern part of the Dabbahu rift segment after Vye-Brown et al. (2012) BGS©NERC including the most recent eruption sites from 2007, 2009 (Ferguson et al., 2010) and 2010. Basalt flows are separated by relative age. Location of the figure marked by box S in figure 4.1.

4.2 Fault mapping - resolution, accuracy, method

The extensive fault line work presented in the geological map (Fig. 4.2 and 4.3) is used as input data for parts of my work and was kindly provided by C. Vye-Brown and the British Geological Survey (BGS). The structures were picked in 3D using the software Geovisionary ^{TM}. Picking resolution and accuracy of the traces differ between the area covered by the 2009 LiDAR survey and the area covered only by the SPOT5 DEM. Structures located within the 2009 LiDAR survey were traced on the high-resolution 0.5 x 0.5 m^2 2009 LiDAR DEM. Structures located outside of the survey area were traced on the 6 x 6 m^2 SPOT 5 DEM. The BGS internal report states (personal communication Charlotte Vye-Brown), "The faults and fissures in the centre of the map in the area covered by the LiDAR DEM were captured at a scale of 1:5000 or less and are accurate to this scale. As a result, the tip end of faults, fault ramps, and the next en-echelon fault sections were identified and accurately mapped." Outside this area structures are mapped at a scale of 1:10000 or less. The broader, weathered faults crossing through the rhyolitic volcanic complexes are also delineated at 1:10000 scale.

4.2.1 Influence of data resolution on fault map

Comparing the fault data set provided by C. Vye-Brown with a fault data set traced from ~30 m resolution Large Format Camera (LFC) imagery (Hayward, 1997) illustrates the tremendous increase in detail provided by the LiDAR DEM. Both fault data sets cover roughly the same area and the total traced fault length is comparable (~2200 km 3D LiDAR vs. ~2500 km LFC) but the number of identified fault segments and their length varies greatly. Hayward (1997) identify 1243 fault segments in the Dabbahu rift with an average length of 1.9 km. In contrast C. Vye-Brown traced 3748 fault segments with an average length of 500 m. It is reasonable to assume that the difference in segment number and average length is, to a large degree, due to the high-resolution of the LiDAR DEM which allows for a better assessment of the stage of fault linkage between segments. To illustrate this I show a small section (4 x 3.5 km) of the 2009 LiDAR DEM calculated at 0.5 x 0.5 m^2 (Fig. 4.4 left) and 30 x 30 m (right). I created the lower resolution 30 x 30 m DEM by applying the inbuilt boxcar filter of the ERDAS ERMapper software to the high-resolution DEM. The high-resolution LiDAR DEM (left) shows that the fault segments, at each of the three marked linkage zones, are currently soft linked, which is expressed by the absence of a through-going surface trace (Peacock and Sanderson, 1991, Trudgill and Cartwright, 1994). In the lower resolution DEM (right) only the segments of the linkage zone at the far left appear separated. The two remaining linkage zones appear hard linked.

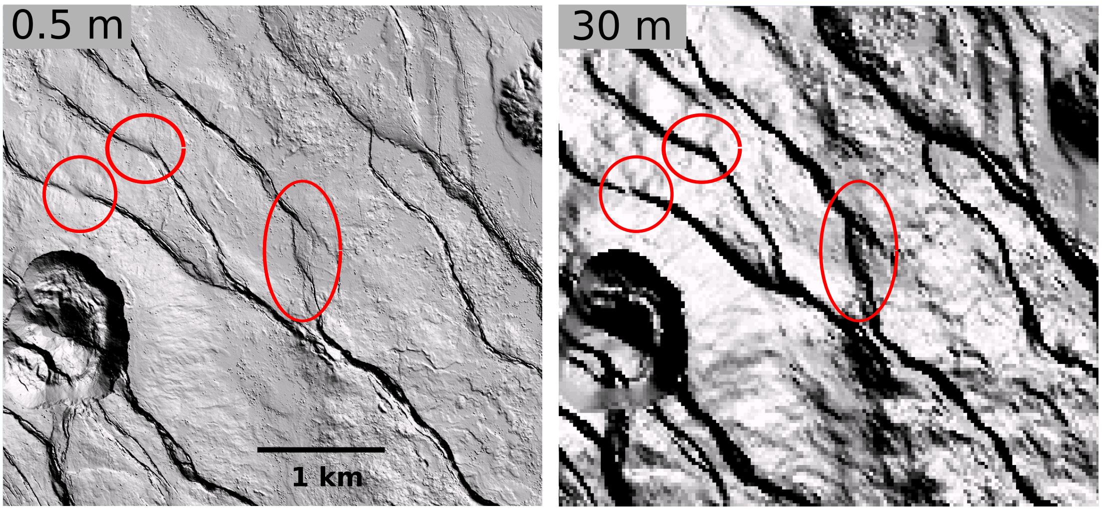

Figure 4.4: Fault linkage expression at different DEM resolution. Soft linked fault segments appear hard linked in lower resolution DEM. Left: High-resolution 0.5 x 0.5 m^2 2009 LiDAR DEM; right: 30 x 30 m 2009 LiDAR DEM. Example section is located at the AVC. Location of the central point of image 12.35N/40.51W. Extent of the image 4 x 3.5 km. Figures are shaded relief with illumination from NE

4.2.2 2D vs. 3D fault mapping

While data resolution is one important factor for accurate fault mapping with the introduction of high-resolution DEMs 2D vs. 3D mapping becomes a factor. K. Sheil (Sheil, 2012) kindly provided me with her fault map which was also derived from the high-resolution LiDAR and SPOT5 DEM. The faults in this map were traced on 2D shaded relief representation of the DEMs. Figures 4.5 and 4.6 show the differences between the two data sets. Figure 4.5 shows the fault maps of the central rift section (left: 2D data set, right: 3D data set). Overall more structures are mapped in 3D and it seems that structures, which appear to be open fissures (green) on the shaded relief have been identified as faults in 3D. In the 2D data set structures have been identified as monoclines but no differentiation between monoclines and and faults was attempted in 3D. In the 2D data set (Fig. 4.6 left a) only ~1100 km of fault traces were mapped (excluding fissures and monoclines) compared to ~2200 km in the 3D data set (Fig. 4.6

right a). On average the 2D segments are shorter (∼350 m) than the 3D segments (∼500 m), which may indicate that the correct identification of the fault tips is more challenging on the 2D shaded relief. Another reason for the shorter segments may be that parts of the segments are classified as monoclines.

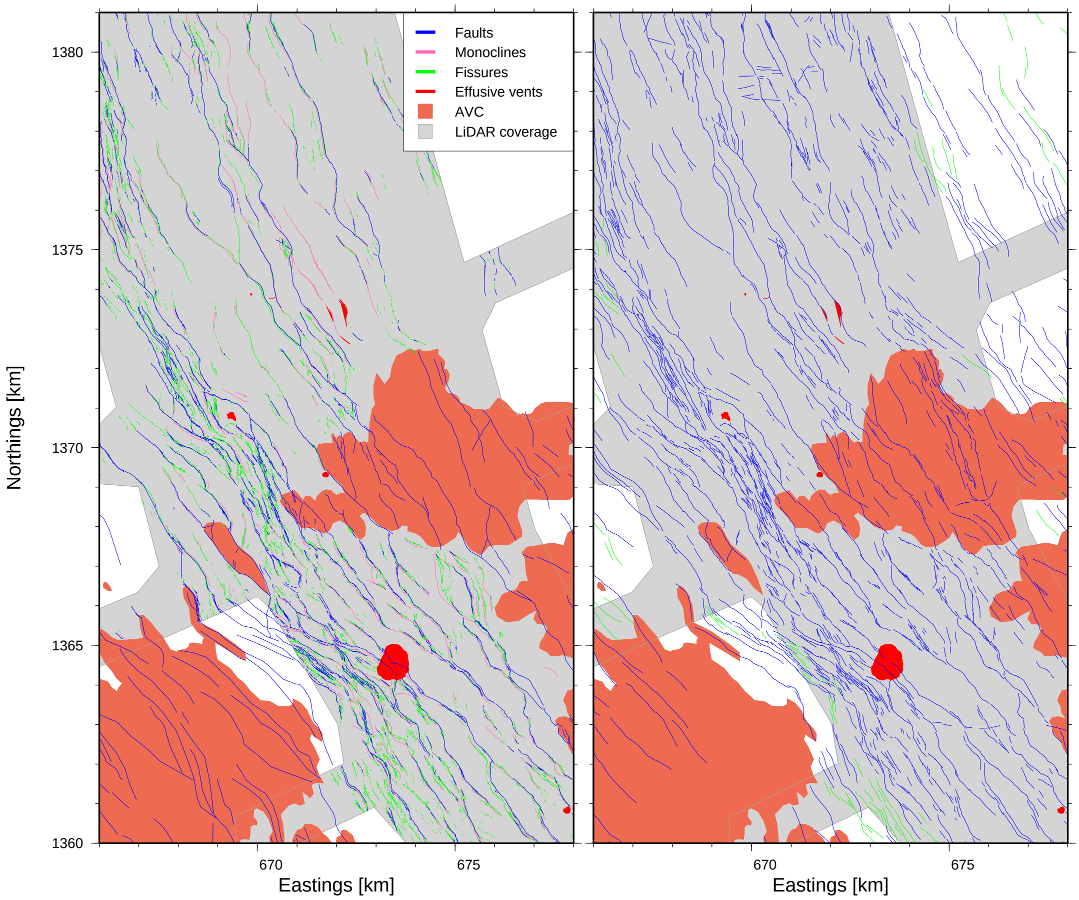

Figure 4.5: Illustration of differences in fault maps manually picked by experienced structural geologists. Left: Structures traced on shaded relief 2D LiDAR and SPOT5 DEM. Right: Structures traced on 3D LiDAR-and SPOT5 DEM. Some of the structures identified as open fissures (green) from the shaded relief DEM have been identified as faults from the 3D visualisation. No differentiation between faults and monoclines was attempted in the 3D data set. Fault sets courtesy of K. Sheil (left) and C. Vye-Brown (right)

4.2.3 Systematic fault analysis

I chose to use the 3D fault set as my primary fault map due to its larger coverage and its simpler differentiation into only faults and fissures. Unless otherwise stated I will refer to the 3D data set of Vye-Brown et al. (2012) as the fault data set.

The fault data shows a change of fault segment direction (Fig. 4.6,b) at the AVC from

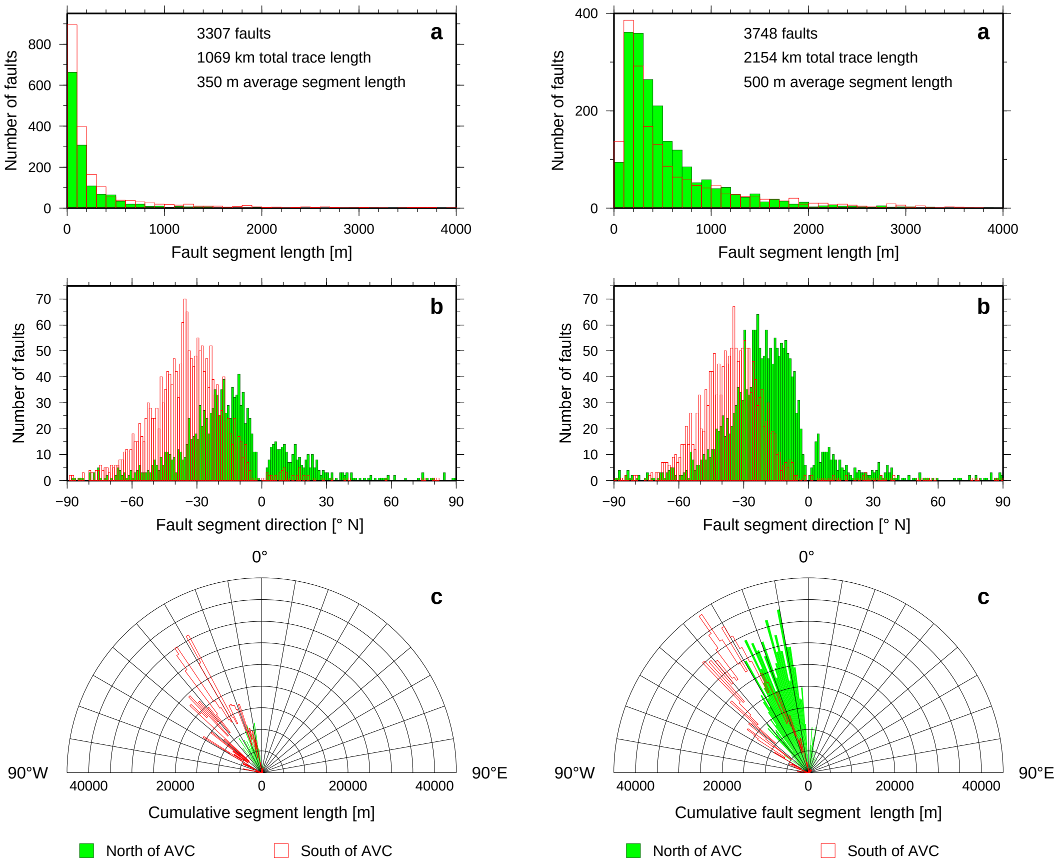

Figure 4.6: Fault data set statistics. Left: mapped on shaded relief 2D, right: mapped in 3D. a) histogram of fault structure length; b) histogram of fault direction from North; c) cumulative fault segment length. The data sets are divided into North of the AVC (green) and South of it (red).

N35°W in the South (red) to N18°W in the North (green). The second smaller peak in the North at N5°E appears to correlate with the direction of the faults and fissures connecting segments across relay ramps. Overall, the fault segment length is slightly larger in the North (green) but their number and hence cumulative length is greater in the South (red) (Fig. 4.6 right c).

I applied the automated algorithm I developed in § 3 to each segment in the fault data set to extract throw along each fault, and examine the results of this systematic analysis in the following sections.

62% of all fault segments within the LiDAR survey area dip westwards with only 38% dipping towards the East (Fig. 4.7) which is in agreement with previous observations (e.g. Grandin et al., 2009).

The dominance of westwards dipping faults (red) is particular striking within the AVC and to the South of it. The area north of the AVC exhibits fewer faults with no dominant dip direction. Fault spacing appears to be larger at the central part, which is probably the result of the recent resurfacing. Near the Dabbahu volcano fault dip directions alternate more evenly. Figure 4.8 shows topographic profiles from the northern (a), central (b) and southern (c) sections of the rift. It illustrates the transition from horst and graben structures near the Dabbahu volcano (a) (Medynski et al., 2013), across the recent resurfaced section (b) to the AVC's book-shelf faulting (c).

Overall I derived >64,000 throw measurements, at 20 m intervals, finding a maximum throw of 82 m and an average throw of 15 m. Figure 4.9 shows the results of this analysis. The derived throw along each fault segment is represented by colour. The faults outside the LiDAR survey have not been measured and are shown for reference only. The faults with the largest throw are the ones crossing the rhyolitic AVC. The western part of the survey area is dominated by closely spaced (<100 m) faults with average throw of <10 m. At the centre and the East the spacing between the faults is wider (∼500 m) and average throw values are ∼15 m. The mainly westwards dipping book-shelf faults of the southern rift segment exhibit consistently larger throw compared to the rest of the segment.

Variations of fault length, spacing and throw have been observed at slow spreading rift centres (Shaw, 1992, Shaw and Lin, 1993). Numerical modelling suggests that crustal thickness variation is the key factor responsible for these variations, estimating that reducing the crustal thickness by half could double and triple fault spacing and height, respectively (Shaw and Lin, 1996). Ebinger et al. (1999) link faults with large throw to larger effective elastic thickness.

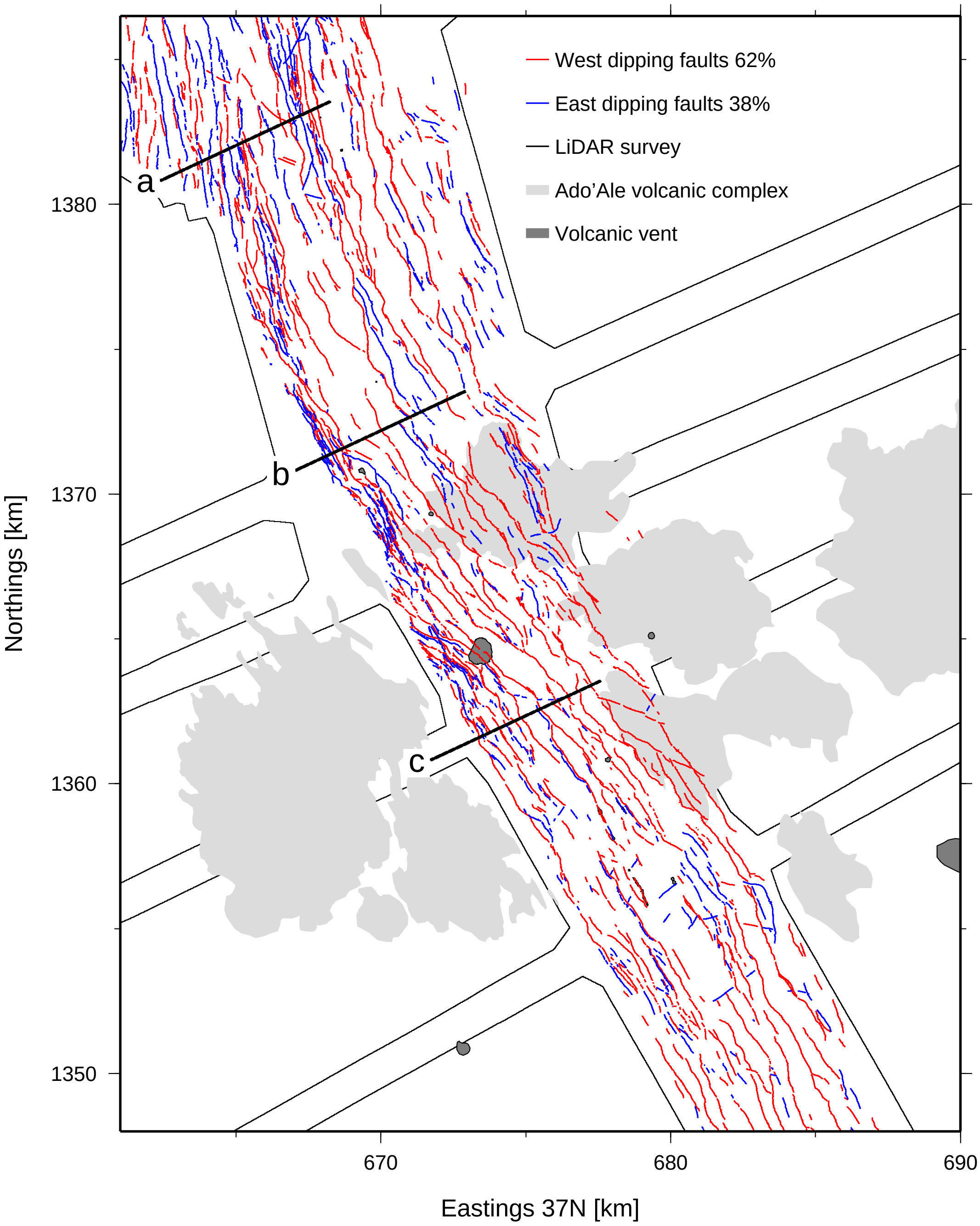

Figure 4.7: Distribution of fault dip direction. The majority of the fault segments, 62 %, are west dipping (red) and only 38 % are dipping towards the east (blue). Profiles a,b and c are shown in figure 4.8.

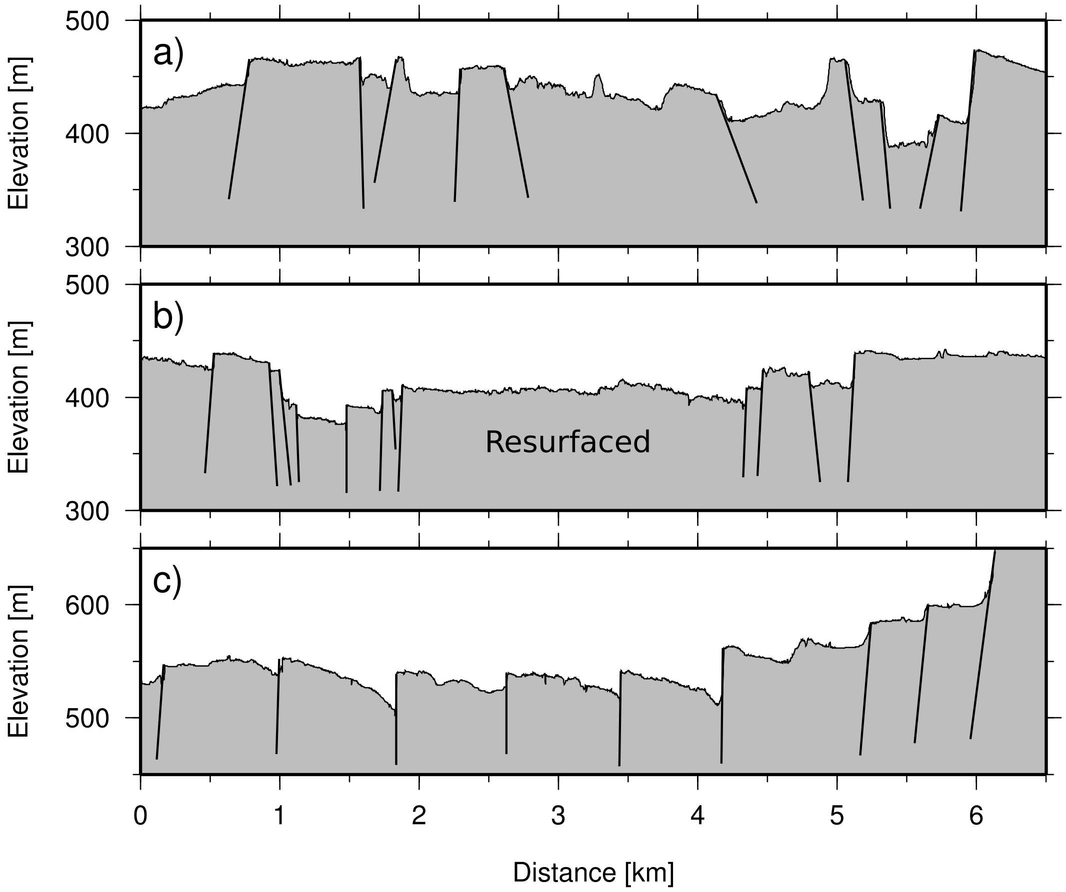

Figure 4.8: Different styles of faulting at the Dabbahu rift segment. Top: Profile across horst and graben structures at the base of Dabbahu volcano, middle: Profile just north of AVC showing horst and graben structures as well as resurfacing, bottom: Profile across bookshelf faulting at AVC. Vertical exaggeration of 10. The location of the profiles is shown in figure 4.7.

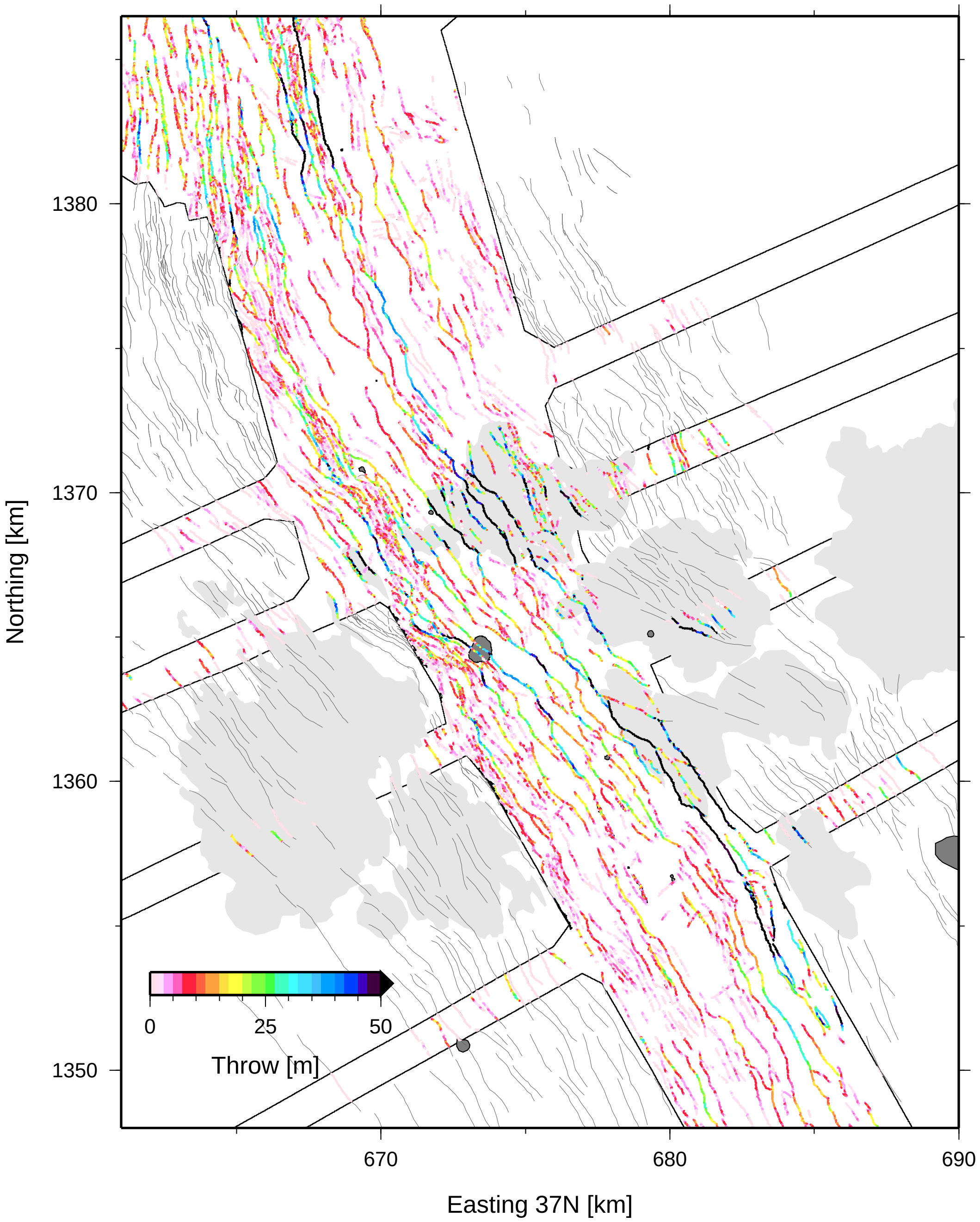

Figure 4.9: Fault map colour-coded by throw. Only faults covered by the LiDAR survey (black outline) have been measured. Faults with the largest throw (> 50 m) are found in the rhyolites of the AVC. Faults outside the LiDAR coverage are not measured and are shown for reference only.

4.3 Fault linkage

Close examination of the Dabbahu rift segment shows that virtually all fault segments interact with their neighbours to some degree, forming extensive arrays consisting typically of more than 10 segments. I did not encounter any clearly isolated fault segments. Throughout the rift segment I observed fault linkage zones at varying stages of their development. In Fig. 4.10 I present a selection of fault linkage stages common for the Dabbahu segment. I classified them into stages after Peacock and Sanderson (1991) (§ 1.1). Fig. 4.10 a) shows early onsets of linkage between 2 to 3 small faults. They physically overlap but the ramp is not yet visible (L1). In figure 4.10 b), I show a classic stage 2 linkage zone (L2): The two faults are connected by a smooth intact ramp. The linkage in figure 4.10 c) is at stage 3 (L3): The ramp connecting the two faults is intersected by small fissures and the back structure distinctly curves towards the front but the ramp is not yet breached. A large number of faults are currently undergoing stage 3 linkage. I show a fully breached ramp indicative for stage 4 linkage (L4a) in figure 4.10 d): The two faults have formed one through-going fault scarp along the back of the ramp. The remnants of the breached ramp are still clearly visible at the hanging wall. The example in figure 4.10 e) illustrates the specific case of stage 4 linkage (L4b) where ramp at the hanging wall has been covered by a recent lava flow and only the bend in the fault trace and the small remaining fault tip on the foot wall reveal the former linkage zone. I identified both upper-ramp and lower-ramp breached ramps (§ 1).

In addition to this regular style of linkage I observed large divergent Y-shaped linkage zones where the main fault splits into two splay faults of similar length but different amounts of throw. It appears as if these features are a result of lower-ramp breached linkage zones where the fault tip of the rear fault remains active. These structures often connect neighbouring fault arrays. In figure 4.11, I show an example of a fault array that exhibits two Y-shaped splays (2 and 4) as well as a L3 (1) and and a L2 (3) linkage zone. The bottom panel shows the $d - L$ pattern of the entire array. A close inspection of the main Y-structure (2) suggests that previously the blue and green structures were hard linked, but currently the hard linked surface trace follows the blue structure. Also the $d - L$ pattern shows that both arms have accumulated significant throw. The smaller Y-structure (4) shows a similar map geometry to the larger structure, but its

$d - L$ shape is not conclusive at this moment. The two linkage zones 1 and 3 exhibit the expected shape with a minimum at the centre of the linkage zone. In both cases linkage takes place between two segments with different average and maximum throws.

I manually picked >100 linkage zones and classified them into the types I just described. The Y-structures are additionally separated into 'South', if the Y opens towards the south, and 'North' if it opens towards the north. Figure 4.12 shows their distribution colour coded by type. It also shows a number of places where lava flows have come over the top of the scarp obscuring potential linkage zones. In the northern part the linkage zones appear to be more separated and slightly further developed. At the western margin of the LiDAR survey, a cluster of south opening Y-structures are located. The linkage zones in the southern part seem less developed with a large number of L2 and L3 structures. They are also very closely spaced.

Fault growth models based on fault linkage commonly propose: 1) a significant throw minimum across the fault ramp during the stages of soft linkage, 2) a shift of the along strike position of the throw maximum from the centre towards the linkage zone and 3) a reduction or elimination of the throw deficit across the linkage zone once hard linkage has occurred (Fig. 4.13) (e.g. Peacock and Sanderson, 1991, Cartwright et al., 1996, Gupta and Scholz, 2000).
To test this I picked the throw minimum at linkage zones and the closest maximum either side of it for all L2-L4 linkage zones, from the $d - L$ shapes derived by my algorithm. For soft linked structures I picked the minimum of the combined curve of both segments. In Fig. 4.14-left I plotted the minimum throw across the linkage zone vs. its two adjacent maxima, which are connected by a red line. The diagonal line marks minimum throw at linkage = maximum throw of adjacent segment. The right panel shows the horizontal distance between the minimum and the maxima. In both panels I distinguish between soft-linked (blue) and hard-linked (green) linkages. If a throw minimum exists across the linkage (1) I expect to see a significant offset between the diagonal line and the maximum throw values for the soft linked structures (blue dots) in figure 4.14-left. For the hard linked structures (green) I would expect one or both maxima to be close to the diagonal line as the throw deficit is reduced (3). I do not observe either of these (1) and (3) in my data set. However, regardless of

linkage type the linkage zones seem to be asymmetric with the maximum throw on one of the segments being close to the minimum throw at the linkage and the difference between the throw maxima is >2 m in 70% of the cases. Differences within ± 1 m lie within the expetecd uncertanty of the measurements. This asymmetry might be due to the relativly young age of the Dabbahu rift segment where the initial disequilibrium between the two segments is still preserved. To progress from this stage to the generally proposed $d-L$ shape with its maximum at the centre, the smaller segment will need to acquire throw faster than the other part. In the next chapter (§ 5) I will test whether this is occurring using InSAR and differential LiDAR.

If the position of the throw maximum shifts towards the linkage zone (2) I expect the horizontal offset for the soft linked segments (Fig. 4.14-right, blue) to be further apart than the horizontal offset of the hard linked segments (green). Again there is no clear evidence for this in my data set.

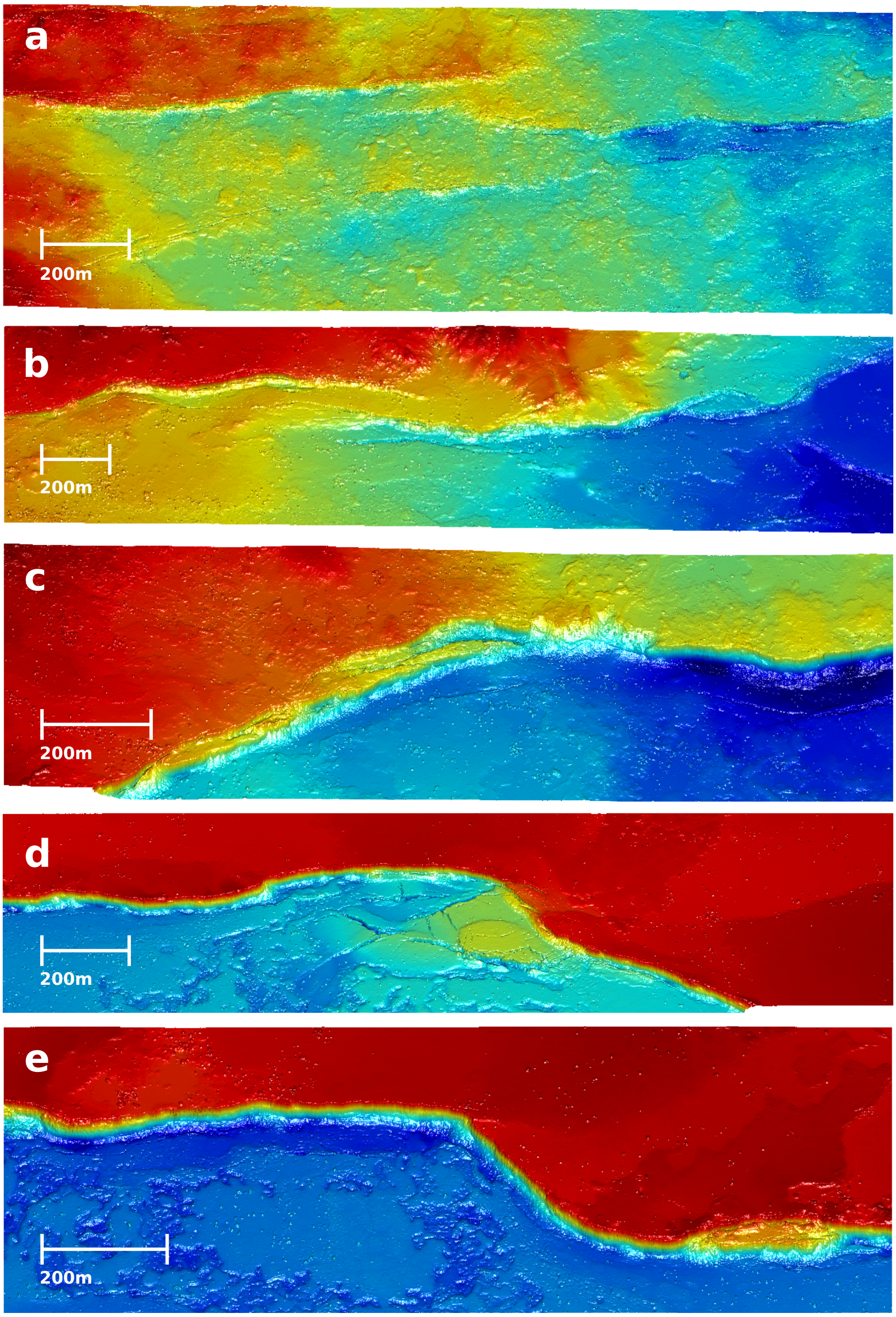

Figure 4.10: Different stages of fault linkage. From top to bottom: a) Onset of relay ramp formation (early stage 2); b) established intact relay ramp (stage 2); c) ongoing destruction of relay ramp (stage 3); d) through going fault scarp and complete destruction of ramp (stage 4); e) old fault linkage zone ramp remains covered by new lava. Position of the linkage zones are marked in figure 4.12. Colour scale is different for each image. Red highest elevation, blue lowest elevation. Throw on the faults increases from the top image downwards.

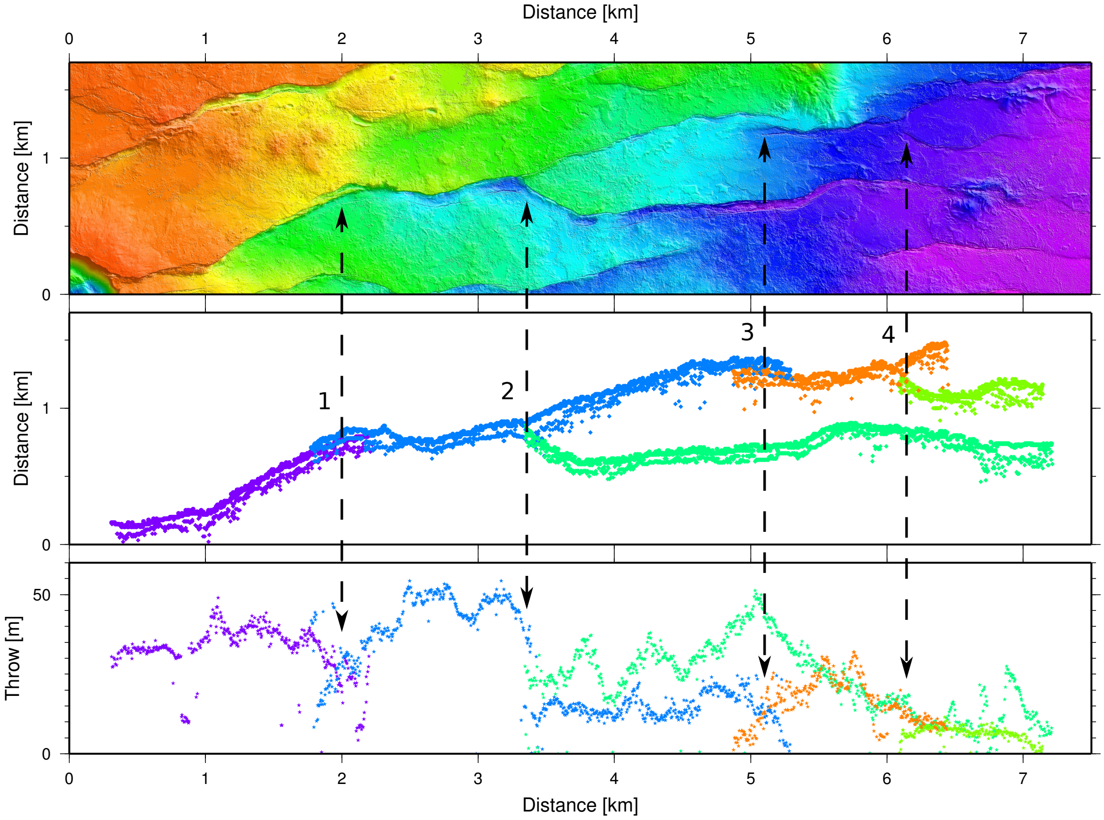

Figure 4.11: Example of fault array. Top panel: LiDAR section rotated in direction of strike, second panel: hanging and footwall cutoff, bottom panel $d - L$ profile. Colours mark individual fault segments. Dashed lines mark linkage zones addressed in the text. Linkage zone 1 is depicted in figure 4.10 c and its position is marked in figure 4.12.

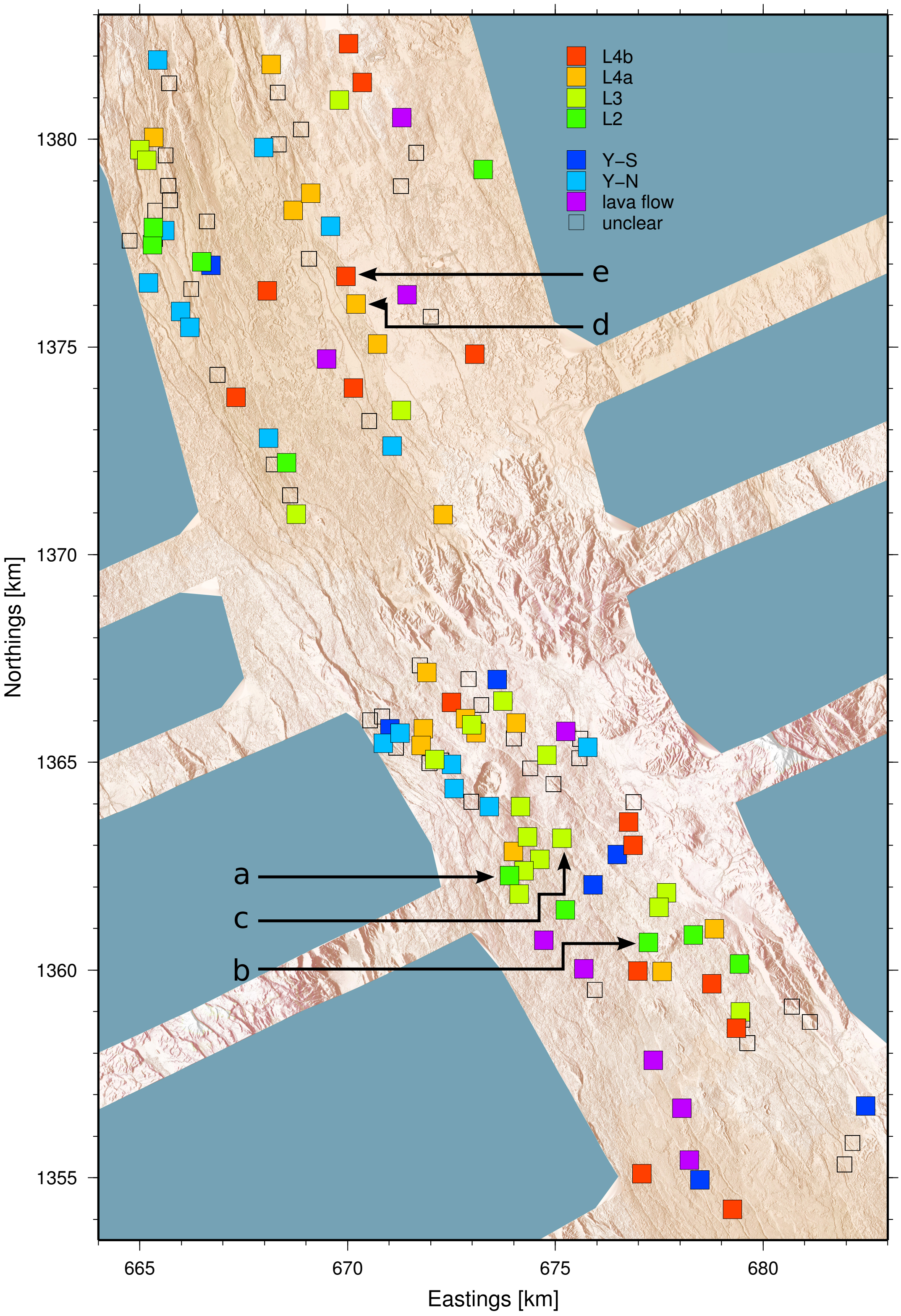

Figure 4.12: Map illustrating the distribution of different types (colour coded) of linkage zones across the Dabbahu rift segment. A detailed description of the individual types is provided in the text. The background image shows the shaded relief LiDAR DEM. Arrows mark the position of the linkage zones presented in figure 4.10

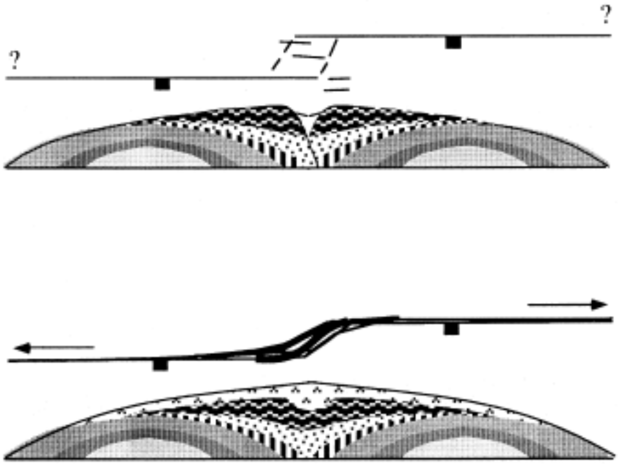

Figure 4.13: Conceptual model of fault growth by linkage. Arrows indicate direction of fault propagation, shading in $d-L$ shape illustrate individual slip events. Top: Lateral fault propagation is suppressed by the stress field, asymmetric accumulation of displacement, position of throw maximum is shifted towards the linkage zone. The faults are soft linked. Bottom: Hard linkage has taken place. The displacement deficit at the linkage zone is gradually reduced. Lateral propagation recommences. Reprinted from Gupta and Scholz (2000) with permission from Elsevier.

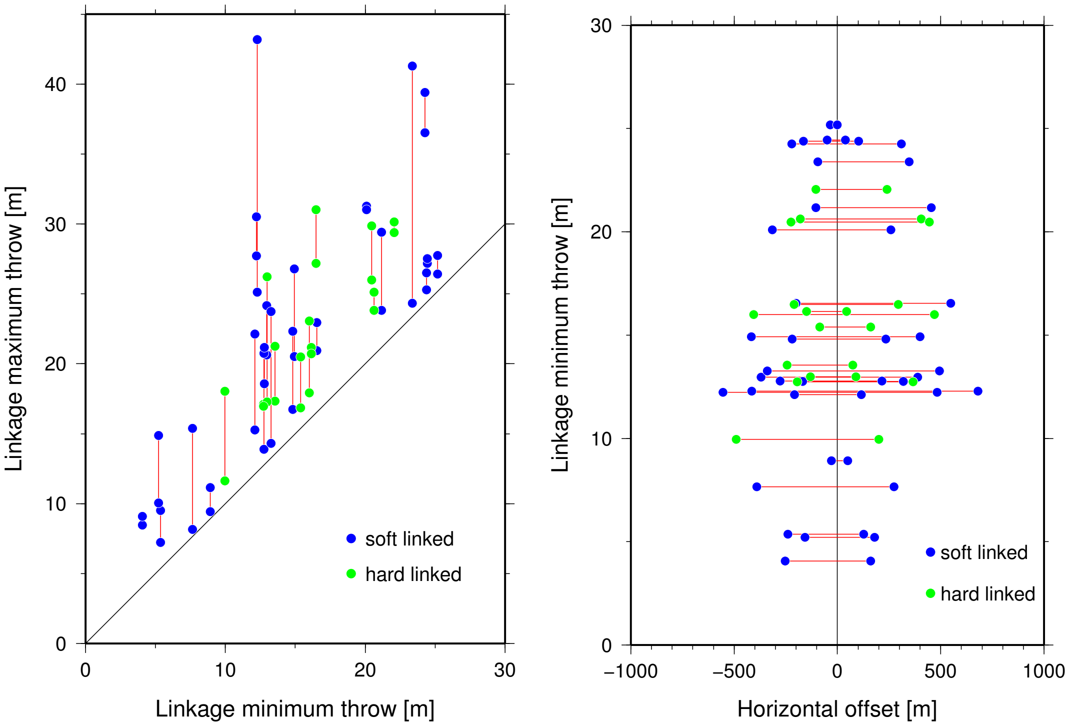

Figure 4.14: Relationship between the minimum throw across a fault ramp and its adjacent segment maxima, separated into soft linked (blue) and hard linked (green) structures. Left: Linkage minimum vs the two closest maxima; right: along-strike distance between minimum and maxima.

4.4 Strain mapping

The systematic analysis of fault displacement presented here enabled me to address several questions regarding the role of faulting in accommodating the extension. How is the strain distributed across the rift segment? How much of the extension is preserved in faulting or lost due to resurfacing? To do this I first estimated the strain recorded by the normal faults at the Dabbahu rift segment.

4.4.1 Method

I followed the method presented by England and Molnar (1997, 2005) to calculate strain and displacement related to the normal faulting at the rift segment. The method is based on formulations of Kostrov (1974), which show that, if all strain within an area is accounted for, the total strain within this area is formed by the sum of all measurements.

England and Molnar (2005) divide the surface into triangles and calculate the average strain for each triangle, based on the amount of slip on the fault segments traversing the triangle. The slip tensor M for each fault segment is defined as

$$M_{ij} \;=\; A(u_i n_j \;+\; u_j n_i) \tag{4.1}$$

with the slip vector, $\vec{u}$, a normal to its surface, $\vec{n}$, and the area of the fault

$$A \;=\; \frac{LZ}{sin\,\delta} \tag{4.2}$$

where length, L, is defined as the part of the fault segment within one triangular element, Z represents the thickness of the faulted layer, and δ is the dip of the fault. The strain tensor ε for each triangular element is then defined as

$$\varepsilon_{ij} \;=\; \frac{1}{2V}\sum_{k=1}^{K} M_{ij,k} \tag{4.3}$$

where K is the number of fault segments within the element and V the product of the triangles surface area Δ and thickness Z. After combining equations 4.1, 4.2 and 4.3, Z is eliminated and the strain can be expressed as

$$\varepsilon_{ij} \;=\; \frac{1}{2\Delta}\sum_{k=1}^{K} L_k\,(\frac{u_{i,k}n_{j,k} + u_{j,k}n_{i,k}}{sin\,\delta_k}) \tag{4.4}$$

This shows that strain within the seismogenic layer of an area can be expressed by surface measurements only. The surface displacements can be determined through integration if the strain field is known throughout the region (Haines, 1982). England and Molnar (1997) ensure continuity by assuming that the strain is constant within each triangle and therefore the displacement varies linearly across each triangle of the mesh covering the area of interest.

4.4.2 Strain mapping from throw measurements

For the calculation I used all 3748 faults of the previously discussed fault data set (§ 4.2). To simplify the calculation, each fault is approximated as a straight line from its first to its last point with its previously calculated strike direction. From my analysis dip and rake are unconstrained. At the surface most faults dip at almost 90°. However the data derived from the differential LiDAR survey (§ 5.3.6 and following) shows that the dip angle, δ of the activated faults with significant slip (> 1 m) is 62° ±17°. I therefore fixed dip to 65° and rake to -90° simulating pure dip-slip faults. I approximated the fault slip, s, from the mean of the derived throw, t, along the fault length with $s = t \,/\, sin(\delta)$. The triangular elements are equilateral with side length of 2 km. I used a code provided by Philip England to perform the calculation. Figure 4.15 shows the results of the analysis.

The LiDAR survey only covers the recently intruded part of the rift segment and therefore any strain accumulated on faults outside of the survey is not included. Also the strain along the border of the survey might be underestimated as faults which are only partly covered by the survey may not be mapped. Furthermore the strain estimated for each cell might be underestimated, as it is solely based on faulting and does not include pure extension across fissures. However, due to the high resolution of the LiDAR data set and the fault mapping in 3D even structures with small vertical offset have been mapped and it is unlikely that major structures have been missed.

Principal strains are largest across the Dabbahu volcano and the AVC. Between the two volcanic centres, the extension appears to be minimal. In the southern part of the rift segment the majority of the strain has accumulated at the eastern flank. This distribution is mainly due to the recent resurfacing events to the north and south-west of the AVC (see previous Fig. 4.2 and Fig. 4.3).

To estimate the total extension due to faulting I integrated the resolved strain compo-

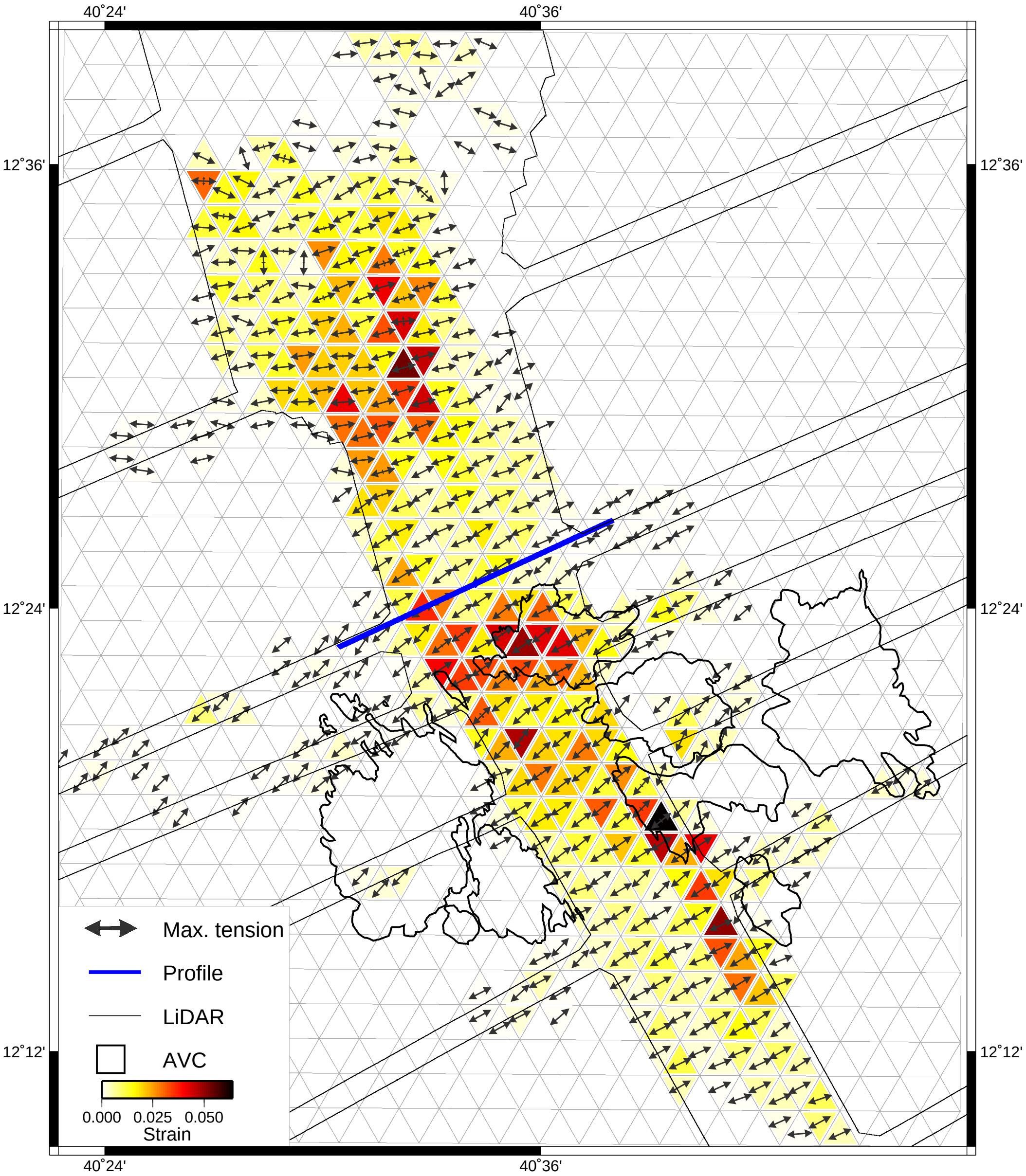

Figure 4.15: Strain map derived from cumulative fault throw. The magnitude of principal extension accumulated in each triangular cell is shown as colour. The direction of extension is given by the arrows. Strain accumulation is largest between Dabbahu volcano and AVC (grey) and located to the West of the rift segment. The profile corresponding to the blue line is shown in figure 4.16

nent across a 15 km long profile just North of the AVC (blue line, Fig. 4.15). For this profile I derived 139 m of cumulative extension. An alternative method to estimate the extension is through a simple bookshelf faulting model, in which the percentage of extension (ξ) can be calculated as

$$\xi = \frac{sin\,(\alpha + \theta)}{sin\,\theta} - 1 \tag{4.5}$$

where α is the dip angle of the rotated fault block and θ the dip angle of the fault plane (e.g Wernicke and Burchfiel, 1982). I observed fault block tilting of 1-10°. 29 faults intersect the 15 km-long cross profile and assuming an average $\alpha = 5°$ and $\theta, = 65°$ I estimate ∼106 m extension. The estimate is of the same order of magnitude as that derived from the strain calculation.

The chosen profile closely correlates with the profile across the lava flow sample locations presented by Ferguson et al. (2013) (sample locations are marked in Fig. 4.2). ^{40}Ar/^{39}Ar dating of the basalt flows along the northern edge of the AVC, indicate that the Dabbahu rift segment has been active for the past ∼200 ka (Ferguson et al., 2013). Assuming that each of the lava flows were emplaced similar to the most recent lavas at the rift centre - extending roughly 2 km from the rift axis, and that the position of the rift axis remained stable throughout the past 200 ka Ferguson et al. (2013) estimate an extension rate at the Dabbahu rift segment of 20 mm/y. At this spreading rate the central rift could accommodate the estimated extension of 139 m across the profile in ∼7 ka. This large discrepancy in the estimated ages of 200 ka vs. 7 ka cannot be explained through errors in the strain estimation alone.

In figure 4.16 I show the comparison between the topography including ^{40}Ar/^{39}Ar dates (top) and the strain across the same profile (bottom). The majority of the strain is accumulated at the flanks of the central graben whereas the strain across the most recently resurfaced zone (∼2 km wide) is almost constant at ∼0.01. While a decrease in strain towards the youngest section of the rift seems reasonable this abrupt decrease from ∼0.035 to ∼0.01 suggests that the most recent resurfacing event buried pre-existing structures and thereby reduced the strain recorded in the faults. Large volume eruptions are commonly associated with rifting episodes and have been observed at the end of the latest Krafla rifting episode in Iceland (e.g. Björnsson et al., 1977). So far no large scale eruption has occurred during the most recent Dabbahu rifting episode but the geology of the segment shows numerous basalt flows spreading across the segment floor (Vye-Brown et al., 2012), suggesting that resurfacing plays a major role in the development of the topography of the Dabbahu rift segment.

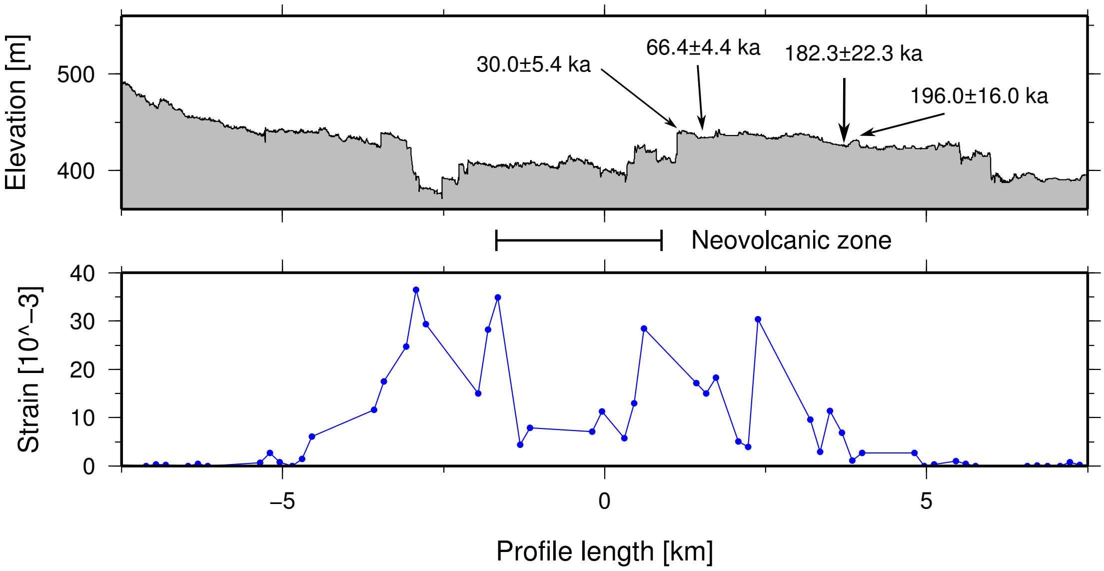

Figure 4.16: Cross-profile of extensional strain just north of AVC (red line in Fig. 4.15). Majority of the strain is located on the flanks of the central rift. The decrease of strain across the central rift section is associated to resurfacing processes. (Top after Ferguson et al., 2013)

4.5 Summary

In this chapter I studied the current state of fault development at the Dabbahu rift segment. I successfully applied my algorithm and extracted throw for all 3748 fault segments mapped by C. Vye-Brown.

The majority of the faults at the Dabbahu rift segment are west dipping. Close to the Dabbahu volcano in the north of the segment horst and graben structures are common but at the AVC and to the south of it bookshelf faulting is the dominant style of faulting. The spacing between fault segments increases from ~100 m in the west to 500-1000 m in the east of the survey area. This possibly indicates a thinning of the crust towards the east of the rift segment (Shaw and Lin, 1996).

Individual fault segments picked from the high-resolution LiDAR DEM by C. Vye-Brown are ~600 m long. Multiple segments connect through fault linkage forming extended fault arrays. The degree of linkage varies throughout the segment from early stage 2 soft linkage to fully hard linked stage 4. Individual faults without any signs of interaction to neighbouring faults are virtually non-existent throughout the rift. My analysis of the linkage zones indicates that the linked faults can exhibit large differences in maximum throw. According to published fault growth models individual and linked faults strive to create an overall bow shaped $d - L$ shape (e.g. Walsh and Watterson, 1988, Peacock, 2002, Cartwright et al., 1996). Assuming this is the case new displacement should accumulate mainly along the fault segments exhibiting less throw. I will test this in the next chapter using data that show how faults slip in individual dyking events (§ 5).

Divergent splay faults are common throughout the rift segment. Divergent splays are usually considered to be the remnant, inactive fault tips left over after linkage is complete (Trudgill and Cartwright, 1994). At the Dabbahu rift segment the length of the splay faults are often of similar length to the main fault and it appears as if they remain active. Again, I will test this in the next chapter (§ 5).

Calculations of the strain accommodated by faulting indicate that only 3.5% of the extension that occured in the past 200 ka is preserved in the fault displacements. One major reason for this appears to be resurfacing by lava flows.

Chapter 5

Incremental displacement/ Fault growth observations

Fault growth models are usually inferred from displacement-length measurements of multiple faults within a common geological setting (e.g. Cartwright et al., 1996). However, displacement and length of faults are the result of multiple slip events. Observations of how new fault slip is distributed along faults exist from analogue modelling (Mansfield and Cartwright, 2001) but no previous observations of fault reactivation of an entire array exist from field data. Here, I have the unique opportunity to observe and quantify fresh fault slip across the Dabbahu rift segment, using InSAR data and both LiDAR surveys. These results will help resolve the question of how fault slip accumulates along faults, and enables me to test theories of fault growth (§ 1.1). In particular I will address the following points.

- What happens at the fault linkage zones?
- Do linkage zones exhibit increased displacement or do they act as barriers?.
- Does the less developed fault segment of a linked fault show signs of 'catching up' via increased displacement?
- How do the divergent splay formations behave. Which segments are re-activated during a dyke intrusion?

In respect to dyke-induced faulting I will look at the following questions

- Where does the fault re-activation occur in respect to dyke intrusions?
- Which faults get reactivated during the intrusion?

I start this chapter with brief introduction to dyke intrusions and their relationship with normal faulting. The following two sections focus on the incremental throw derived from the InSAR data and differential LiDAR. Each section starts with a description of how I derived incremental throw measurements from the respective data set before showing the results. In the final section of this chapter I will summarise and discuss my results with regard to previously published models of fault growth.

5.1 Dyke intrusion and faulting

Dyke intrusions are an important part of continental break up (e.g. Maguire et al., 2006, White et al., 2008, Thybo and Nielsen, 2009, Daniels and Bastow, 2014). They are blade-like magmatic intrusions accompanying extension (e.g. Behn et al., 2006). Some of the best examples have been observed in Iceland and Afar (Wright et al., 2012).

As a dyke intrudes into the upper crust it creates tension above the dyke and compression at its sides. This leads to the characteristic displacement signal of subsidence above the dyke, uplift at the flanks and horizontal extension perpendicular to the dyke (Fig. 5.1), which is accompanied by normal faulting and fissure opening (Behn et al., 2006, Pollard et al., 1983, Rubin and Pollard, 1988, Bull et al., 2003, Tentler, 2005). Due to the compression, faults far from the dyke are expected to be locked and faulting above the dyke is favoured (e.g. Rubin and Pollard, 1988, Rubin, 1992, Bull et al., 2003). 2 m of slip on normal faults during dyke intrusions has been observed in Iceland (Björnsson et al., 1977, Tryggvason, 1984) and Afar (Rowland et al., 2007).

Simulations of rift extension within an elastic-viscoplastic medium suggest that the ratio between magma influx and tectonic extension is an important factor for the topographic development of rifts (Behn et al., 2006). Low magma influx leads to narrow deep rift zones while high magma influx causes a more shallow rift with horst and graben structures. Data from seismic moment studies (Solomon et al., 1988), cumulative fault throw (Escartin et al., 1999) from slow spreading mid oceanic ridges, and geodetic data (Bilham et al., 1999) from the Main Ethiopian rift estimate that ∼80% of the extension is accommodated by dyke intrusion and 20% by extensional faulting. Estimates for the initial intrusion at the Dabbahu rift segment in 2005 showed the seismic moment release could only accommodate <10% of the observed geodetic moment (Wright et al., 2006, Rowland et al., 2007).

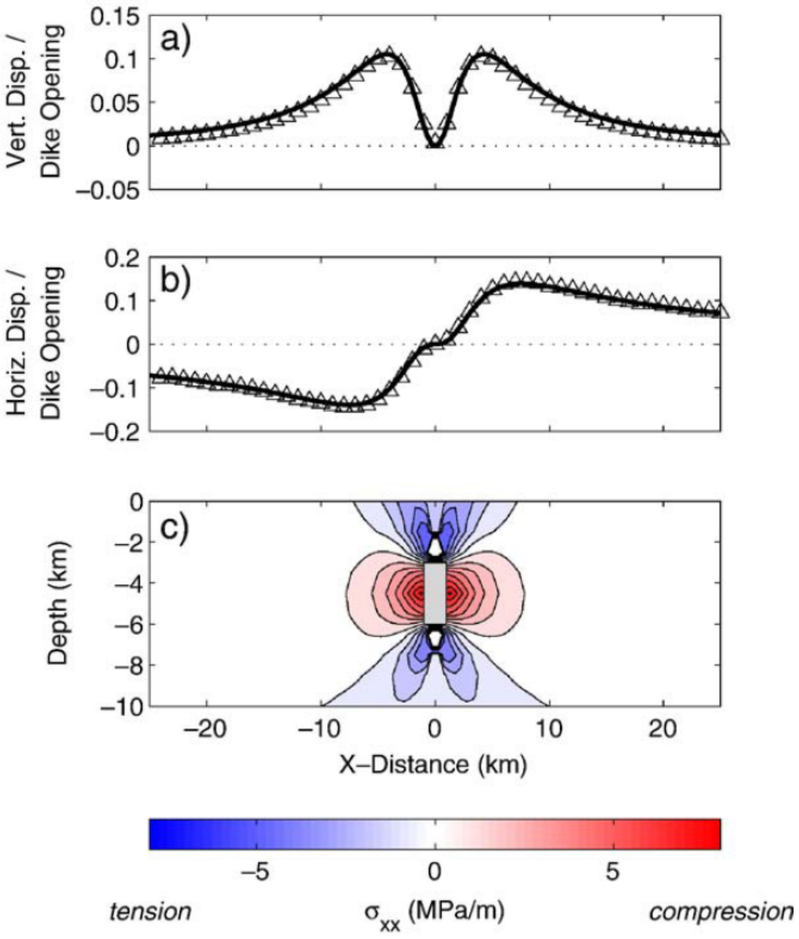

Figure 5.1: Surface displacement from dyke opening in a purely elastic layer normalised by the dyke opening. For the calculation a dyke is emplaced in a 20 km thick elastic layer and stretches from 3-6 km depth. a) vertical displacement, b) horizontal opening, c) horizontal deviatoric stress σ_{xx}. Reprinted from Behn et al. (2006) with permission from Elsevier

5.2 Incremental fault slip derived from InSAR data

The analysis in this section is based on the October 2008 dyke intrusion. To date it is the largest intrusion since the initial event in 2005 (Hamling, 2010, Wright et al., 2012). It intruded the Ado'Ale volcanic complex and the area to the North of it and elastic dislocation modelling, based on ENVISAT interferograms, suggests a dyke of ∼11 km length with maximum opening of ∼3 m and a total injected volume of ∼0.17 km^3, with opening in the depth range of 1-8 km (Fig. 5.2 Hamling, 2010).

In § 2.2 I showed that ALOS data is better suited for the purpose of studying the fault slip than ENVISAT data. The longer wavelength ($\lambda = 23$ cm) of the ALOS data enables me to unwrap the interferogram above the area of fault slip. To identify and

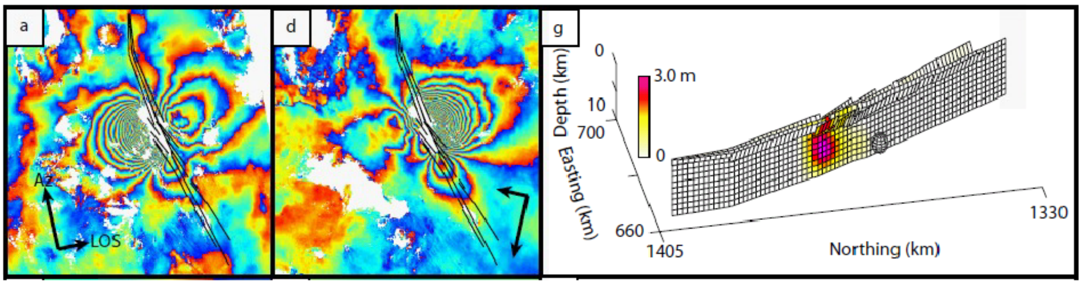

Ascending Descending Dyke model

Figure 5.2: Elastic dislocation model of the October 2008 dyke intrusion from Hamling (2010). a) and b) ascending and descending ENVISAT interferograms. c) best fitting dyke model with maximum opening of ∼3 m.

derive throw, I processed the ALOS satellite data according to the method described in § 2.2. The ALOS images used for the analysis cover three frames (220, 230 and 240) of the ascending track 599 (Fig. 5.3) and were acquired on 14.09.2008 and 15.12.2008.

The ALOS data covering the Dabbahu rift is only available from its ascending track, which means I cannot solve for true 3D-displacement but only resolve displacement in the line of sight (LOS) of the satellite. Figure 5.4 shows the ALOS interferogram of the October 2008 dyke intrusion. The top image shows the wrapped interferogram and the bottom image the interferogram after the unwrapping process. The semi-circular fringe pattern in the east and west of the interferogram indicate flank uplift. The uplift signal is larger on the western flank because the vertical uplift and the westward motion both translate into surface movement towards the satellite. At the eastern flank the uplift causes movement towards the satellite while the eastward motion leads to movement away from the satellite, which causes a partial cancellation of the signal and therefore fewer fringes. Surface uplift effectively shortens the distance between the ground and the satellite causing a negative range change and subsidence produces a positive range change. In the unwrapped interferogram (Fig. 5.4 bottom) the large negative signal at the western flank (blue) and the subsidence at the centre (red) are the predominant signals. The area of subsidence correlates to the more complicated fringe pattern in figure 5.4 (top). A closer look at the subsided area shows that it is made up of individual elongated areas. A visual comparison with the LiDAR DEM shows that the edges of these areas correlate with the location of the fault scarps (Fig. 5.5). This indicates fault slip along pre-existing faults. Along some of the fault scarps the displacement is

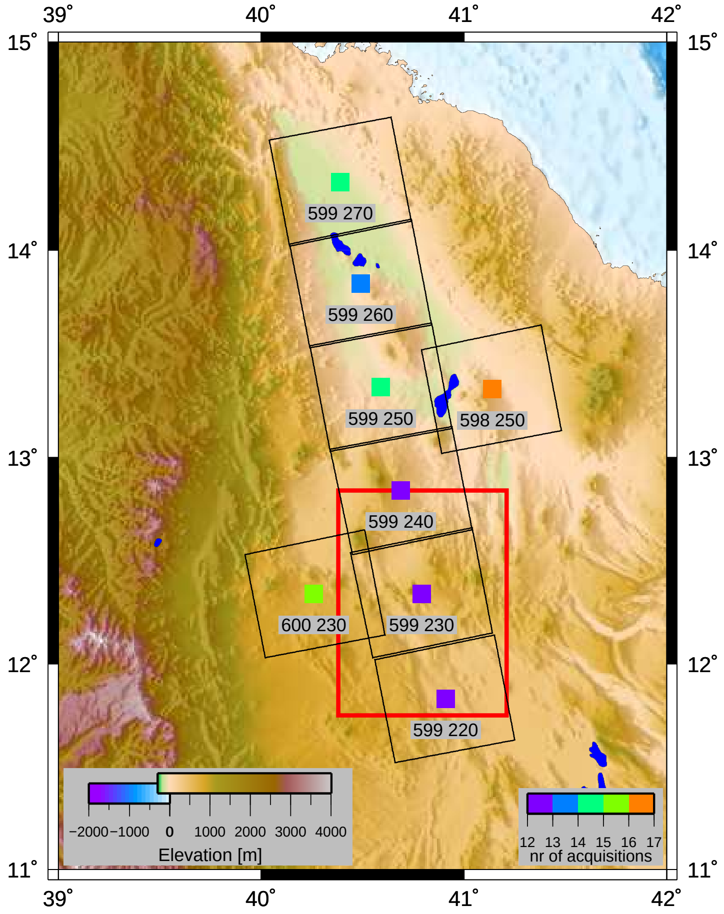

Figure 5.3: Location of ALOS acquisitions. Individual frames are marked as black rectangles. First number indicates the number of the track, the second number marks the frame. Colour-coded squares illustrate the number of acquisitions. Thick red rectangle marks the location of the Dabbahu rift segment. Map: 1 arc sec SRTM DEM Farr et al. (2007)

not defined (white areas), which is a result of the unwrapping process. I will address this in § 5.2.2. Slip on a fault creates a discontinuity in the interferogram at which the displacement is undefined.

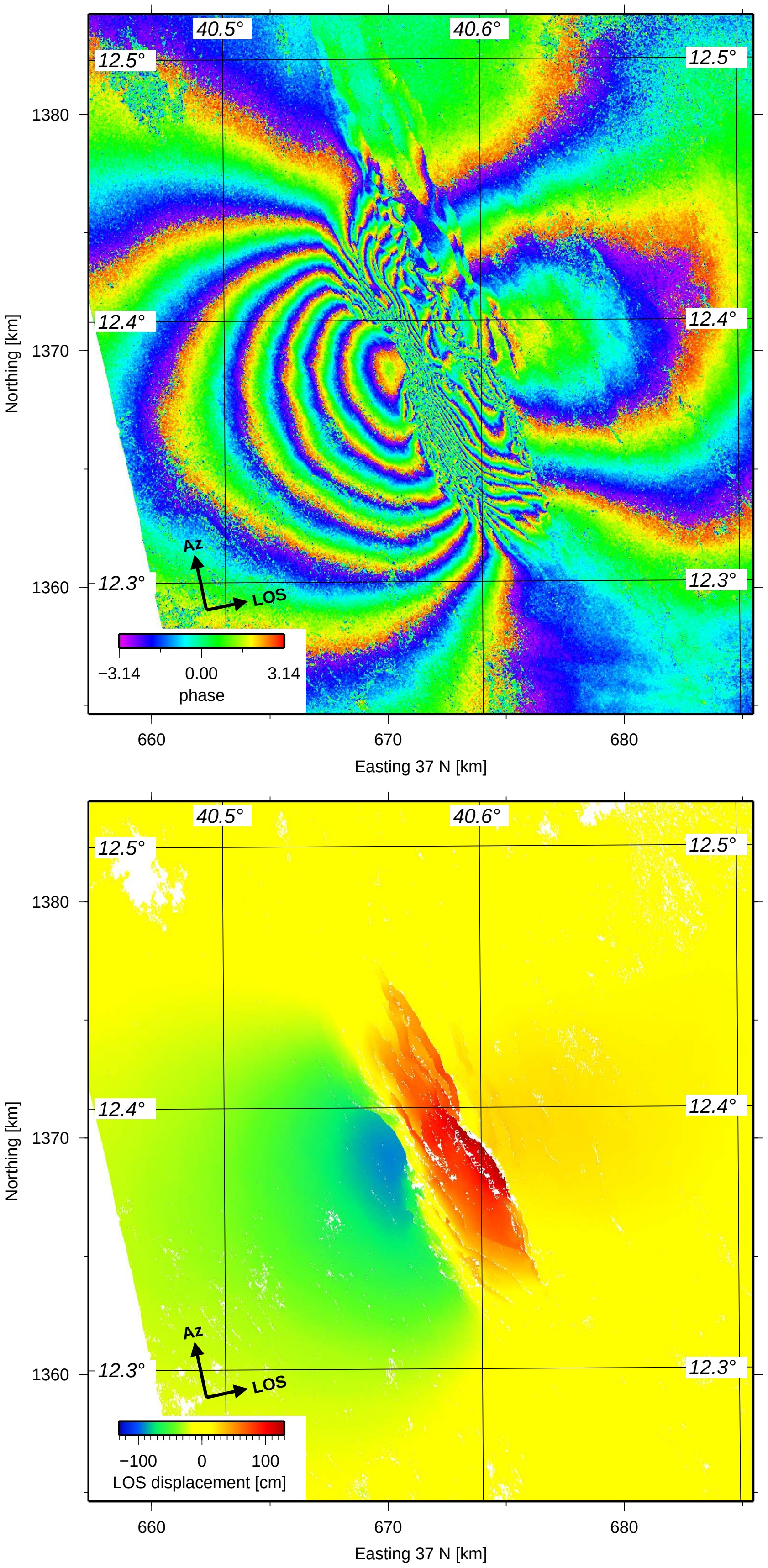

Figure 5.4: Ascending ALOS interferogram covering the October 2008 dyke intrusion. Arrows mark satellite flight direction, Az, and look direction, LOS. Top: Observed interferogram before median filtering, bottom: Unwrapped interferogram. Blue indicates uplift and red subsidence.

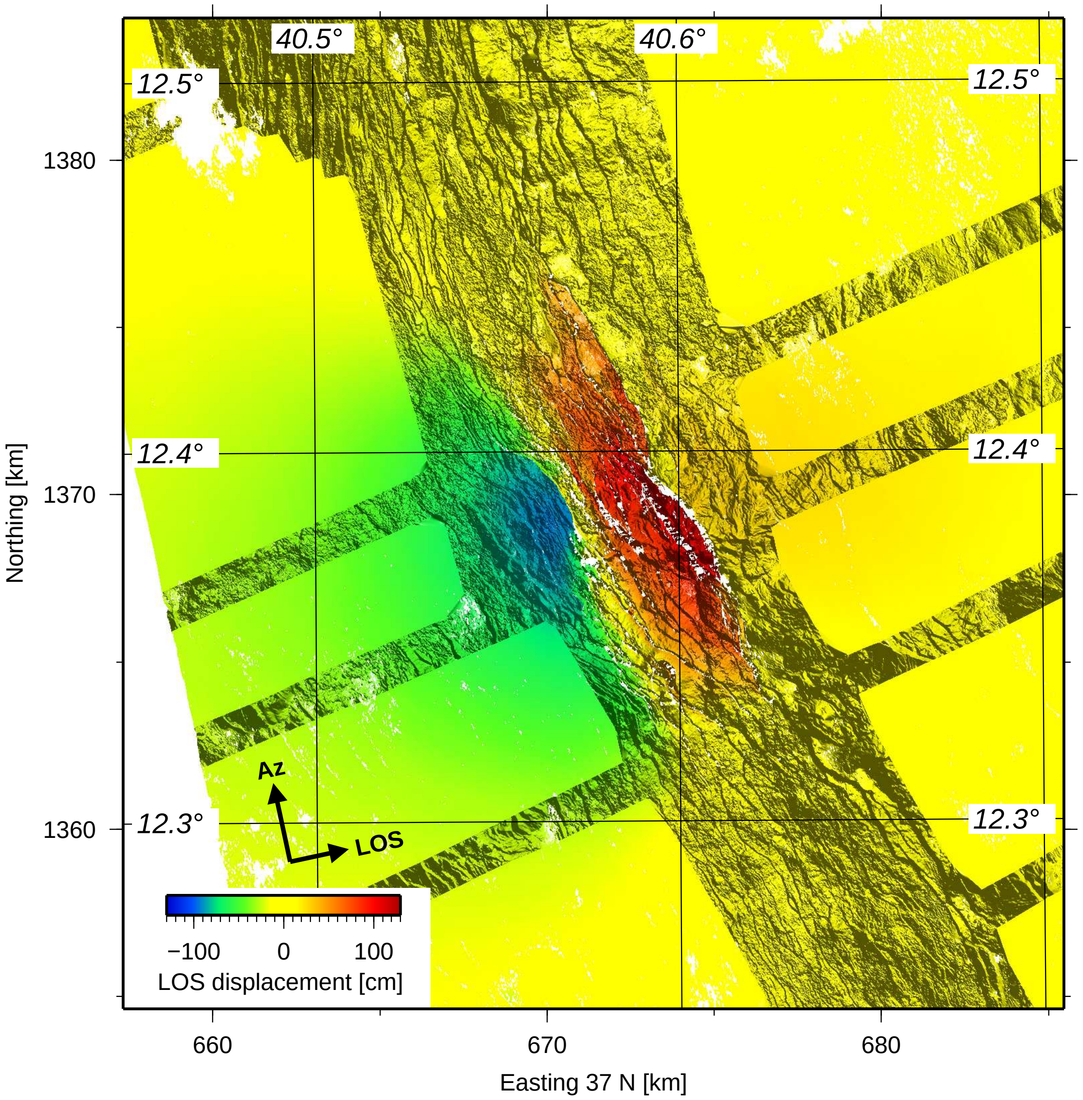

Figure 5.5: Comparison between the unwrapped interferogram of the October 2008 dyke intrusion and the high-resolution LiDAR DEM. Individual, elongated areas of subsidence correlate with fault scarps in the LiDAR DEM. LiDAR DEM is shaded from NE and is used to modulate the intensity of the InSAR data.

5.2.1 Identification of fault slip

To distinguish between slip at a fault and the overall dyke induced displacement I calculate the gradient of the LOS displacement in EW direction. The long wavelength background displacement produces small gradient changes over relatively large distances. In contrast, slip on faults produces a larger gradient change across a short distance. In the gradient map (Fig. 5.6), lines of larger gradients, which indicate slipped structures are visible. A negative gradient (red) implies relative displacement toward the West and positive gradient (blue) indicates relative displacement in eastward direction. The gradient indicates minimal fault slip towards the west at the uplifted western flank (box 1, faint red traces). Box 2 marks the transition from uplift to subsidence, which is indicated by the large eastwards gradient overprinting this section. Regardless of this signal, slip on individual fault traces is apparent. The clearest fault slip signals are visible towards the east (box 3). Overall the larger gradients appear to be on the faults with relative westward displacement.

I compared the topographic expression with the LOS displacement along a profile marked by the black line in Fig. 5.6 to better assess which structures slipped during the intrusion and in which direction. I manually picked all the faults crossing this profile on the 0.5 x 0.5 m^2 LiDAR DEM as well as each slip signal by looking at the LOS displacement gradient as well as the unwrapped interferogram. Fig. 5.7 shows the result of this analysis. From top to bottom the figure shows the topographic profile, the displacement gradient, unwrapped LOS displacement and the original phase. Pre-existing faults appear as steps in the topography. It is noteworthy that the majority of the faults are westwards dipping. If slip occurred, the displacement gradient exhibits a sharp minimum or maximum for westwards and eastwards movement respectively. I inverted the profile of the LOS displacement to match the topography. A positive signal therefore indicates uplift and a negative signal subsidence. Slip on faults appears as step. I differentiate between pre-existing faults which slipped during the intrusion (yellow), slip without a pre-existing surface fault (dark grey) and pre-existing faults which did not slip (light grey). The image shows that all of the pre-existing faults at the centre of the rift have been reactivated during the intrusion (yellow). I also found slip signals which are not related to any surface breaking faults (dark grey). I interpret these signals as slip on buried faults which either have not yet broken the surface or

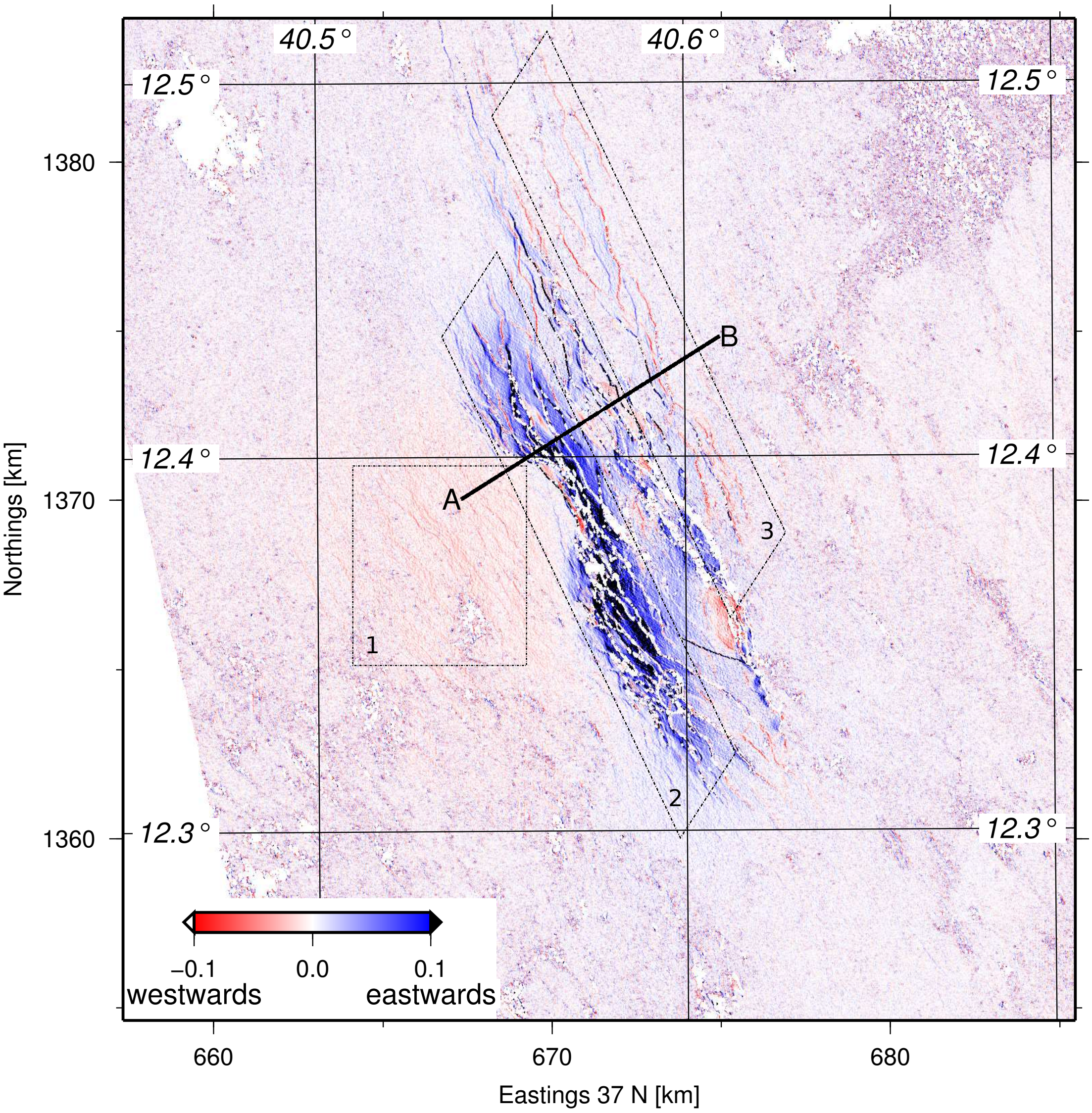

Figure 5.6: Gradient calculated in E-W direction of the LOS displacement of the October 2008 dyke intrusion. Slip along faults is visible as thin lines of larger gradient changes. Slip in westward direction is marked in red and eastwards slip in blue. The holes along fault scarps at the centre of the deformed region are a result of the unwrapping process. Box 1: area of flank uplift, box 2: transition from uplift to subsidence, box 3: clear fault slip signal. Line position of profile shown in figure 5.7.

have been resurfaced during previous volcanic eruptions. At the western flank I did not observe any slip on the pre-existing faults (light grey).

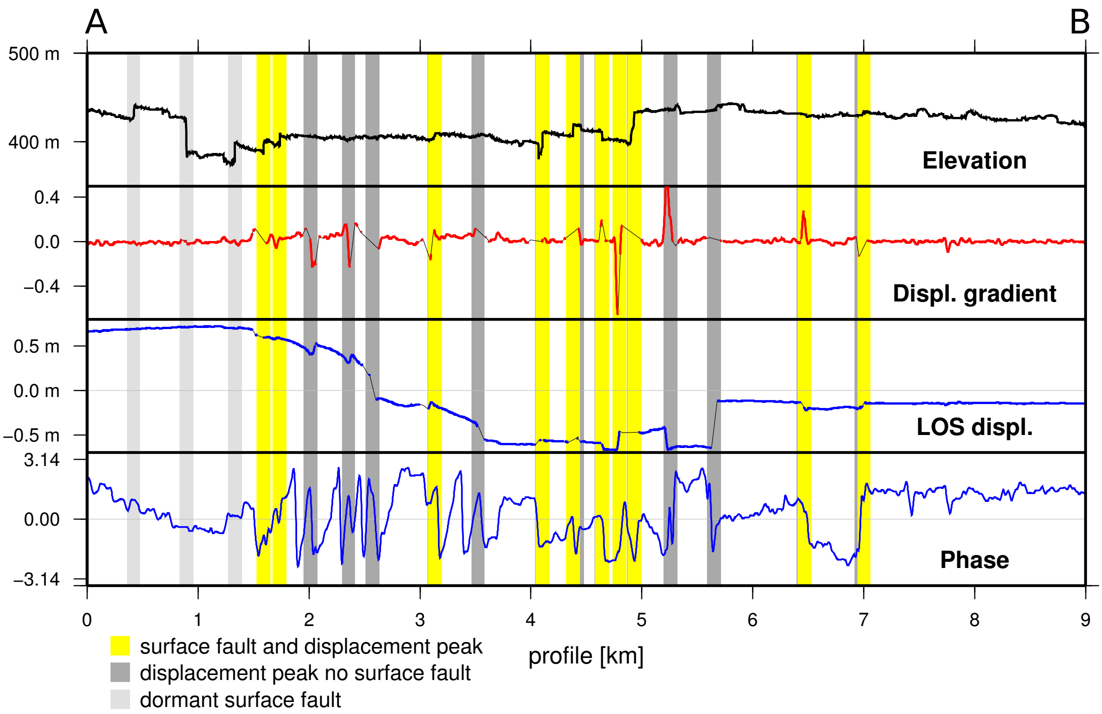

Figure 5.7: Comparison between topography and displacement signals.Top row: topography; second row: displacement gradient calculated in E-W direction in red; third row: unwrapped LOS displacement profiles; bottom row: wrapped phase. Yellow vertical lines mark faults reactivated during the October 2008 dyke intrusion. Dark grey vertical lines mark slip without a surface fault (slip on buried fault). Light grey vertical lines mark pre-existing faults which did not slip during the October 2008 intrusion. Location of the profile marked on figure 5.6.

5.2.2 Extraction of fault slip in LOS

The LOS displacement surface can be treated like a DEM. The horizontal resolution of the displacement data is lower (20 x 20 m^2) but slip on a fault presents itself as a step similar to a fault scarp in the DEM (Fig. 5.7 LOS displacement profile). This allowed me to adjust my algorithm (§ 3) to extract fault slip in LOS from the displacement data. Instead of topographic profiles extracted from the high-resolution LiDAR, I extract LOS displacement profiles from the unwrapped interferogram and optimise the parameter for the larger pixel size and slightly different signal shape. The only difficulty with the displacement data is caused by the data holes along some fault scarps (Fig. 5.4 bottom). These holes are introduced during the unwrapping process. The standard unwrapping procedures expects that the phase changes slowly and smoothly (e.g. Ghiglia and Pritt, 1998) but slip on a fault causes an abrupt phase change. If this change is too large it forms a discontinuity in the interferogram at which the displacement is undefined. To be able to derive fault slip for all the faults I pad the holes in the phase using the relationship between the wrapped and the unwrapped phase. The unwrapped phase, Ψ, is defined as (e.g. Ferretti et al., 2007)

$$.\Psi = \Phi + 2\pi\, n \tag{5.1}$$

where n is the integer number of cycles to be added to each pixel of the wrapped phase, Φ. I included a subfunction into my algorithm which checks if the displacement profile includes any holes. If this is the case I determine n for the two points at either side of the hole with

$$n = (\Psi - \Phi)/2\,\pi \tag{5.2}$$

I then choose the smaller value for n to calculate Ψ for the hole from the wrapped interferogram with equation 5.1. Once the holes are padded I apply my algorithm to extract the slip in LOS. The chosen parameters to extract the LOS displacement are listed in table 5.1. Due to the lower resolution of the interferogram (20 x 20 m^2) I increased sm, fpw and hpw (Table 5.1). This also means that small-scale features ($\leq$40 m) of the faults (§ 3.2) can be ignored. The measurement of the slip in LOS is mainly affected by random noise in the data, which results in the slightly broader scatter of measurements in the incremental $d-L$ profiles compared to the cumulative $d-L$ shape derived from the LiDAR data. I will show data examples in § 5.2.4.

Search margin	sm	80 m
Footwall plain width	fpw	50 m
Hangingwall plain width	hpw	60 m
Minimum significant vertical offset	v_{min}	0.3
Maximum tolerated vertical offset	v_{max}	0.7
Maximum tolerated fissure opening	fw	40 m
Profile spacing		20 m and 5 m
rloess window size		10 points

Table 5.1: Chosen algorithm parameters to extract slip in LOS from ALOS InSAR data. Refer to § 3.4.1 for a detailed description of these parameters.

5.2.3 Conversion of fault slip in LOS to incremental throw

I cannot derive incremental throw directly from the ALOS data but I can convert the slip in LOS or range change, r, into throw, t, assuming I know strike and dip of the faults. The range change, r of a point on one side of a fault, relative to a point on the other side, is defined as

$$r = -\vec{u} \cdot \hat{l} \tag{5.3}$$

where $\vec{u}$ is the fault slip vector and $\hat{l}$ is the unit vector in LOS pointing from ground to satellite. Assuming that the slip direction of the faults is down-dip and, perpendicular to strike $\vec{u}$ can be expressed through

$$\vec{u} = s\,\hat{u} \tag{5.4}$$

where s is the magnitude of the slip vector. Using equation 5.4 the range change, r, can be written explicitly as

$$r = s(\hat{u}_x\hat{l}_x + \hat{u}_y\hat{l}_y + \hat{u}_z\hat{l}_z) \tag{5.5}$$

and throw, t, can be estimated with

$$t = s\,\hat{u}_z \tag{5.6}$$

The directional unit vectors of $\hat{l}$ are defined as (e.g. Hanssen, 2001)

$$\begin{aligned} \hat{l}_x &= -sin(\Theta - 270)\,sin(\gamma) \\ \hat{l}_y &= -cos(\Theta - 270)\,sin(\gamma) \\ \hat{l}_z &= cos(\gamma) \end{aligned} \tag{5.7}$$

with the incidence angle γ and the azimuth Θ of the satellite. The azimuth and incidence angle for track 599 at the location of the dyke are Θ = -12.26° and γ=37.3° respectively. The components of $\hat{u}$ are

$$\begin{aligned} \hat{u}_x &= sin(strike + 90)\,cos(dip) \\ \hat{u}_y &= cos(strike + 90)\,cos(dip) \\ \hat{u}_z &= sin(dip) \end{aligned} \tag{5.8}$$

In figure 5.8(top) I plotted the amount of throw, calculated for 1 m of LOS range change, for the full range of dip (0-90°) and strike (0-360°) angles. It shows that for faults with a dip <50° the estimated throw can vary greatly with strike. The set of red curves, which exhibit a maximum for a dip of 40° correspond to faults with a slip direction close to the LOS of the satellite (dip $\approx \gamma$, strike $\approx \Theta$, 310-360°). For slip on faults with a dip >50° the direction of strike is less important.

At the Dabbahu rift segments the majority of the faults strike at 148° and 328° (see § 4.2.3). In figure 5.8-bottom I show the estimated throw for faults striking at ±20° of the average strike for west- and eastwards dipping faults. For a dip of 60° the calculated throw ranges from 1.92-2.24 m for eastwards dipping faults and from 0.87-0.97 m for westwards dipping faults. The range decreases with increasing angles for dip. I fixed the dip angle at 65°, which is reasonable for the subvertical faults at the rift and strike at 150° for west dipping faults and -30° for east dipping faults. Inserting the appropriate values into equation 5.6 throw can be estimated by

$$t_w = 0.94\,r \tag{5.9}$$

$$t_e = 1.90\,r \tag{5.10}$$

5.2.4 Cumulative vs. incremental fault slip

I have chosen two neighbouring fault arrays north of the AVC to show and discuss fault growth observed throughout the rift segment. Figure 5.9 gives an overview of the geometry and geologic setting of the array. In the top left panel I show the hill-shaded coloured DEM for reference. In the top right panel I plotted the colour-coded cumulative throw, extracted from the 2009 high-resolution LiDAR DEM on top of the geological map of the region (Vye-Brown et al., 2012). The array is partly located within the most recent lava flows (dark blue). The bottom left panel exhibits the gradient of LOS displacement and the bottom right panel shows the colour-coded incremental throw caused by the October 2008 intrusion on top of the geological map. I derived both the cumulative and the incremental throw through the application of my algorithm.

The array is ∼10 km long and up to ∼2 km wide. It is formed by 16 mainly westwards dipping fault segments that are undergoing different stages of soft linkage. The northern half of the array is formed by a collection of diverging splay faults which

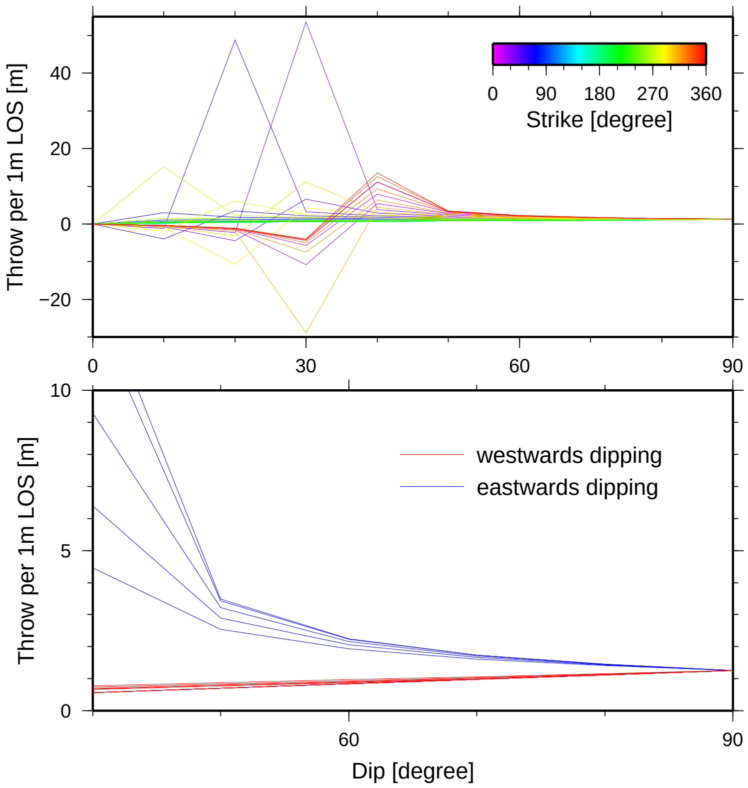

Figure 5.8: Influence of strike and dip of faults on throw estimates from LOS displacement. Top: Throw estimated for 1 m of LOS displacement vs. dip angle. Lines are colour coded for strike ranging 0-360° of strike. Bottom: Throw estimated for the fault strike found at the Dabbahu segment. Blue east dipping with strike 330° ±20° and red west dipping with strike 140° ±20°.

join the main fault structure at the points E and F in figure 5.9. The main structure of the fault array is marked by the points C-G in figure 5.9. A second smaller array of eastwards dipping faults is located to the east of the main structure and joins the array at the points K and H.

In the following section I will present the cumulative and incremental $d - L$ data of the array and discuss the results in terms of overall fault development.

1. Segment activation

   Towards the southern end of the array a short fault (Fig. 5.9 G-L) cuts across the horst connecting the west and eastwards dipping fault segments of the array and creating a small lens shaped horst block marked by the points G-L-M-H-G in Fig. 5.9. The fault segments surrounding the block are the westwards dipping segments L-G and G-H and the eastwards dipping segments L-M and M-H The displacement gradient (Fig. 5.9 bottom left) clearly shows that no slip occurred

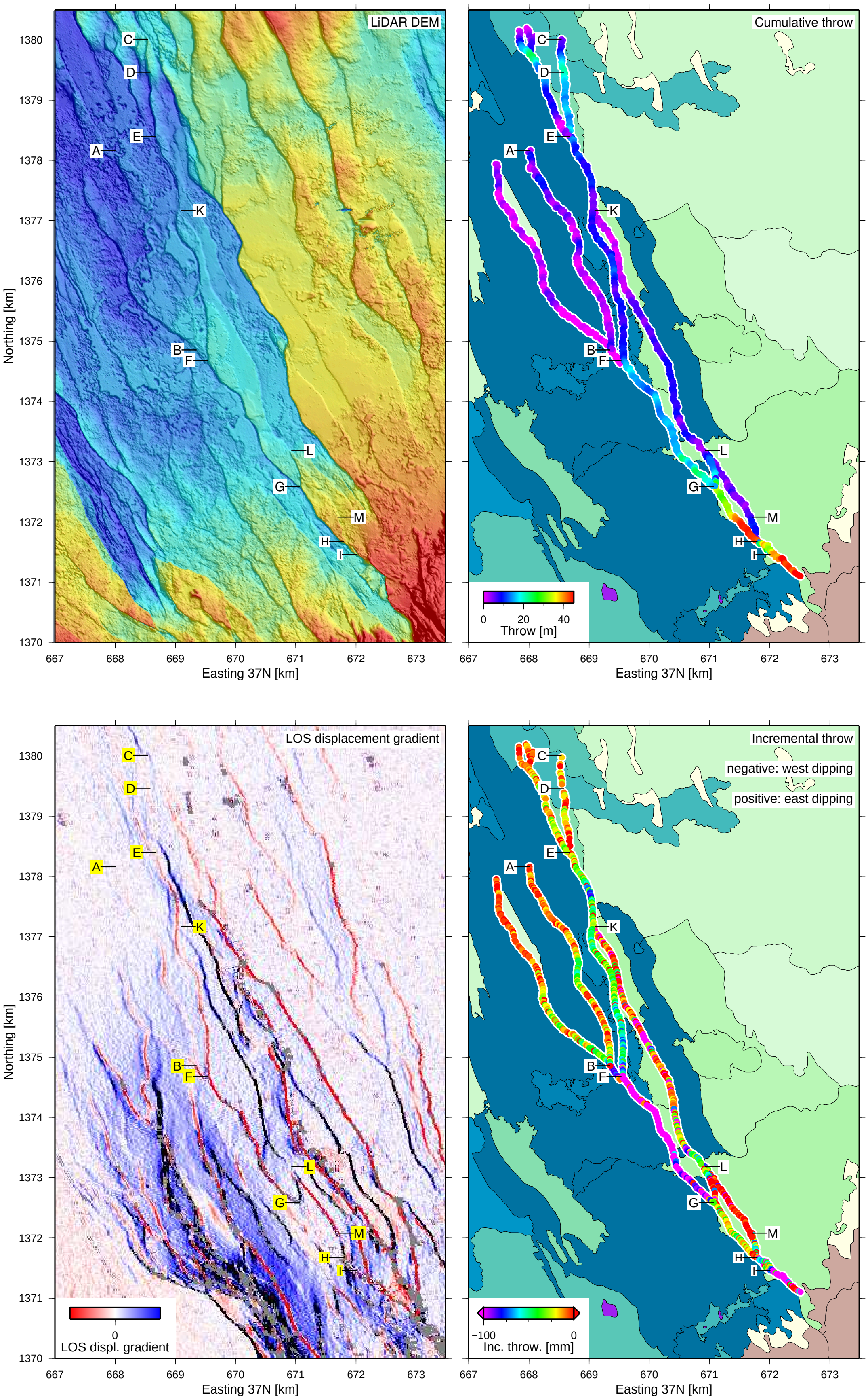

Figure 5.9: Fault array activated during the October 2008 dyke intrusion. Top left: LiDAR DEM; top right: colour-coded cumulative throw on top of geological map after Vye-Brown et al. (2012) BGS©NERC; bottom left: LOS displacement gradient; bottom right: colour-coded incremental throw from the October 2008 dyke intrusion on top of the geological map. Key for geological map is given in figure 4.2.

on the westwards dipping segment G-H but instead it shows that the slip towards the west occurred on the smaller eastwards dipping segment L-M.

2. Total cumulative vs. incremental throw

   Figure 5.10 shows the comparison between the cumulative $d - L$ distribution and the incremental $d - L$ profile along the array. The top panel shows the array plotted parallel to strike. The individual fault segments are colour-coded. The middle and bottom panels present the cumulative and incremental throw respectively. I plotted the $d - L$ shapes individually for each segment and the total $d - L$ shape of the array in grey. The total cumulative throw of the array is roughly bowl shaped with larger throw at either end of array (~45 m and ~55 m). The central 6 km exhibit small scale corrugation varying throw between ~20-30 m. I attribute this unusual throw distribution pattern to resurfacing. As shown in figure 5.9 the central part of the array is set within the most recent flood basalts. The total incremental throw distribution shows that the majority of the fresh throw was accumulated along the last 5 km of the profile. It is dominated by slip on the on the long eastwards dipping fault segment (brown).

3. Maintenance of fault segmentation

   I compared the cumulative $d - L$ shape of the main fault structure with its incremental $d - L$ profile (Fig. 5.11-blue). The cumulative $d - L$ profile (centre panel) exhibits multiple minima and maxima. This small-scale corrugation is commonly observed in $d - L$ profiles for normal faults (e.g. Manighetti et al., 2001, Cowie and Roberts, 2001, Peacock, 2002). The pattern is usually associated with fault segmentation and the early stages (soft linkage) of fault linkage (e.g. Peacock and Sanderson, 1991, Cowie and Roberts, 2001). Published models of fault growth by linkage propose, that once two fault segments form one through-going fault, new slip is accumulated at the former linkage zone reducing and eventually eliminating the displacement deficit (e.g. Peacock and Sanderson, 1991, Trudgill and Cartwright, 1994, Cartwright et al., 1995, Willemse et al., 1996, Crider and Pollard, 1998, Gupta and Scholz, 2000, Peacock, 2002).

   The main fault segment (blue) of the array is hard-linked across its entire length. I marked the local minima in the cumulative $d - L$ profile with dashed vertical

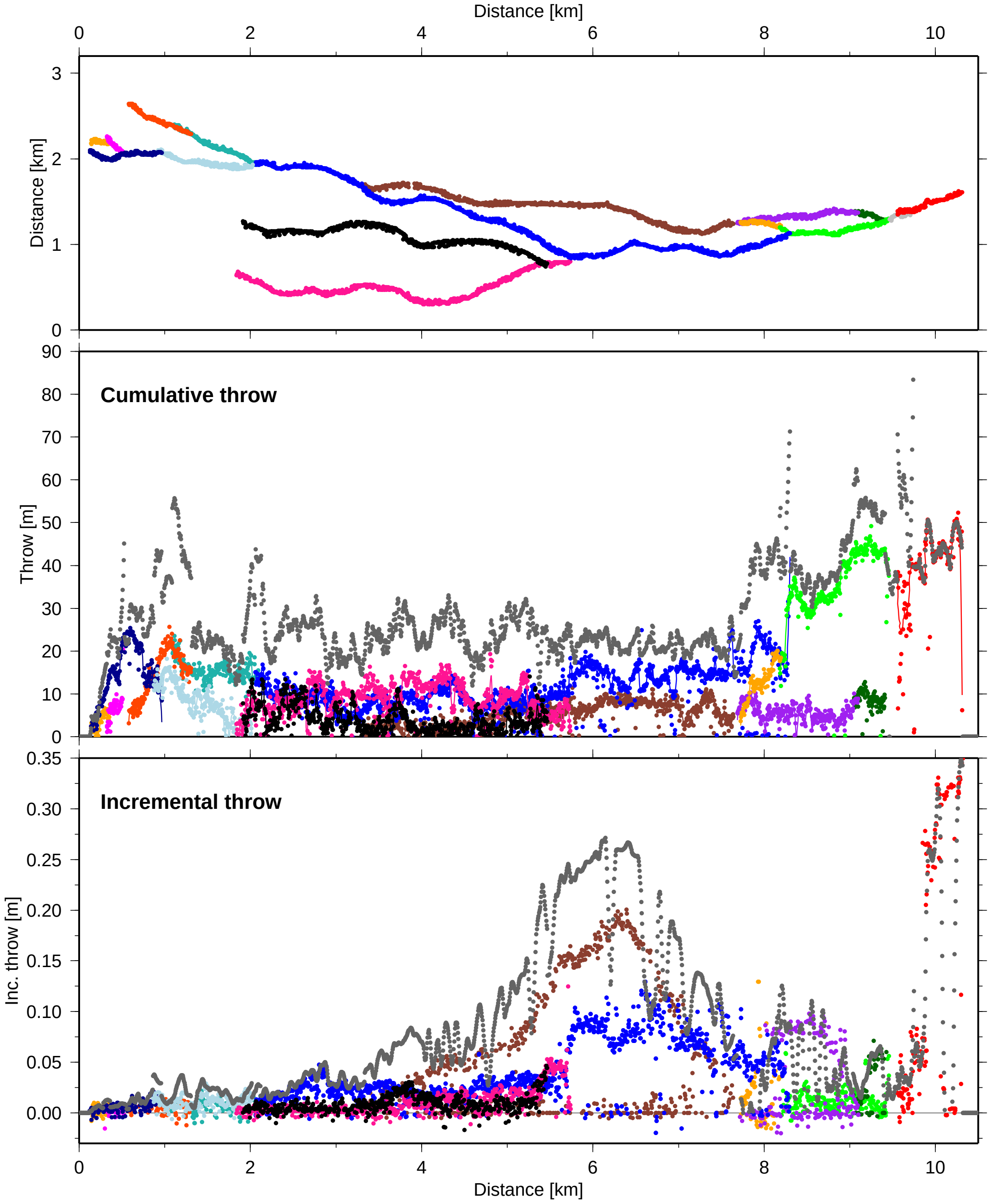

Figure 5.10: Total cumulative vs. incremental throw. Top: Fault array plotted parallel to strike. Middle: Cumulative throw, Bottom: Incremental throw. Colours relate to the individual fault segments. Total throw is marked in grey.

lines (Fig. 5.11-middle). The minima roughly correlate with step changes rather than maxima in the incremental $d-L$ profile (bottom). The step change is most pronounced at the fourth minimum where the incremental throw increases from ∼2.5 cm to ∼10 cm. This suggests that fault segments maintain the ability to slip independently even after the segments are physically linked. This behaviour has previously only been observed during analogue modelling of normal fault growth (Mansfield and Cartwright, 2001).

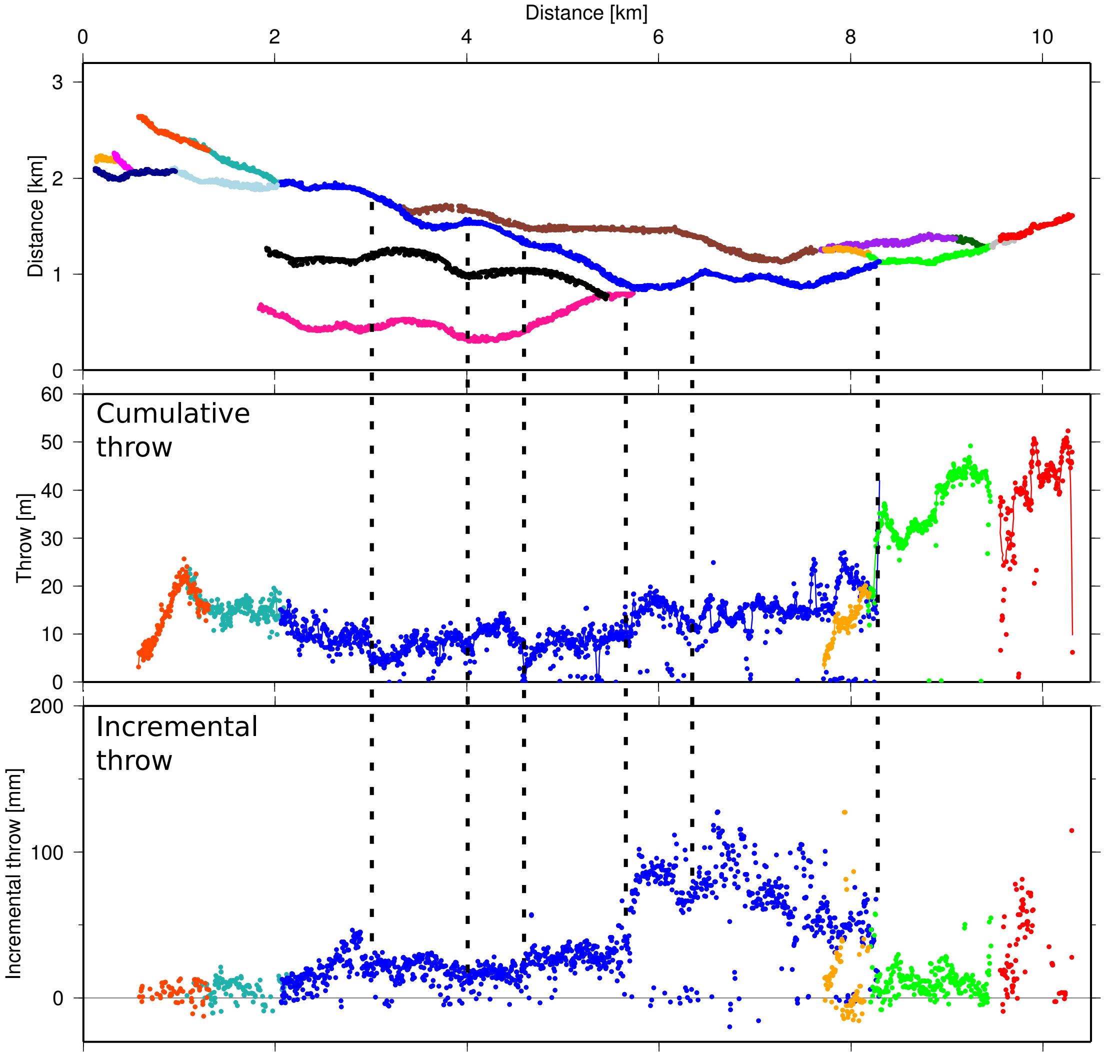

Figure 5.11: Comparison of cumulative (middle panel) and incremental (bottom panel) $d-L$ shapes of the main fault segment (blue) of the array. Top panel shows the surface traces of the fault segments forming the array. Segments are colour-coded and correlate to the $d-L$ profiles. Dashed lines mark local minima of the cumulative $d-L$ pattern which correlate with step changes in the incremental $d-L$ shape.

4. Slip on a buried fault

The displacement gradient (Fig. 5.9 bottom left) shows a faint, but distinct line indicating displacement between the points A and B. I closely examined the LiDAR DEM (Fig. 5.9 top left) and could not identify a clear fault scarp between the two points - only a small monocline is present. I mapped the apparent fault trace from the displacement gradient and applied my algorithm. The incremental $d - L$ profile exhibits throw of up to 4 cm (Fig. 5.12 bottom). The cumulative $d - L$ profile illustrates that currently no surface break exists. Significant apparent throw is only present in the first half of the cumulative $d - L$ profile and it is caused by lava flow edges (Fig. 5.12 middle). Due to its setting within the area of most recent resurfacing it is most likely that the slip occurred at a fault buried during a previous eruption.

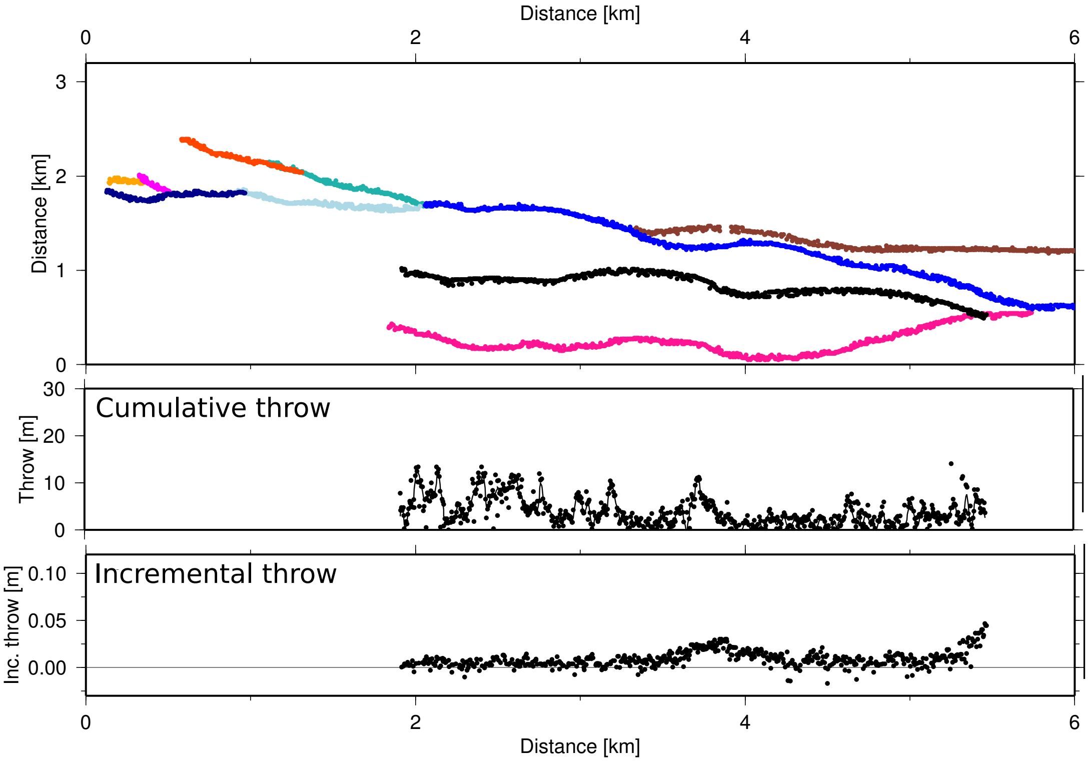

Figure 5.12: Example of slip on buried fault (coloured black). Top: Surface traces of the fault segments forming the array. Segments are colour-coded and correlate to the $d - L$ profiles. Middle: Cumulative $d - L$ profile. The signal in the first half is caused by the edges of a lava flow. Bottom: Incremental $d - L$ shape.

The second array (Fig, 5.13) is situated to the east of the first array. It is formed by 9 fault segments. The main structure exhibits throw of more than 40 m. At its northern end it separates into a 4 diverging splay faults (A). It is currently hard linked across the splay furthest to the east. At the points B and C the fault is hard linked. At point B the remnants of the fault ramp have been covered by a lava flow but at point C the broken ramp is visible at the hangingwall (Fig. 5.14).

At both linkage zones, faults with considerably less throw (max throw 2-3 m) join the main structure. At linkage B the small structure is also westwards dipping. From the LiDAR data alone it appears as if this structure is the fault tip of the rear fault segment. Usually these fault tips are thought to become inactive after fault linkage has occurred (e.g. Trudgill and Cartwright, 1994, Crider and Pollard, 1998). The structure can be traced for over ∼4 km. The gradient map of the LOS displacement also shows a very clear signal of fault slip on this structure. In fact the majority of the new throw on this array was accumulated on this structure (∼10 cm). I have observed this behaviour on multiple locations at the Dabbahu segment. The smaller fault joining at linkage C is eastwards dipping and was also activated during the intrusion.

I extracted incremental throw for all of the faults of the fault data set (§ 4.2). Figure 5.15 shows that the largest throw is located on two structures at the eastern margin of the rift segment. Maximum throw of 1.1 m is found within the ryholites of the AVC. East of these structures hardly any slip occurred. To the west in an area ∼4-5 km wide, most faults have been re-activated during the intrusion. Throw on the re-activated faults ranges from 5-40 cm. In the South the area of fault activation comes to a sharp end perpendicular to the rift axis. In the North the end of the activation zone is not as clear due to the limited number of faults at the rift centre due to resurfacing.

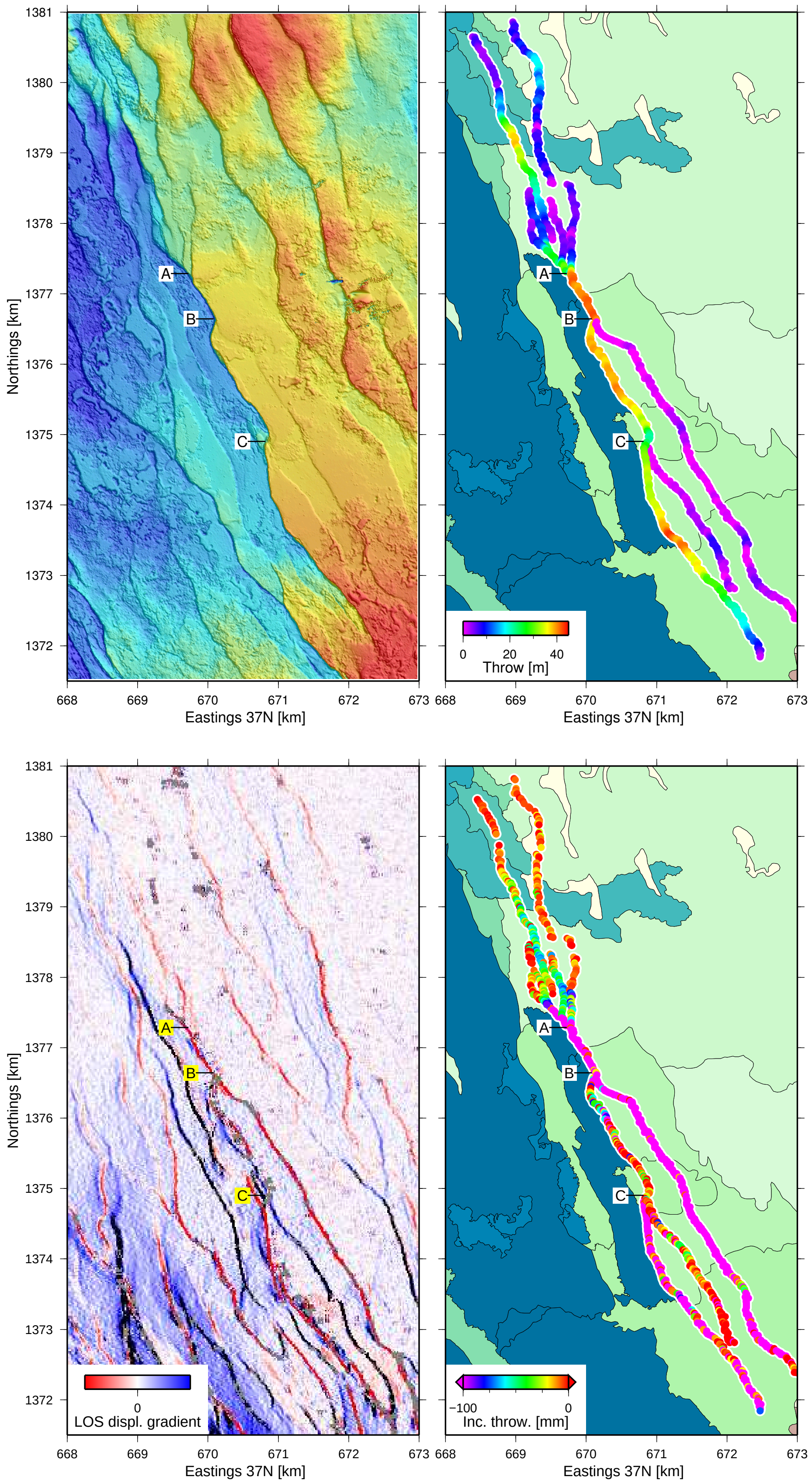

Figure 5.13: Fault array activated during the October 2008 dyke intrusion. Top left: LiDAR DEM, top right: colour-coded cumulative throw on top of geological map after Vye-Brown et al. (2012) BGS©NERC, bottom left: LOS displacement gradient, bottom right: colour-coded incremental throw from the October 2008 dyke intrusion on top of the geological map.

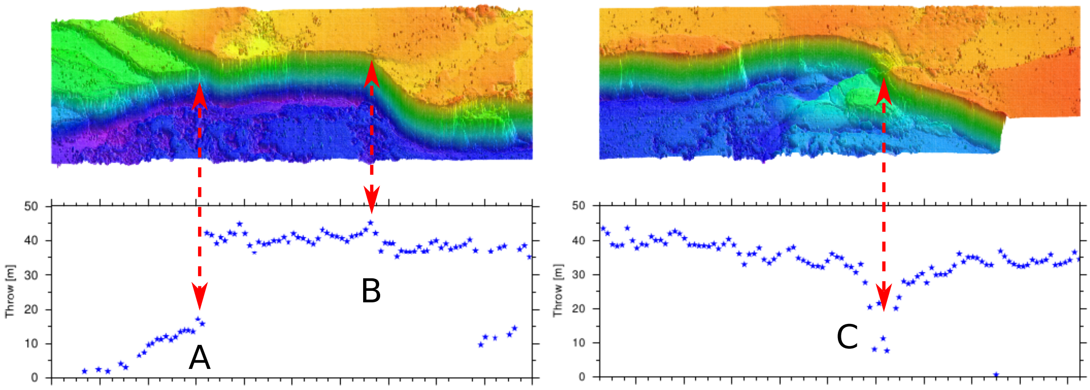

Figure 5.14: Details of the two hard linked linkage zones of figure 5.13. Top: close up of the linkage zone, bottom: section of the cumulative $d-L$ shape. Left: Linkage B, the fault ramp is covered by a lava flow. On the footwall a small offset between the throw on the segment either side of the linkage zone exist. Right: Linkage C: The broken ramp remained at the hangingwall. The large deficit in throw is caused by the remnants of the ramp.

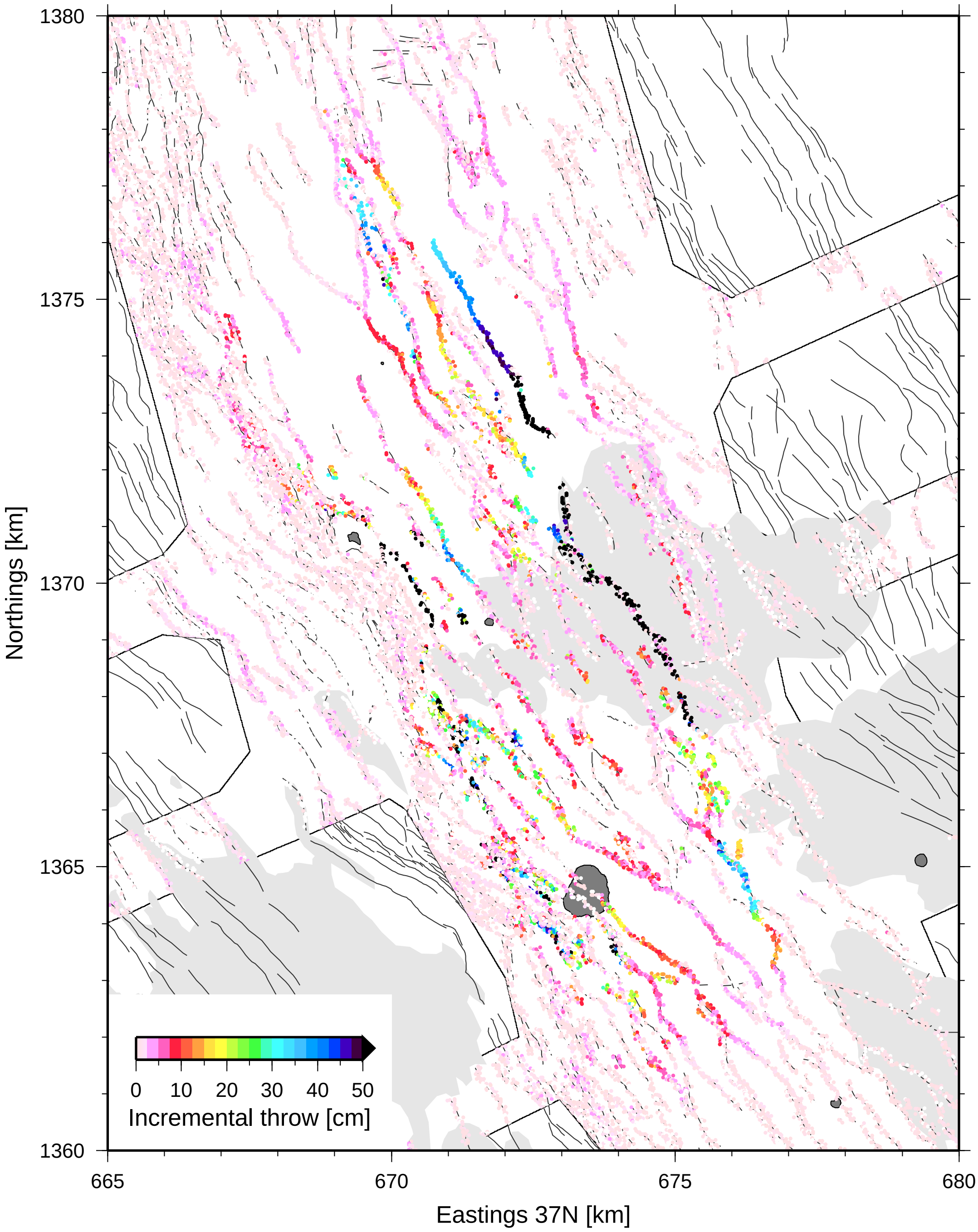

Figure 5.15: Map of incremental throw derived from InSAR. Throw measurements are colour coded. The colour scale extends to 50 cm slip but slip of up to 1.1 m (black) occurred at the eastern flank.

5.3 Incremental fault slip from differential LiDAR

The analysis in this section is based on displacement data, derived from the two high-resolution LiDAR surveys, which cover the May 2010 dyke intrusion.

5.3.1 Determination of difference between LiDAR surveys

In § 2.1.5 I described the procedure to create a DEM from scattered data points using natural neighbour interpolation. Each data point is used during the interpolation and therefore the distribution of points affects the DEM. The return distribution of airborne LiDAR surveys depends on flight altitude, yaw, pitch and roll of the aircraft (§ 2.1). DEMs of the same area but derived from different point clouds will therefore always exhibit small discrepancies even if the scanned surface remains unchanged. To estimate the magnitude of these discrepancies I created two DEMs with 0.5 x 0.5 m^2 pixel size, for a small area from two adjacent tracks of the 2009 LiDAR survey. I then calculated the difference between them by simply subtracting one DEM from the other pixel by pixel. The difference between the two DEMs, which is caused only by the different distributions of returns is shown in figure 5.16. The figure presents a close-up of an area of 50 x 50 m^2 (top) and a larger area of 500 x 500 m^2 covering multiple fault scarps (bottom). Across flat or smoothly varying surfaces the differences are small (Fig. 5.16-top) but for areas with sharp edges caused for example by faults and fissures (Fig. 5.16-bottom) the differences are significant. The introduced apparent vertical differences on individual pixels is up to 2 m. The apparent vertical difference reduces for lower resolution DEMs but remains a factor especially along the sharp edges of fault scarps. Furthermore by differencing two DEMs any horizontal change is translated into a vertical change introducing additional errors.

These errors become important when comparing data from surveys before and after an intrusion event. To reduce them I use the Iterative Closest Point (ICP) algorithm developed by Nissen et al. (2012), which is applied directly to the data point clouds. The ICP method was first developed by Besl and McKay (1992) and Chen and Medioni (1992). The basic principle is that points on the ground do not displace individually but that points within a small region all move in the same way. In terms of the ICP algorithm this means that a small subset of the original three-dimensional data set

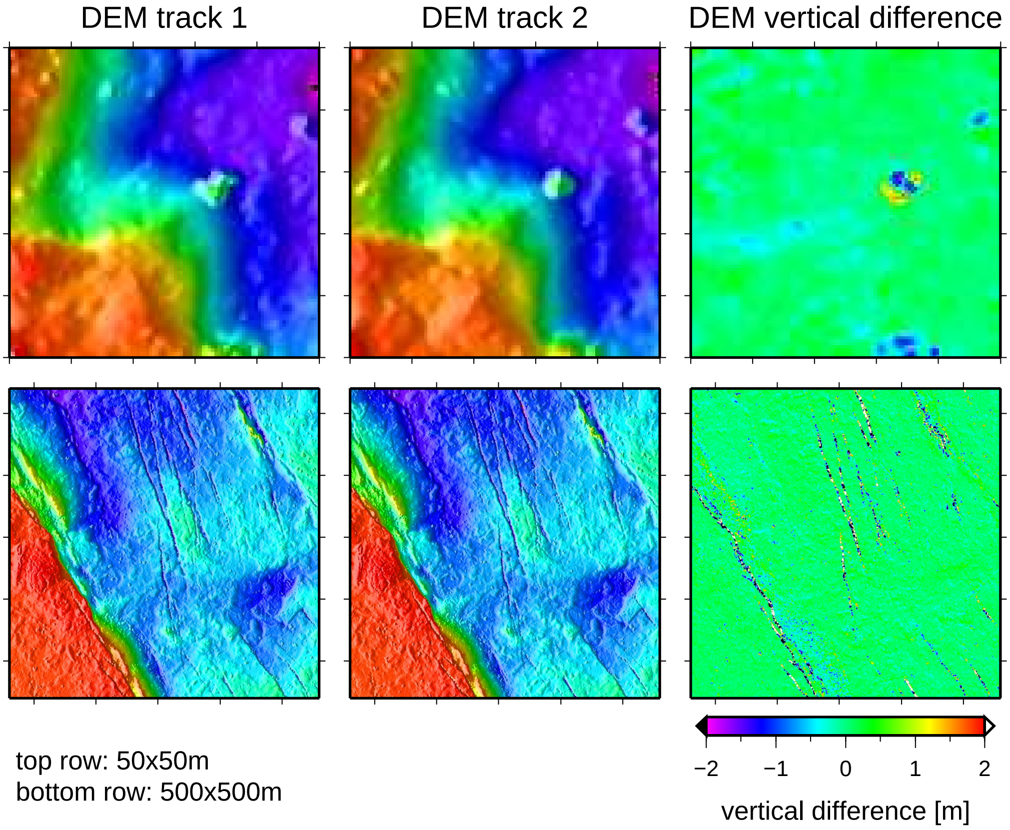

Figure 5.16: Simple differencing of two 0.5 x 0.5 m^2 DEMs created from adjacent tracks of the 2009 LiDAR survey. First and second column DEM of the two adjacent LiDAR tracks. Third column vertical difference between the two DEMs. Top row area covers 50 x 50 m^2, bottom row area covers 500 x 500 m^2.

('source') can be transformed into the later ('target') data set by multiple rigid body transformations consisting of rotation and translation. The best fitting transformation for each data subset, is determined by a three step iterative process. Fig. 5.17 illustrates the individual steps. 1) Each source point is paired with its closest target point. 2) The transformation which minimises the mean square error (MSE) of the paired points is calculated. 3) The transformation is applied to the source points and the process is repeated until MSE cannot be further reduced or a threshold is met. The advantage of the ICP algorithm is that it not only resolves vertical displacement but also horizontal displacement. The sum of translations in x, y and z directions over all iterations corresponds to E-W, N-S and vertical displacements (Nissen et al., 2012).

The size of the data subsets or windows into which the data are divided depends mainly on the survey with the lower return density. For my analysis of the displacement at the Dabbahu rift I found that splitting the LiDAR point clouds into 25 x 25 m^2 windows provides good results. This corresponds to ∼200 and ∼650 returns per window for the 2009 and 2012 data set respectively.

In figure 5.18 I compare the vertical displacement derived through DEM differencing (left) and the application of the ICP algorithm (right). To ensure a fair comparison I calculated the DEM difference from 25 x 25 m^2 DEMs of the LiDAR surveys, which I created using the procedure explained in § 2.1. The overall signal is similar but the random noise is more prevalent in the vertical displacement derived through DEM differencing. The differences between the two methods are particularly clear along the fault scarps. The DEM difference exhibits diffuse displacement across ∼5 pixels along the scarps where the ICP algorithm shows a distinct displacement across ∼2 pixels. The irregular shaped feature with apparent displacement of < 2 m is the northern tip of the small lava flow, which accompanied the May 2010 intrusion.

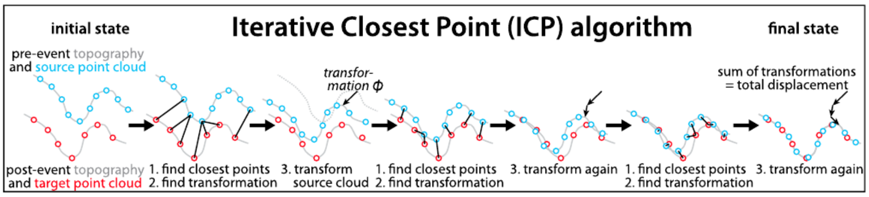

Figure 5.17: Illustration of the processing steps of Iterative Closest Point algorithm. 1) Pair each 'source' point with its closest 'target' point. 2) Determine best fitting transformation. 3) Apply transformation to source points and repeat from 1. Reprinted from Nissen et al. (2012) with permission from John Wiley and Sons.

5.3.2 Displacement caused by the May 2010 intrusion

Between the first LiDAR survey in 2009 and the second survey in 2012 only one dyke intrusion occurred, in May 2010. Seismic activity commenced on 20.05.2010 in the southern part of the rift (approx Northing 1360 km UTM zone 37 N) at a depth of 6±1 km and rapidly progressed upwards to about 2 km depth (Fig. 5.19). After a short break the seismicity migrated simultaneously towards the South and the North, following a pattern typical for the injection of magma (e.g. Rubin, 1992, Ebinger et al., 2008). In the southern part the seismicity remained deeper and was more diffuse. At

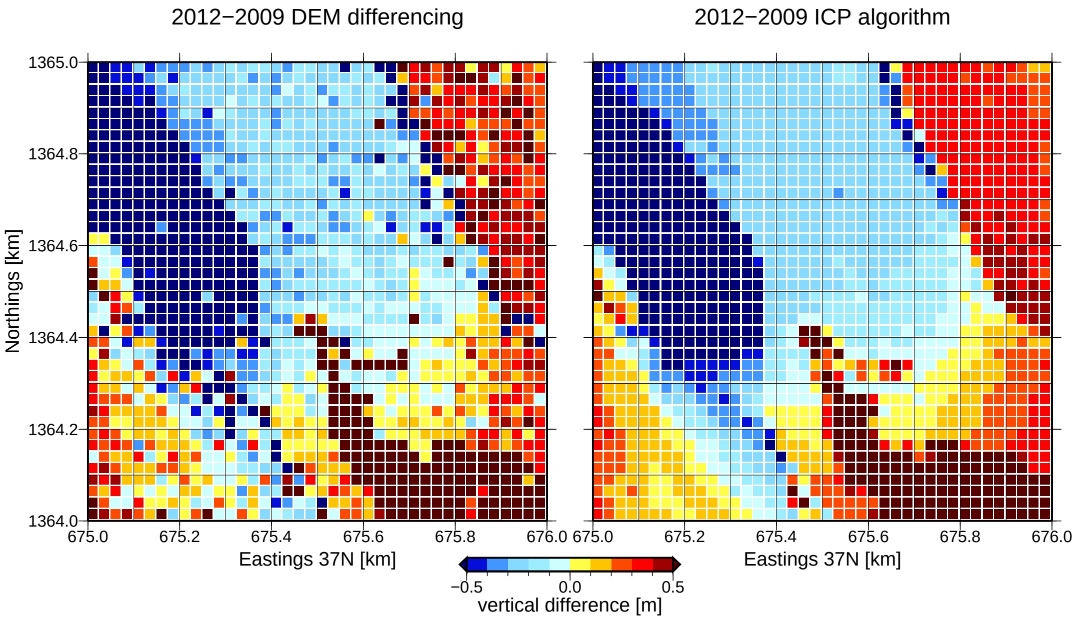

Figure 5.18: Comparison of vertical displacement estimated by pixel by pixel DEM differencing (left) and the ICP. algorithm (right). Pixel size in both images 25 x 25 m^2. The data sets are described in § 2.1

the AVC seismicity migrated further upwards to a minimum depth of 1 km (personal communication Derek Keir). The May 2010 intrusion was one of the smaller dyking

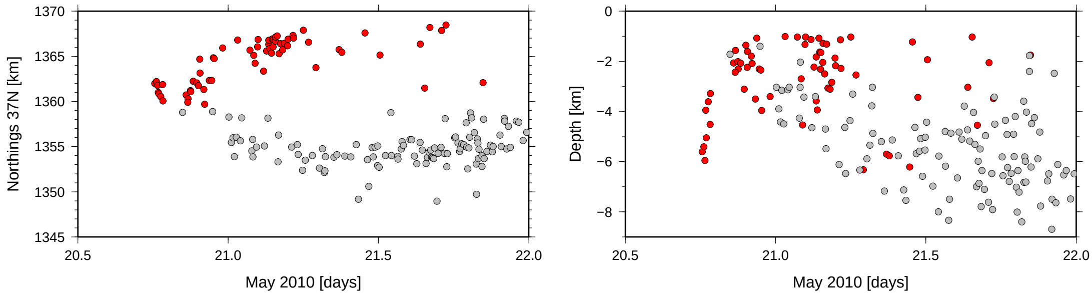

Figure 5.19: Seismicity of the May 2010 dyke intrusion from local seismic network. Left: North-South migration of seismicity over time. Right: Depth migration of seismicity over time. Red seismicity north of Northing 1360 km UTM zone 37 N, grey seismicity south of Northings 1360 km UTM zone 37 N. (Personal communication Derek Keir)

events. Elastic dislocation modelling from ENVISAT data estimated a maximum dyke opening of 1.6 m close to the surface (0-2 km depth, Fig. 5.20 black arrows) at the Ado'Ale Volcanic complex (personal communication Ian Hamling).

I applied the ICP algorithm to the complete area of overlap of the two LiDAR surveys and compared the displacement data with the modelled dyke. Figure 5.20 shows the

vertical (bottom), E-W (middle) and N-S (top) displacement. The displacement signal is clearest for the vertical component. Displacement on the two horizontal component is noisier and especially the N-S component shows striping associated with individual flight tracks of the surveys.
The displacement data shows the characteristic signal of central subsidence and flank uplift above and horizontal opening perpendicular to the shallow part of the dyke intrusion. The maximum displacement in each direction is approximately 1 m. The area south of the AVC, where the dyke remained at deeper depth (4-10 km, grey arrows), is broadly uplifted (∼0.3 m) but no subsidence occurred. The small isolated patch of apparent uplift in the far south is caused by sediment influx on a floodplain of a small river.

As I stated in § 2.1 no ground control points exist in the survey area which could be used to verify the georeferencing of the two surveys and subsequently verify the derived displacement data. To assess if significant georeferencing errors exist between the surveys, I analysed the displacement data away from the intrusion site (Fig. 5.21). The E-W and N-S displacement component (bottom row) exhibit mean offsets of 0.06±1.74 m and -0.08±1.48 m, respectively, which implies that the horizontal georeferencing is correct. The stripes of larger offsets are caused by the bias in the boresight roll angle of the Leica ALS-II sensor (§ 2.1.4). The vertical component shows a mean uplift of 0.17±0.35 m. Between 2006 and 2010 ∼ 25 cm of uplift was recorded in this region using InSAR data (Hamling et al., 2014). I therefore believe it is justified to assume that the uplift shown in my displacement data is real and not a result of misregistration.

5.3.3 May 2010 eruption

The lava flow of the eruption covers an area of less than 1 km^2 (Fig. 5.18). To bring out the geomorphology and estimate the erupted volume of the lava flow, I calculated the difference, pixel by pixel, between the 2009 and 2012 0.5 x 0.5 m^2 LiDAR DEMs using the ERDAS ERmapper software package. I chose to use DEM differencing for this analysis. The ICP method cannot be applied because the assumption that neighbouring surface points are deformed in the same way does not apply here. Also in comparison to the extent of the lava flow errors due to the return distribution of the

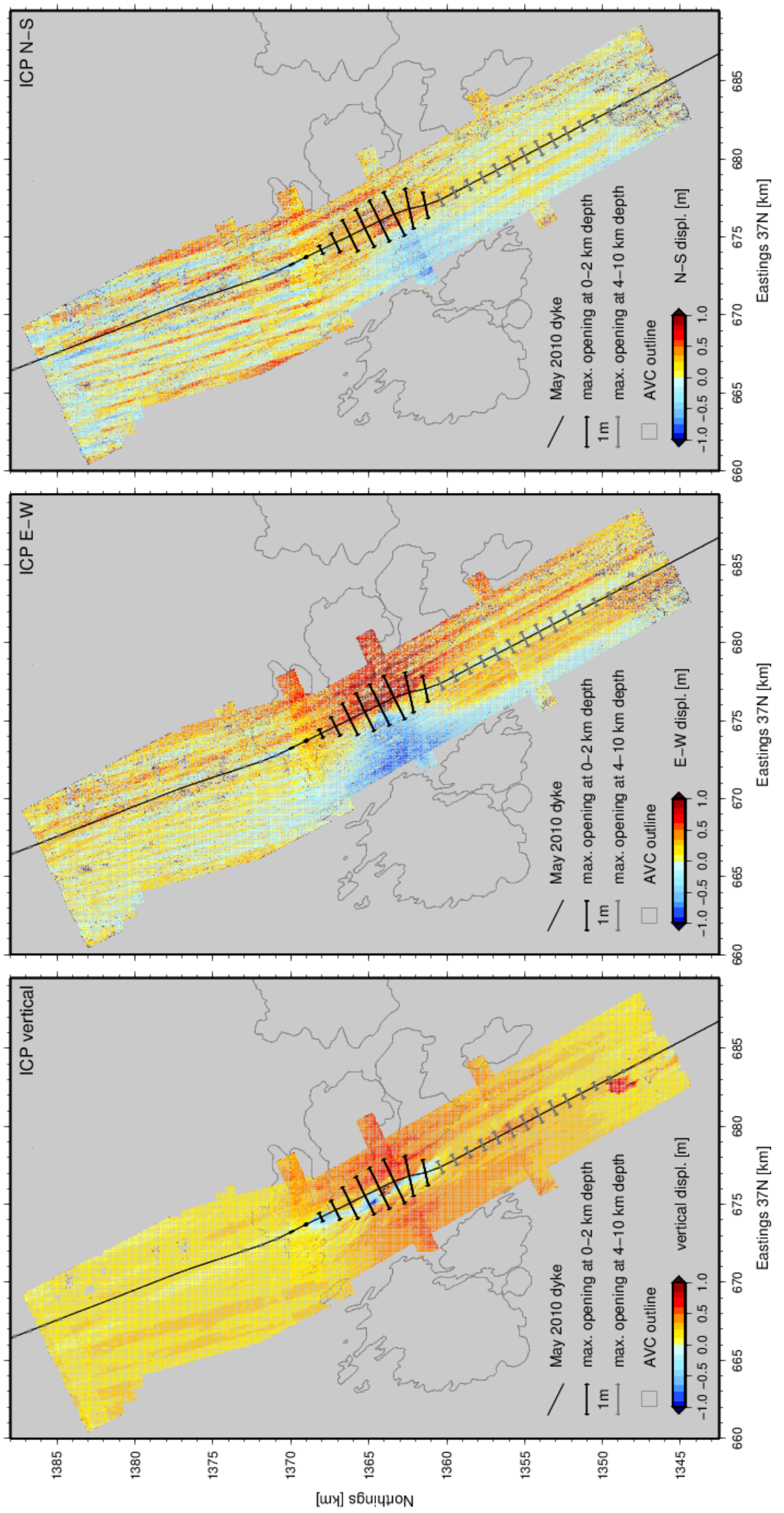

Figure 5.20: Surface displacement between the 2009 and 2012 LiDAR surveys. From left to right: vertical, East-West and North-South displacement. Black line position of the May 2010 dyke intrusion from elastic dislocation model based on ascending and descending ENVISAT interferogram (personal communication Ian Hamling). Arrows indicate maximum modelled dyke opening. Black arrows: maximum dyke opening at 0-2 km depth, grey arrows: maximum dyke opening at 4-10 km depth.

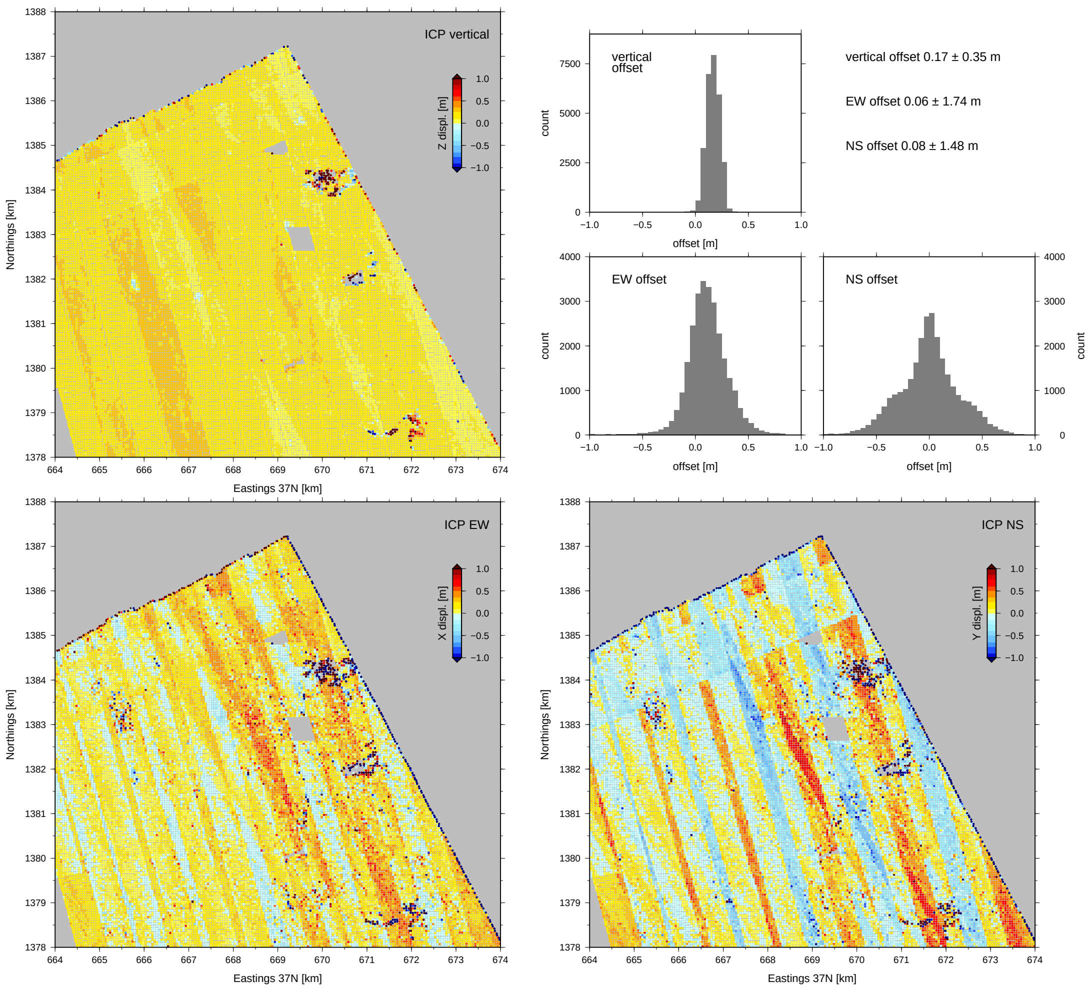

Figure 5.21: Analysis of displacement between the two LiDAR surveys, derived from ICP calculation, away from the May 2010 intrusion site. Top left: vertical offset; bottom left: East-West offset; bottom right: North-South offset. Top right: histograms of offset [m]. top: vertical offset (mean 0.17±0.35 m); bottom left: East-West offset (mean 0.06±1.74 m); bottom right: North-South offset (mean -0.08±1.48 m).

survey point clouds can be neglected.

Figure 5.22 (top) shows the difference between the two LiDAR DEMs. The main lava flow is located on top of a fault block. It exhibits a row of small scoria cones (∼30-40 m diameter) in the West. The flow appears to have propagated towards the east and south from the scoria cone. A second smaller flow is located at the hangingwall of the fault to the west of the main flow. From the topographic data it appears as if they are two separate flows. Also the surface of the second flow appears smooth, in comparison to the main flow, as a result of the hotter temperature during its emplacement (personal communication Talfan Barnie). The fault scarp also shows signs that two rock falls occurred. The debris are visible on top of the lava flow.

To estimate the extruded volume, I removed the background displacement by fitting a regression plane to the fault block hosting the eruption, excluding the new lava flow, and subtracting it from the displacement. The plane exhibits 20-30 cm of uplift and dips from SE to NW which is in agreement with the dyke induced flank uplift. The corrected image is shown in figure (Fig. 5.22 bottom). I then calculated the extruded volume for each pixel of the flow and estimated the total extruded volume to be 230,000±4,000 m^3, which is roughly 100 times smaller than the volume erupted in 2007 and 2009.

5.3.4 Observations of fault slip

In the following sections I will focus on the displacement at the AVC.

The vertical displacement (Fig. 5.23 top left) shows a narrow (∼1 km) zone of subsidence at the survey centre. The transition from subsidence to uplift is abrupt on its eastern side whereas the transition towards the west appears gradual. This gradual change exhibits an almost saw-tooth shaped pattern as it alternates between ramp-shaped displacement increases and sudden displacement decreases. In figure 5.23 (top right) I plotted the local fault network on top of the vertical displacement. The correlation between the sudden displacement decreases and the fault traces indicates fault slip and the displacement ramps suggest book-shelf faulting. The dark brown patch at the centre of the image shows the location of the small eruption that I discussed in § 5.3.3. The geometric locus of maximum horizontal opening (Fig. 5.23 bottom row) coincides roughly with the eruption site.

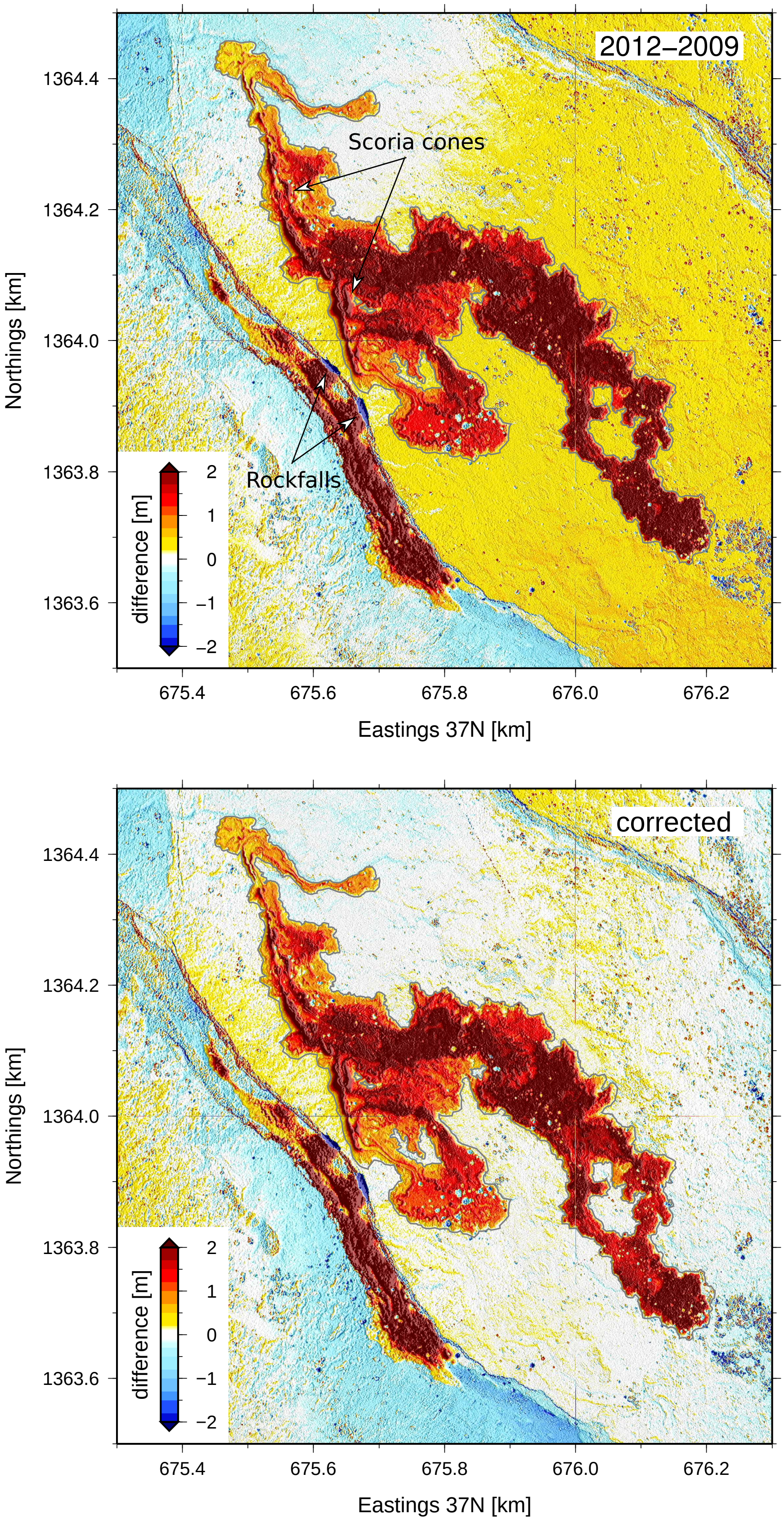

Figure 5.22: May 2010 eruption: Simple differencing between the 2009 and 2012 LiDAR DEM. Top: uncorrected, bottom: corrected for general dyke induced uplift by fitting a plane across the fault block hosting the eruption. The eruption occurred along a row of small scoria cones (∼ 30-40 m diameter). The lava flow extends mainly to the east and south. Along the fault to the west of the eruption two rockfalls sites are visible.

For a better understanding of the correlation between the dyking and the faulting at the AVC I extracted 4 profiles across the rift segment (Fig. 5.24) and compared the vertical displacement with the topography and the earthquake locations as proxy for the position of the dyke (Fig. 5.25). The topography of each profile is shown in grey and the vertical displacement is plotted in red for uplift and blue for subsidence. The earthquakes are sized by their local magnitude and colour-coded by day. If a moment tensor solution exists for the event the double-couple solution is plotted as a back hemisphere projection. They are consistent with normal faulting (Seismic data courtesy of Derek Keir and Manaloh Belachew). There is a clear correlation between the drops in the vertical displacement and the faults in the topography. The largest amount of displacement (∼1 m) was accumulated at the fault structure which limits the area of subsidence in the east (profiles 1-3 in fig. 5.25). This is similar to my observations from the October 2008 intrusion § 5.2. The saw-tooth displacement pattern towards the west is particular well defined on profile 2 of figure 5.25. There appears to be a slight east to west shift in the earthquake locations as they reach shallower depth which could indicate that the dyke intruded at an angle. Unfortunately the uncertainties of the earthquake location are too large (vertical 500 m and horizontally 1000 m, personal communication Derek Keir) to be able to associate individual earthquakes with slip on specific faults.

5.3.5 Extraction of 3-D fault slip from differential LiDAR data

For the quantitative analysis of the fault slip induced by the May 2010 intrusion I adjusted my algorithm (§ 3) to extract incremental fault slip from the displacement data. As was the case for the InSAR analysis (§ 5.2.2) the vertical displacement data can be used like a DEM. Instead of topographic profiles extracted from the high-resolution LiDAR, I extract profiles from the vertical displacement data and optimise the parameter for the larger pixel size and slightly different signal shape. The chosen parameters to extract the incremental throw are listed in table 5.2. Due to the lower resolution of the vertical displacement data (25 x 25 m^2) I increased sm, fpw and hpw (Table 5.2). In the same manner as the original algorithm determines the hanging and footwall cutoff from the topography, the adjusted algorithm determines the cutoffs from the vertical displacement. I extract the horizontal displacement for the position of the cutoffs to estimate the incremental horizontal displacement in E-W and N-S direction. In order to reduce the error due to the striping in the horizontal displacement data I recalculated the displacement between the surveys with a larger window size of 100 x 100 m and extracted the incremental horizontal displacement from this data set.

Search margin	sm	80 m
Footwall plain width	fpw	50 m
Hangingwall plain width	hpw	60 m
Minimum significant vertical offset	v_{min}	0.3
Maximum tolerated vertical offset	v_{max}	0.7
Maximum tolerated fissure opening	fw	40 m
Profile spacing		20 m and 5 m
rloess window size		10 points

Table 5.2: Chosen algorithm parameters to extract slip from differential LiDAR data. Parameters are discussed in § 3.4.1

5.3.6 3-dimensional fault slip

In order to visualise the 3-dimensional fault slip I converted the incremental displacement measurements into trend, plunge and the amount of slip. Trend is measured in the horizontal plane. It is the angle between North and the projection of the slip vector onto the horizontal plane. Plunge is defined as the downward angle between the horizontal plane and the slip vector. The amount of slip is the length of the slip vector. In figure 5.26 I plot trend (direction of arrow), plunge (colour of arrow) and amount of slip (arrow length) along the fault traces. The area of dyke induced subsidence is marked in light grey for reference. The majority of dip-slip, with plunge $\geq 65°$ (green to red), occurs in a narrow ∼3 km wide area including the area of subsidence. These are also the faults exhibiting the largest amount of slip of up to ∼1.2 m. The dip direction is predominantly westwards. At the centre of the image arrows indicating slip >2 m are displayed. They correlate to the small volcanic eruption and do not relate to true fault slip. Along the length of most of the faults a gradual change in trend and plunge angle occurs. The striping in the horizontal components does affect the measurements and is responsible for the occurrences of sudden and extreme changes in trend. I therefore hesitate to interpret small scale variations of plunge and trend along individual faults. At the flanks the slip is dominated by horizontal displacement. Similar to the displacement pattern of the October 2008 intrusion fault slip does not extend significantly beyond the dyke's lateral extent.

5.3.7 Cumulative vs. incremental fault slip

I described the linkage zones of the fault array in figure 5.27 in § 4.3 and will now only focus on the incremental throw on this array. The array was activated during both the October 2008 and the May 2010 intrusions. Panel 4 shows the incremental throw induced by the October 2008 dyke intrusion. The first 4 km of the array show significant throw (5-20 cm) but no slip is observed on the following 4 km which are located outside of the main activation zone of the intrusion. During the May 2010 intrusion the fault array was completely within the activation zone and fresh throw is visible on all fault segments (Panel 5). It is not possible to distinguish the slip on the individual fault segment at the first linkage zone (purple and blue, panel 2), using the InSAR measurements but the differential LiDAR measurements show that both segments were activated independently. The second linkage, the divergent splay (green and blue), is more interesting. As stated in § 4.3, the structure is hard-linked along the blue structure. During the October 2008 intrusion only the blue structure accumulated significant new throw. The cumulative throw along the blue structure steps down from ∼50 m to ∼10 m which does not seem to influence the accumulation of new slip which smoothly tapers of as the end of the activation zone is reached. During the May 2010 intrusion both the blue and the green segment were activated and again the slip along the blue segment does not seem to be affected by the linkage, exhibiting an almost bow shaped pattern of fresh throw.

5.3.8 Incremental strain mapping

I also estimated the mean strike, dip, rake and slip for each fault from the incremental throw and horizontal displacement measurements. For faults with slip > 1 m the mean dip is $62° \pm 17°$ which seems reasonable. I then used the values, calculated for each fault, to estimate the amount of strain accommodated by faulting during the May 2010 intrusion. For the strain calculations I followed the method introduced by England and Molnar (2005), which is explained in detail in § 4.4. The algorithm was kindly provided to me by Philip England. The results of the strain calculation are shown in figure 5.28. The cells exhibiting the largest amount of extensional strain are located just to the east of the rift centre. The extensional strain along the profile marked on the map also shows a small amount of asymmetry with its maximum slightly shifted towards the east. I integrated the strain across the profile, and found the extension across the profile to be 1.5 m. Considering that maximum opening of the dyke is estimated to be 1.6 m (personal communication Ian Hamling) it seems reasonable to suggest that faulting can indeed accommodate the majority of the strain in the upper layer of the crust induced by dyke intrusions beneath.

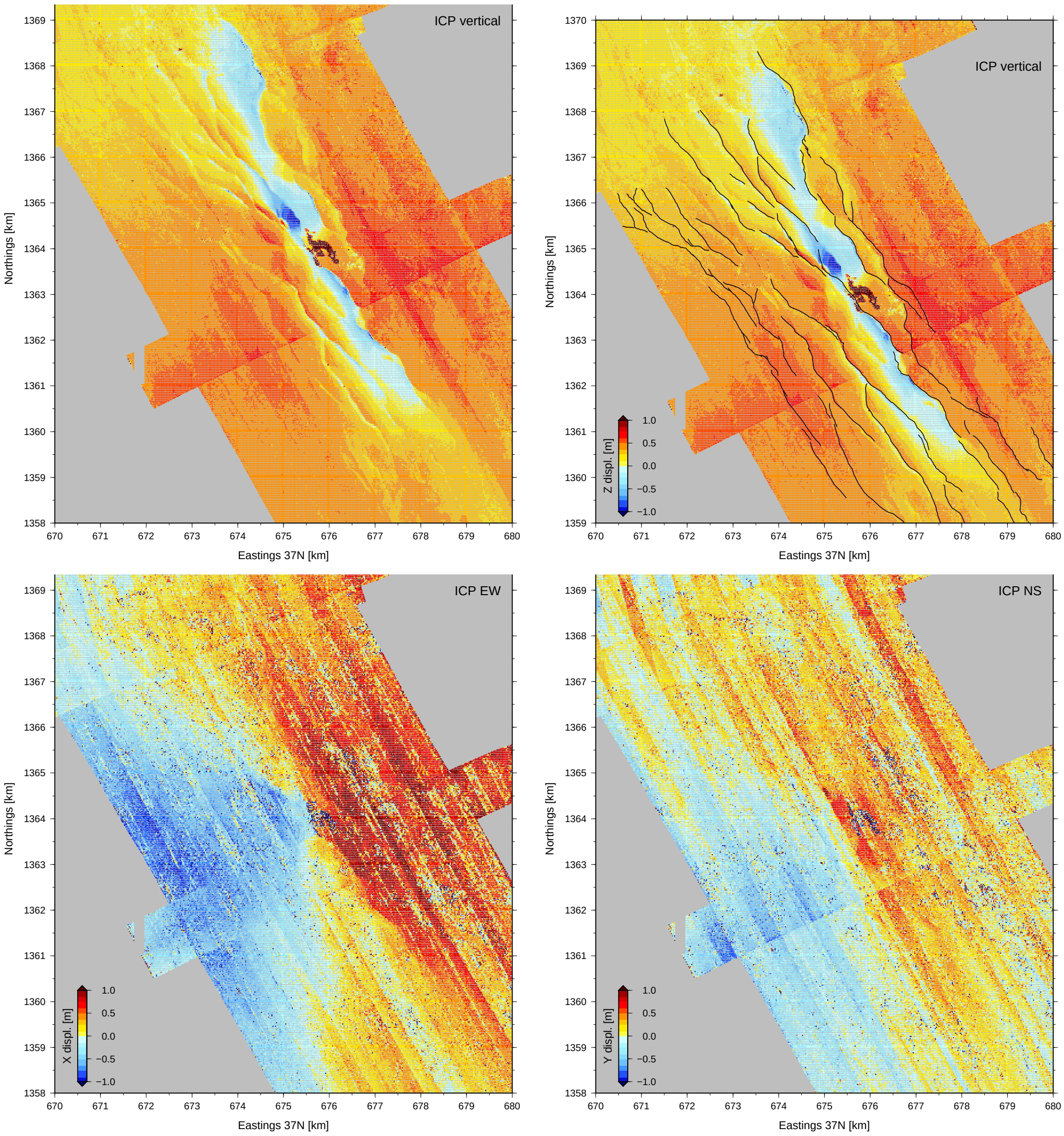

Figure 5.23: ICP displacement of the May 2010 dyke intrusion top left: Vertical displacement, top right Vertical displacement including fault traces manually picked by myself, bottom left EW displacement, bottom right NS displacement.

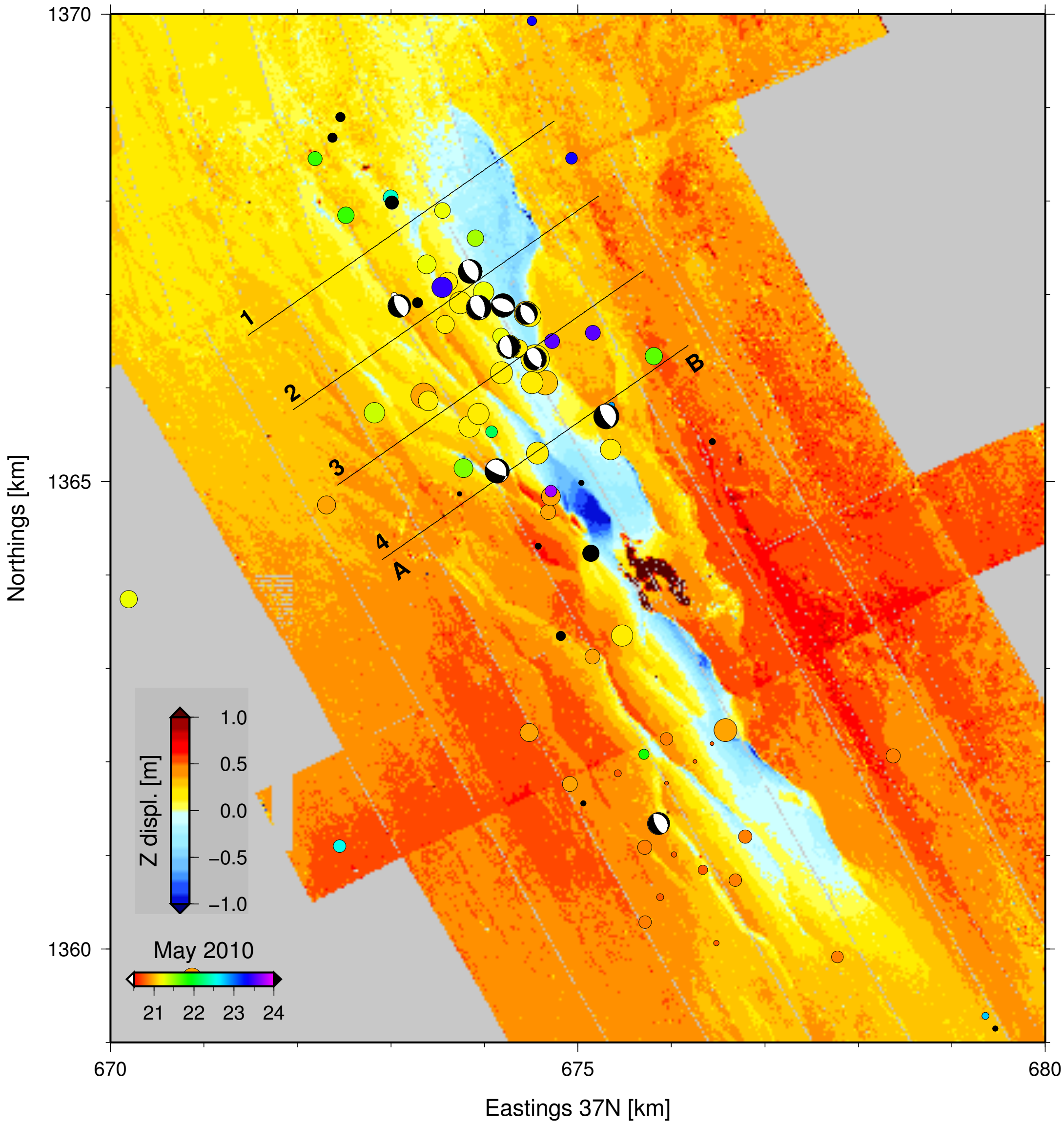

Figure 5.24: Vertical displacement and seismicity of the May 2010 dyke intrusion. Earthquakes are colour coded by time and size is dependant on magnitude. Focal mechanism from moment tensor inversion (personal communication Derek Keir and Manaloh Belachew). Profiles correspond to figure 5.25.

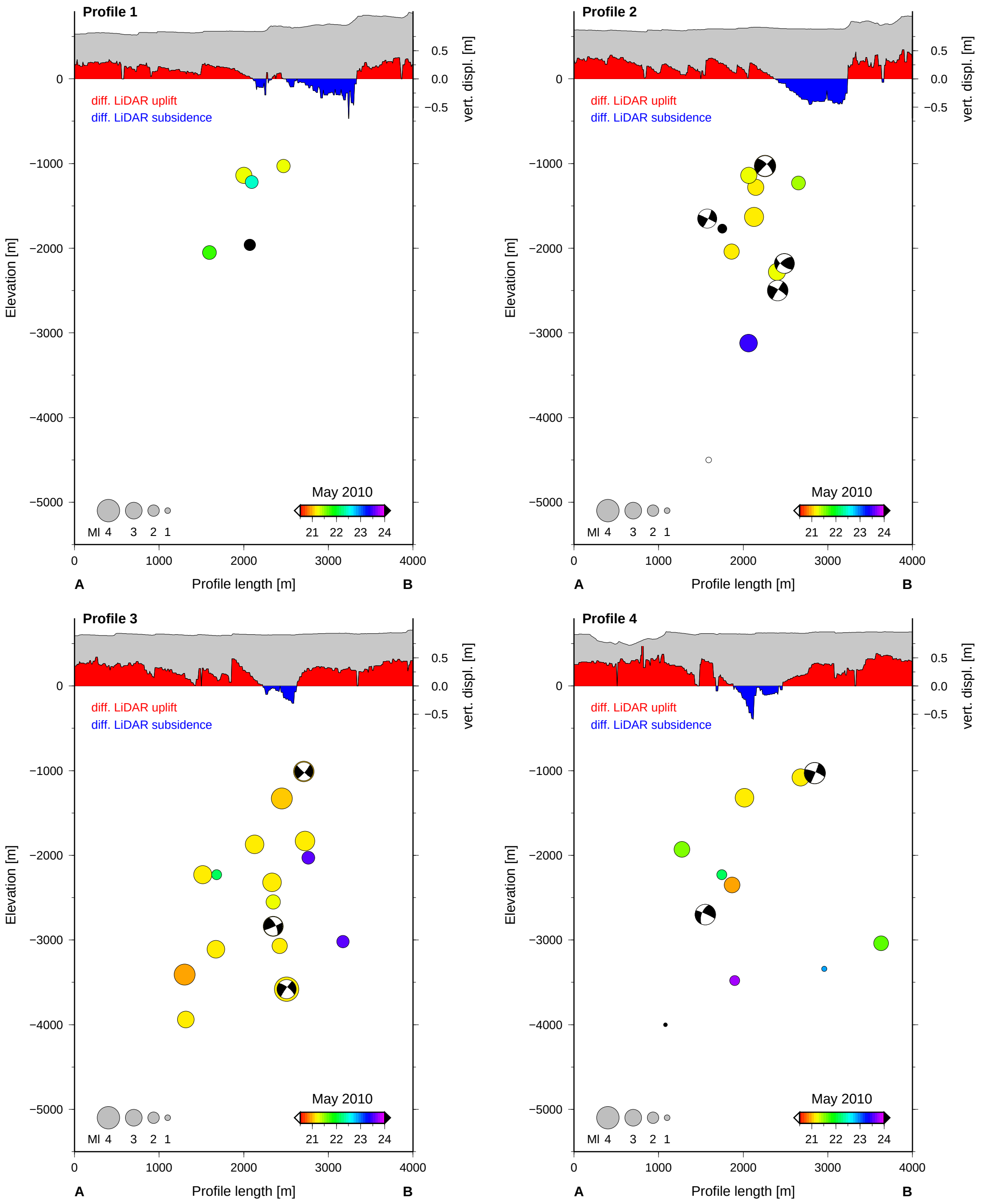

Figure 5.25: Cross profiles corresponding to 5.24. Profiles are extracted perpendicular to the rift axis. Topography is plotted in grey and surface displacement in red (uplift) and blue (subsidence). Local seismicity (courtesy of Derek Keir, moment tensors by Manaloh Belachew) is scaled by local magnitude and colour coded by time.

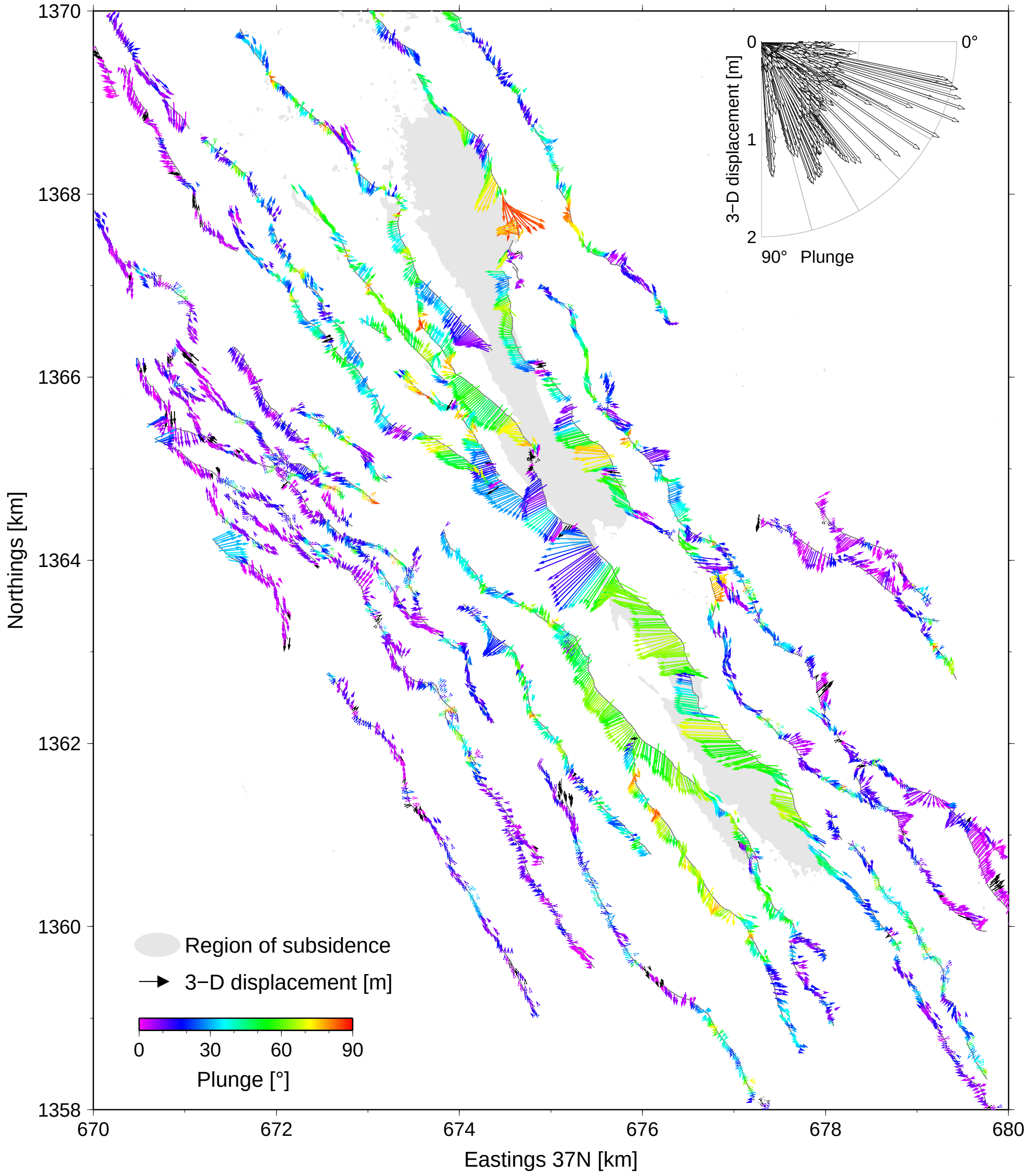

Figure 5.26: Fault slip induced by the May 2010 dyke intrusion. Trend and amount of slip are shown by arrow direction and arrow length, respectively. The colour of the arrows indicates plunge. Subsided region in grey. The diagram in the top right corner shows the distribution of slip in respect of the plunge angle.

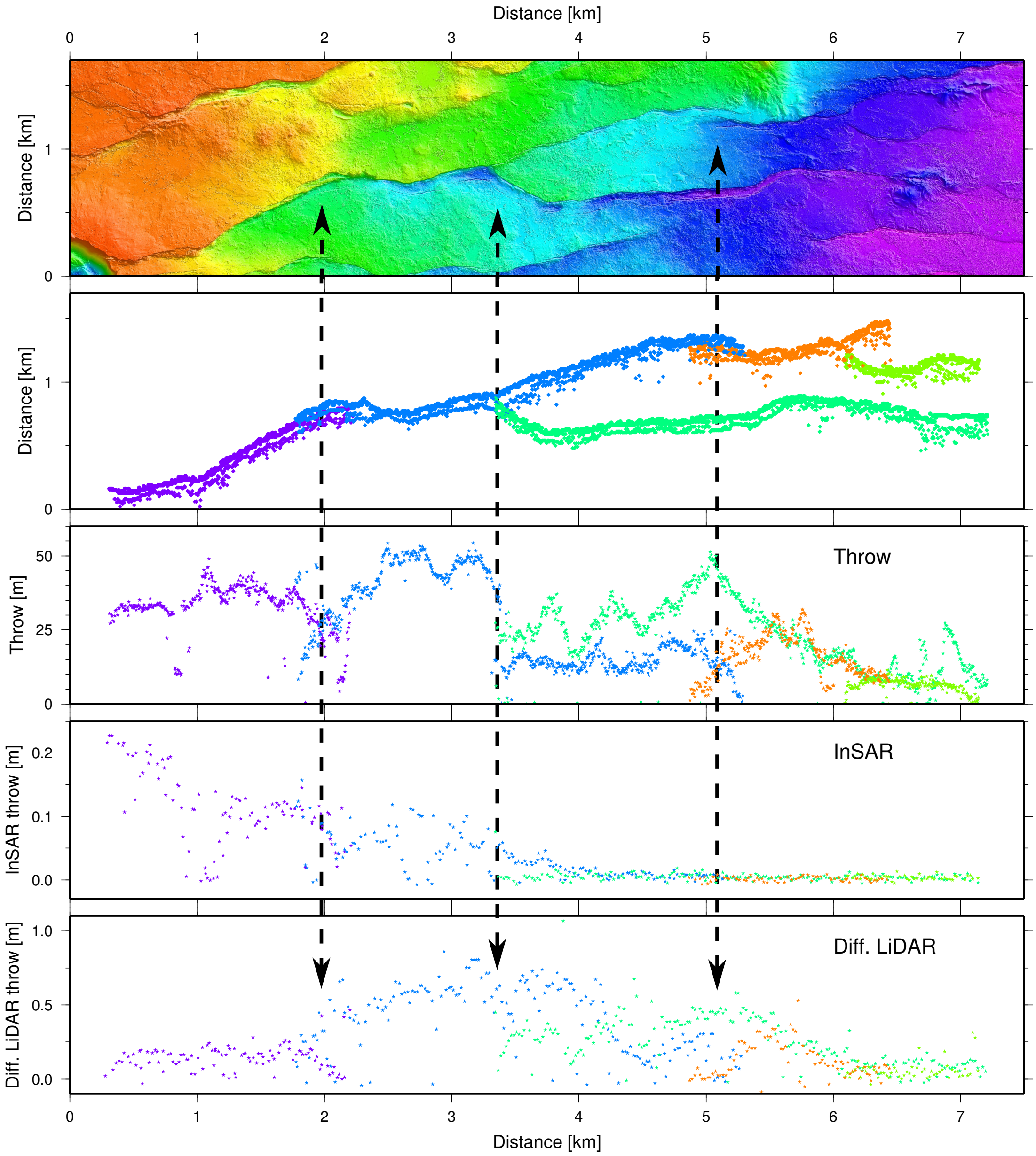

Figure 5.27: Comparison of cumulative throw with fresh throw induced during two dyke intrusions. Top panel: 60° rotated LiDAR DEM, second panel: Hanging and footwall cutoffs in map view, third panel: Cumulative throw, fourth panel: Incremental throw from the October 2008 intrusion using InSAR data, fifth panel: Incremental throw from the May 2010 intrusion using differential LiDAR data. Colours indicate individual fault segments.

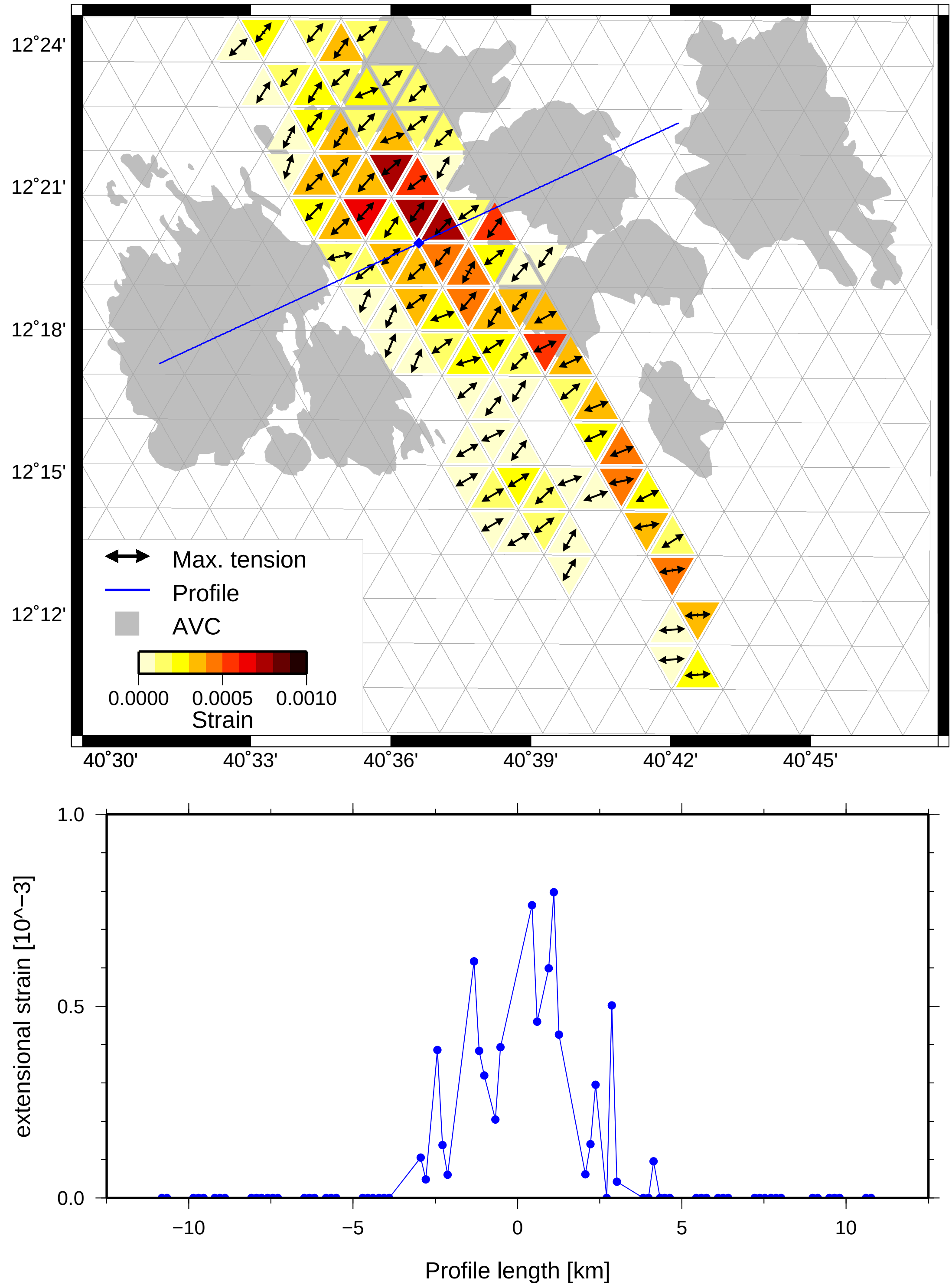

Figure 5.28: Top: Strain map calculated from incremental fault slip derived from 3-D displacement data. The arrows indicate the direction of maximum tension and the colours correspond to the magnitude of extensional strain in each triangular cell. Bottom: Profile of the extensional strain, indicated by the blue line in the top diagram, accommodated by faulting during the May 2010 intrusion. Total displacement 1.5 m

5.4 Summary and discussion

In this chapter I successfully demonstrated that ALOS InSAR and differential LiDAR data can be used to identify and quantify dyke induced fault slip on individual fault segments at the Dabbahu rift.

To conclude this chapter I will discuss the findings of this chapter in relation to the questions raised at its beginning.

- Do hard linked linkage zones exhibit increased displacement or do they act as slip barriers?
  I did not find signs for increased displacement accumulating at hard linked linkage zones. In contrast, my observations suggest that two scenarios are possible at hard linked linkage zones.
  Firstly examples presented here show that local minima in the cumulative $d-L$ profiles, which can be associated with hard linked linkage zones, correlate with minima of the incremental $d-L$ profiles, suggesting that the individual fault segments maintain a level of independence allowing them to slip separately. This behaviour was previously only observed during fault growth in analogue models (Mansfield and Cartwright, 2001).
  Secondly I found cases at which the connected fault segments act as one throughgoing fault. The former linkage zone does not appear to affect the distribution of newly accumulated throw and the incremental $d-L$ shape of the linked structure is roughly bow shaped.
  The combination of these two scenarios may explain the small scale corrugation or saw tooth pattern commonly observed in $d-L$ patterns (e.g. Manighetti et al., 2001, Cowie and Roberts, 2001, Peacock, 2002).

- Does the less developed fault segment show signs of increased displacement?
  I did not observe any cases where the less developed fault segment accumulated more throw compared to its larger neighbouring fault segment. If one of the linked segments accumulated a significantly larger amount of throw it was the already larger segment which accumulated it.

- How do divergent splay faults behave?

  Splay faults are often believed to be the remnant, inactive fault tip of the rear segment after fault linkage is completed along a lower-ramp breach (e.g Trudgill and Cartwright, 1994, Crider, 2001). The Dabbahu rift segments exhibit many divergent splay faults which are of similar length to the supposedly active front segment. While they exhibit less throw compared to the front segment their length suggests that the remnant fault tips remain active. The displacement data from the InSAR data as well as the differential LiDAR data both indicate that this is indeed the case. I observed displacement along the linked fault as well as on the supposedly inactive tip of the rear segment. I also found a case that suggests that the rear fault destroyed the linkage with the front segment and now accumulates displacement along its original path.

- Where does the fault re-activation occur in respect to dyke intrusions? Which faults get reactivated during the intrusion?

  During both the October 2008 and the smaller May 2010 intrusion, faults within a broad zone of 3-4 km width parallel to the dyke were reactivated. In both cases the majority of the dyke induced displacement (∼1 m) accumulated along one or two large fault structures which border the area of subsidence on the east. Minimal fault slip occurred further east of these boundary faults.

  For the October 2008 intrusion the area of subsidence correlated with the region of fault activation. Hardly any fault slip occurred on the uplifted flanks. In contrast the subsided area of the May 2010 intrusion was narrow (1-2 km) and apart from the bordering fault in the east all of the fault slip occurred on the uplifted flanks. The differential LiDAR data shows bookshelf faulting at the AVC. The strain analysis showed 1.5 m extension during the May 2010 intrusion which correlates to the 1.6 m maximum dyke opening from elastic dislocation modelling (personal communication Ian Hamling).

.

Chapter 6

Conclusions

The recent Dabbahu rifting episode is the first of its kind that has been extensively monitored using advanced remote sensing techniques such as InSAR and LiDAR. Here I was able to combine these technologies in a unique way to investigate dyke-induced faulting across the Dabbahu rift segment and provide new insights into fault development.

6.1 Fault throw algorithm

I successfully developed an algorithm to automatically extract throw along surface fault traces from a high-resolution LiDAR DEM, by identifying the hanging and footwall cutoffs. The quality of my derived cutoffs is comparable to field work data, with both giving vertical errors of ∼1 m (Dawers and Anders, 1995).

The displacement-length data, $d - L$, produced by my algorithm is robust and repeatable. I also reduced the amount of subjectivity during the cutoff identification process by applying strict criteria. The algorithm is controlled by multiple parameters which can easily be adjusted to different data sets. I also successfully applied the algorithm to displacement data derived from InSAR and differential LiDAR. Furthermore my algorithm is quick and independent of specialist software. For analysis of fault data in Afar, this algorithm was an essential tool. Fieldwork was impossible, except for a handful of faults, and the sheer number of fault structures rendered manual picking infeasible.

6.2 Dyke-induced faulting

During the recent 2005-2010 rifting episode at the Dabbahu rift in total 14 individual dyking events occurred (e.g. Wright et al., 2006, Hamling et al., 2009, Barisin et al., 2009, Grandin et al., 2009, Hamling et al., 2010). Each of them caused surface deformation and fault slip. The two dyke intrusions studied in detail here took place in October 2008 and May 2010. Both intrusions were injected towards the east of the rift axis (Hamling et al., 2010). I used ALOS InSAR data to investigate the October 2008 intrusion and differential LiDAR data to investigate the May 2010 event.

In order to identify and extract fault slip induced by the October 2008 intrusion I used ALOS InSAR data. The longer wavelength of 23 cm of ALOS data allowed me to unwrap the interferogram above the dyke intrusion where the slip occurred. I processed the data with the standard ROI_PAC software (Rosen et al., 2004) package. I was further able to process the data at its highest resolution due to the availability of the high-resolution LiDAR from 2009. Once the ALOS data were unwrapped I calculated the gradient of the LOS displacement to highlight the slipped faults. I then converted LOS displacement into vertical throw by imposing a dip angle of 65°. This is reasonable for the steep faults at the Dabbahu rift segment.

To extract the displacement from the May 2010 intrusion I used the two LiDAR surveys from 2009 and 2012. Simple DEM differencing introduces too many errors into the analysis and I therefore applied the ICP algorithm developed by Nissen et al. (2012). It provides not only vertical displacement but also horizontal displacement. The horizontal components are noisier due to striping in the LiDAR data set, caused primarily by boresight roll angle errors.

In both cases fault activation was limited to an area roughly 3-4 km wide parallel to the intrusion. During the October 2008 intrusion subsidence occurred across the 4 km wide zone and all fault activation took place within that zone. The area of subsidence was much narrower for the May 2010 intrusion (∼1-2 km) and most of the reactivated faults were located on the uplifted areas. In both cases the majority of the dyke-induced displacement (∼1 m) accumulated along one or two large fault structures that border the area of subsidence on the east. Hardly any fault slip occurred further east of these boundary faults. The May 2010 intrusion occurred at the AVC which is dominated by westwards dipping bookshelf faults. These were activated by the intrusion. The May 2010 intrusion was accompanied by a small eruption. By comparing the two LiDAR DEMs, I estimated the erupted volume to be 230,000±4,000 m^3.

The dyke intrusions of the 2005-2010 rifting episode were all emplaced to the east of the rift axis (Hamling, 2010, Hamling et al., 2010). While it is unknown where the dykes of previous rifting episodes were emplaced, the distinct bookshelf faulting at the AVC may suggest that some previous intrusions behaved similarly. Coulomb stress modelling shows that if bookshelf faulting exists before the intrusion the faults will be activated in their pre-existing sense (Fig. 6.1). Furthermore during each dyke intrusions faults are only activated within a zone whose width is dependent on the depth of the intrusion. Numerical models propose that the width is ±2-3 times the depth to the top of the dyke intrusion (Behn et al., 2006, Rubin, 1992). It is therefore possible to speculate that at some point in the development of the rift the dykes were emplaced mainly beneath the westwards dipping faults, in order to create the well developed bookshelf faulting at the AVC. However, the width of the cumulative strain zone (Fig. 6.2) cannot be explained by repeated dyke intrusions at the same position as the 2005-2010 sequence. Therefore it is likely that dykes move throughout the rift zone. From the available data it is not possible to assess whether this is a steady migration or random.

6.3 Fault growth at the Dabbahu rift segment

The Dabbahu rift segment exhibits a highly connected network of faults and fissures. Along the length of the Dabbahu rift segment the style of faulting changes from horst and graben formations in the north, which are commonly observed at rift zones, to predominantly bookshelf faulting at the central Ado'Ale volcanic complex. In total I extracted $d-L$ profiles for 3748 fault segments that had been mapped by C. Vye-Brown. The largest cumulative fault throw of ~80 m is measured along fault scarps in the east of the segment crossing the ryholitic AVC. Faults north of the AVC record ~140 m of extension, derived from strain measurements, implying extensive resurfacing. Fault linkage zones at various stages of linkage and divergent splay faults are common

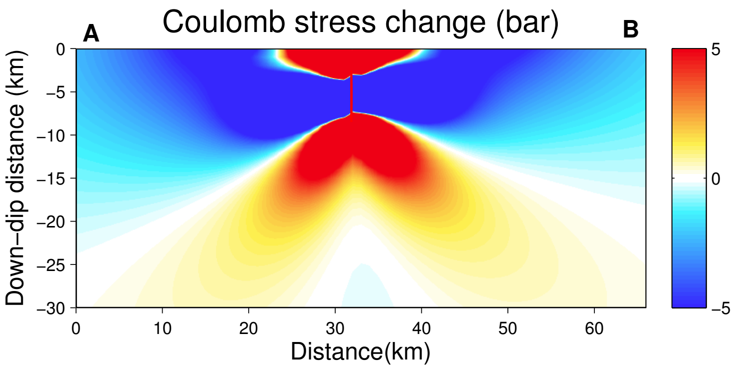

Figure 6.1: Coulomb stress change on faults caused by opening a vertical, N-S dike. The dike is 39 km long and extends from 2.5-8.5 km in depth. The opening magnitude is tapered with maximum opening of 1.5 m. The Coulomb stress is resolved on westwards dipping faults with strike/dip/rake 180/65/-90. Young's modulus is 10e+05 bars, Poisson's ratio is 0.25, Coefficient of friction is 0.4. The calculations were carried out using the software Coulomb 3.3 (Toda et al., 2011). Courtesy of Richard Walters.

throughout the rift segment. Isolated individual faults are virtually non-existent at the Dabbahu rift. Individual fault zones often comprise more than 10 segments at different stages of linkage.

Published models of fault growth through linkage predict that once two segments are hard linked the displacement deficit across the linkage zone will be reduced (e.g. Peacock and Sanderson, 1991, Cartwright et al., 1995, Willemse et al., 1996, Crider and Pollard, 1998, Gupta and Scholz, 2000, Peacock, 2002). However, my incremental and cumulative displacement data from the Dabbahu rift segment does not show any signs of increased displacement accumulation across the former linkage zones. In contrast I see evidence that one of two scenarios take place.

1. Fault segments maintain their independence and slip individually even after fault linkage is complete. Throw accumulates at the centre of the individual segments and hardly any new throw as acquired at the former linkage zone. This behaviour has previously only been observed during analogue modelling (Mansfield and Cartwright, 2001).

2. Fault segments act as one throughgoing fault after linkage is complete. In that case the former linkage zone appears to have no influence on the distribution of

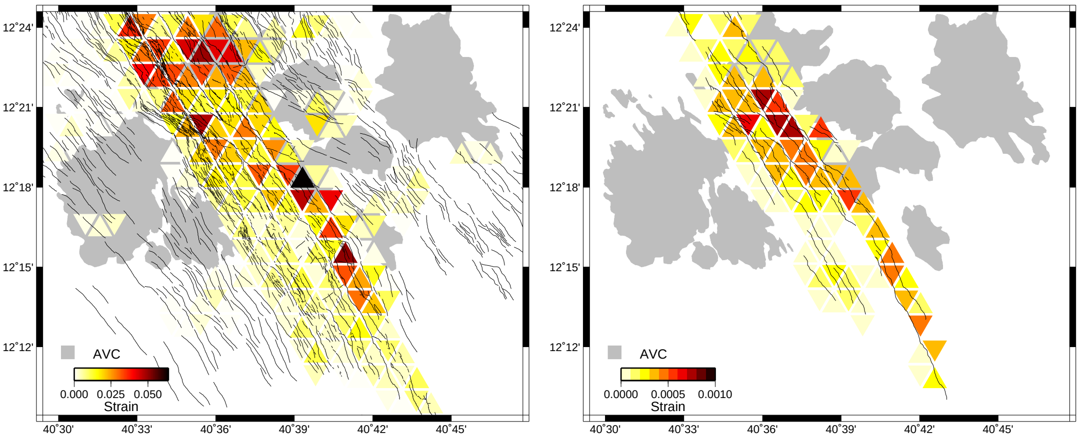

Figure 6.2: Comparison between cumulative (left) and incremental strain from May 2010 intrusion (right). Strain is colour-coded. Note the difference in magnitude. Faults marked as black lines. Left: The cumulative strain could only be estimated for the area covered by the LiDAR survey but the faults indicate that the zone is much wider. Right: The zone of the incremental strain is much narrower. Only the activated faults are marked.

the new throw. The throw distribution of the connected fault is roughly bow shaped. The overall throw of the linked fault is increased but the deficit at the linkage zone remains.

The combination of these two scenarios may explain the small scale corrugation or saw tooth pattern commonly observed in $d-L$ pattern (e.g. Manighetti et al., 2001, Cowie and Roberts, 2001, Peacock, 2002).

Furthermore models of fault growth through linkage propose that during the linkage process the local maximum of the two linking fault segments shifts towards the linkage zone (e.g. Gupta and Scholz, 2000). I could not see any clear evidence supporting this theory from the $d-L$ profiles of 36 soft and hard linked linkage zones. I also compared the local maxima either side of the linkage zone with each other and the throw minimum at the linkage zone (Fig. 4.14). In 70% of the cases the vertical difference between the two local maxima is >2 m, suggesting that fault linkage commonly takes place between segments of different maximum throw.

Splay faults are often believed to be the remnant, inactive fault tip of the rear segment after fault linkage is completed along a lower-ramp breach (Fig. 6.3) (e.g Trudgill and Cartwright, 1994, Crider, 2001). The Dabbahu rift segments exhibits many divergent splay faults which are of similar length to the supposedly active front segment. While they exhibit less throw compared to the front segment their length suggests that the remnant fault tips remain active. The displacement data from the InSAR data as well as the differential LiDAR data both indicate that this is indeed the case. I observed displacement along the linked fault as well as on the supposedly inactive tip of the rear segment. I also found a case that suggests that the rear fault destroyed the linkage with the front segment and now accumulates displacement along its original path.

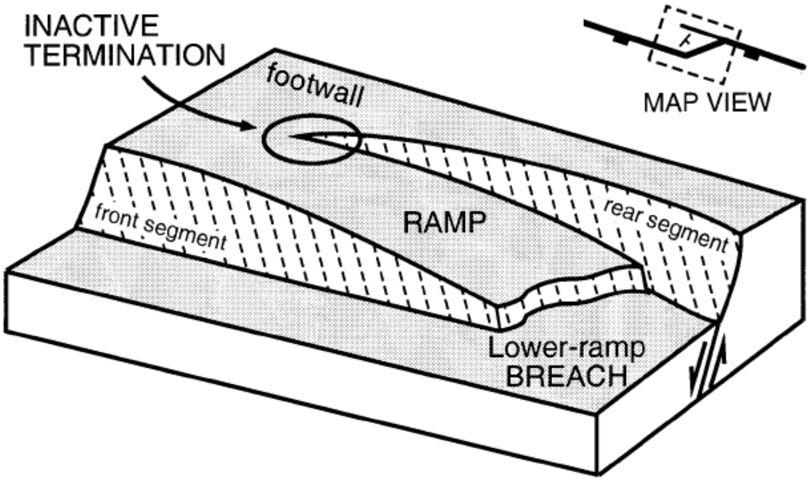

Figure 6.3: Lower-ramp breach, faults are connected from the front segment. The remaining fault tip is assumed to become inactive. Reprinted from from Crider (2001) with permission from Elsevier..

This unexpected reactivation of fault segments and the large amount of fault interaction is possibly due to the changes of the local stress field with each intrusion.

6.4 Future work

In my thesis I focused to a great extent on the development of an algorithm to extract throw. Now that this tools exists to quickly derive cumulative throw from high-resolution DEMs it could be applied to other regions for which such data exists such as Iceland, Hawaii and mid-oceanic ridges. It would be particularly interestingly to compare the $d - L$ profiles derived from the Dabbahu rift segment with slow-spreading ridges and examine if there is a change in the shape of the $d - L$ profiles.

In order to complete this study, the remaining two dyke intrusions for which ALOS InSAR data exist could be analysed and, in conjunction with the cumulative $d - L$ profile, more comprehensive fault growth models for dyke induced faulting could be developed.

At the moment the age constraints at the Dabbahu rift segment are too sparse to allow for an estimation of the amount of resurfacing from the strain measurements but in the future this might be a possibility. A more dense sampling of the ages of the lavas would be valuable.

The cumulative and incremental throw data sets could possibly be used to constrain the position of dyke through numerical modelling and improve our understanding of dyke-induced faulting. For example, boundary element models could be used to test the hypothesis that the faults respond passively to the opening of the dykes.

References

Ackermann, R. V., and R. W. Schlische (1997), Anticlustering of small normal faults around larger faults, *Geology*, *25*(12), 11271130. 1.1

Acocella, V., K. Spinks, J. Cole, and A. Nicol (2003), Oblique back arc rifting of Taupo Volcanic Zone, New Zealand, *Tectonics*, *22*(4), 1045, doi:10.1029/2002TC001447. 3.1

Allken, V., R. S. Huismans, H. Fossen, and C. Thieulot (2013), 3D numericalmodelling of graben interaction and linkage: a case study of the Canyonlands grabens, Utah, *Basin Research*, *25*(4), 436449, doi:10.1111/bre.12010. 1.1

Amante, C., and B. W. Eakins (2008), ETOPO1 1 Arc-Minute Global Relief Model: Procedures, *Data Sources and Analysis, National Geophysical Data Center, NESDIS, NOAA, US Department of Commerce, Boulder, CO*. 1.7

ARSF (2009), Data Quality Report - 2009 LiDAR, ARSF - Data Analysis Node, *Tech. rep.*, ARSF. 2.1.4

ARSF (2012), Data Quality Report - 2012 LiDAR, ARSF - Data Analysis Node, *Tech. rep.*, ARSF. 2.1.4

Ayele, A., E. Jacques, M. Kassim, T. Kidane, A. Omar, S. Tait, A. Nercessian, J.-B. de Chabalier, and G. King (2007), The volcano-seismic crisis in Afar, Ethiopia, starting September 2005, *Earth and Planetary Science Letters*, *255*(1-2), 177–187, doi:10.1016/j.epsl.2006.12.014. 1.3, 1.3, 1.8

Ayele, A., D. Keir, C. Ebinger, T. J. Wright, G. W. Stuart, W. R. Buck, E. Jacques, G. Ogubazghi, and J. Sholan (2009), September 2005 mega-dike emplacement in the Manda-Harraro nascent oceanic rift (Afar depression), *Geophysical Research Letters*. 1.3, 1.3

Baltsavias, E. (1999), Airborne laser scanning: existing systems and firms and other resources, *ISPRS Journal of Photogrammetry and Remote Sensing*, *54*(23), 164–198, doi:10.1016/S0924-2716(99)00016-7. 2.1.4

Barberi, F., and J. Varet (1977), Volcanism of Afar: Small-scale plate tectonic implications, *Geol. Soc. Am. Bull.*, *88*, 1251–1266, doi:10.1130/0016-7606(1977)88⟨1251:VOASPT⟩2.0.CO;2. 1.2

Barberi, F., H. Tazieff, and J. Varet (1972), Volcanism in the Afar depression: Its tectonic and magmatic significance, *Tectonophysics*, *15*(1-2), 19–29, doi:10.1016/0040-1951(72)90046-7. 1.2

Barisin, I., S. Leprince, B. Parsons, and T. Wright (2009), Surface displacements in the September 2005 Afar rifting event from satellite image matching: Asymmetric uplift and faulting, *Geophysical Research Letters*. 1.3, 6.2

Barnett, J. A. M., J. Mortimer, J. H. Rippon, J. J. Walsh, and J. Watterson (1987), Displacement geometry in the volume containing a single normal fault, *AAPG Bulletin*, *71*(8), 925–937. 1.1

Bastow, I. D., A. A. Nyblade, G. W. Stuart, T. O. Rooney, and M. H. Benoit (2008), Upper mantle seismic structure beneath the Ethiopian hot spot: Rifting at the edge of the African low-velocity anomaly, *Geochemistry, Geophysics, Geosystems*, *9*(12). 1.2

Begg, J. G., and V. Mouslopoulou (2010), Analysis of late Holocene faulting within an active rift using lidar, Taupo Rift, New Zealand, *Journal of Volcanology and Geothermal Research*, *190*(12), 152–167, doi:10.1016/j.jvolgeores.2009.06.001. 3.1, 3.1

Behn, M. D., W. R. Buck, and I. S. Sacks (2006), Topographic controls on dike injection in volcanic rift zones, *Earth and Planetary Science Letters*, *246*(34), 188–196, doi:10.1016/j.epsl.2006.04.005. 5.1, 5.1, 6.2

Bender, P. L., D. G. Currie, S. K. Poultney, C. O. Alley, R. H. Dicke, D. T. Wilkinson, D. H. Eckhardt, J. E. Faller, W. M. Kaula, J. D. Mulholland, H. H. Plotkin, E. C. Silverberg, and J. G. Williams (1973), The Lunar Laser Ranging Experiment, *Science*, *182*(4109), 229–238, doi:10.1126/science.182.4109.229. 2.1

Besl, P., and N. D. McKay (1992), A method for registration of 3-D shapes, *IEEE Transactions on Pattern Analysis and Machine Intelligence*, *14*(2), 239–256, doi:10.1109/34.121791. 5.3.1

Beyene, A., and M. G. Abdelsalam (2005), Tectonics of the Afar Depression: A review and synthesis, *Journal of African Earth Sciences*, *41*(1-2), 41–59, doi:10.1016/j.jafrearsci.2005.03.003. 1.2

Bilham, R., R. Bendick, K. Larson, P. Mohr, J. Braun, S. Tesfaye, and L. Asfaw (1999), Secular and tidal strain across the Main Ethiopian Rift, *Geophysical Research Letters*, *26*(18), 2789–2792, doi:10.1029/1998GL005315. 5.1

Björnsson, A., K. Sæmundsson, P. Einarsson, E. Tryggvason, and K. Grönvold (1977), Current rifting episode in north Iceland, *Nature*, *266*(5600), 318–323, doi:10.1038/266318a0. 4.4.2, 5.1

Bull, J. M., T. A. Minshull, N. C. Mitchell, K. Thors, J. K. Dix, and A. I. Best (2003), Fault and magmatic interaction within Iceland's western rift over the last 9 kyr, *Geophysical Journal International*, *154*(1), F1–F8, doi:10.1046/j.1365-246X.2003.01990.x. 5.1

Bürgmann, R., D. D. Pollard, and S. J. Martel (1994), Slip distributions on faults: effects of stress gradients, inelastic deformation, heterogeneous host-rock stiffness, and fault interaction, *Journal of Structural Geology*, *16*(12), 1675–1690, doi:10.1016/0191-8141(94)90134-1. 1.1, 3.1

Bürgmann, R., P. A. Rosen, and E. J. Fielding (2000), Synthetic aperture radar interferometry to measure Earth's surface topography and its deformation, *Annual Review of Earth and Planetary Sciences*, *28*(1), 169209. 2.2, 2.14

Cartwright, J. A., B. D. Trudgill, and C. S. Mansfield (1995), Fault growth by segment linkage: an explanation for scatter in maximum displacement and trace length data from the Canyonlands Grabens of SE Utah, *Journal of Structural Geology*, *17*(9), 1319–1326. 1.1, 1.1, 1.3, 3.1, 3, 6.3

Cartwright, J. A., C. Mansfield, and B. Trudgill (1996), The growth of normal faults by segment linkage, *Geological Society, London, Special Publications*, *99*(1), 163177. 4.3, 4.5, 5

Çiftçi, N. B., and E. Bozkurt (2007), Anomalous stress field and active breaching at relay ramps: a field example from Gediz Graben, SW Turkey , *Geological Magazine*, *144*(04), 687–699, doi:10.1017/S0016756807003500. 1.1

Chen, Y., and G. Medioni (1992), Object modelling by registration of multiple range images, *Image and Vision Computing*, *10*(3), 145–155, doi:10.1016/0262-8856(92)90066-C. 5.3.1

Childs, C., J. Watterson, and J. J. Walsh (1995), Fault overlap zones within developing normal fault systems, *Journal of the Geological Society*, *152*(3), 535–549, doi:10.1144/gsjgs.152.3.0535. 1.1

Cleveland, W. S. (1979), Robust Locally Weighted Regression and Smoothing Scatterplots, *Journal of the American Statistical Association*, *74*(368), 829–836, doi:10.2307/2286407, ArticleType: research-article / Full publication date: Dec., 1979 / Copyright 1979 American Statistical Association. 3.3.3

Cowie, P. A., and G. P. Roberts (2001), Constraining slip rates and spacings for active normal faults, *Journal of Structural Geology*, *23*(12), 1901–1915, doi:10.1016/S0191-8141(01)00036-0. 3, 5.4, 6.3

Cowie, P. A., and C. H. Scholz (1992a), Displacement-length scaling relationship for faults: data synthesis and discussion, *Journal of Structural Geology*, *14*(10), 1149–1156, doi:10.1016/0191-8141(92)90066-6. 1.1, 1.1, 3.1

Cowie, P. A., and C. H. Scholz (1992b), Physical explanation for the displacement-length relationship of faults using a post-yield fracture mechanics model, *Journal of Structural Geology*, *14*(10), 1133–1148, doi:10.1016/0191-8141(92)90065-5. 1.1, 3.1

Crider, J. G. (2001), Oblique slip and the geometry of normal-fault linkage: mechanics and a case study from the Basin and Range in Oregon, *Journal of Structural Geology*, *23*(12), 19972009. 1.1, 1.6, 5.4, 6.3, 6.3

Crider, J. G., and D. D. Pollard (1998), Fault linkage: Three-dimensional mechanical interaction between echelon normal faults, *Journal of Geophysical Research: Solid Earth*, *103*(B10), 24,37324,391, doi:10.1029/98JB01353. 1.1, 1.1, 3, 5.2.4, 6.3

Crone, A. J., and K. M. Haller (1991), Segmentation and the coseismic behavior of Basin and Range normal faults: examples from east-central Idaho and southwestern Montana, U.S.A., *Journal of Structural Geology*, *13*(2), 151–164, doi:10.1016/0191-8141(91)90063-O. 1.1

Curlander, J. C., and R. N. McDonough (1991), *Synthetic aperture radar systems and signal processing*, New York: John Wiley & Sons. 2.2

Daniels, K. A., and I. D. Bastow (2014), Thermal models of dyke intrusion during development of continent-ocean transition, *Earth and Planetary Science Letters*, *385*, 145–153, doi:10.1016/j.epsl.2013.09.018. 5.1

Davies, R. K., M. Crawford, W. F. Dula, M. J. Cole, and G. A. Dorn (1997), Outcrop interpretation of seismicscale normal faults in southern Oregon: Description of structural styles and evaluation of subsurface interpretation methods, *The Leading Edge*, *16*(8), 1135–1142, doi:10.1190/1.1437750. 1.1

Dawers, N. H., and M. H. Anders (1995), Displacement-length scaling and fault linkage, *Journal of Structural Geology*, *17*(5), 607–614, doi:10.1016/0191-8141(94)00091-D. 1.1, 3.4.2, 3.4.3, 6.1

Dawers, N. H., M. H. Anders, and C. H. Scholz (1993), Growth of normal faults: Displacement-length scaling, *Geology*, *21*(12), 1107–1110, doi:10.1130/0091-7613(1993)021⟨1107:GONFDL⟩2.3.CO;2. 1.1, 1.1

Dziewoński, A. M., T.-A. Chou, and J. H. Woodhouse (1981), Determination of earthquake source parameters from waveform data for studies of global and regional seismicity, *Journal of Geophysical Research*, *86*(B4), 2825, doi:10.1029/JB086iB04p02825. 1.7

Ebinger, C. J., J. A. Jackson, A. N. Foster, and N. J. Hayward (1999), Extensional basin geometry and the elastic lithosphere, *Philosophical Transactions of the Royal Society of London. Series A: Mathematical, Physical and Engineering Sciences*, *357*(1753), 741–765, doi:10.1098/rsta.1999.0351. 4.2.3

Ebinger, C. J., D. Keir, A. Ayele, E. Calais, T. J. Wright, M. Belachew, J. O. S. Hammond, E. Campbell, and W. R. Buck (2008), Capturing magma intrusion and faulting processes during continental rupture: seismicity of the Dabbahu (Afar) rift, *Geophysical Journal International*, *174*(3), 1138–1152. 1.3, 1.3, 5.3.2

Ekström, G., M. Nettles, and A. Dziewoński (2012), The global CMT project 2004–2010: Centroid-moment tensors for 13,017 earthquakes, *Physics of the Earth and Planetary Interiors*, *200-201*, 1–9, doi:10.1016/j.pepi.2012.04.002. 1.7

Elliott, J. R., J. Biggs, B. Parsons, and T. J. Wright (2008), InSAR slip rate determination on the Altyn Tagh Fault, northern Tibet, in the presence of topographically correlated atmospheric delays, *Geophysical Research Letters*, *35*(12). 2.2

England, P., and P. Molnar (1997), The field of crustal velocity in Asia calculated from Quaternary rates of slip on faults, *Geophysical Journal International*, *130*(3), 551–582, doi:10.1111/j.1365-246X.1997.tb01853.x. 4.4.1, 4.4.1

England, P., and P. Molnar (2005), Late Quaternary to decadal velocity fields in Asia, *Journal of Geophysical Research: Solid Earth*, *110*(B12), n/an/a, doi:10.1029/2004JB003541. 4.4.1, 5.3.8

ERDAS (2011), ERDAS ER Mapper 2011®. 2.1.5

Escartin, J., R. C. Searle, N. C. Mitchell, A. P. Slootweg, and P. Cowie (1999), Quantifying tectonic strain and magmatic accretion at a slow spreading ridge segment, Mid-Atlantic Ridge, 29 deg N, *Journal of Geophysical Research*, *104*, 10. 5.1

Farr, T. G., P. A. Rosen, E. Caro, R. Crippen, R. Duren, S. Hensley, M. Kobrick, M. Paller, E. Rodriguez, L. Roth, D. Seal, S. Shaffer, J. Shimada, J. Umland, M. Werner, M. Oskin, D. Burbank, and D. Alsdorf (2007), The shuttle radar topography mission, *Reviews of Geophysics*, *45*(2), RG2004, doi:10.1029/2005RG000183. 2.2, 2.15, 4.1, 5.3

Favalli, M., A. Fornaciai, and M. T. Pareschi (2009), LIDAR strip adjustment: Application to volcanic areas, *Geomorphology*, *111*(3), 123135. 2.1.4

Ferguson, D. J., T. D. Barnie, D. M. Pyle, C. Oppenheimer, G. Yirgu, E. Lewi, T. Kidane, S. Carn, and I. Hamling (2010), Recent rift-related volcanism in Afar, Ethiopia, *Earth and Planetary Science Letters*, *292*(3-4), 409–418, doi:10.1016/j.epsl.2010.02.010. 1.3, 4.1, 4.3

Ferguson, D. J., A. T. Calvert, D. M. Pyle, J. D. Blundy, G. Yirgu, and T. J. Wright (2013), Constraining timescales of focused magmatic accretion and extension in the Afar crust using lava geochronology, *Nature Communications*, *4*, 1416, doi:10.1038/ncomms2410. 4.1, 4.2, 4.4.2, 4.16

Fernandez, J. (2011), Lifting the Canopy Veil, *Imaging Notes*, *26*(2). 2.1, 2.1

Ferretti, A., A. Monti-Guarnier, C. Prati, and F. Rocca (2007), *InSAR Principles: Guidelines for SAR Interferometry Processing and Interpretation*, ESA Publications. 2.2, 5.2.2

Geosystems AG, L. (2007), Leica ALS50-II Airborne Laser Scanner Product Specifications. 2.1.1, 2.4

Ghiglia, D. C., and M. D. Pritt (1998), *Two-Dimensional Phase Unwrapping: Theory, Algorithms, and Software*, Wiley-Blackwell, New York. 5.2.2

Gillespie, P., J. Walsh, and J. Watterson (1992), Limitations of dimension and displacement data from single faults and the consequences for data analysis and interpretation, *Journal of Structural Geology*, *14*(10), 1157–1172, doi:10.1016/0191-8141(92)90067-7. 1.1, 3.1, 3.1

Glennie, C. (2007), Rigorous 3D error analysis of kinematic scanning LIDAR systems, *Journal of Applied Geodesy*, *1*(3), doi:10.1515/jag.2007.017. 2.1.4

Gold, C. M. (1989), *Surface interpolation, spatial adjacency and GIS*, chap. 3, CRC Press. 2.1.5

Goldstein, R. M., and C. L. Werner (1998), Radar interferogram filtering for geophysical applications, *Geophysical Research Letters*, *25*(21), 40354038. 2.2

Grandin, R., A. Socquet, R. Binet, Y. Klinger, E. Jacques, J.-B. de Chabalier, G. C. P. King, C. Lasserre, S. Tait, P. Tapponnier, A. Delorme, and P. Pinzuti (2009), September 2005 Manda Hararo-Dabbahu rifting event, Afar (Ethiopia): Constraints provided by geodetic data, *Journal of Geophysical Research: Solid Earth*, *114*(B8), n/an/a, doi:10.1029/2008JB005843. 1.3, 4.2.3, 6.2

Gross, M. R., G. Gutierrez-Alonso, T. Bai, M. A. Wacker, K. B. Collinsworth, and R. J. Behl (1997), Influence of mechanical stratigraphy and kinematics on fault scaling relations, *Journal of Structural Geology*, *19*(2), 171–183, doi:10.1016/S0191-8141(96)00085-5. 1.1

Gupta, A., and C. H. Scholz (2000), A model of normal fault interaction based on observations and theory, *Journal of Structural Geology*, *22*(7), 865–879, doi:10.1016/S0191-8141(00)00011-0. 1.1, 1.3, 1.4, 4.3, 4.13, 3, 6.3, 6.3

Gupta, S., P. A. Cowie, N. H. Dawers, and J. R. Underhill (1998), A mechanism to explain rift-basin subsidence and stratigraphic patterns through fault-array evolution, *Geology*, *26*(7), 595598. 1.1, 1.5, 3.3.1

Habib, A., K. I. Bang, A. P. Kersting, and J. Chow (2010), Alternative methodologies for LiDAR system calibration, *Remote Sensing*, *2*(3), 874–907, doi:10.3390/rs2030874. 2.1.4

Haines, A. J. (1982), Calculating velocity fields across plate boundaries from observed shear rates, *Geophysical Journal International*, *68*(1), 203–209, doi:10.1111/j.1365-246X.1982.tb06969.x. 4.4.1

Hamling, I. (2010), Measuring and modelling deformation during the Dabbahu (Afar) rifting episode, Phd thesis, University of Leeds. 2.14, 5.2, 5.2, 6.2

Hamling, I. J., A. Ayele, L. Bennati, E. Calais, C. J. Ebinger, D. Keir, E. Lewi, T. J. Wright, and G. Yirgu (2009), Geodetic observations of the ongoing Dabbahu rifting episode: new dyke intrusions in 2006 and 2007, *Geophysical Journal International*, *178*(2), 9891003, doi:10.1111/j.1365-246X.2009.04163.x. 1.3, 1.10, 6.2

Hamling, I. J., T. J. Wright, E. Calais, L. Bennati, and E. Lewi (2010), Stress transfer between thirteen successive dyke intrusions in Ethiopia, *Nature Geosci*, *3*(10), 713–717, doi:10.1038/ngeo967. 6.2

Hamling, I. J., T. J. Wright, E. Calais, E. Lewi, and Y. Fukahata (2014), InSAR observations of post-rifting deformation around the Dabbahu rift segment, Afar, Ethiopia, *Geophysical Journal International*, *197*(1), 33–49, doi:10.1093/gji/ggu003. 5.3.2

Hanssen, R. F. (2001), *Radar Interferometry: Data Interpretation and Error Analysis*, vol. 2, Springer. 2.2, 5.2.3

Hayward, N. J. (1997), A quantitative comparison of oceanic and continental rift segmentation, PhD, University of Leeds. 4.2.1

Hayward, N. J., and C. J. Ebinger (1996), Variations in the along-axis segmentation of the Afar Rift system, *Tectonics*, *15*(2), 244257, doi:10.1029/95TC02292. 1.2, 1.7, 1.2

Hodgkinson, K. M., R. S. Stein, and G. C. P. King (1996), The 1954 Rainbow Mountain-Fairview Peak-Dixie Valley earthquakes: A triggered normal faulting sequence, *Journal of Geophysical Research: Solid Earth*, *101*(B11), 25,45925,471, doi:10.1029/96JB01302. 1.1, 1.5

Hofmann, C., V. Courtillot, G. Feraud, P. Rochette, G. Yirgu, E. Ketefo, and R. Pik (1997), Timing of the Ethiopian flood basalt event and implications for plume birth and global change, *Nature*, *389*(6653), 838–841, doi:10.1038/39853. 1.2

Holland, M., J. L. Urai, and S. Martel (2006), The internal structure of fault zones in basaltic sequences, *Earth and Planetary Science Letters*, *248*(1-2), 301–315, doi:10.1016/j.epsl.2006.05.035. 3.2, 3.2

Hooper, A., P. Segall, and H. Zebker (2007), Persistent scatterer interferometric synthetic aperture radar for crustal deformation analysis, with application to Volcán Alcedo, Galápagos, *Journal of Geophysical Research: Solid Earth*, *112*(B7), B07,407, doi:10.1029/2006JB004763. 2.2

Hooper, A., D. Bekaert, K. Spaans, and M. Arkan (2012), Recent advances in SAR interferometry time series analysis for measuring crustal deformation, *Tectonophysics*, *514517*, 1–13, doi:10.1016/j.tecto.2011.10.013. 2.2

Huising, E., and L. Gomes Pereira (1998), Errors and accuracy estimates of laser data acquired by various laser scanning systems for topographic applications, *ISPRS Journal of Photogrammetry and Remote Sensing*, *53*(5), 245–261, doi:10.1016/S0924-2716(98)00013-6. 2.1.4

Kearey, P. (2009), *The Encyclopedia of the Solid Earth Sciences*, John Wiley & Sons. 3.1, 3.3.1

Keir, D., I. J. Hamling, A. Ayele, E. Calais, C. Ebinger, T. J. Wright, E. Jacques, K. Mohamed, J. O. Hammond, M. Belachew, E. Baker, J. V. Rowland, E. Lewi, and L. Bennati (2009), Evidence for focused magmatic accretion at segment centers from lateral dike injections captured beneath the Red Sea rift in Afar, *Geology*, *37*(1), 59–62, doi:10.1130/G25147A.1. 1.3

Kim, Y.-S., and D. J. Sanderson (2005), The relationship between displacement and length of faults: a review, *Earth-Science Reviews*, *68*(3-4), 317–334, doi:10.1016/j.earscirev.2004.06.003. 1.1, 1.1, 1.3, 3.3.1

Kim, Y.-S., J. R. Andrews, and D. J. Sanderson (2000), Damage zones around strike-slip fault systems and strike-slip fault evolution, Crackington Haven, southwest England, *Geosciences Journal*, *4*(2), 53–72, doi:10.1007/BF02910127. 1.3

Kim, Y.-S., J. R. Andrews, and D. J. Sanderson (2001), Reactivated strikeslip faults: examples from north Cornwall, UK, *Tectonophysics*, *340*(34), 173–194, doi:10.1016/S0040-1951(01)00146-9. 1.1

Kim, Y. S., D. C. P. Peacock, and D. J. Sanderson (2004), Fault damage zones, *Journal of Structural Geology*, *26*(3), 503517. 3.3.1

Kostrov, V. V. (1974), Seismic moment and energy of earthquakes, and seismic flow of rock, *Izv. Acad. Sci. USSR Phys. Solid Earth*, *1*, 2344. 4.4.1

Krabill, W. B., and C. F. Martin (1987), Aircraft positioning using global positioning system carrier phase data, *Navigation*, *34*(1), 1–21. 2.1.3

Lahitte, P., P.-Y. Gillot, T. Kidane, V. Courtillot, and A. Bekele (2003), New age constraints on the timing of volcanism in central Afar, in the presence of propagating rifts, *Journal of Geophysical Research*. 1.2, 1.2, 4.1

Latypov, D. (2002), Estimating relative lidar accuracy information from overlapping flight lines, *ISPRS Journal of Photogrammetry and Remote Sensing*, *56*(4), 236–245, doi:10.1016/S0924-2716(02)00047-3. 2.1.4

Lee, J.-S., K. P. Papathanassiou, T. L. Ainsworth, M. R. Grunes, and A. Reigber (1998), A new technique for noise filtering of SAR interferometric phase images, *Geoscience and Remote Sensing, IEEE Transactions on*, *36*(5), 14561465. 2.2

Li, Z., E. J. Fielding, P. Cross, and R. Preusker (2009), Advanced InSAR atmospheric correction: MERIS/MODIS combination and stacked water vapour models, *International Journal of Remote Sensing*, *30*(13), 33433363. 2.2

Lim, K., P. Treitz, M. Wulder, B. St-Onge, and M. Flood (2003), LiDAR remote sensing of forest structure, *Progress in Physical Geography*, *27*(1), 88106. 2.1

Maguire, P. K. H., G. R. Keller, S. L. Klemperer, G. D. Mackenzie, K. Keranen, S. Harder, B. O Reilly, H. Thybo, L. Asfaw, and M. A. Khan (2006), Crustal structure of the northern Main Ethiopian Rift from the EAGLE controlled-source survey; a snapshot of incipient lithospheric break-up, *SPECIAL PUBLICATION-GEOLOGICAL SOCIETY OF LONDON*, *259*, 269. 5.1

Manighetti, I., P. Tapponnier, P. Y. Gillot, E. Jacques, V. Courtillot, R. Armijo, J. C. Ruegg, and G. King (1998), Propagation of rifting along the Arabia-Somalia plate boundary: Into Afar, *Journal of Geophysical Research*, *103*(B3), 4947–4974. 1.2

Manighetti, I., G. C. P. King, Y. Gaudemer, C. H. Scholz, and C. Doubre (2001), Slip accumulation and lateral propagation of active normal faults in Afar, *Journal of Geophysical Research-Solid Earth*, *106*(B7), 13,667–13,696. 3.1, 3.1, 3, 5.4, 6.3

Mansfield, C., and J. Cartwright (1996), High resolution fault displacement mapping from three-dimensional seismic data: evidence for dip linkage during fault growth, *Journal of Structural Geology*, *18*(23), 249–263, doi:10.1016/S0191-8141(96)80048-4. 3.1

Mansfield, C., and J. Cartwright (2001), Fault growth by linkage: observations and implications from analogue models, *Journal of Structural Geology*, *23*(5), 745763. 1.4, 5, 3, 5.4, 1

Marrett, R., and R. W. Allmendinger (1991), Estimates of strain due to brittle faulting: sampling of fault populations, *Journal of Structural Geology*, *13*(6), 735–738, doi: 10.1016/0191-8141(91)90034-G. 1.1

Massonnet, D., and K. L. Feigl (1998), Radar interferometry and its application to changes in the Earth's surface, *Reviews of Geophysics*, *36*(4), 441500, doi:10.1029/97RG03139. 2.2, 2.2

MATLAB (2012), *version 7.14.0.739 (R2012a)*, The MathWorks Inc., Natick, Massachusetts. 2.1.5

Maune, D. (2001), *Digital Elevation Model Technologies and Applications: The DEM Users Manual*, ASPRS, Maryland. 2.1, 2.1.4

McClusky, S., R. Reilinger, G. Ogubazghi, A. Amleson, B. Healeb, P. Vernant, J. Sholan, S. Fisseha, L. Asfaw, R. Bendick, and L. Kogan (2010), Kinematics of the southern Red , *Geophysical Research Letters*. 1.2, 1.7

Medynski, S., R. Pik, P. Burnard, A. Williams, C. Vye-Brown, D. Ferguson, P.-H. Blard, L. France, G. Yirgu, J. Seid, D. Ayalew, and A. Calvert (2013), Controls on magmatic cycles and development of rift topography of the Manda Hararo segment (Afar, Ethiopia): Insights from cosmogenic ^{3}He investigation of landscape evolution, *Earth and Planetary Science Letters*, *367*, 133–145, doi:10.1016/j.epsl.2013.02.006. 4.2.3

Morley, C. K., R. A. Nelson, T. L. Patton, and S. G. Munn (1990), Transfer zones in the East African rift system and their relevance to hydrocarbon exploration in rifts, *AAPG Bulletin*, *74*(8), 1234–1253. 1.1

Nissen, E., A. K. Krishnan, J. R. Arrowsmith, and S. Saripalli (2012), Three-dimensional surface displacements and rotations from differencing pre- and post-earthquake LiDAR point clouds, *Geophysical Research Letters*, *39*(16), L16,301, doi:10.1029/2012GL052460. 5.3.1, 5.17, 6.2

Passalacqua, P., T. Do Trung, E. Foufoula-Georgiou, G. Sapiro, and W. E. Dietrich (2010), A geometric framework for channel network extraction from lidar: Nonlinear diffusion and geodesic paths, *Journal of Geophysical Research: Earth Surface (20032012)*, *115*(F1). 2.1

Peacock, D., and D. Sanderson (1991), Displacements, segment linkage and relay ramps in normal fault zones, *Journal of Structural Geology*, *13*(6), 721–733, doi:10.1016/0191-8141(91)90033-F. 1.1, 1.1, 1.3, 4.2.1, 4.3, 3, 6.3

Peacock, D., and D. Sanderson (1996), Effects of propagation rate on displacement variations along faults, *Journal of Structural Geology*, *18*(23), 311–320, doi:10.1016/S0191-8141(96)80052-6. 1.1

Peacock, D. C. P. (2002), Propagation, interaction and linkage in normal fault systems, *Earth-Science Reviews*, *58*(1-2), 121–142, doi:10.1016/S0012-8252(01)00085-X. 1.1, 1.2, 4.5, 3, 5.4, 6.3, 6.3

Peacock, D. C. P., and E. A. Parfitt (2002), Active relay ramps and normal fault propagation on Kilauea Volcano, Hawaii, *Journal of Structural Geology*, *24*(4), 729742. 1.1

Polit, A. T., R. A. Schultz, and R. Soliva (2009), Geometry, displacement-length scaling, and extensional strain of normal faults on Mars with inferences on mechanical stratigraphy of the Martian crust, *Journal of Structural Geology*, *31*(7), 662–673, doi:10.1016/j.jsg.2009.03.016. 3.1, 3.1

Pollard, D. D., and A. Aydin (1984), Propagation and linkage of oceanic ridge segments, *Journal of Geophysical Research*, *89*(B12), 10.017–10.028. 1.2

Pollard, D. D., P. T. Delaney, W. A. Duffield, E. T. Endo, and A. T. Okamura (1983), Surface Deformation in Volcanic Rift Zones, in *Developments in Geotectonics*, *Processes of Continental Rifting*, vol. Volume 19, edited by P. Morgan and B. Baker, pp. 541–584, Elsevier. 5.1

Rippon, J. H. (1984), Contoured patterns of the throw and hade of normal faults in the Coal Measures (Westphalian) of north-east Derbyshire, *Proceedings of the Yorkshire Geological and Polytechnic Society*, *45*(3), 147–161, doi:10.1144/pygs.45.3.147. 1.1

Rodriguez, E., and J. M. Martin (1992), Theory and design of interferometric synthetic aperture radars, in *Radar and Signal Processing, IEE Proceedings F*, vol. 139, p. 147159, IET. 2.2

Rosen, P., S. Hensley, I. Joughin, F. K.Li, S. Madsen, E. Rodriguez, and R. M. Goldstein (2000), Synthetic aperture radar interferometry, *Proceedings of the IEEE*, *88*(3), 333–382, doi:10.1109/5.838084. 2.2

Rosen, P. A., S. Hensley, G. Peltzer, and M. Simons (2004), Updated repeat orbit interferometry package released, *Eos, Transactions American Geophysical Union*, *85*(5), 47–47, doi:10.1029/2004EO050004. 2.2, 6.2

Roth, R. B., and J. Thompson (2008), Practical application of multiple pulse in air (MPiA) lidar in large-area surveys, *Proceedings of International Archives of the Photogrammetry, Remote Sensing and Spatial Information Sciences*, p. 183188. 2.1.2

Rowland, J. V., E. Baker, C. J. Ebinger, D. Keir, T. Kidane, J. Biggs, N. Hayward, and T. J. Wright (2007), Fault growth at a nascent slow-spreading ridge: 2005 Dabbahu rifting episode, Afar, *Geophysical Journal International*, *171*(3), 1226–1246, doi:10.1111/j.1365-246X.2007.03584.x. 1.3, 3.2, 4.1, 5.1, 5.1

Rubin, A., and D. Pollard (1988), Dike-induced faulting in rift zones in Iceland and Afar, *Geology*, *16*, 413–417, doi:10.1130/0091-7613(1988)016⟨0413:DIFIRZ⟩2.3.CO;2. 1.1, 1.3, 3.2, 5.1

Rubin, A. M. (1992), Dike-induced faulting and graben subsidence in volcanic rift zones, *Journal of Geophysical Research: Solid Earth*, *97*(B2), 18391858, doi:10.1029/91JB02170. 5.1, 5.3.2, 6.2

Scholz, C. H. (1991), *The Mechanics of Earthquakes and Faulting*, Cambridge University Press. 1.1

Schultz, R. A., and H. Fossen (2002), Displacement-length scaling in three dimensions: the importance of aspect ratio and application to deformation bands, *Journal of Structural Geology*, *24*(9), 1389–1411, doi:10.1016/S0191-8141(01)00146-8. 1.1

Shaw, P. R. (1992), Ridge segmentation, faulting and crustal thickness in the Atlantic Ocean, *, Published online: 06 August 1992; | doi:10.1038/358490a0*, *358*(6386), 490–493, doi:10.1038/358490a0. 4.2.3

Shaw, P. R., and J. Lin (1993), Causes and consequences of variations in faulting style at the mid-atlantic ridge, *Journal of Geophysical Research: Solid Earth*, *98*(B12), 21,839–21,851, doi:10.1029/93JB01565. 3.1, 4.2.3

Shaw, W. J., and J. Lin (1996), Models of ocean ridge lithospheric deformation: Dependence on crustal thickness, spreading rate, and segmentation, *Journal of Geophysical Research: Solid Earth*, *101*(B8), 17,977–17,993, doi:10.1029/96JB00949. 4.2.3, 4.5

Sheil, K. (2012), Structural and statistical analysis of the Dabbahu Rift (Afar, Ethiopia) using multiple datasets of remote imagery, MSc thesis, University of Auckland. 4.2.2

Siebert, L., and T. Simkin (2002), Volcanoes of the world: an illustrated catalog of holocene volcanoes and their eruptions. smithsonian institution, global volcanism program digital information series, GVP-3, *Ser., GVP-3, Smithsonian Inst., Washington, DC [Available at http://www. volcano. si. edu/world/.]*. 1.7

Solomon, S. C., P. Y. Huang, and L. Meinke (1988), The seismic moment budget of slowly spreading ridges, *Nature*, *334*(6177), 58–60, doi:10.1038/334058a0. 5.1

Tentler, T. (2005), Propagation of brittle failure triggered by magma in Iceland, *Tectonophysics*, *406*(1), 1738. 5.1

Thybo, H., and C. A. Nielsen (2009), Magma-compensated crustal thinning in continental rift zones, *Nature*, *457*(7231), 873–876. 5.1

Toda, S., R. S. Stein, V. Sevilgen, and J. Lin (2011), Coulomb 3.3 graphic-rich deformation and stress-change software for earthquake, tectonic, and volcano research and teaching–user guide, *U.S. Geological Survey Open-File Report 2011–1060*. 6.1

Trudgill, B., and J. Cartwright (1994), Relay-ramp forms and normal-fault linkages, Canyonlands National Park, Utah, *Geological Society of America Bulletin*, *106*(9), 11431157. 1.1, 1.1, 1.6, 4.2.1, 4.5, 3, 5.2.4, 5.4, 6.3

Tryggvason, E. (1984), Widening of the Krafla fissure swarm during the 1975-1981 volcano-tectonic episode, *Bulletin Volcanologique*, *47*(1), 47–69, doi:10.1007/BF01960540. 5.1

Ussyshkin, R. V., and M. Boba (2008), Performance characterization of a mobile LiDAR system: expected and unexpected variables, in *ASPRS Conference Proceedings*. 2.1.1

van Wyk de Vries, B., and O. Merle (1996), The effect of volcanic constructs on rift fault patterns, *Geology*, *24*(7), 643–646, doi:10.1130/0091-7613(1996)024⟨0643:TEOVCO⟩2.3.CO;2. 4.1

Vaughn, C., J. L. Button, W. B. Krabill, and D. Rabine (1996), Georeferencing of airborne laser altimeter measurements, *International Journal of Remote Sensing*, *17*(11), 2185–2200, doi:10.1080/01431169608948765. 2.1.3

Vye-Brown, C., S. Medynski, K. Smith, L. Field, and T. Wright (2012), Geological map of the Dabbahu (Manda-Hararo) Rift, North, 1:100,000 scale. 3.1, 4.1, 4.2, 4.3, 4.2.3, 4.4.2, 5.2.4, 5.9, 5.13

Walsh, J., A. Nicol, and C. Childs (2002), An alternative model for the growth of faults, *Journal of Structural Geology*, *24*(11), 1669–1675, doi:10.1016/S0191-8141(01)00165-1. 1.1, 1.3

Walsh, J. J., and J. Watterson (1987), Distributions of cumulative displacement and seismic slip on a single normal fault surface, *Journal of Structural Geology*, *9*(8), 10391046. 1.1

Walsh, J. J., and J. Watterson (1988), Analysis of the relationship between displacements and dimensions of faults, *Journal of Structural Geology*, *10*(3), 239–247, doi:10.1016/0191-8141(88)90057-0. 1.1, 3.1, 4.5

Watterson, J. (1986), Fault dimensions, displacements and growth, *Pure and Applied Geophysics*, *124*(1), 365–373, doi:10.1007/BF00875732. 1.1, 1.1

Wernicke, B., and B. Burchfiel (1982), Modes of extensional tectonics, *Journal of Structural Geology*, *4*(2), 105–115, doi:10.1016/0191-8141(82)90021-9. 4.4.2

Wesnousky, S. G. (1986), Earthquakes, quaternary faults, and seismic hazard in California, *Journal of Geophysical Research: Solid Earth*, *91*(B12), 12,58712,631, doi:10.1029/JB091iB12p12587. 1.1

Wesnousky, S. G. (2008), Displacement and Geometrical Characteristics of Earthquake Surface Ruptures: Issues and Implications for Seismic-Hazard Analysis and the Process of Earthquake Rupture, *Bulletin of the Seismological Society of America*, *98*(4), 1609–1632, doi:10.1785/0120070111. 1.1, 1.4

White, R. S., L. K. Smith, A. W. Roberts, P. A. F. Christie, N. J. Kusznir, A. M. Roberts, D. Healy, R. Spitzer, A. Chappell, and J. D. Eccles (2008), Lower-crustal intrusion on the North Atlantic continental margin, *Nature*, *452*(7186), 460–464. 5.1

Willemse, E. J., D. D. Pollard, and A. Aydin (1996), Three-dimensional analyses of slip distributions on normal fault arrays with consequences for fault scaling, *Journal of Structural Geology*, *18*(23), 295–309, doi:10.1016/S0191-8141(96)80051-4. 1.1, 1.1, 3, 6.3

Willemse, E. J. M. (1997), Segmented normal faults: Correspondence between three-dimensional mechanical models and field data, *Journal of Geophysical Research: Solid Earth*, *102*(B1), 675692, doi:10.1029/96JB01651. 1.1, 1.1

Wojtal, S. F. (1994), Fault scaling laws and the temporal evolution of fault systems, *Journal of Structural Geology*, *16*(4), 603–612, doi:10.1016/0191-8141(94)90100-7. 1.1

Wojtal, S. F. (1996), Changes in fault displacement populations correlated to linkage between faults, *Journal of Structural Geology*, *18*(23), 265–279, doi:10.1016/S0191-8141(96)80049-6. 1.1

Wolfenden, E., C. Ebinger, G. Yirgu, P. R. Renne, and S. P. Kelley (2005), Evolution of a Volcanic Rifted Margin: Southern Red Sea, Ethiopia, *Geological Society of America Bulletin*, *117*(7-8), 846–864, doi:10.1130/B25516.1. 1.2

Wright, T. J., C. Ebinger, J. Biggs, A. Ayele, G. Yirgu, D. Keir, and A. Stork (2006), Magma-maintained rift segmentation at continental rupture in the 2005 Afar dyking episode, *Nature*, *442*(7100), 291–294, doi:10.1038/nature04978. 1.3, 1.3, 5.1, 6.2

Wright, T. J., F. Sigmundsson, C. Pagli, M. Belachew, I. J. Hamling, B. Brandsdttir, D. Keir, R. Pedersen, A. Ayele, C. Ebinger, P. Einarsson, E. Lewi, and E. Calais (2012), Geophysical constraints on the dynamics of spreading centres from rifting episodes on land, *Nature Geoscience*, *5*(4), 242–250, doi:10.1038/ngeo1428. 1.3, 5.1, 5.2

Yirgu, G., C. J. Ebinger, and P. K. H. Maguire (2006), The Afar volcanic province within the East African Rift System: introduction, *Geological Society, London, Special Publications*, *259*(1), 1–6, doi:10.1144/GSL.SP.2006.259.01.01. 1.3